Mechanical Characterisation of Printed Nanosheet Network Thin Films

Aaron Sinnott

A thesis submitted for the degree of
Doctor of Philosophy in Physics

Under the supervision of
Prof. Graham Cross

School of Physics
Trinity College Dublin

2024

Declaration

I declare that this thesis has not been submitted as an exercise for a degree at this or any other university and it is entirely my own work.

I agree to deposit this thesis in the University's open access institutional repository or allow

the Library to do so on my behalf, subject to Irish Copyright Legislation and Trinity College Library conditions of use and acknowledgement.

I consent to the examiner retaining a copy of the thesis beyond the examining period, should they so wish (EU GDPR May 2018).

Elements of this work that have been carried out jointly with others have been acknowledged in the text where applicable, with the contributions of each member noted.

Aaron Sinnott

Aaron Sinnott

Acknowledgements

I'd like to thank Prof. Cross for his extremely valuable supervision during the course of this project, and for the opportunity to work in his group. From providing avenues to continue my work remotely over Covid, to allowing me endless freedom in how best to follow my research, I couldn't have asked for a more supportive supervisor. He had confidence in me and my results at times I was second guessing myself, and was always on the lookout for ways to help my progression beyond the lab work. He's had endless patience listening to me explain my convoluted analysis like some madman and I wouldn't have made it to the end without his guidance. I also thank Prof. Coleman for always giving this project his attention and expertise despite an extremely busy schedule, and to Prof. Moebius for allowing himself to be dragged into almost every results meeting for his input.

I'd also like to thank all the members of the group who helped me throughout the past four years, particularly Majid who has heard "Hey Majid do you know how to use the…" more times than he'd probably like. Johnny Coleman's group deserve a special mention for adopting a nanomechanics student and nodding along while he rambles about lock-in points and surface roughness. Particularly Adam for never once telling me to get lost after asking for yet another sample, Cian and Luke for somehow getting results out of an increasingly deteriorating FIB, Eoin for picking up where Adam left off when he left for 'career development' (and definitely not to get away from my nagging), and to all of the above for several Christmas gluhweins and conferences for 'respectable professionals'.

To my friends both in college and who were wise enough to stay in the real world, thank you for the good times and distraction from all the work over the last four years.

To my family, I can only say thank you for all the support. One day I'll have an answer to 'so what is it you actually do?' that makes some sort of sense. To Anna, Cathal, and Sophie, somehow I'm still the most childish of us, so if you could slow down a little and let me catch up that'd be great. To my Parents, there hasn't been a day in my life you haven't supported me in every way you can, and I wouldn't have made it anywhere without it. Thank you both and I hope I'll make you proud.

Abstract

The response of materials to applied stress and the resulting deformation is a fundamental cornerstone of condensed matter physics and materials research. From exciting new prospects such as the conductive nanosheet networks formed from printed two-dimensional material dispersions like graphene, to more longstanding puzzles such as the fundamental nature of plasticity in the entangled threads of polymer glasses, there exists a host of poorly understood mechanisms and interactions yet to be unravelled by the scientific community. On top of this, means for accurate and comprehensive mechanical exploration of thin film materials has only recently been made possible due to new nanomechanical advances, opening up further unexplored avenues of investigation.

In this work, I perform explorations into the nanomechanical properties and processing of thin films of disordered matter ranging from complex printed networks of graphene and MoS_2 nanosheets to glassy polymers. These materials, though differing in fundamental structure, can be examined using a common nanomechanical framework. Using carefully aligned flat punch indentation of stiffly supported thin films, I implemented the recently developed layer compression test which allows for *in situ* constitutive analysis of compressive stress vs strain behaviour providing close approximation to a uniform, confined uniaxial strain state to compressive strains well beyond the plastic yield point. A finite element exploration was performed to examine the degree of fidelity to uniaxial strain as a function of tip diameter to film thickness aspect ratio, α, and film to substrate modulus ratio, S. It was found that utilising a simple analytical substrate correction, variations to within 1% error are achievable with typical experimental parameters.

The uniform compression imposed by the layer compression test was utilised experimentally to perform the first explorations of pressure dependent mechanics of thin film polystyrene and sprayed graphene nanosheet networks. This revealed a 45% stiffening in the regime of elastic compression up until the yield point for both materials, despite large fundamental morphological differences between them. Yielding of thin film PMMA was also observed in the layer compression test, in contrast to previous studies which found that PMMA would not yield in a compressive uniaxial strain geometry. This was attributed to an increase of shear compared to pure uniaxial strain, introduced by the layer compression test contact geometry. Micropatterned polystyrene thin films were also prepared via spherical tip compression to probe densification using β-NMR spectroscopy, which probes the sidegroup relaxation dynamics via the decay anisotropy of implanted ^{8}Li. A clear reduction in relaxation rate was observed for micropatterned film in comparison to an unpatterned counterpart.

The layer compression test was further utilised to explore the compressive mechanical nature of printed nanosheet network thin films of liquid phase exfoliated graphene and MoS_2. A viscoelastic response was observed, owing to the combined sheet bending and slippage modes of deformation present. Important mechanical properties such as the effective elastic moduli and yield stress and strain were measured and quantified for networks with a range of parameters, with changes to these properties from densification also measured. The results were compared favourably to a folding sheet model adapted from crumpled sheet mechanics. Creep experiments were performed to quantify time dependent mechanics under applied strain, and the effect of chemical cross linking on the mechanical nature of MoS_2 networks was also explored.

Strain recovery and morphological changes with compression were analysed on the compressed network regions using focused ion beam cross sections and electron microscope tomography to gauge the compatibility of the networks with mechanical post processing for morphological improvements. Significant strain recovery was noted over long timescales, limiting the potential of compressive post processing. However, recovery was noted to drop significantly with introduction of shear deformation, and more extremely to near zero magnitude at a sharply defined stress point, dubbed the lock-in point. This lock-in phenomena was also associated with a distinct change in mechanical response of the networks, indicating a fundamental change in material behaviour at this point that is maintained in ambient conditions for graphene networks when pressure is removed. This lock-in point provides promising avenues for post processing and further exploration.

In summary, this work provides the first nanomechanical exploration of sprayed nanosheet network thin films for applications in printed electronics and shines light on various processes of deformation as well as previously unknown pressure induced behavioural changes, with implications for the manufacture and operation of a range of printed electronic technologies.

Publications

1. A.D. Sinnott, A. Kelly, C. Gabbett, J. Munuera, L. Doolan, M. Mobius, S. Ippolito, P. Samorí, J.N. Coleman, G.L.W. Cross "Mechanical Properties of Conducting Printed Nanosheet Network Thin Films Under Uniaxial Compression" Advanced Materials, in press (**2023**)

2. A.D. Sinnott, A. Kelly, C. Gabbett, M. Mobius, J.N. Coleman, G.L.W. Cross "Pressure Dependent Mechanical Properties of Thin Films under Uniaxial Strain via the Layer Compression Test" Journal of Materials Research (**2023**)

3. A.D. Sinnott, O. Brazil, and G.L.W. Cross "The effect of contact aspect ratio and film to substrate elastic modulus ratio on stress vs strain up to the point of yield during flat punch thin film indentation of an elastic-plastic film" Frontiers in Materials 9 (**2022**): 906204

4. D. Fujimoto, O. Brazil, WC. Oliver, MF. Jadidi, AD. Sinnott, I. McKenzie, A. Chatzichristos, MH. Dehn, VL. Karner, RF. Kiefl "^{8}Li Spin Relaxation as a Probe of the Modification of Molecular Dynamics by Inelastic Deformation of Glassy Polystyrene" Journal of Physics: Conference Series 2462 (**2022**): 012053

5. A.D. Sinnott, A. Kelly, C. Gabbett, L. Doolan, S. Ippolito, M. Mobius, P. Samorí, J.N. Coleman, G.L.W. Cross "Strain Recovery and Cohesive Lock-In of Nanosheet Network Thin Films Under High Strain Compression" Pending

6. A.D. Sinnott, A. Kelly, C. Gabbett, L. Doolan, J.N. Coleman, G.L.W. Cross "Morphological Characterisation of Uniaxially Compressed Printed Graphene Nanosheet Thin Films" Pending

Table of Contents

List of Figures

Introduction

Nanomechanics is the study of the mechanical nature of systems with one or more dimensions being best measured in the range of nanometers (typically sub 100nm). The explosion of technological and scientific interest surrounding materials and systems on the nanoscale in the last decades has led to an increasing need to characterize and study these systems and materials in a repeatable and controlled way. Thin film materials in particular have become the focus of much interest in a range of fields including optoelectronics [1], superlubricity [2, 3], bio engineering [4], printed electronics [5-7], and a host of other disciplines. While a range of comprehensive techniques exist to measure the bulk mechanical properties of materials, and despite in the last 30 years the introduction of minimally destructive analysis of micro geometries through eg. nanoindentation [8], characterization of nanoscale thin film materials remains a significant challenge [9-12]. On top of this, there exists a range of deviations from bulk behaviour in these nanoscale systems, stemming from geometric effects of these length scales (eg, confinement effects from substrate proximity, greatly increased surface area compared to bulk counterparts, greater adhesive contributions in granular or partly granular systems, etc), making many established effects that can be readily attributed to bulk materials no longer hold true for these systems. There exists therefore a clear need for a system of comprehensive and reliable measurement of the mechanical nature of thin film materials in the current technological and scientific climate surrounding materials research.

On top of the need for a method of comprehensive mechanical testing of thin films, there is a glaring gap in knowledge of the fundamental mechanisms of deformation in a range of otherwise well studied materials. While the deformation of materials with a well-structured and orderly atomic lattice (such as crystals and metals) based around lattice dislocations has been understood for some time [13], there exists a glaring gap of knowledge in the deformation pathways and carriers of plasticity in amorphous systems [14]. Although amorphous materials, such as the vast family of polymer glasses and non-equilibrium solids, inhabit almost every aspect of modern life, there exists no comprehensive system of understanding around their mechanical response. The absence of such a rigorous analytical understanding of the deformation of such materials necessitates that the industry standard means of characterisation is done through empirical testing. This adds massive monetary costs and greatly stretches the timeframe of any commercial project involving amorphous materials, with the materials testing market set the reach one billion dollars in value in the coming years [15]. The sheer vastness of polymer and amorphous systems stretches over such a large range of material morphologies that ubiquitous testing techniques are needed to efficiently quantify their behaviour; from temperature dependant viscous melts to amorphous glasses in a non-equilibrium state, liquid crystals and semi crystalline states, composite materials, foams, granular systems and more. While the current understanding surrounding some such non equilibrium systems will be explored in Chapter 1, exploration of thin film variants of these materials can give greater understanding into their deformation behaviour through the confinement imposed by a thin film geometry, as well as other useful features more readily present in thin films (such as interfacial effects, easier control of temperature uniformity than in bulk samples, etc).

Lastly, there exists a range of novel materials with no or limited literature analogues which currently exist almost exclusively in thin film form, such as networks comprised of nanosheet flakes, nanowire/nanotube networks, or composites consisting partially of one or more of these. These materials show incredible technological promise in a range of fields from energy storage [16, 17], strain sensors [18, 19], printed electronics [5-7] , textile electronics [20], and an extensive range of mechanical and electrical improvements to existing materials through the formation of composite materials [21, 22]. Developing a systematic means of understanding around the mechanical testing and characterisation of these is essential to ensure the materials science community can keep pace with the rapidly growing family of such materials.

In this thesis, the mechanics of thin films will be explored primarily with techniques derived from nanoindentation. Though a relatively young field, nanoindentation is already well established in both the scientific community and among industry, with adoption only set to grow in the coming years. Examples include the medical industry, where biosensors are used to characterise and combat certain bacterial strains [23, 24], and to measure the robustness of cell membranes and rupture mechanics to better understand the stability of these systems [25, 26]. In the semiconductor industry, nanoscale straining techniques are applied to apply compressive and tensile forces to tailor electron/hole mobility in transistor channels [27, 28], and in advanced nanolithography techniques based around nanomechanical techniques [29, 30]. As such, nanoindentation has already cemented itself as a key component of many processes across a range of industries and research fields, and adoption of incremental improvements in nanoindentation techniques can be implemented easily and efficiently for users in a host of applicable areas.

The purpose of this thesis is to explore and apply a novel nanomechanical testing technique called the Layer Compression Test (LCT) that is uniquely suited to addressing these issues. This test allows for mechanical testing of thin film materials with thicknesses far lower than what conventional nanoindentation techniques can provide [31-33]. It also has several key benefits over other techniques such as large contact area, analysis of the elastic-plastic transition, and more that will be discussed in further detail in Chapter 3, and that combined uniquely position it as a means of testing materials and geometries that are more typically troublesome for other indentation techniques [10]. While the LCT provides a powerful means of analysis, it is a newly developed technique, and up until this point has primarily been experimentally examined on thin film polymer materials [31-35]. As part of the work presented here, I include more detailed analysis of the LCT in the elastic regime using finite element simulation, expanding our understanding of the LCT, and of the parameters required to obtain accurate results.

The unique properties of the LCT (namely the large contact area and confinement effect) allow us to explore for the first time the compressive mechanical nature of networks of sprayed two dimensional flakes, deposited using inkjet spraying of exfoliated flake dispersions [5, 6, 18, 36, 37]. These networks offer large technological promise in the field of mass-producible printed electronic devices but have gone largely unexplored mechanically due to their inherent morphological complexity. The degree of morphological complexity eludes analysis from established nanomechanical process for which correction techniques are complex and limited to singular morphological features [38-41]. The exploration of the compressive mechanical response of these networks will be explored in close detail in this work, starting with the development of the processes and techniques needed to overcome the challenges associated with such complex materials, to results ranging from the degree of elastic vs anelastic response, effect of morphological parameters such as porosity and sheet thickness on the stiffness and modulus of the networks, recovery mechanisms, effect of post processing via chemical cross linking, and more.

Ch 1 : Materials and Characterisation

In this chapter I explore the materials that will be of interest in this thesis. This primarily focuses around polymer glasses and sprayed nanosheet networks. All aspects of these materials applicable to this work will be approached here, including morphology, synthesis, and characterisation and drawing from polymer mechanics, granular physics, crumpled sheet mechanics, and nanosheet networks. Due to the complexity of these fields, only the topics applicable to the materials and processes presented in this thesis will be addressed in detail.

1.1 Polymer Glass Structure

Polymers comprise long molecular chains of repeating monomer units. The unique chemical, morphological, and mechanical dynamics of polymers have made them an extensively studied material finding use in swathes of industrial and technological spaces. In this thesis polymers will be used as a reference demonstrator of the dynamics of yield and plasticity in a complex amorphous system. As such only the details of polymer dynamics pertinent to this will be explored here.

Typical polymers consist of covalently bonded carbon atoms along the main chain, and side groups of varying composition and size that can define morphological and chemical properties between otherwise similar chains. Polymer chains are highly tailorable through the chemical composition of the side groups, the chain length, and the tacticity of the chain. The tacticity refers to how side groups are arranged along the chain: Isotactic with all groups on the same side, syndiotactic on alternating sides, and atactic being random arrangement. Polymer chains may also not always be linear, with branching or cross-linking between chains possible. The degree of branching / cross linking is largely a chemical consideration but has large effects on the dynamics of polymer motion [42]. This branching and the tacticities are demonstrated in Fig. 1.1.

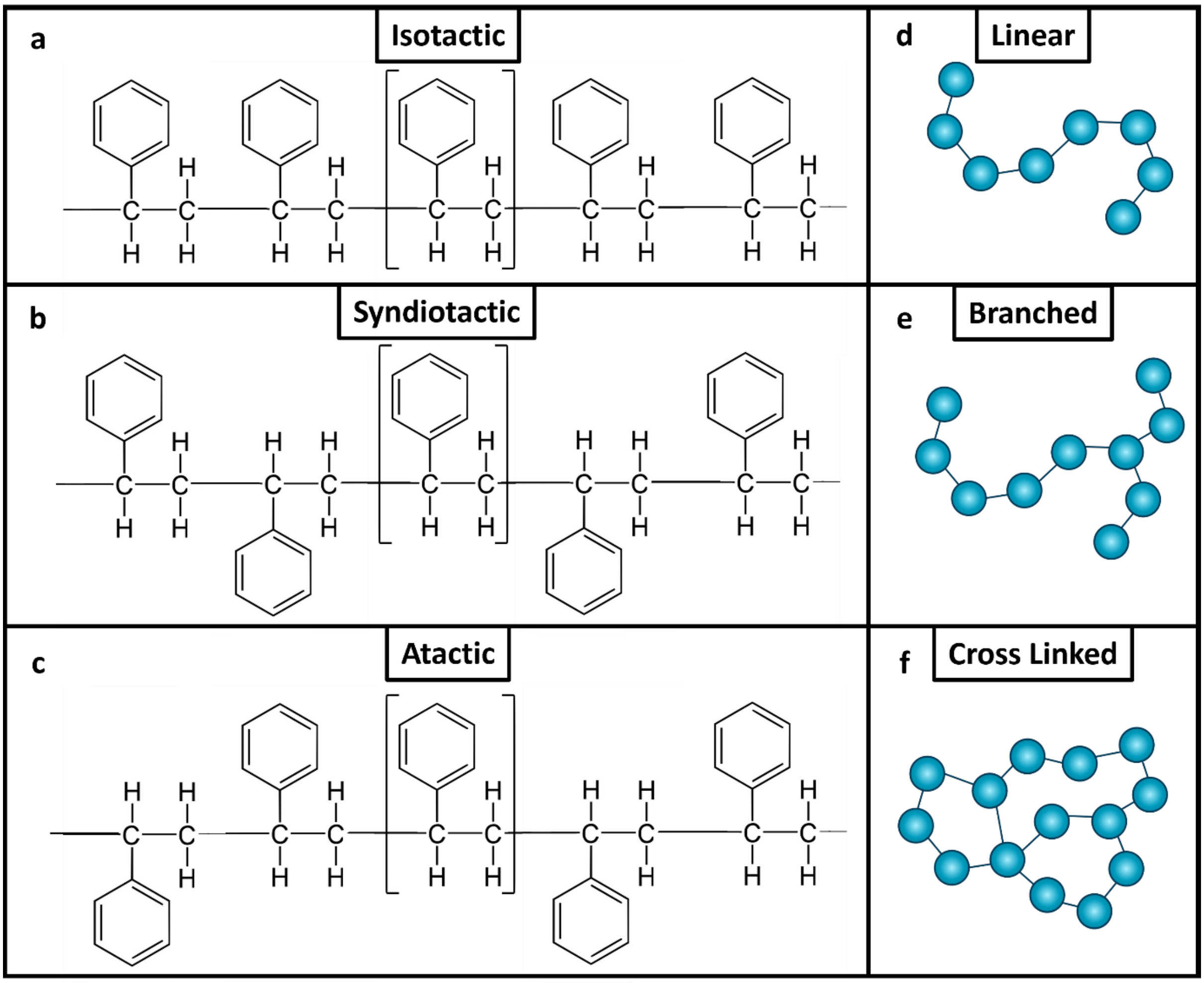

***Fig. 1.1, (a-c)** Section of a Polystyrene polymer chain. The section enclosed in brackets is the repeated monomer unit. The three tacticities of isotactic, syndiotactic, and atactic are shown. **(d-f)** shows the case of a linear, branched, and cross linked polymer where the spheres represent a monomer unit*

Solid polymer morphology depends on factors such as tacticity and thermomechanical sample preparation history. For example, syndiotactic polymers with small sidechains which are cooled from the melt stage slowly may orient themselves in a semi crystalline structure. Conversely, fast quenching or highly atactic chain composition tends to produce a non-equilibrium amorphous solid state known as a glass. The glass transition temperature is defined as the temperature below which polymer chains no longer have the time to perform thermal rearrangements on experimental timescales, forming the glass state which is an amorphous solid. This actually occurs over a narrow temperature range wherein the polymer settles into the glassy state as opposed to a discrete phase change of fully crystallizing solids [42].

The theory of Rouse dynamics [43] can be used to describe the behaviour of a single chain, however polymer materials consist of many such chains, often in an entangled state if of sufficient length [44]. In the melt phase this entanglement can be described by considering reptation dynamics (a theory of entangled chain motion envisioned as lateral confinement by a transient tube of surrounding molecules) which considers thermal effects, entanglement and its relation to viscosity, chain length, and other factors [45]. While melt dynamics offer insights into chain motion that affects the final state below the glass transition, it is currently not possible to predict the properties of the non-equilibrium glassy state from our current understanding of melt dynamics, which are often limited to short timeframe molecular simulations [44]. As it is this final glassy state that is of interest here, I will not consider melt dynamics in detail and will instead focus on the glassy state.

The glass transition is not unique to polymers and can occur in systems such as metals [46] and colloids [47]. The glass transition represents a thermal transition resulting in massively reduced kinetics [48]. Ie, there is little morphological discontinuity in the material at either side of the glass transition temperature, it is instead governed by insufficient thermal energy for continued motion. As such, glassy solids maintain a large degree of long range disorder and large regions of available free volume. Entangled polymers in the melt may relax via a spectrum of processes including α relaxation, which is long range chain movement, and β relaxation, which is short range and localised motions of the polymer ‘spine’. There are further secondary relaxation modes beyond β with incrementally decreasing dominance, such as γ and δ. While the glass transition is accompanied by a dramatic decrease in the α relaxation of the polymer chain (relaxation times increasing by roughly 14 orders of magnitude over the glass transition range) [44], the β relaxation is less strongly suppressed by lower temperatures as it does not require long range chain motion [48, 49].

Polymer glasses may densify over time as these relaxations explore available local energy minima and the material densifies. The latter process is referred to as thermal aging [44]. However, the amorphous nature and large degree of free volume remain even after long aging times and constitute a complex non equilibrium system for which mechanical properties can vary dramatically. As such the mechanical properties of polymer glasses can differ drastically depending on their morphology and thermal history. For example, literature values on the Young's modulus of glassy polystyrene range between 2.4 and 3.4 GPa [50, 51]. This variation can be induced by both thermal and mechanical history. While thermal aging occurs over long time periods at temperatures below the glass transition, a more pronounced time dependency exists for the quenching period as the temperature is reduced past the glass transition and the polymer chains solidify into a glassy state. Due to the kinetic rather than morphological nature of the glass transition, the speed at which a polymer is quenched below the glass transition has a profound effect on the available free volume (defined as the volumetric fraction comprised of void space or 'unoccupied volume' between polymeric chains), with longer quenching times giving polymer chains more time to settle into local energy minima.

Thermomechanical sample preparation history can also affect the morphological characteristic of the polymer, with polymer glasses often exhibiting strain hardening or softening with mechanical deformation [42]. In addition, the properties of amorphous, free-volume materials can have a sensitive dependence on their instantaneous mechanical state. For example, as part of the work presented in this thesis, I explore the dependence of uniaxial strain (US) deformation on the elastic and yield response of amorphous thin films, as well as attenuation of relaxation processes with mechanically induced densification.

1.2 Polymer Thin Film Synthesis : Spin Coating

Spin coating or spin casting is a method of producing thin films of a material with extremely flat topographies and thicknesses as low as a few nm. The technique finds much use in photolithography to deposit photoresist layers [52], as well as in any application where thin substrate coatings are needed such as insulators [53, 54], organic semiconductors [55], and a wide range of other uses in the R&D and semiconductor industry. It finds use also in deposition of nanoparticles [56] for uses in hydrophobic coatings [57] and superlubricity research [58], and for depositing highly aligned networks of nanosheets [59] (though I forego study of such networks in this work for more scalably produced sprayed systems). Spin coating fundamentally works off of the principle of depositing a liquid solution (or dispersion in the case of non-soluble nanomaterials) of a material of interest in a suitable solvent, on to a flat substrate that is spun at high speed to spread the solution evenly over the substrate via centrifugal force. A combination of the centrifugal force and evaporation of the solvent produces a smooth film of uniform thickness.

For polymer films, the choice of solvent for the liquid solution is important. Typically, solvent – solute pairs are chosen based on their Hildebrand solubility parameter, for which the pair should be closely matched. In this work I consider only Polystyrene (PS) thin films (Hildebrand solubility parameter $\delta \approx 18.4$ MPa$^{1/2}$) which are suitable for dilution in Toluene ($\delta = 18.2$ MPa$^{1/2}$). Light ultrasonication is typically used to aid in dispersing the polymer. The concentration of the solution will affect both the viscosity, as well as the rate of solvent evaporation. Recently it has become possible to determine analytically the required concentration and rotational speed for a desired film thickness if certain parameters are known [60], which is

$$t \approx 0.8 x_0 \left(\frac{\omega^2}{3\nu E}\right)^{-\frac{1}{3}} \tag{1.1}$$

Where t is the desired thickness, x_0 is the initial concentration, ω is the rotational speed, ν is the kinematic viscosity, and E is the evaporation rate. This approximation holds well within normal experimental bounds. In practice, however, many of these parameters are time consuming to measure accurately and so empirical observations of the required concentration and rotational speed for a given solvent – solute pair is often favoured instead [61]. After depositing the solution and allowing it to spread to the desired thickness, an annealing step is often performed at the glass transition temperature (~120°C for PS) to remove excess solvent. Subsequent thermal quenching of the film down to room temperature must be carefully controlled and monitored as it can have a profound effect on the morphological and therefore mechanical characteristic of the polymer film, as discussed in more detail in Section 1.1. This stepwise process is shown schematically in Fig. 1.2.

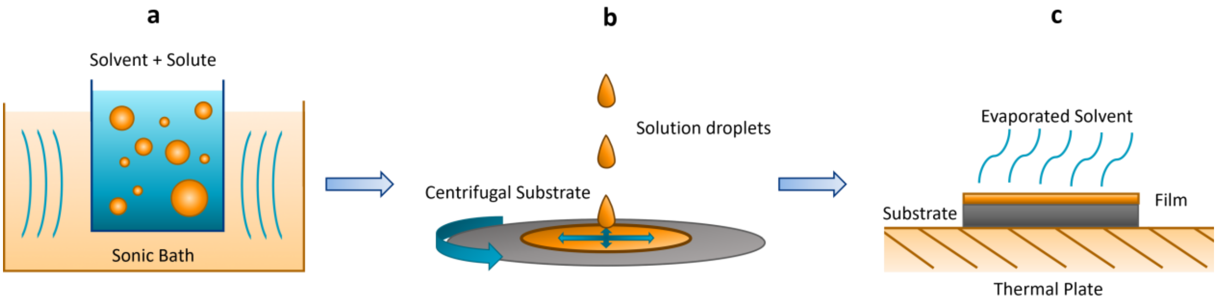

Fig. 1.2, *Spin coating process starting with* ***(a)*** *dissolution of the required film material in a suitable solvent, aided by ultrasonication,* ***(b)*** *spin coating at the necessary RPM based on the solution viscosity and required thickness, and* ***(c)*** *thermal annealing to remove excess solvent*

1.3 Granular Materials

Nanosheet network films which constitute a large portion of the research in this thesis are fundamentally a granular system of individual flakes. While the specifics of production, morphology and mechanics pertaining to nanosheet films will be explored in a following section, it is prudent to introduce concepts of granular mechanics beforehand. Granular systems are those made up of non-chemically bonded aggregates of discrete solid particles in contact. While they may be cohesive in nature through various processes, fundamentally the interaction potential between the particles is much smaller than those internal to each particle. For the system to be considered granular, interparticle media should be kept to a minimum. The presence of excessive inter particle media alters the definition towards a colloid or liquid dispersion in the case of a liquid medium, or a composite in the case of a solid medium. However, smaller amounts of media may be included without altering the definition away from granular and can have profound effects on the material's properties, such as small amounts of water introducing attractive capillary forces, and so there is no defined cut-off in definition except that the medium should not greatly surpass the interparticle contribution to the mechanical response. Crucially, granular materials typically exhibit no thermal motion, in that the thermal motion typical of molecular materials and governed by k_BT is arrested by either a larger gravitic potential, mgh, or other cohesive property.

The morphological nature of granular systems depends highly on the properties of the grain themselves, with the simplest being a system of packed spheres, but can be significantly more complex if comprised of bars, sheets, or other more complex geometries. Understanding the behaviour of granular systems is a longstanding and complex field of study due to both the fundamentally novel nature of granular material deformation, and the variations between those of different grain properties [62].

From a mechanical standpoint, this complexity is in no small part due to the resistance of granular systems to be described by the deformation of a single traditional phase of matter. Depending on the process by which stress is applied, they may exhibit properties of solids, liquids, gasses, as well as properties more unique to their granular nature [63]. A granular material at rest tends to sit in an equilibrium like a solid, but may flow like a liquid under the application of shear stress [64], though this flow is strain rate dependent and often thixotropic in nature [65, 66]. It may exhibit inelastic flow like a gas as the interaction between grains is inelastic in nature [67], or undergo elastic compression under hydrostatic pressure in a close packed geometry [68]. The negligible thermal component in a granular material (k_BT) is superseded by the potential energy of comparatively massive grains in a gravitational field (mgh, being a factor of ~10^{12} times higher than k_BT at room temperature for standard granular materials like sand [63]). For particularly small particulates, such as the nanosheet networks explored here, mgh is of little consideration. Instead, the thermodynamic fluctuations are arrested by vdW interactions, with the vdW binding energy for graphene being ~10^{-14} J vs k_BT ~10^{-21} J [69]. In either case, this precludes standard thermodynamic arguments for explaining granular motion and is the basis of solid-like behaviour at rest. However, supply sufficient vibrational energy and granular media may act in a manner very reminiscent of thermally active fluids [62, 70, 71].

Overall, granular mechanics depends strongly on the nature of the granular material as well as on the applied deformation. There is no comprehensive descriptor of granular deformation and instead properties are often extracted in the form of ubiquitous parameters based on the applied force. For example a viscosity or flow rate under a high shear influence between two plates, or a compressive Young's modulus for hydrostatic compression of soils [72, 73]. Analytical descriptions of granular material morphology are far from complete, with the majority of work focusing around jammed spherical systems [74], building from frictionless models to incorporate friction and oblong non spherical particles [75]. Mechanisms to describe mechanical behaviour is likewise uncomprehensive. While there is some research on granular mechanics from the approach of modelling individual particles [76-79], the majority of study in this area uses a continuum approach which models the response of the material as a whole, excluding singular particulate interactions. This continuum approach is the same as is generally considered for amorphous glasses explored in this thesis, for which similarities in behaviour have been found with granular systems due to the shared amorphous nature [80]. Here, I take a simple continuum approach to the mechanical analysis of the granular nanosheet networks presented in this thesis. I use confined uniaxial compression to extract solid – like properties, and creep experiments to characterise flow under applied pressure. The processes behind this continuum analysis will be explored in more detail in Chapter 2.

1.4 Nanosheet Network Structure and Synthesis

1.4.1 Graphene

While nanoparticles have had recorded use throughout history (particularly in the use of pigments [81]), it is only recently that we have developed the necessary technology to develop and study them on a grander scale, with graphene leading the charge in the two dimensional material space. The concept of single layer graphite has existed for some time, with many scientific sources commenting on the layered structure of graphite and the possibility of isolating a monolayer many decades before the isolation of graphene itself [82-84]. Geim and Novosolov's work in 2004 saw the first demonstration of true monolayer graphene production [85], which was previously thought impossible due to thermal excitations that would destabilise a flat monolayer [86]. It was soon after discovered that graphene exhibits small scale wrinkling, which suppresses the thermal fluctuations and stabilises the sheet, averting the conflict between the existence of graphene monolayers to fundamental thermodynamics [87]. Since then, there has been an explosion of interest and research around two dimensional materials, with graphene remaining the quintessential centre of the field.

The research interest around graphene is based largely on its remarkable electrical and mechanical properties, made possible due to its orbital structure. The sp^2 hybridised carbon atoms that make up graphene form three σ bonds with each nearest neighbour in a honeycomb structure, which allows the two dimensional nature of the sheet due to the ~120° bond angle [88]. This honeycomb structure is shown in Fig. 1.3. This affords it immense mechanical stability, with a tensile modulus of <1,000 GPa and tensile yield of ~130 GPa making it one of the strongest materials ever recorded [88-90], and with the Nobel prize announcement famously stating that one square meter of graphene sheet could support a typical housecat, despite weighing less than the cat's whisker [91]. Despite remarkable mechanical properties, research into its mechanical properties is not as extensive as its electrical properties. The stark difference between its in and out of plane bonding strengths allow the production of nanosheets through scalable exfoliation techniques, discussed further in this chapter.

The nature of its electrical properties stem also from the sp^2 hybridisation. As carbon has four valence electrons and the sp^2 hybridisation only accounts for bonding of three, there exists one more electron in the unhybridized p orbital perpendicular to the graphene plane. These form together in a half filled band of delocalised electrons above the lattice, giving graphene remarkable electron transport properties [83]. The band structure of graphene make it semi-metallic in the mono and bi layer, and the periodic nature of the lattice allow the electrons to behave as quasiparticles called Dirac Fermions with effectively zero electron mass [88]. This gives it exceptional carrier mobilities, ballistic (non-diffusive) transport, and a low dependence on temperature [88, 92].

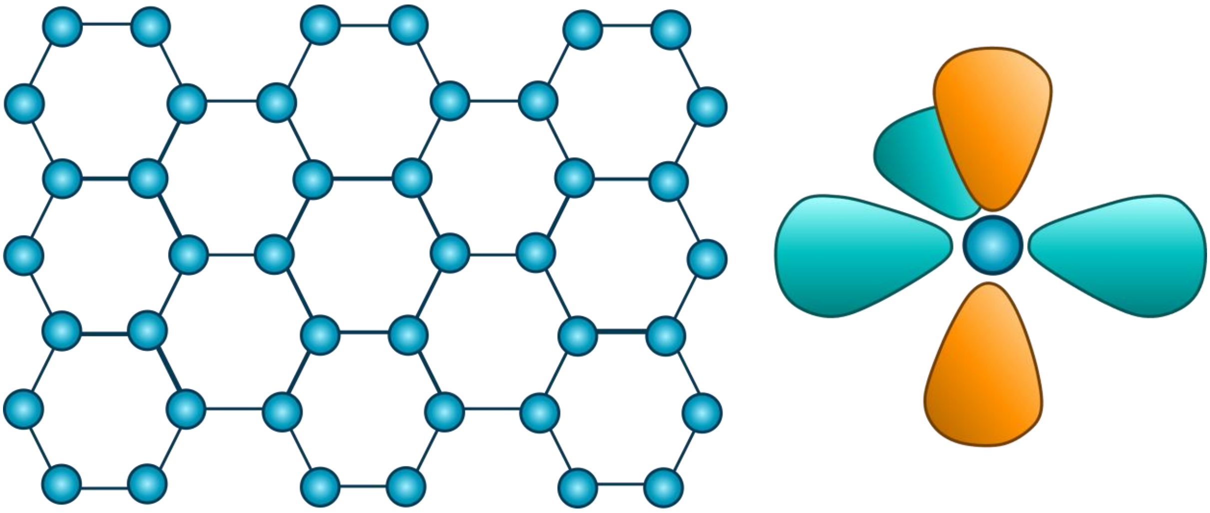

Fig. 1.3, *Honeycomb lattice structure of a graphene sheet (left) and orbital structure (right) showing sp^2 hybridised orbitals (teal), and out of plane pi orbital (orange). The sp^2 orbitals are responsible for its planar honeycomb structure and mechanical strength, while the pi orbitals overlap above and below the graphene sheet into a delocalised electron cloud, and facilitate high electron mobility*

1.4.2 Exfoliation Techniques

The discovery of graphene led to the synthesis of a range of other two dimensional materials from layered bulk counterparts. While the properties of these materials and of graphene open up a range of potential applications [93]. The potential applications as explored in laboratory settings is vast and was recognised from graphene's inception, but there has remained a critical problem of viable industry scale production techniques for defect free nanosheets. Geim and Novoselev's original discovery via adhesive layer mechanical exfoliation opened up the possibility of graphene production, but lacked scalability [85]. Since then, a range of techniques have been developed for the production of graphene. 'Bottom up' techniques which rely on growing thin films from precursor elements, such as chemical vapour deposition (CVD) [94] and atomic layer deposition (ALD) [95], have proven more challenging to scale upwards than 'top down' techniques, which rely on exfoliation of bulk material to form the nanosheets. Several viable large scale exfoliation methods exist, such as liquid phase exfoliation (LPE) [36, 96] and electrochemical exfoliation (EE) [97], all of which operate using a similar principle of shearing flakes of two dimensional material (eg graphene) from their bulk counterpart (eg graphite) in a liquid solution. Advantages of exfoliation techniques for the production of nanosheets on a large scale include tunable flake sizes, in addition to the simplicity of production and the ability to scale these techniques to very large batch sizes [36, 96, 98].

1.4.3 Liquid Phase Exfoliation

Liquid phase exfoliation is one of the easiest and cheapest exfoliation techniques for layered materials as it relies primarily on overcoming the interlayer vdW forces using ultrasonic energy and so generally does not require complex solvents or electrochemistry, allowing batch sizes to be much larger than for other exfoliation techniques [96]. Typically, LPE proceeds in a stepwise manner; firstly an ultrasonication step in solution to separate the layers, then a solution stabilisation step, and finally size selection of the produced sheets, usually through cascade centrifugation.

Ultrasonication proceeds via converting high frequency mechanical oscillations into ultrasonic waves to provide agitation and energy to facilitate the exfoliation process. Both vibration and cavitation can play a role in separating the layers from the bulk. Cavitation is the more vigorous process of the two, and works via the production of bubbles in the solution by increasing the distance between liquid molecules. The bubbles subsequently expand and collapse, causing rapid high energy events in the liquid that can separate flakes from the bulk crystal material [99, 100]. Bath sonication is a less vigorous process whereby the vibrational modes induced by the sonication delaminate nanosheets from the crystal directly [101].

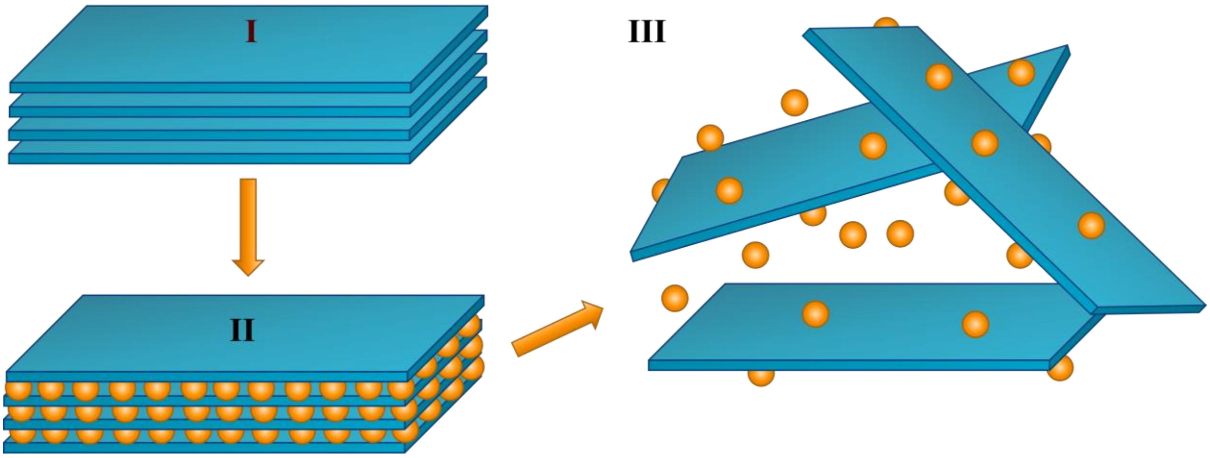

Fig. 1.4, *Exfoliation of pristine bulk crystal by introduction of suitable solvent and kinetic energy via sonication to separate nanosheets from the bulk, presented in a stepwise manner in* ***(I)*** *through* ***(III)***

Stabilisation of the resulting nanosheet solution is important to prevent aggregation of the flakes, and this is done either through careful choice of a stabilising solvent, or via surfactant processes. Stabilisation via solvent may also allow for more effective exfoliation in the sonication stage depending on the solvent choice [102]. In the most simple case, solvents are chosen by surface energy considerations, as if the solvent and nanosheet surface energies match, the concentration of the solution can be increased significantly while avoiding aggregation [36]. A more comprehensive approach considers intermolecular potentials between the solvent and nanosheets and is well described by the Flory-Huggins interaction parameter, which is used extensively for aggregate solutions such as paint mixes, polymer blends, etc [103-106]

$$\chi = \frac{v_0}{kT}\left[\left(\delta_{D,x} - \delta_{D,y}\right)^2 + \frac{\left(\delta_{P,x}-\delta_{P,y}\right)^2}{4} + \frac{\left(\delta_{H,x}-\delta_{H,y}\right)^2}{4}\right] \tag{1.2}$$

Where v_0 is the molecular volume, T is the absolute temperature, and k is the Boltzman constant. δ are the Hildebrand solubility parameters, where subscripts x, y correspond to the solute and solvent, and subscripts D, P, and H correspond to dispersive, polar, and hydrogen bonding components respectively. For $\chi > 0$, solute : solute interactions are dominant and aggregation will occur, while if $\chi < 0$ the solution will be stable. The solvents most commonly used are N-methyl-2-pyrrolidone (NMP) and dimethylformamide (DMF), which highlights the largest drawback with solvent stabilisation:

toxicity and environmental impact. Though recent research has been focussed around exploring safer and more eco-friendly alternatives [101, 107, 108], surfactant stabilisation remains an alternative.

Surfactant stabilisation is performed in aqueous solution and works via adsorption of a molecule on the nanosheet surface [101, 109, 110]. Surfactants are amphiphilic (containing a hydrophobic and hydrophilic component), the hydrophobic end attaches to the nanosheet, and the hydrophilic portions self-repel from other attached surfactant molecules, preventing aggregation. While surfactant stabilisation has many benefits over solvent based techniques (being that it is cheaper, more environmentally friendly, safer, and may produce smaller nanosheets), it also exhibits certain drawbacks when compared to solvent techniques; the surfactants interfere with transport properties in a sprayed network, and aqueous spraying presents problems with viscosity and volatility compared to other solvents. This may be mitigated by solvent transfer before the spraying stage, or by using liquid surfactants which are easier to remove from a printed film.

Exfoliation techniques produce suspended nanosheets of various sizes, though limits do exist on the aspect ratio achievable via sonication based liquid exfoliation [111]. Even within these bounds, it is prohibitively difficult to control nanosheet size in the exfoliation stage. Instead, a post exfoliation size selection step is employed to create solutions with nanosheet sizes with the required polydispersity. This is general done via cascade centrifugation [112]. A centrifugal force is applied to a sample of liquid dispersion which acts to separate the nanosheets by mass, with the higher mass sheets gathering towards the furthest end of the container. This creates a gradient in the liquid dispersion based on nanosheet size, from which the portion containing the required size range can be extracted. This gradient can be controlled by tailoring the rotational speed (measured typically in rotations per minute (RPM)) of the centrifugation step based on the mass of the particles in the dispersion and the required mass range for the application. In cascade centrifugation, several centrifugal steps are performed to get the desired size range. A slow initial step sediments the largest, unexfoliated particles, which are extracted and removed from the solution. This process is repeated with increasingly higher RPM, extracting increasingly smaller particle ranges from the dispersion until the required size range is produced. A light sonication step is performed on the resulting solution to redisperse the nanosheets back into the solution from the sediment.

Carefully controlled centrifugation can produce dispersions with the desired size, but more careful size determination after the fact can be of benefit. While there are many ways in which this may be done, including electron microscopy [37], I focus instead in this work on UV-Vis spectroscopy, and atomic force microscopy (AFM).

1.5 Nanosheet size Characterisation

1.5.1 UV-Vis spectroscopy

UV-Vis spectroscopy is typically used to characterise the electronic structure of a material, but has found use in analysing size dispersions in nanosheet solutions [113]. UV-Vis spectroscopy works via applying light with a range of wavelengths (energies) to a dispersion and measuring how much light is absorbed and transmitted by the solution for each energy, and can be represented in an extinction spectra which is the sum of the absorption and scattering contributions [114]. Absorption occurs via excitation of the electron energy levels in a material and results in a sharp absorption peak. However, scattering within the solution can also occur, which acts to broaden the extinction peak. In nanosheet dispersion this scattering is dependent on the size of the nanosheets in the dispersion [113]. Decoupling the scattering and absorption components of the extinction allows analysis of nanosheet size through this broadening, allowing in-situ solution phase characterisation of average nanosheet length in a sample [115].

1.5.2 Atomic Force Microscopy (AFM)

A more rigorous means of nanosheet size determination is through statistical AFM measurements. AFM was developed in the 1980’s and operates primarily on a contact based surface topography determination [116]. A sharp probing tip (typically ~10nm diameter or smaller depending on required fidelity) attached to a flexible cantilever (~40 N/m stiffness, but much stiffer can be used for mechanical probing (~350 N/m)) is moved over the surface of a sample of interest. As the tip moves over the surface, the cantilever bends to accommodate the changing topography, and a laser is shone onto and reflected off the cantilever tip onto a photodiode, which can relate the movement of the laser to the cantilever motion. Typically however, the laser deflection is instead used to provide feedback for a piezo which keeps the cantilever deflection constant, and the voltage signal required to do this is then used to determine surface topography. This is represented schematically in Fig. 1.5.

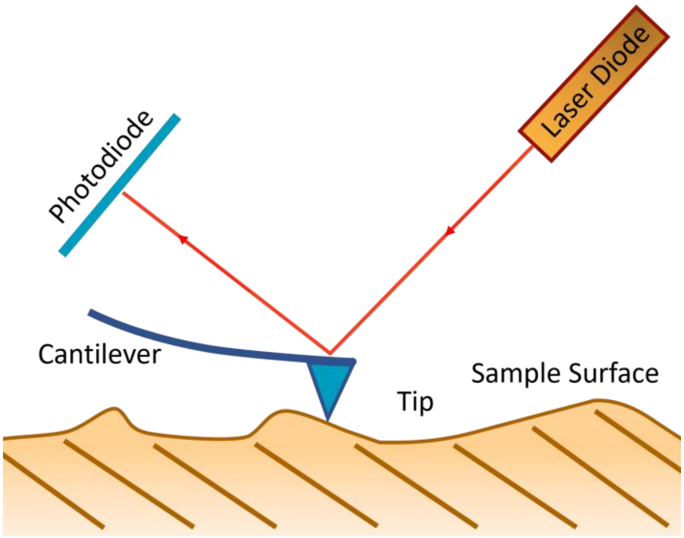

Fig. 1.5, *Schematic representation of AFM operation where the deflection of a cantilever across a sample surface can give information on sample topography in conjunction with a reflected laser. The laser is reflected off the cantilever onto a photodiode which adjusts the height of the sample to maintain a constant cantilever deflection as the tip is moved across the surface*

Several modes of scanning are employed for different applications, these include contact modes (where the tip is ‘dragged’ across the surface), tapping modes (where the tip is in an oscillatory intermittent contact with the sample) and non-contact mode (where the cantilever oscillates at a resonant frequency above the sample). These are all useful for a variety of different applications with their own drawbacks. For example, contact mode can be used to extract friction measurements but results in greater wear on the tip (through increased shear forces on the tip) and sample [117], while tapping mode can be tailored for light indentations that can be used to extract mechanical properties in a similar manner to nanoindentation that will be described in better detail in Chapter 3 [118, 119]. The regions contact and tapping modes occupy on the Lennard – Jones potential graph are shown in Fig. 1.6. This graph shows the interactive potential between a particle pair [120, 121]. When using sharp AFM tips, this potential well approximates the contact between tip and sample. The potential is expressed by the function

$$V_{LJ}(r) = 4\varepsilon\left[\left(\frac{\sigma}{r}\right)^{12} - \left(\frac{\sigma}{r}\right)^{6}\right] \tag{1.3}$$

where r is the interparticle distance, ε is distance of the minima of the potential well, and σ is the distance at which the force is 0.

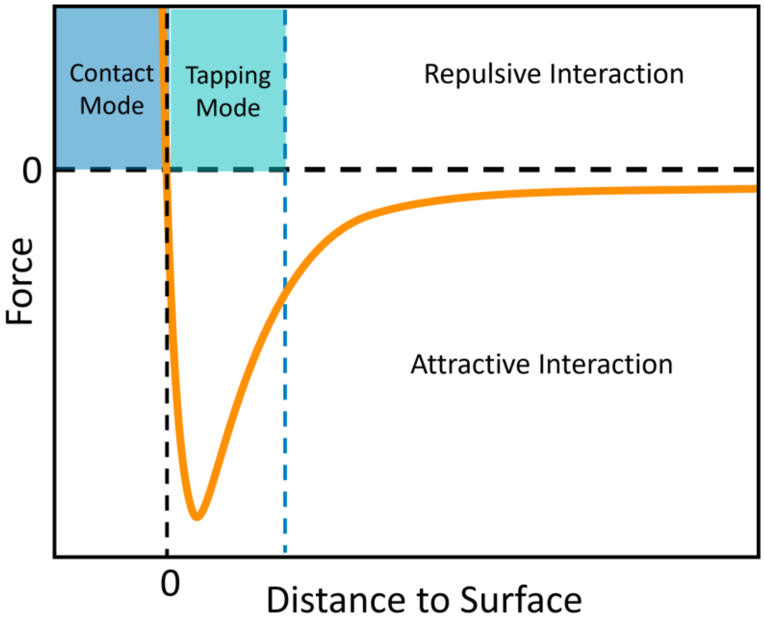

***Fig. 1.6**, Lennard – Jones potential for an AFM tip and sample surface. Contact mode operates in a region of repulsive potential and positive force between sample and tip, creating increased wear on both. Tapping mode mitigates this by oscillating off the surface with only intermittent contact*

Fundamentally however, AFM extracts topographical information which can give information on the shape and height of surface features. This allows for size determination of a nanosheet dispersion by depositing the flakes on a flat substrate and measuring their height and lateral size from the two furthest points on the flake (from here on out referred to as length). A statistical study performed on enough nanosheets gives a reliable average and dispersity of nanosheet sizes in a given solution. While AFM provides a comprehensive and accurate size distribution, it comes with the drawbacks of large measurement time, more complex preparation (requiring substrate deposition with minimal flake overlap), as well as tip maintenance to minimise imaging artefacts that can arise with complex geometries and soft matter.

1.6 Deposition Techniques and Network Formation

The primary focus of the nanosheet dispersions discussed above in this work is in the analysis of thin film nanosheet network materials. In order to produce these from the dispersions, uniform deposition methods must be considered. To this end, there are two commonly used and reliable means of depositing a thin film of nanosheet networks on a substrate : Spray coating, and inkjet printing.

Spray coating is the more straightforward of the two, and utilises an airbrush which has found ubiquitous use in applications where even particulate coatings have been desired, particularly in art and coatings manufacture. Functionally, a liquid dispersion (in this case a nanosheet dispersion), is gravity fed into a nozzle blocked by a stopping needle. Trigger activation causes the needle to retract and a simultaneous flow of nitrogen in adjacent channels to the liquid meet at the nozzle exit point. The nitrogen flow disperses the liquid in micron scale droplets evenly on the required surface. Parameters can be tuned by altering the nozzle size, flow rate, and working distance from the substrate. The substrate is typically heated to remove solvent from the dispersion coating, leaving a stacked nanosheet structure behind (volatile solvents can be used to expedite the drying process) [5, 122].

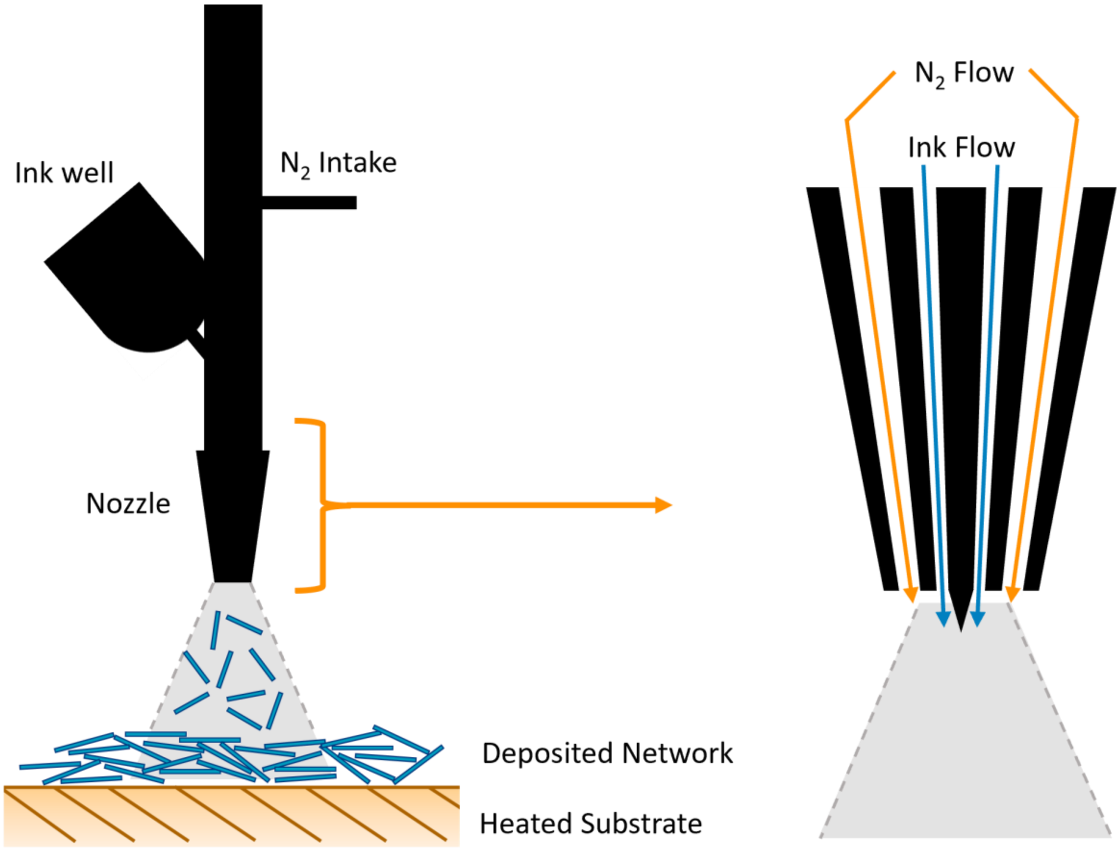

***Fig. 1.7**, Schematic of a spray coating process depositing a nanosheet ink to forma network, with a cross section of the nozzle showing dual channel nitrogen and ink flow around a retracting needle*

While spray coating was utilised to produce the networks in this thesis, more precise non-contact techniques exist, including inkjet [123, 124] and aerosol-jet printing [125]. These are lower waste, higher precision processes that can direct-print channels as low as 10µm wide. This makes them more desirable for precise manufacture, as well as for materials where large exfoliated batch sizes are an issue. Of the two, aerosol jet printing allows for a wider range of inks, owing to reduced sensitivity to ink viscosity (inkjet printing typically allowing for viscosities in the range of 0.001 to 0.02 Pas, and aerosol printing allowing a range between 0.001 and 1 Pas [126]). Spray coating was chosen here in favour of these techniques due to the ease of tuning batch parameters and the ability to spray large ubiquitous areas that allow for mechanical testing with a smaller concern for locational differences on the same sample. Many contact deposition techniques also exist such as screen printing [127, 128] and roll-to-roll processes [129, 130] which each have distinct advantages (eg, sheet alignment) and disadvantages (eg, scalability and print speed) over non-contact processes, but were not utilised in the work presented here so will not be explored in detail.

1.7 Network Morphology

A 2D nanosheet network following the deposition and solvent removal described above is a semi aligned, stacked structure. Films of this nature have direct application in the use of strain sensors if applied to a flexible substrate [18], and also in the production of printed capacitors [123] and transistors [5] when stacking nanosheet materials of different electrical properties (conducting, semiconducting, and insulating [93]). SEM images (top down and FIB cross section), as well as a schematic cross section of a spray coated graphene nanosheet network are shown in Fig. 1.8. The semi aligned structure leads to high volumetric porosities in the range of 40% to 50% for as-sprayed films, with the porosity and network morphology depending on the deposition parameters as discussed above in Section 1.6, but also on the size and aspect ratio of the nanosheets [37]. The potential of these networks for use in electronic applications is highly dependent on the network morphology, which has been shown to greatly affect the performance of the resulting devices [131].

This morphological reliance is largely due to the limited charge transport at nanosheet junctions [132, 133]. While charge transport in individual conductive sheets can be high, the charge transport at the interface between sheets is much lower, with networks showing much reduced conductivity compared to their constituent sheets [5]. For example, transition metal dichalcogenide (TMD) networks such as MoS_2 and WSe_2 were found to have carrier mobilities a factor of ~10^3 lower than for the parent nanosheet. This gap widens further for materials with higher sheet conductivities. The role of the junction resistance in this reduced mobility can be seen in experiments involving more highly aligned sheet systems. Spin coated MoS_2 with highly aligned sheets have reported conductivities over four orders of magnitude higher than printed MoS_2 [59], highlighting the large role sheet contact must play in the conductivity of nanosheet networks. This all makes sense fundamentally, as the mechanism for charge transport between sheets is attributed primarily to thermally assisted electron quantum tunnelling [134], a largely inhibiting mechanism of charge transport. Experiments on graphene nanoribbon FETs have demonstrated the temperature dependant charge hopping mechanism [135] which has been observed also on Mxenes [136]. The same has been shown for nanotube networks [137].

Compounding this problem is the polydispersity and inhomogeneity of the network, meaning that not all junctions are equal, with certain sheets having closer contact and higher conductivities than others. This results in the path of least resistance for charge transport often being an indirect or even tortuous one, which can further decrease effective charge transport in the networks. The complexity of relating all the components of a material's charge transport, scaling with nanosheet size, extending to a network system, and accounting for porosity and polydispersity, has eluded true analytical description in a single equation, though some groundwork and models do exist.

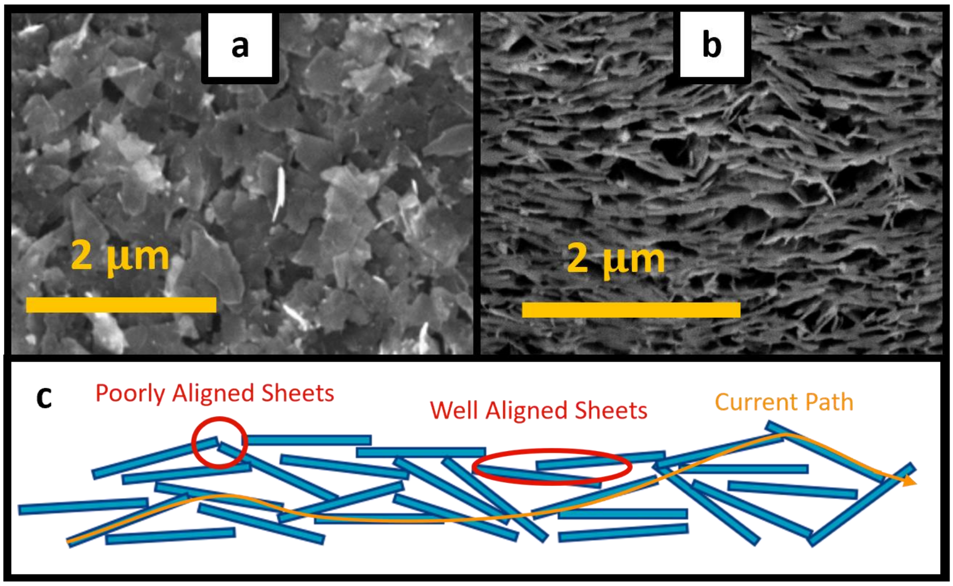

Fig. 1.8, *Top down* ***(a)***, *and cross section* ***(b)*** *of a spray coated graphene network (average flake length ~300nm).* ***(c)*** *Schematic cross section showing high resistance poorly aligned sheets, and lower resistance more closely aligned sheets, as well as demonstrating the potentially indirect or tortuous nature of the current path of least resistance*

An approximation for network conductivity in a junction – limited network (ie high sheet conductivity) can be estimated as follows [131]: It has been shown that for networks of nanotubes, the network resistance is the sum of all tube resistances and junction resistances, and that the ratio between the resistance of all tube and junction contributions is equal to the ratio between a single tube and junction [138]

$$R_{net} \approx R_{N,net} + R_{J,net} \tag{1.4}$$

$$\frac{R_{N,net}}{R_{J,net}} = \frac{R_N}{R_J} \tag{1.5}$$

Where R is the resistance, and the subscripts N, J, and net correspond to the nanotube, junction, and network respectively. For nanosheet networks (indicated by subscript NS from this point onwards), it is postulated that the resistance is due only to junctions in the network ($R_{net} \approx R_{J,net}$)

$$\frac{R_{NS,net}}{R_{net}} \approx \frac{R_{NS}}{R_J} \tag{1.6}$$

Rewriting the nanosheets network resistance $R_{NS,net}$ as conductivity gives

$$\sigma_{NS,net} = \frac{L_{net}}{A_{net} R_{NS,net}} \tag{1.7}$$

Where A_{net} and L_{net} are the area and length of the full network. We can relate this conductivity to individual nanosheets by considering the volume fraction of the network occupied by the nanosheets

$$\sigma_{NS,net} = \sigma_{NS} \phi \tag{1.8}$$

Where ϕ is the volume fraction of nanosheets in the network, defined as the ratio between the volume occupied by nanosheets and the total network volume. Assuming the network comprises only of nanosheets and void space, it is equal to $(1 - P)$ where P is the volumetric network porosity. Approximating nanosheets as square sheets, $A_{NS} = L_{NS} t_{NS}$ where t is sheet thickness, then

$$\sigma_{NS} = \frac{L_{NS}}{A_{NS} R_{NS}} = \frac{1}{t_{NS} R_{NS}} \tag{1.9}$$

We can then combine the above relations to arrive at the following

$$\sigma_{net} = \frac{L_{net}}{A_{net}R_{net}} \approx \frac{\phi}{R_J t_{NS}} \tag{1.10}$$

This approximation implies that the network conductivity increases linearly with increasing volume fraction (decreasing porosity), as well as with decreasing the junction resistance. More comprehensive models are currently in development that are pending publishing, though they show the same dependence on volume fraction and junction resistance. As such is it clear that morphology, specifically sheet alignment and volume fraction, play a key role in the conductivity of these networks.

Analytical descriptions of these important parameters in such a system are severely lacking, however. Closest analogues to a packed platelet system such as Philipse' random contact equation [139, 140], which attempts to predict packing fraction ϕ as a function of the aspect ratio of the discs (Length / Thickness) and average contact number. However the system has some key limitations, such as the assumptions of stiff disks, independent contacts, random packing, and oriental disorder. Such assumptions are ultimately the downfall of the comparison to nanosheet networks, as the resulting model suggests for disks with aspect ratio close to 100 (typical of Liquid Phase Exfoliated Graphene flakes) a packing fraction of less than 6%, far below measured packing fractions of sprayed nanosheet systems which show packing fractions in the range of 50-60%.

1.8 Effect of Mechanical Processing on Conductivity and Morphology

The impact of morphology on the electrical properties of printed nanosheet networks suggests the possibility of mechanical post processing to tailor their properties through morphological changes. So far, investigations of mechanical post-processing involve compression under R2R calendaring with little information known on the applied deformation state or change in morphological characteristic. Previous publications have reported a compression ratio, defined as

$$C_R = \frac{h_0 - h}{h_0} \tag{1.12}$$

where h is the film thickness after compression and h_0 is the initial film thickness. Calendaring experiments on networks of various conductive nanosheet materials all show a similar relationship between compression ratio and conductivity, with an order of magnitude increase in conductivity generally found for C_R reaching a value of 0.9 [110, 128, 131, 141-144]. The ubiquity of the relation between compression ratio for different materials would suggest a key mechanism of conductivity increase being a reduction in porosity. It should be noted that such compression ratios should not be considered analogous to strain, and that a high compression ratio of 0.9 does not account for large influences from non-compressive processes, such as lost material to lateral deformation or adhesion to the rollers. In the absence of careful application of strain, and/or strict morphological characterisation after compression, the degree of alignment improvement these high compression ratios actually induce is poorly understood.

As such, there is a clear need to identify the mechanical nature of these networks to elucidate the response to compression. This may shine light on the evolution of porosity and alignment during and after compressive strains, and allow for improvements to mechanical post processing methods that can allow for improved device performance in a highly scalable process such as roll to roll compression. Further chapters of this thesis will therefore focus on establishing the groundwork of compressive mechanical and morphological characterisation of such printed networks, with the results extending to post processing techniques such as calendaring.

1.9 Crumpled Sheets

A crumpled sheet structure represents a system of one continuous planar material bent and compressed in a way that the sheet is ununiformly deformed in a network of ridges and folds with large regions of available free volume. This is best visualised like crumpling a sheet of paper or tinfoil in your hand. Research into sheet crumpling is performed in a number of ways, with the most simple being hand crumpling, but with other methods such as uniform wire nets [145, 146], ambient pressure chambers [147], and uniaxial compression in cylindrical confinement also explored [145, 146, 148-

151], the last of which being an extremely similar stress state to that applied in our layer compression test indentations, described in more detail in Chapters 2 and 3. The crumpling of graphene sheets has also been explored in a similar manner via molecular dynamic simulations [152, 153]. While the nanosheet network films explored in this work are a granular flake system, the high aspect ratio of the sheets and large amounts of available free volume facilitates comparison to the local bending structure of a sheet. Although the comparison is not expected to extend to an interconnected network of ridges and folds as in a crumpled sheet, we can infer information on local folds from work done in this research space that we may apply to our own system as nanosheets have been shown to yield and bend in a ridge forming process [154].

The energy required to crumple a sheet is mainly expended through the formation of sharp ridges, which store substantially more energy than vertices or smooth bends [155, 156]. This is due to the local bending within a ridge, where bonds on its convex side are stretched substantially, while bonds on its concave side are compressed. This is visualized in Fig. 1.9 for planar nanosheets. FIB-SEM tomography of graphene networks has shown that ridges can form in these networks even before compression. Regions of highly misaligned sheets near free volume pores can form further ridges under compression (Fig. 1.9.) Together these may absorb a large amount of the energy stored in a compressed network. The energy stored in a single ridge is thought to scale as [157, 158]

$$E \propto \kappa \left(\frac{\chi}{h}\right)^{\beta} \tag{1.13}$$

where κ is the bending stiffness, χ is the ridge length, h is the sheet thickness, and the exponent β equals $1/3$ for continuum elastic sheets [159]. For highly crumpled sheets the energy becomes further related to the lateral size of the sheet and radius of the crumpled ball. However in this work I consider smaller individual sheets with limited crumpling in the nanosheet network film, for which complex intersecting ridge and vertex structures are unlikely to develop. As such, with the contribution of smooth folds and vertices to the energy storage small in comparison (and in for the case of vertices, practically not present in an exfoliated nanosheet structure), we assume the total energy stored in the system as the sum of all such ridges [155]:

$$E_T \approx \kappa \sum_i \left(\frac{\chi_i}{h}\right)^{\frac{1}{3}} \tag{1.14}$$

which will be used to help model the compressive response of nanosheet network materials in Chapter 6.

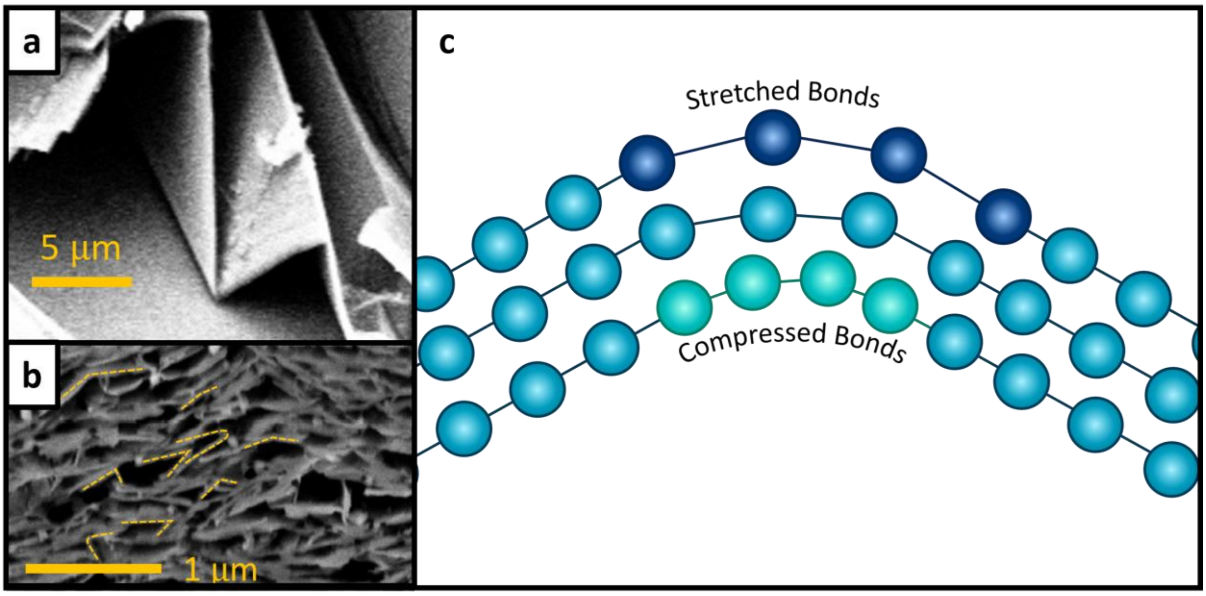

Fig. 1.9, (a) *Ridge formation in cleaved multilayer graphene sheets (formed from flat punch nanoindentation of polycrystalline graphite),* ***(b)*** *FIB cross section of a graphene nanosheet network highlighting ridge formation even in uncompressed networks, with free volume available for further formation under compression.* ***(c)*** *Bond stretching and compression in a layered material that results in energy storage in a ridge*

When external forces are removed, the ridges in a crumpled system can relax and unfurl. For macroscopic sheets formed from eg. aluminium foil, it is found this occurs in a two-step process: An initial rapid relaxation, followed by a slower relaxation as the ridges slowly unbend [148]. The slow process can occur over the course of hours, or up to weeks depending on the material, deformation history and/or environmental conditions. To what degree this behaviour manifests in the nanosheet network will be explored more in Chapter 7.

Finally, I exercise caution in relating this system to our networks for more complex parameters such as yield stress, strain rate, etc, which will be explored in Chapter 2, as the mechanisms behind such processes is poorly understood from a fundamental standpoint in both amorphous materials in general and crumpled sheets. Any unknown influence that the differences between the materials (eg the interconnected nature of the ridge and vertex structure of a crumpled sheet, or the granular nature of the network thin films) has on such parameters makes comparisons between them fraught with assumptions. Because of this, I limit the comparisons only to those for which the mechanisms can be isolated and compared, such as the energy storage in ridge formation discussed above.

1.10 Nanosheet Network Production Parameters

Several nanosheet network films were produced for exploration in the course of this thesis. As some of these networks appear in several subsequent chapters, their production is detailed here.

Graphene films were produced in batches via a well-established liquid phase exfoliation technique. This was done using 2g of bulk graphite from Asbury Carbons in 80ml of de-ionized water (for a concentration of 25 mg/ml). This was sonicated for 1h using a Sonics Vibra-cell VCX-750 ultrasonic processor under a horn tip probe at 50% amplitude, and a pulsed periodic on:off ratio of 6:2 to prevent overheating. The resulting solution was separated into two 50ml vials and centrifuged for 1h at 5 krpm. The top layer of water supernatant was then discarded. The remaining sediment solution was redispersed in 80ml of fresh water and 160mg sodium cholate surfactant was added (2 mg/ml). This was then sonicated with the same parameters as before for 7h. The resulting solution is a stock dispersion of polydisperse nanosheets that can be further size selected.

Size selection was done via liquid cascade centrifugation. The stock dispersion was first centrifuged at 1000 rpm for 90 mins. 80% of the supernatant was removed such that the sediment was not disturbed. Centrifugation at increasingly high rpm was then performed to isolate increasingly smaller sheets. 1000 rpm for 90 minutes, 2500 rpm for 90 minutes, 6000 rpm for 90 minutes, and 7000 for 90 minutes. For each of these the supernatant was removed and the samples were solvent exchanged to isopropyl alcohol (IPA) to form the basis of the inks. Solvent exchange was performed by redispersing the sediment in 80ml IPA and centrifuging at 6000 rpm for 90 mins. All supernatant was then discarded and the sediments were redispersed again in 80 ml IPA. A final supernatant disposal and redispersion in 40ml IPA was performed to form the inks.

A scattered deposit of each sample was applied to a glass substrate in order to allow for AFM size selection. This was performed by using AFM imaging to characterise the size of a range of individual flakes and extracting an average from this distribution. A distribution from one of the graphene samples is shown in Fig. 1.10 to demonstrate this. The slow nature of the AFM sampling technique limits the count number and therefore the statistical averaging possible. However, the technique is well established and known to provide accurate values even at these count levels, thanks in no small part to the size selection being performed via well practiced and established production methodology (solution concentration, centrifugation speed, etc) [93, 96, 98, 99, 160]. Nanosheet layer thickness is estimated at 1nm per layer (more precisely being 2nm for the first layer and 0.95nm for subsequent layers) to account for the effect of overestimation of thickness due to water etc, and is a well-established estimate for LPE graphene sheets [98].

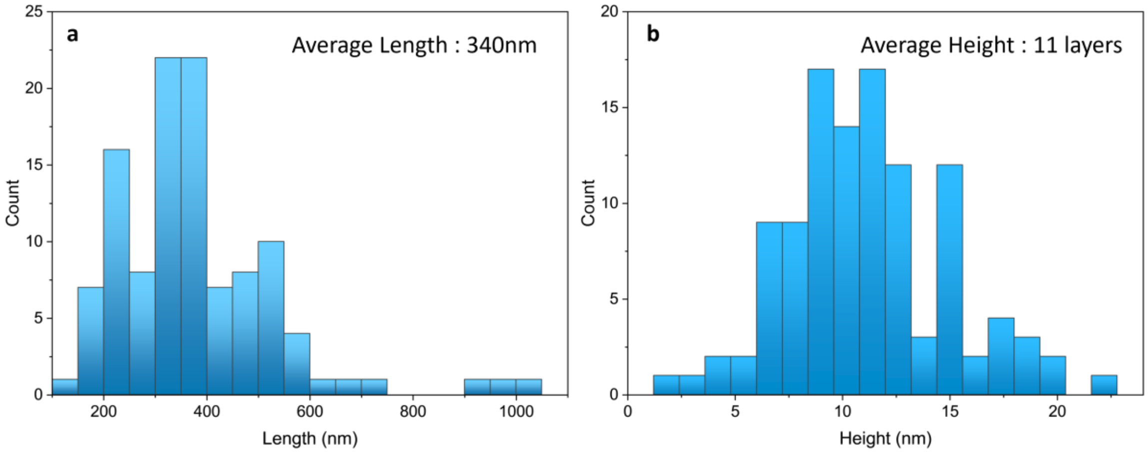

Fig. 1.10, *Length **(a)** and height **(b)** distribution of graphene sheets in sample II as measured via AFM sampling*

These batches were deposited with a spray coating process on glass substrates with a thin (~50nm) gold layer between the two, with resulting film thicknesses measured using precise substrate to surface determination with the nanoindenter and verified with FIB-SEM cross sections. These networks are labelled for convenience from this point on as graphene samples *I*, *II, III,* and *IV*, with increasing average nanosheet size from *I* through *IV*. These parameters can be seen in full in Table 1.1. Zero strain porosities of each sample as a function of average sheet size is known for networks prepared in this way [37], and was verified to hold true for our samples using FIB-SEM tomography, as displayed in our porosity study in Chapter 6.

Samples of MoS_2 networks were prepared using an identical method, except that the MoS_2 was directly exfoliated in IPA instead of deionised water so required no final solvent exchange step. Two identical samples of the MoS_2 network were prepared from the same batch of LPE nanosheet ink. This consisted of an unprocessed control sample and an identical sibling sample processed via sulphur vacancy healing by introduction of 1,4-benzenedithiol molecules [161, 162], prepared by collaborators in the University of Strasbourg, and used here to investigate the effect of chemical cross linking on the mechanical response and elucidate modes of deformation, explored in further detail in Chapters 6 and 7.

Sample	Sheet Thickness (layers)	Average Sheet Length (nm)	Film Thickness (μm)	Zero Strain Volume Fraction
I	8	300	6.3	0.6
II	11	340	7.9	0.58
III	20.5	640	9.7	0.54
IV	40.9	932	11.5	0.5
MoS_2	6 (18)	300	10	NA

Table 1.1. *Sheet and network parameters for networks used in this study. Networks labelled I through IV are liquid phase exfoliated graphene networks.* MoS_2 *networks used were also exfoliated using liquid phase exfoliation techniques, which have a larger layer thickness than graphene. Sheet thickness and length values given are averages based on AFM measurements, with accuracies typically to within ~5%. Zero strain volume fraction is predicted from previous morphological studies on samples with the same preparation [37], and verified on Sample I via FIB-SEM tomography*

Ch 2. Continuum Mechanics

In this chapter, analytical considerations of the mechanics of continuous media are outlined. Starting with simpler isotropic elastic behaviour, I eventually expand consideration to materials experiencing severe anisotropy of their mechanical properties (ie. differing mechanical properties in different directions), and for differing contact geometries. Only the cases of anisotropy and contact geometry applicable to this work will be presented in detail here (namely, transverse isotropy for the case of anisotropy, and confined uniaxial compression for the case of unique contact geometry). I then consider inelastic continuum processes of yield and plastic flow. Finally, I review time dependent viscoelasticity pertinent to creep and stress relaxation processes that manifest in the nanosheet networks as well.

2.1 Elasticity

Continuum mechanics is the study of material deformation assuming a continuous material without atomistic/molecular/particulate considerations. It assumes that deformation is not defined by combined motion of discrete particles and instead is a continuous process independent of length scale. This assumption becomes inadequate in the small scale limit where atomistic stresses and strains require consideration [163-165]. The length scale above which continuum mechanics operates with accuracy is dependent on the length scale of any discrete particles or grains within the material which can operate collectively at their scale. For molecular materials this is defined by molecular or atomistic lengths, but may be larger in granular systems or composites where individual particles may be defined by grains rather than molecules. Typically, for amorphous molecular materials such as polymer glasses, length scales above ~10nm suffice for evaluation via continuum mechanics. For granular systems such as nanosheet networks, I utilise large contact volumes relative to the grain size in order to allow for a continuum approach (typically contact dimensions being ~100 times the corresponding grain length in the same dimension, with volumes then being in the range of 10^6 times the grain volume).

For the majority of real world applications, non-atomistic continuum considerations are of importance. While atomistic/particle simulation can give understanding to the processes behind interactions at the molecular scale, the complete picture above these small length scales is best approached with continuum considerations. For the amorphous thin films presented in this thesis, such as polymers and amorphous glasses, a continuum approach best describes the combined nature of complex interactions that govern elastic and plastic deformation, yield, shear and flow. For nanosheet networks, their use relies fundamentally on the combined nature of the flake system. This necessitates a continuum picture of behaviour be observed to define their behaviour beyond individual sheet contacts, which may vary due to variable flake sizes, alignments, contact areas, etc within the network.

In continuum mechanics there are two types of forces that can be applied: Body and surface/contact forces. The former are forces that operate throughout the body as a whole such as gravity or from electromagnetic fields. The latter is of greater interest in this work and is the force applied by a tensile, compressive or shear force at an object's surface. A significant difference between the two is the often non-uniform nature of stress applied to a body under contact forces. A simple and common demonstration of a contact force is that of a two-dimensional bar of material fixed at one end and stretched by application of a tensile force at the other end, as demonstrated in Fig. 2.1.

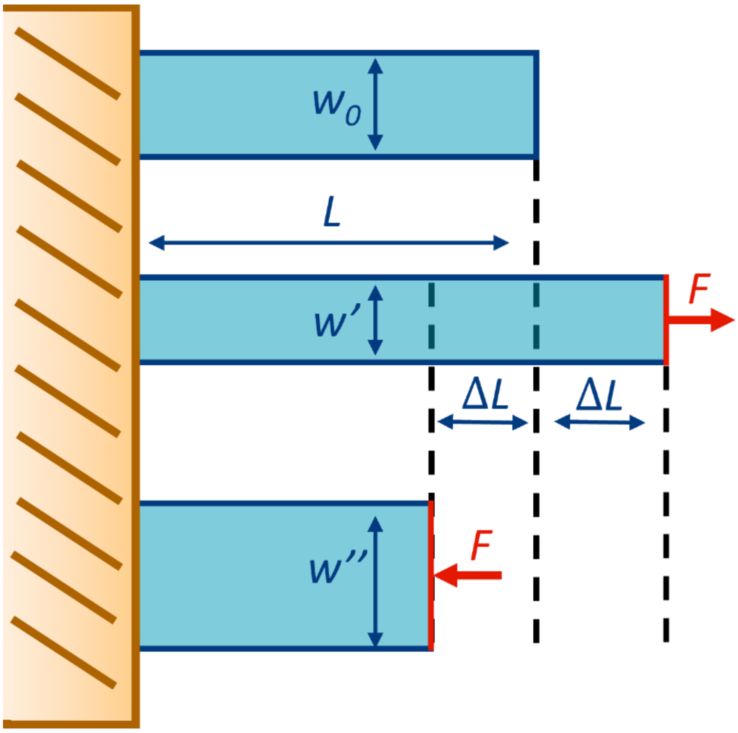

Fig. 2.1. *Simple uniaxial tension and compression on a bar fixed at one end with force applied evenly along the side opposite to the anchor point*

The fixed surface anchors the position of the left end of the bar, which reacts to the tensile force applied to the right end by stretching (here along the x-axis). Stress σ is defined as the area over which the force is applied

$$\sigma = \frac{F}{A} \tag{2.1}$$

where F is the applied force and A is the area of application of that force. The resulting deformation of the material can be described by the engineering strain

$$\varepsilon = \frac{\Delta L}{L} \tag{2.2}$$

Where L is the original length of the material, and ΔL is the change in length due to the applied force. As it is stretched, the bar thins along its perpendicular axis (here the y-axis) according to the Poisson effect. The same analysis can be applied in a compressive system, whereby the material is subjected to compressive forces rather than tensile, and will expand in the perpendicular direction as opposed to thinning. In Fig. 2.1 this is represented by a reversal in the direction of the applied force. The definition of stress and strain remain the same as in Eq. 2.1 and 2.2, but it is important to note the distinction between compressive and tensile strains, particularly beyond the elastic regime.

Hooke's law is an elastic constitutive relation that defines the relationship between stress and strain in the elastic regime and is given by

$$\sigma = E\varepsilon \tag{2.3}$$

where the spring constant in this case, *E,* is known as Young's modulus. It is a measure of the intrinsic stiffness of a material.

The degree of expansion / thinning of the material upon compression / tension is given by Poisson's ratio, defined as the ratio between the lateral strain to the strain in the loading direction

$$\nu = \frac{\varepsilon_{\perp}}{\varepsilon} \tag{2.4}$$

Poisson's ratios typically range from 0 to 0.5 and is restricted to -1 and 0.5. Values > 0.5 correspond to contraction under compressive force and expansion on tensile force and is typically limited to materials with geometries engineered to facilitate this, known as auxetic materials [166].

This simple picture can be extended from one dimension to three dimensions via a tensor (matrix) definition of stress and strain. If we consider a cubic element within an arbitrarily shaped body, we can split the components of stress into individual directional components. There exists one component for each axis; σ_{xx}, σ_{yy}, and σ_{zz}, as well as 6 additional components for directional combinations. The full matrix is therefore

$$\boldsymbol{\sigma} = \begin{bmatrix} \sigma_{xx} & \sigma_{xy} & \sigma_{xz} \\ \sigma_{yx} & \sigma_{yy} & \sigma_{yz} \\ \sigma_{zx} & \sigma_{zy} & \sigma_{zz} \end{bmatrix} \tag{2.5}$$

For static problems, mirrored elements are equivalent (ie $\sigma_{12} = \sigma_{21}$) such that the matrix is symmetric

$$\boldsymbol{\sigma} = \begin{bmatrix} \sigma_{xx} & \sigma_{xy} & \sigma_{xz} \\ & \sigma_{yy} & \sigma_{yz} \\ & & \sigma_{zz} \end{bmatrix} \tag{2.6}$$

The diagonal components of this matrix are forces acting on a plane and are known as normal stresses (σ_{xx}, σ_{yy}, and σ_{zz}), while the diagonal components are known as shear stresses and act perpendicularly to these. A three dimensional representation of this on a cubic element is shown in Fig. 2.2 as well as a two dimensional representation of the same for clarity.

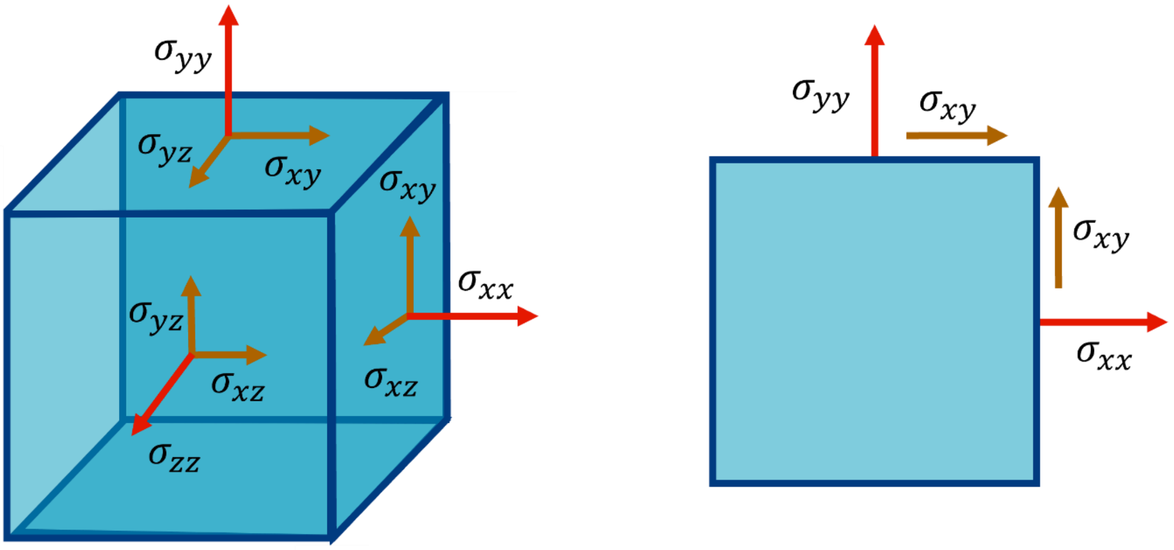

Fig. 2.2, *Normal and shear stress components on a cubic (three dimensional) and square (two dimensional) volume segment of a material under stress*

In the situation where all normal stresses are equal, and all shear stresses are zero, the material will change in volume with no change in shape (referred to also as dilation). This is called hydrostatic pressure

$$\boldsymbol{\sigma} = \begin{bmatrix} \sigma_H & 0 & 0 \\ 0 & \sigma_H & 0 \\ 0 & 0 & \sigma_H \end{bmatrix} \tag{2.7}$$

Stress can be decomposed into a hydrostatic component and a deviatoric component, where the hydrostatic component can be viewed as responsible for volume changes and the deviatoric component for changes to the body’s shape (referred to also as distortion). In this instance the hydrostatic stress is equivalent to the average of the normal stresses. The hydrostatic stress is often also referred to as the octahedral normal stress

$$\sigma_H = \frac{1}{3}(\sigma_{xx} + \sigma_{yy} + \sigma_{zz}) \tag{2.8}$$

The deviatoric component can be found by subtracting Eq. 2.7 from the stress matrix

$$\boldsymbol{\sigma} = \begin{bmatrix} \sigma_{xx} & \sigma_{xy} & \sigma_{xz} \\ \sigma_{yx} & \sigma_{yy} & \sigma_{yz} \\ \sigma_{zx} & \sigma_{zy} & \sigma_{zz} \end{bmatrix} = \begin{bmatrix} \sigma_H & 0 & 0 \\ 0 & \sigma_H & 0 \\ 0 & 0 & \sigma_H \end{bmatrix} + \begin{bmatrix} \sigma_{xx} - \sigma_H & \sigma_{xy} & \sigma_{xz} \\ \sigma_{yx} & \sigma_{yy} - \sigma_H & \sigma_{yz} \\ \sigma_{zx} & \sigma_{zy} & \sigma_{zz} - \sigma_H \end{bmatrix} \tag{2.9}$$

Strain can similarly be decomposed into normal and shear components

$$\boldsymbol{\varepsilon} = \begin{bmatrix} \varepsilon_{xx} & \varepsilon_{xy} & \varepsilon_{xz} \\ & \varepsilon_{yy} & \varepsilon_{yz} \\ & & \varepsilon_{zz} \end{bmatrix} \tag{2.10}$$

The normal components $\varepsilon_{xx/yy/zz}$ are defined as the strain along the given principle direction, while the shear components are defined as half the sum of the displacement along each composite direction, given by the Saint-Venant relation

$$\varepsilon_{ij} = \frac{1}{2}(\frac{\partial n_j}{\partial i} + \frac{\partial n_i}{\partial_j}) \tag{2.11}$$

Where n_{ij} are the displacement of a point in the given volume in the direction specified.

Relating stress and strain in a three-dimensional system as in Eq. 2.3 requires all components in Eq. 2.6 and 2.10 be related to one another. This necessitates a 6 x 6 stiffness matrix *C*. The inverse matrix to relate strain to stress is known as the compliance matrix *S*, but this will not be explored here.

$$\boldsymbol{\sigma} = C\boldsymbol{\varepsilon} \quad / \quad \boldsymbol{\varepsilon} = S\boldsymbol{\sigma} \tag{2.12}$$

$$\begin{bmatrix} \sigma_{xx} \\ \sigma_{yy} \\ \sigma_{zz} \\ \sigma_{yz} \\ \sigma_{xz} \\ \sigma_{xy} \end{bmatrix} = \begin{bmatrix} C_{11} & C_{12} & C_{13} & C_{14} & C_{15} & C_{16} \\ C_{21} & C_{22} & C_{23} & C_{24} & C_{25} & C_{26} \\ C_{31} & C_{32} & C_{33} & C_{34} & C_{35} & C_{36} \\ C_{41} & C_{42} & C_{43} & C_{44} & C_{45} & C_{46} \\ C_{51} & C_{52} & C_{53} & C_{54} & C_{55} & C_{56} \\ C_{61} & C_{62} & C_{63} & C_{64} & C_{65} & C_{66} \end{bmatrix} \begin{bmatrix} \varepsilon_{xx} \\ \varepsilon_{yy} \\ \varepsilon_{zz} \\ 2\varepsilon_{yz} \\ 2\varepsilon_{xz} \\ 2\varepsilon_{xy} \end{bmatrix} \tag{2.13}$$

This matrix, also symmetrical along the diagonal such that $C_{ab} = C_{ba}$, accounts for the response of the material to applied force in all directions, and so can be used to extract relations for materials with different stiffnesses and Poisson's ratios in different directions. For the work presented in this thesis, I will consider two such cases: Firstly, the case for standard molecular amorphous materials such as polymers where stiffness and Poisson's ratio is the same in all directions, ie the standard isotropic case. Secondly, the case for a material with the same stiffness and Poisson's ratio along two principle directions and a separate stiffness and Poisson's ratio along the third principle direction, a case of anisotropy known as transverse linear isotropy, which best describes the nanosheet network thin films that will be discussed in more mechanical detail in a later section. I will first approach the simpler isotropic case. For an isotropic material, the matrix in Eq. 2.13 becomes

$$\begin{bmatrix} \sigma_{xx} \\ \sigma_{yy} \\ \sigma_{zz} \\ \sigma_{yz} \\ \sigma_{xz} \\ \sigma_{xy} \end{bmatrix} = \frac{E}{(1+v)(1-2v)} \begin{bmatrix} 1-v & v & v & 0 & 0 & 0 \\ v & 1-v & v & 0 & 0 & 0 \\ v & v & 1-v & 0 & 0 & 0 \\ 0 & 0 & 0 & (1-2v)/2 & 0 & 0 \\ 0 & 0 & 0 & 0 & (1-2v)/2 & 0 \\ 0 & 0 & 0 & 0 & 0 & (1-2v)/2 \end{bmatrix} \begin{bmatrix} \varepsilon_{xx} \\ \varepsilon_{yy} \\ \varepsilon_{zz} \\ 2\varepsilon_{yz} \\ 2\varepsilon_{xz} \\ 2\varepsilon_{xy} \end{bmatrix} \tag{2.14}$$

With this in mind the bulk modulus *K*, which defines the materials stiffness to purely hydrostatic loading is defined as [167]

$$K = \frac{E}{3(1-2v)} \tag{2.15}$$

And the shear modulus *G*, which defines the material response to shear deformation is

$$G = \frac{E}{2(1+v)} \tag{2.16}$$

In this thesis, a state of confined uniaxial compression, known as uniaxial strain (US), will be of particular focus. This is the case where material expansion and deformation is suppressed in all directions except for the loading direction, and is distinct from the much more common unconfined analogue known as uniaxial stress. These conditions are contrasted in Fig. 2.3.

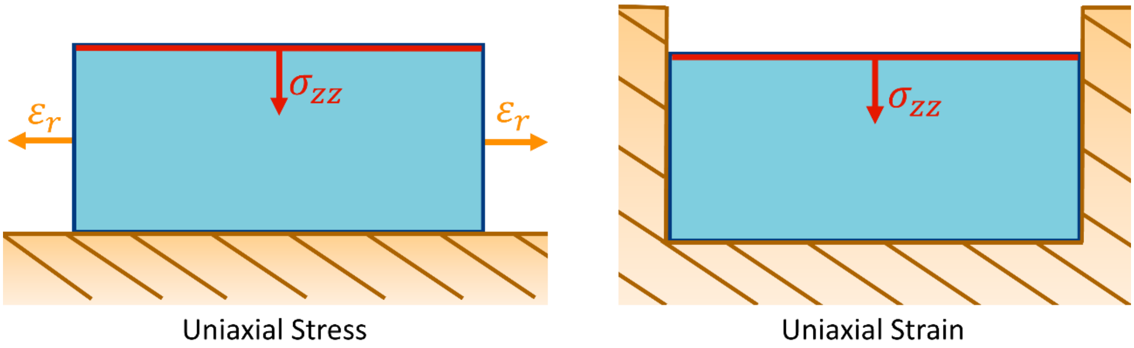

Fig. 2.3, *Schematic cross-section of a cylindrical body under uniaxial stress, whereby stress is applied in a singular loading direction on an unconfined material and expansion due to the elastic Poisson effect or incompressible plastic flow will occur. Radial coordinates are used here for simplicity in demonstrating the expansion direction. This is compared with uniaxial strain, whereby rigid confinement on all sides other than the surface of applied stress prevents lateral expansion*

A state of uniaxial strain necessitates that all strains except for that in the loading direction (here the *z* direction) are zero. This simplifies Eq. 2.14 such that we can extract a stress – strain relation for the singular loading direction

$$\sigma_{zz} = M\varepsilon_{zz} = \frac{1-v}{(1+v)(1-2v)}E\varepsilon_{zz} \tag{2.17}$$

where *M* is known as the confined modulus. As such, in this confined geometry, the slope of the stress vs strain curve is given by M instead of E and so is a function of the Poisson's ratio of a material as well as the Young's modulus, with M increasing with v. This is representative of the confining geometry preventing elastic Poisson or plastic flow expansion upon compression by maintaining a confining counter-stress at the walls.

In this geometry a cylindrical coordinate system is most convenient to define the stress on the confining wall, which can determine the point of confinement failure in situations without an ideally stiff confining jacket [168]

$$\sigma_{rr} = \sigma_{\theta\theta} = \frac{v}{1-v}\sigma_{zz} \tag{2.18}$$

2.2 Elastic Anisotropy

For the case of confinement in a material with transverse isotropy, we must consider the existence of two Young's moduli, *E* and *E'*, and two Poisson's ratios, *v* and *v'*, owing to differing material properties in each direction

$$E = E_{xx} = E_{yy} \ \ / \ \ E' = E_{zz} \tag{2.19}$$

While Eq. 2.4 well defines Poisson's ratio for a isotropic two dimensional bar, in the case of three dimensional anisotropy, we can extend our nomenclature for defining Poisson's ratio

$$v_{ij} = \frac{\varepsilon_j}{\varepsilon_i} \tag{2.20}$$

Where *i* is the loading direction, and *j* is the direction of expansion / contraction. These can be visualised below in Fig. 2.4. For our case of transverse linear isotropy, this results in two Poisson's ratios

$$v = v_{xy} = v_{yx} \ \ / \ \ v' = v_{zy} = v_{zx} \tag{2.21}$$

Where v' is the transverse Poisson's ratio.

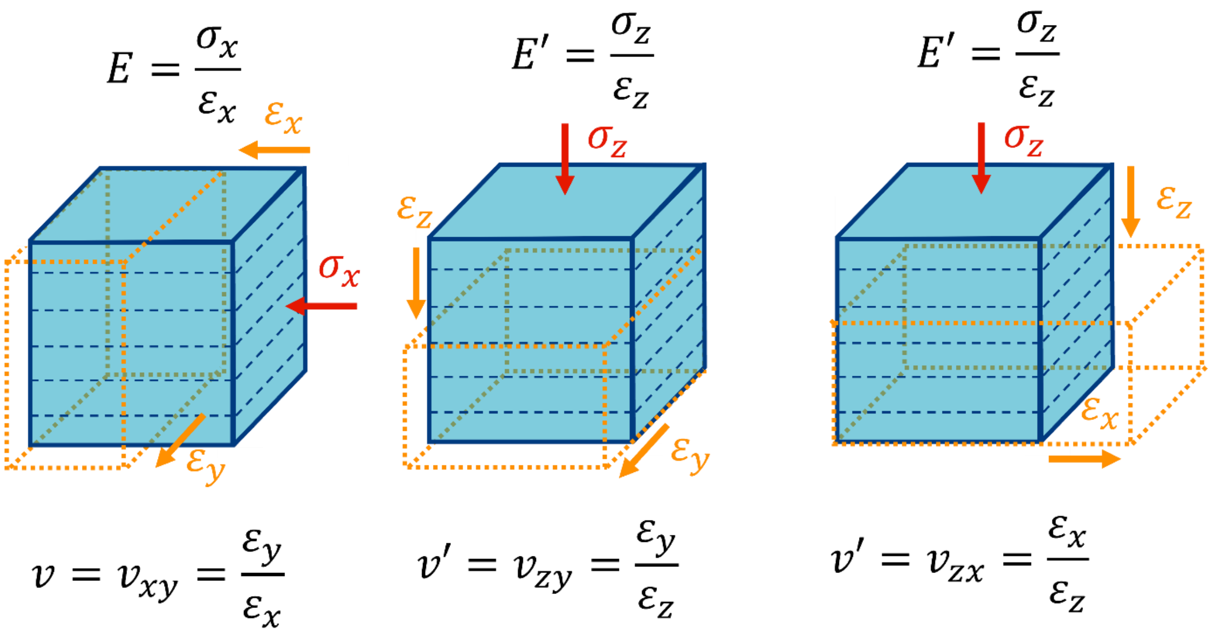

Fig. 2.4, *Demonstration of the two Young's moduli E and E', and two Poisson's ratios v and v', on compression of a transverse linear isotropic material. Dashed blue lines represent the plane of anisotropy, where the mechanical properties are different when loading in the z direction in comparison to the x and y directions*

It should be noted that the transverse Poisson's ratio can be chosen as above, $v' = v_{zy} = v_{zx}$, but it is possible to also work within the framework of $v^* = v_{xz} = v_{yz}$ as the transverse Poisson's ratio. These are dependent on the relation that $v'/E' = v^*/E$ [169]. For the work presented in this thesis I choose to work within the framework of v'.

Using the general matrix definition of $\sigma = C\varepsilon$ as in Eq. 2.13, and accounting for the symmetries present in the case of transverse isotropy, we obtain [170]

$$\begin{bmatrix} \sigma_{xx} \\ \sigma_{yy} \\ \sigma_{zz} \\ \sigma_{yz} \\ \sigma_{xz} \\ \sigma_{xy} \end{bmatrix} = \begin{bmatrix} C_{11} & C_{12} & C_{13} & & & \\ & C_{11} & C_{13} & & & \\ & & C_{33} & & & \\ & & & C_{44} & & \\ & & & & C_{44} & \\ & & & & & C_{66} \end{bmatrix} \begin{bmatrix} \varepsilon_{xx} \\ \varepsilon_{yy} \\ \varepsilon_{zz} \\ 2\varepsilon_{yz} \\ 2\varepsilon_{xz} \\ 2\varepsilon_{xy} \end{bmatrix} \tag{2.22}$$

Where the constants C_{ab} are given by

$$C_{11} = \frac{E\left(E(v')^2 - E'\right)}{(v^2-1)E' + 2E(1+v)(v')^2} \tag{2.23}$$

$$C_{12} = -\frac{E\left(E(v')^2 + vE'\right)}{(v^2-1)E' + 2E(1+v)(v')^2} \tag{2.24}$$

$$C_{13} = -\frac{EE'v'}{(v-1)E' + 2E(v')^2} \tag{2.25}$$

$$C_{33} = \frac{(v-1)(E')^2}{(v-1)E' + 2E(v')^2} \tag{2.26}$$

$$C_{44} = G' \approx \left(\frac{1}{E} + \frac{1+2v'}{E'}\right)^{-1} \tag{2.27}$$

$$C_{66} = G = \frac{E}{2(1+v)} \tag{2.28}$$

It should be noted that the value for G' is an estimate based on the Saint-Venant relation given in Eq. 2.11 for the transverse shear modulus in this case of anisotropy. For uniaxial strain, all strains except ε_{zz} are 0, and therefore Eq. 2.22 reduces to two components; a lateral stress (ie a stress on the confining walls) $C_{13}\varepsilon_{zz}$, and the stress in the loading direction $C_{33}\varepsilon_{zz}$.

The relations given above adequately describe the low strain elastic behaviour of an isotropic and transverse isotropic continuum material. At larger strain there exists much mechanical nuance and further detail regarding the deformation of such materials, but the relations given above are sufficient to describe the processes required for understanding the low strain mechanical response of materials explored in this thesis. In the case of a simple elastic-plastic material, deformation below the elastic limit will recover applied strain when force is removed, recapturing its original shape and volume. While this holds true at low strains, beyond a critical point of strain any additional deformation becomes permanent. This point is known as yield and deformations beyond this point are referred to as plastic deformation. Both will be discussed in the follow section on yield and plasticity.

2.3 Yield and Plasticity

The elastic deformation described in the previous section holds true for low strain deformation. For a simple elastic-plastic material (which is an adequate descriptor for many amorphous solids under reasonable loading conditions), higher strain deformation can cause a yielding event whereby any further material deformation becomes permanent and energy introduced via deformation is either expended through dissipative processes, or stored through morphological changes. This marked transition in the nature of deformation is largely material dependent, meaning the process which governs yield and plasticity depends strongly on the material morphology, and so short descriptors of the morphology and carrier of plasticity in ordered compared to amorphous material systems is given below before a continuum picture is presented.

2.3.1 Metals and Crystals

In well-ordered lattice material such as metals and crystals, the close packed and ordered nature of the lattice results in an even distribution of applied stresses in an ideal, defect free lattice. In practice, lattices are rarely ideal and present a range of possible defects (some of which are visualised in Fig. 2.5). These defect sites act as regions of stress concentration when force is applied and as such yield and plasticity are nucleated around dislocations and defects in the lattice [13]. Once a yielding event occurs in the proximity of such a site it can cause cascading fracture or plastic flow through the rest of the lattice depending on the means of applied stress. The means of failure depends on the form of the defect, but these cases are more suited to ordered rather than amorphous materials and will not be approached in detail in this thesis.

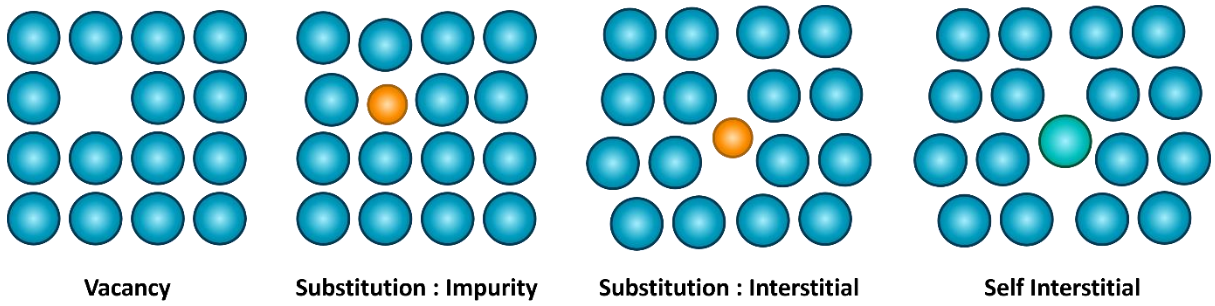

Fig. 2.5, *Examples of defects in metallic/crystal lattices around which plastic yield can nucleate*

2.3.2 Disordered Material : Amorphous Glasses

As discussed in Chapter 1, atomic glasses (including metals, alloys, covalent small molecule, and polymers) are thermodynamically non-equilibrium systems characterised by the presence of free volume and ageing phenomena. Despite extensive study, the precise atomistic mechanisms that act as the carrier of plasticity in amorphous glasses is still under dispute, with much current work focusing on computational simulation to shine light on the process [171]. But there exists some well-established theories regarding yield in disordered solids. Currently, it is speculated that plastic deformation in glasses consists of a single mechanism common to disordered solids regardless of molecule size, interaction potential, bonding, etc [172, 173]. This is supported somewhat further by the observation that amorphous solids experience a constant relationship between Young's modulus E and yield stress Y, even across large variations in structure and orders of magnitude of stiffness [174]. Such plasticity carriers nucleate and grow into macroscopic shear transformations, which eventually share some similarity to the deformation of crystalline solids at larger scales (such as shear band deformation, as demonstrated below in Fig. 2.6).

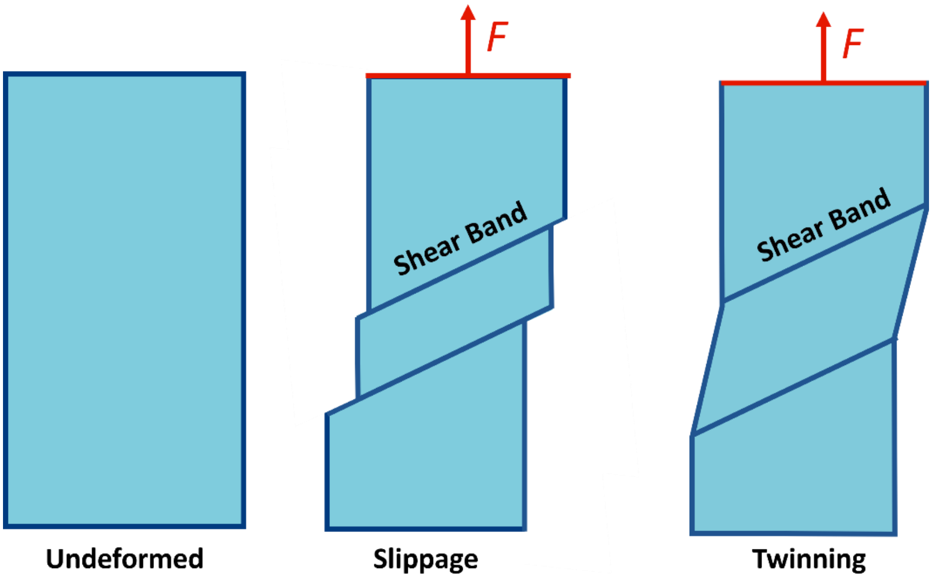

Fig. 2.6, *Plastic deformation occurring through shear band deformation on a block of a disordered material. This can result in slippage, or potentially twinning in the case of crystalline solids*

The means of nucleation of these shear zones is up for some debate, with two leading theories being the Shear Transformation model (ST) and Shear Transformation Zone model (STZ). The former is the earlier of the two theories and proposes that plasticity carriers do not exist in the material before stress is applied, and nucleate in clusters that undergo increased relaxation upon applied stress [172, 173] resulting in an avalanche of plastic carriers nucleating around those zones. The STZ theory proposes that small groups of disordered units exist in the unstressed material and are surrounded by a more densely packed region than the volumetric average. These 'units' can be atoms, chain clusters or other structural descriptors depending on the material. Clusters are typically 4-10 atoms large in a metallic glass. Upon the application of sufficient shear stress, these undergo local orientation rearrangement and nucleate plasticity mostly in the direction of the new orientation axes [175, 176]. This theory more closely describes the shear band phenomena that is well observed for disordered solids [177, 178].

Despite these theories, much work remains before the mechanism(s) of plasticity in amorphous solids are understood fully. There remain many unresolved questions such as if precursors to plastic deformation exist before applied stress, the size of initial plastic events before the macroscopic shear band phenomena, the role of free volume in the activation sites, and the enhancement of relaxation around nucleation sites [14, 179, 180]. As such, improved means of mechanical probing around the yield transition can help shine light on means of plastic deformation in glassy polymers and amorphous solids at large.

2.3.3 Continuum Yield and Plasticity

In a continuum picture, the specific mechanism of plasticity that produces yield is unimportant so long as the bulk deformation behaviour is consistent. The von Mises criterion that is followed here assumes invariant material properties with applied strain. This is a good first order approximation for materials with a close packed structure and for unconfined compression. It often holds less true for amorphous materials under certain conditions however (such as densification through a hydrostatic compression). These pressure effects will be explored in greater detail for the case of amorphous thin films in Chapter 5, with only the simple von Mises picture presented here.

Fundamental to the onset of yield in the continuum model is the presence of shear stress. In particular, hydrostatic stress alone does not cause yielding in materials with a close packed and homogeneous structure. However there is some contention around this for amorphous materials. Some theories put forward that shear may evolve around sites of disorder within an amorphous structure even under hydrostatic stress and allow for yielding under these conditions [181]. Regardless, it is accepted that shear plays a fundamental role in material yield in ordered and disordered matter while being modulated to varying degrees under hydrostatic stress conditions. As such I will consider the decoupling of strain into dilation and distortion components. As shown in Eq. 2.8, the octahedral normal stress is the average of the three principle stresses. Where the three principle stresses are not equal, the octahedral shear stress is given by [182]

$$\tau_{oct} = \frac{1}{3}\sqrt{\left(\sigma_{xx} - \sigma_{yy}\right)^2 + \left(\sigma_{yy} - \sigma_{zz}\right)^2 + (\sigma_{zz} - \sigma_{xx})^2 + 6(\sigma_{xy}^2 + \sigma_{yz}^2 + \sigma_{xz}^2)} \tag{2.29}$$

A material will yield when the octahedral shear stress reaches a critical value

$$\tau_{oct} \geq \tau_{oct_0} \tag{2.30}$$

In axial loading, such as that demonstrated in Fig. 2.1 only one of the principle stresses has a value $\neq 0$. For example $\sigma_{xx} = \sigma_0$, $\sigma_2 = \sigma_3 = 0$. This gives the yielding criteria in axial loading as [183]

$$\tau_{oct_0} = \tau_{oct} = \frac{1}{3}\sqrt{(\sigma_0 - 0)^2 + (0 - 0)^2 + (0 - \sigma_0)^2} = \frac{\sqrt{2}}{3}\sigma_0 \tag{2.31}$$

Where σ_0 is the yield stress. Nomenclature choices often also represents this as σ_Y. To avoid confusion with the principle stress in the y direction (σ_{yy}) I represent it here as σ_0. In later sections where such principle strains are not of direct consideration, σ_Y or simply Y may be used to denote the yield stress. While this describes the amount of shear required for a system to undergo yield, rearrangement of the above describes the yield stress

$$\sigma_0 = \sigma_{vm} = \frac{1}{\sqrt{2}}\sqrt{\left(\sigma_{xx} - \sigma_{yy}\right)^2 + \left(\sigma_{yy} - \sigma_{zz}\right)^2 + (\sigma_{zz} - \sigma_{xx})^2 + 6(\sigma_{xy}^2 + \sigma_{yz}^2 + \sigma_{xz}^2)} \tag{2.32}$$

This equation describes the von Mises yield surface, which is a cylinder around the hydrostatic axis ($\sigma_{xx} = \sigma_{yy} = \sigma_{zz}$). Intersection with this curve results in yielding. The yield curve is given by the circular intersection with the octahedral plane ($\sigma_{xx} + \sigma_{yy} + \sigma_{zz} = 0$), with a radius of $\sqrt{\frac{2}{3}}\sigma_0$, and defines the materials capacity for shear before yield. From this comes the implication that yield is independent of hydrostatic stress. This yield surface is visualised in Fig. 2.7. Often in literature a two dimensional approach is used, which simplifies the yield surface from a cylinder to an ellipse (from its intersection with the planes formed by principle axes).

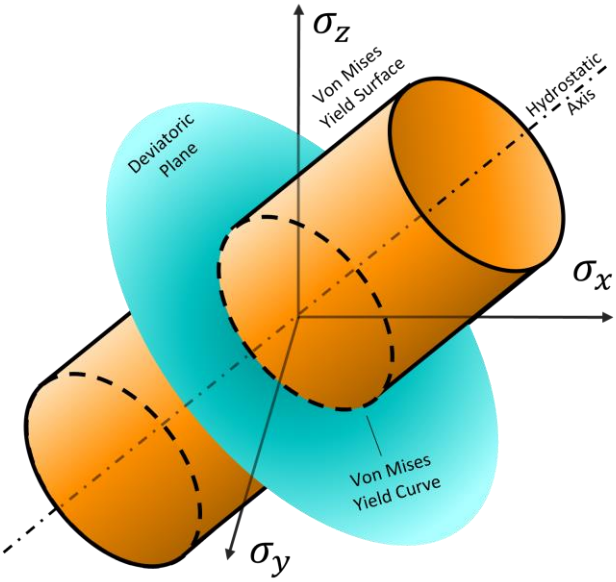

Fig. 2.7, *Visualisation of the conical von Mises yield surface which revolves around the hydrostatic axis of* $\sigma_{xx} = \sigma_{yy} = \sigma_{zz}$*, and the von Mises yield curve which is the intersection of this surface with the octahedral plane wherein* $\sigma_{xx} + \sigma_{yy} + \sigma_{zz} = 0$

Once intersection with the yield surface occurs, plastic deformation commences as the material can no longer accommodate further elastic shear stress. From this point, shear stress remains at the level of the shear surface (a constant value for pressure independent materials), and material deformation continues via plastic flow. This kind of deformation can be described by the Levy-Mises relations for a time increment δt [184]

$$\frac{\delta \varepsilon_{xx}}{\sigma_{xx}-\frac{1}{2}(\sigma_{yy}+\sigma_{zz})} = \frac{\delta \varepsilon_{yy}}{\sigma_{yy}-\frac{1}{2}(\sigma_{zz}+\sigma_{xx})} = \frac{\delta \varepsilon_{zz}}{\sigma_{zz}-\frac{1}{2}(\sigma_{xx}+\sigma_{yy})} \tag{2.33}$$

These formulas can be combined with the relations for elastic behaviour presented earlier to describe the plastic deformation of a simple elastic-plastic material in the Prandtl-Reuss equations [185]

$$d\varepsilon_{ij} = \frac{1+v}{E} d\sigma_{ij} - \frac{v}{E}\delta_{ij} d\sigma_{kk} + d\lambda s_{ij} \tag{2.34}$$

Where λ is the scalar plastic multiplier and s_{ij} are the deviatoric components of strain. In this relation the first two terms denote elastic deformation, and the later describes plastic deformation.

In Fig. 2.8 we can visualize the stress vs. strain behaviour of a simple elastic-plastic material undergoing uniaxial tension or compression.

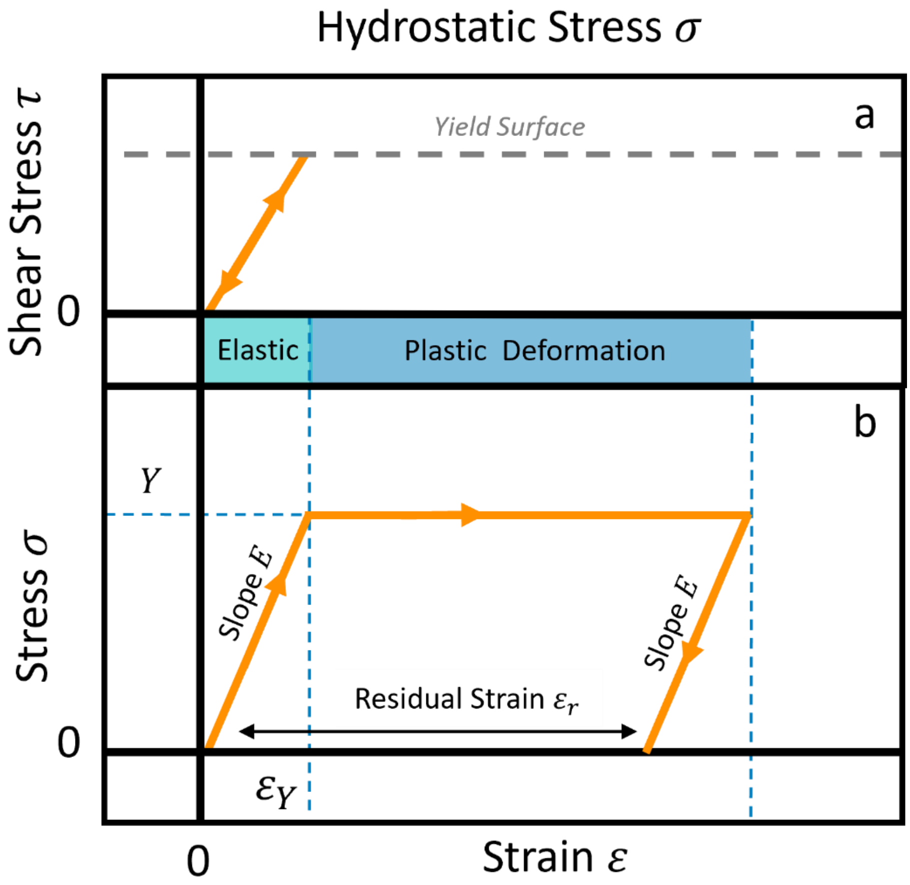

Fig. 2.8, (a) *Shear vs hydrostatic stress and* ***(b)*** *stress vs strain curve for a simple elastic-plastic material under uniaxial tension or unconfined uniaxial compression. The regimes of elastic and plastic deformation are denoted along with the yield stress and strain, and residual strain after unload*

The initial slope of the stress vs strain curve in Fig. 2.8 is the Young's modulus, E as discussed in the section on continuum elasticity. At the yield point where the shear intersects the yield surface, the material can facilitate the generation of no further shear and strain continues at a constant stress level as the material undergoes plastic deformation. When stress is removed, the material recovers elastically with a slope E to zero stress. The resulting strain at zero stress is known as the residual strain and is the final deformation of the material after elastic recovery.

Confined uniaxial strain deformation alters this simple picture considerably as shown in Fig. 2.3. Here, the initial slope of the stress vs strain curve is the larger confined modulus M as discussed in Section

2.1 (Eq. 2.17), as is the unload slope when load is removed before the yield point. The yield criteria is also changed for confined compression, with intersection with the von Mises yield surface increasing as a function of v in a similar vein to the confined modulus M. This can be understood qualitatively as being due to the relative generation of more hydrostatic to deviatoric stress per increment of imposed elastic strain in confined conditions. The confined yield stress in uniaxial loading can be expressed as

$$Y_c = \left(\frac{1-v}{1-2v}\right) Y \tag{2.35}$$

Where the subscript c denotes 'confined', and Y is the unconfined yield stress, replacing the nomenclature of σ_0 from earlier to more easily distinguish between confined and unconfined states. The confined and unconfined yield stresses are therefore identical for $v = 0$, while the confined state approaches ∞ as $v \rightarrow 0.5$.

Beyond yield, the combined effects of inelastic shape change and deviatoric-free elastic strain in confinement can produce novel and unconventional mechanical behaviour. In unconfined uniaxial stress, yielded elastic-plastic material will expand outwards under combined influence of incompressible plastic flow and the elastic Poisson effect. In uniaxial strain, the confining walls apply an equal counter-stress on the body against all directions of expansion, the net results of which is that only the hydrostatic component of stress can continue to grow. The material accepts no further deviatoric deformation, and is instead deformed purely via a volume change with a stress vs strain slope given by the bulk modulus K (Eq. 2.15). Note that K ranges from $\frac{E}{3}$ for $v = 0$ to ∞ for $v \rightarrow 0.5$ (the latter volume preserving elastic deformation), meaning it is ostensibly always greater than a slope of 0 for pure plastic flow in the unconfined uniaxial stress condition. The increased elastic slope M, confined yield Y_c, and bulk modulus K, are demonstrated in Fig 2.9 (a) compared to the case of unconfined compression as in Fig. 2.8.

The existence of an increasing stress in the material beyond the plastic yield point in the confined case also facilitates a different behaviour in the unloading portion. At the instant load is decreased again, the material recovers with a slope M (equivalent behaviour to the unload slope of E in the unconfined geometry). As this continues, the internal shear stress decreases also towards 0 at the same rate as during the loading portion. However, as the shear reaches 0, residual loading stress held by the confining walls act to introduce additional, directionally opposite shear into the material even as the walls continue to resist outwards relaxation. This causes shear to increase again in the unloading portion at the same rate as during loading and may facilitate a second intersection with the yield surface, causing a change of unload slope to the bulk modulus, K, which continues to 0 stress. Due to the equivalence of the rate of shear development during loading and recovery, the following relation holds

$$\sigma_{max} - Y_{c,u} = 2Y_c = \frac{2(1-v)}{1-2v} Y \tag{2.36}$$

Where σ_{max} is the maximum stress reached, $Y_{c,u}$ is the yield stress in the unloading yield, Y_c is the confined yield stress in the loading portion, and Y is the unconfined yield stress. Fig. 2.9 (b) and (c) demonstrate the generation of shear on unloading that facilitates this second intersection with the yield surface. As shear is a scalar quantity, Fig. 2.9 (c) is the more accurate depiction, with Fig. 2.9 (b) provided for clarity on the process.

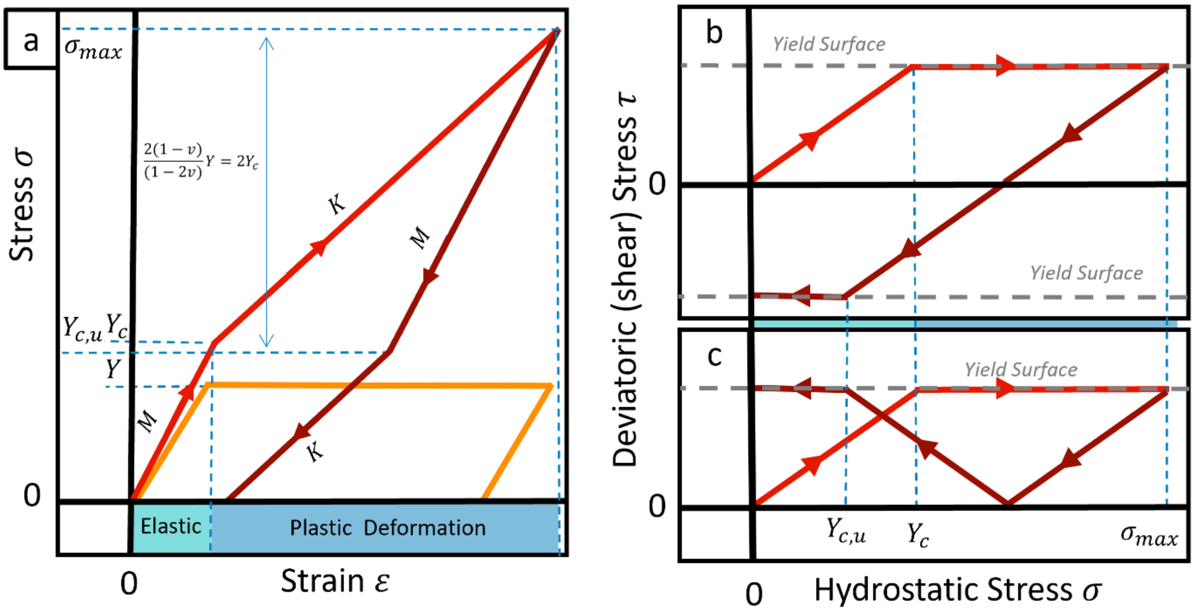

Fig. 2.9, (a) *Stress vs strain behaviour for confined uniaxial strain (red) vs unconfined uniaxial strain (orange) compression. The initial slope of the uniaxial strain curve is the confined modulus M, with a transition to the bulk modulus K at the confined yield stress Y_c, all of which are higher than their unconfined counterparts, as functions of the Poisson's ratio of the material.* ***(b, c)*** *Shear evolution of confined uniaxial strain vs applied stress, showing intersection with the yield surface that causes yielding. The intersection with the yield surface on unloading as the shear grows due to the confining wall stress causes a second yielding event in unloading at Y_c. While* ***(b)*** *most clearly demonstrates how this shear grows in again in the unloading regime,* ***(c)*** *is the more accurate depiction as shear is a positive scalar quantity*

2.3.4 Limitations on Testing of Anisotropic Materials

The above relations on confined continuum yield and plasticity assume isotropic, linear elastic material properties. Any deviation from isotropy, such as the transverse linear isotropy of nanosheet network films, complicates the analysis greatly. Directionally dependant elastic moduli, plastic yield and plastic flow may alter the influence of the confining walls on the generation and response to shear and applied pressure. Several models have been proposed to model the yield surface of an anisotropic medium under unconfined compression, such as the work of Taylor in 1938 [186] as well as Hill in 1948 and 1979 [187, 188] (with the assumptions in such models often introducing inaccuracy depending on the loading criteria [189]), and the more modern general anisotropic yield criterion [190].

Regardless of the model used, yield surfaces in anisotropic media are greatly complicated from the cylindrical von Mises shear surface discussed above, with far more complex yield surfaces generated depending on the level of anisotropy. To the best of the author's knowledge, no rigorous analytical solution exists for the yield surface for confined yield and plastic compression of anisotropic media. Should such a solution exist, application to the graphene networks explored in this work would be beyond the capabilities of current mechanical testing technologies. For example, an analogous anisotropic yield criteria corresponding to the isotropic case presented earlier in Eq. 2.32 as proposed originally in Hill's model takes the form [187]

$$Y = \sqrt{F\left(\sigma_{yy} - \sigma_{zz}\right)^2 + G(\sigma_{zz} - \sigma_{xx})^2 + H\left(\sigma_{xx} - \sigma_{yy}\right)^2 + 2L\sigma_{yz}^2 + 2M\sigma_{xx}^2 + 2N\sigma_{xy}^2} \quad (2.37)$$

Where F, G, H, L, M and N are constants determined experimentally. The actual number of constants required will depend on the degree of anisotropy in the material. Note that this expression handles a purely plastic material only, with no consideration of anisotropic elasticity. A major restriction of nanomechanical testing is the limited testing geometries available to constrain a large number of experimental parameters. Thus such determinations for anisotropic thin films are beyond current techniques, and as such this will not be considered in detail in this thesis.

Explorations of the bulk modulus can be performed on bulk anisotropic materials by considering calculations of singular anisotropic unit cells [191], or for materials with structural induced anisotropy (such as pores), considering the bulk modulus of the non-porous portions [192]. For granular systems, it is known that the bulk modulus behaves differently than for a fluid due to the nature of the grain-grain contacts [193], which numerical simulations have attempted to address for certain systems [194], and can vary greatly depending on the grain shape [195]. However, determination of the bulk modulus in a novel thin film granular system such as the nanosheet networks, and how this may be compared to the post-yield slope K under uniaxial strain compression is unclear. As with the yield stress, nanomechanical techniques to explore such parameters on thin films are as of yet undeveloped and as such our analysis of yield and bulk modulus via uniaxial compressive strains will be limited to isotropic amorphous materials such as polymer glasses.

2.4 Pressure dependencies of the yield surface

The analysis above for moduli and yield surfaces are further complicated by the presence of excess free volume in amorphous materials. In the case of close packed structures such as crystals and metals, the relations for yield and modulus as presented in Sections 2.3 hold true. However, for the range of materials with a non-equilibrium or amorphous morphology, the very act of applying stress can change their intrinsic mechanical properties. As an example let us consider a solid material with an amorphous morphology and a material volume fraction of ϕ (ie, this fraction of the material volume is occupied by solid material, and $1-\phi$ is free volume). Let us also consider this material has a yield strain of ε_y, and is compressed to ε_x where $\varepsilon_x < \varepsilon_y$. In this case, the free volume of the material has reduced, before reaching the yield point, to a value of $\phi + \varepsilon_x$ (assuming void space compression occurs before atomistic potential compression, which is often a good approximation). In this case, the material morphology has demonstrably changed to that of a less porous, denser material before the onset of yield.

This often causes the yield point to change as the material characteristic is changed, and results in a pressure dependent yield surface, usually manifesting as higher yield points under compression, and lower yield points under tension. As well as this, the elastic properties of the material also often changes with applied pressure for similar reasons. The causes for this are varied, for example the densification may decrease the atomistic separation, requiring more force for compression (Lennard Jones potential demonstrated in Fig. 1.6) for particulate systems like metallic glasses, or rearrangements of the amorphous structure. It may collapse unstable void spaces in porous media, leaving only more stable and sturdier pores. In polymers it alters the ability for chains to move and rearrange with further applied stress. The intrinsic means of mechanical pressure dependency are as numerous as the materials that manifest them [196-200].

Though the mechanisms behind the yielding phenomenon are not entirely understood, a known important quantity in the yielding process is shear stress. Octahedral shear stress acts to mediate material yield in particular, with hydrostatic pressure alone being unable to cause yielding in materials with a homogenous, close packed molecular structure. For amorphous materials the role of octahedral shear stress is less clear, and some theories suggest that yielding may occur around sites of local disorder under nominally macroscopic hydrostatic conditions [181]. As discussed above, a material will yield when the octahedral shear stress exceed a critical threshold, ${\tau_{oct}}_0 = \frac{\sqrt{2}}{3}\sigma_o$. In the case of uniaxial strain compression, the octahedral shear stress evolves as a function of the applied pressure. Following from the von Mises criterion for uniaxial strain this is expressed as [181, 201]

$$\tau_{oct} = \frac{2\sqrt{2}}{3}\frac{G}{K}P \tag{2.38}$$

Where P is the applied pressure, G is the shear modulus, and K is the bulk modulus. Therefore, the material will yield when the applied pressure reaches a point such that $\tau_{oct} > \tau_{oct_0}$. For free volume amorphous materials, the required octahedral shear stress for yield evolves with the applied pressure. For low contact pressures, this is a linear relation in the von Mises condition [44, 202]

$$\tau_{oct_P} = \tau_{oct_0} + \mu_{vm} P \tag{2.39}$$

Where μ_{vm} is the Von Mises pressure coefficient. This is a simple linear pressure dependency which may not hold for more complex material morphologies. For example, the Cam-clay model for soils considers the granular nature of rough and frictional spoil particulates, which gives an elliptical yield surface [203, 204]. In this thesis I consider only the more general linear von Mises yield surface criterion.

It is only when sufficient pressure is applied for the octahedral shear stress to overtake the yield surface (in both the pressure dependant and static case), that a transition to plastic deformation will occur. However, it is possible for the shear surface to evolve faster than the octahedral shear stress and therefore for yield to be indefinitely prohibited should shear stress generation be prohibitively inhibited (ie, the criteria of $\mu_{vm} > \frac{2\sqrt{2}}{3}\frac{G}{K}$). This will clearly be more common in geometries that limit shear deformations. This has been observed experimentally on amorphous materials, for example in experiments performed by Ravi-Chandar in which they were unable to cause a sample of PMMA to yield under uniaxial strain compression [205].

Such investigations surrounding the yield transition offer insight into the propagation of elastic vs plastic strains and may help to shine light on the poorly understood carriers of plasticity in amorphous systems such as polymers. As an example, the pressure dependency of the yield surface in polymer systems is often attributed to a reduction in molecular motions as the material densifies, more specifically the α and β chain relaxations [206, 207]. Chapter 5 of this thesis focuses on the exploration of pressure dependencies in amorphous thin film systems and how this may be approached experimentally for such challenging geometries.

2.5 Viscoelasticity

Viscoelasticity is a property whereby a material shows a time dependent component to its deformation under applied stress. Ie, there is a viscous or dissipative component to the deformation contrasting with the linear elastic component. This often arises in amorphous media that may undergo structural rearrangement under applied stress, even in the otherwise elastic regime. For example, in polymers below their glass transition temperature, liquid-like melt motion arising from thermally induced full chain motion is highly suppressed. However as discussed in Chapter 1, the glass transition is a kinetic thermal transition rather than a morphological one, and the morphological nature of the network remains largely that of its liquid state without the necessary thermal energy to flow. Because of this, the chains may still exhibit inelastic deformation even before yield, due to a time-dependent viscous component of their constitutive behaviour [208, 209].

Viscoelastic solids generally show the following mechanical properties:

- Hysteretic behaviour: Hysteresis in the stress vs strain curve below the yield point, caused by energy dissipation as heat.
- Time dependent stiffness : ie, stiffness that depends on the rate over which stress or strain is applied.
- Creep Behaviour : An instantaneously applied and held constant stress causes an increasing and tapering strain at that maintained stress.
- Stress relaxation: An instantaneously applied and held constant strain causes a reducing and tapering stress to maintain that strain.

These are demonstrated in Fig. 2.10.

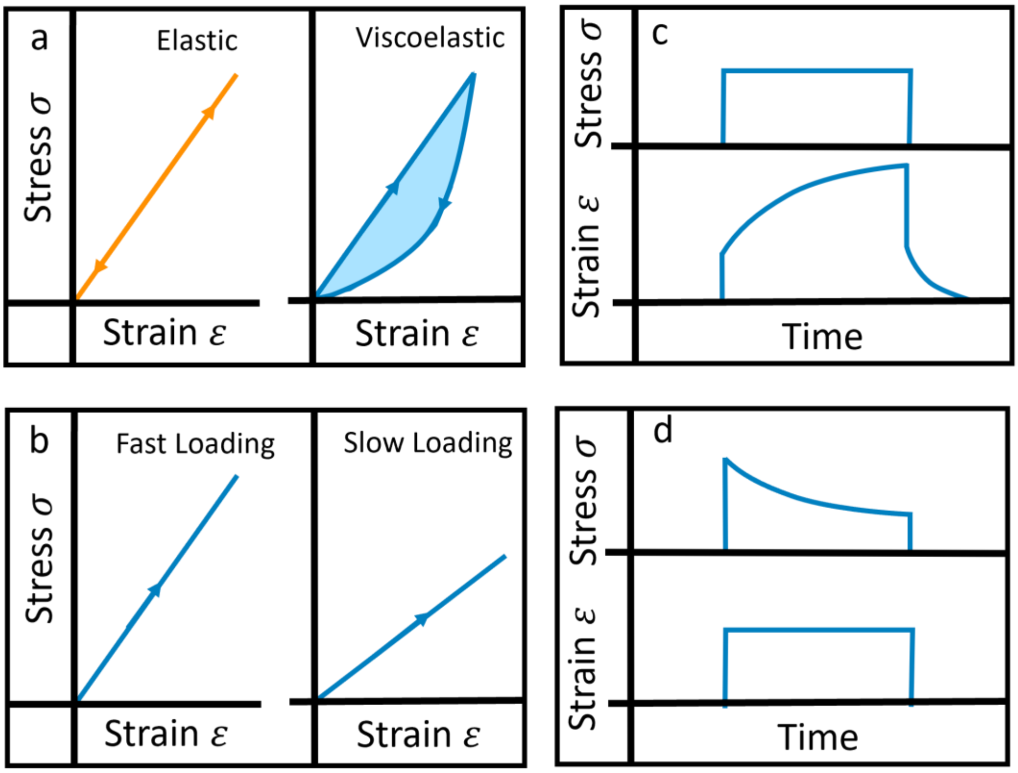

Fig. 2.10, Features of viscoelasticity evident in stress vs strain curves. ***(a)*** *Hysteretic behaviour below the yield point caused by heat dissipation,* ***(b)*** *Rate dependant stiffness, where stiffness changes depending on the speed of applied stress,* ***(c)*** *Creep, where stepwise application and hold of a constant stress causes continuing strain, and* ***(d)*** *Stress relaxation, where stepwise application and hold of a constant strain causes a reducing stress*

Like elasticity, viscoelasticity can be modelled linearly. Linear viscoelastic models are generally built from a system of springs and dashpots, representing the elastic and dissipative components, respectively. The most simple of these incorporate one of each. The trade-off for such a simplistic model is a large degree of inaccuracy. Constructing more complex spring-dashpot models can increase the fidelity to a true viscoelastic system at the cost of complexity in modelling. Generally a balance is struck between accuracy and complexity. The Maxwell and Kelvin-Voigt models are primary single spring and dashpot models; the Maxwell model consisting of a spring and dashpot in series, and the Kelvin-Voigt model consisting of the same in parallel. These are represented in Fig. 2.11. The maxwell model predicts stress relaxation but does not accurately represent creep, while the Kelvin-Voigt model predicts creep but is often inadequate for stress relaxation. The maxwell model is the simplest analytical descriptor of a viscoelastic fluid, while the Kelvin-Voigt model is the simplest descriptor of a viscoelastic solid, the later being more pertinent to the materials explored in further chapters.

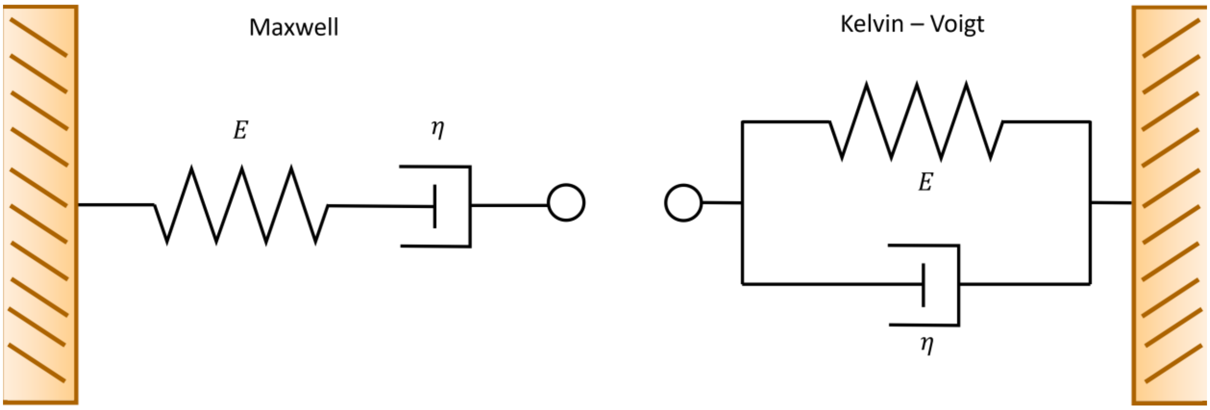

Fig. 2.11, *Maxwell and Kelvin – Voigt models of viscoelasticity, each incorporating one spring with spring constant E and one dashpot with viscosity η*

The stress and strain relation for the Maxwell model is as follows [209]

$$\dot{\varepsilon} = \frac{\sigma}{\eta} + \frac{\dot{\sigma}}{E} \tag{2.40}$$

Where E is the spring constant of the spring, η is the viscosity component represented by the dashpot, and the dot notation is the standard time derivative. The same for the Kelvin – Voigt model is

$$\sigma = \varepsilon E + \eta\dot{\varepsilon} \tag{2.41}$$

With the drawbacks of these simple representations, a two spring, one dashpot representation is often used instead. This is known as a standard linear viscoelastic model, also called a Zener model, and has two representations, a Maxwell representation and a Kelvin representation, depending on the arrangement of these. These models are represented in Fig. 2.12 and offer a more complete estimation of viscoelastic behaviour under general loading conditions (for example uniaxial compression), incorporating creep and stress relaxation. They may return inaccurate results however for more obscure loading conditions.

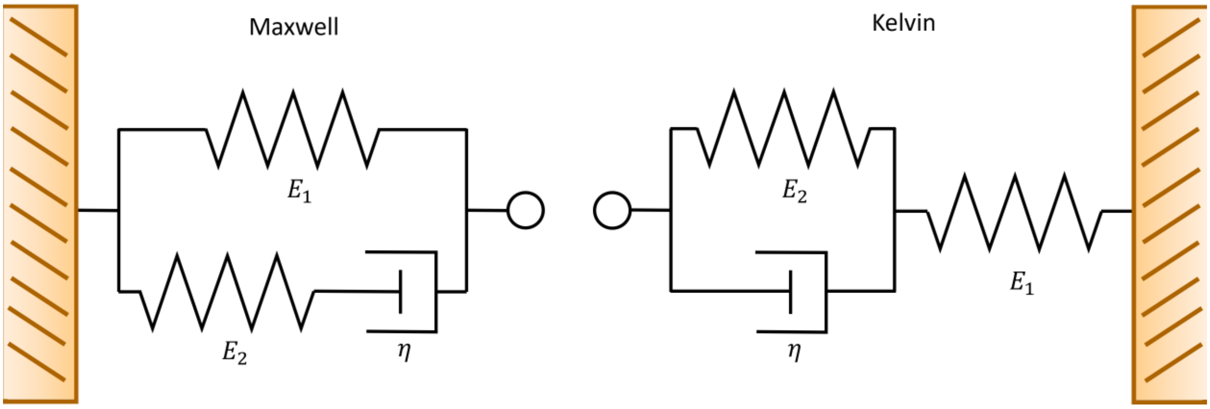

Fig. 2.12, *Maxwell and Kelvin representation of Zener models. These models better represent complete viscoelastic behaviour than the single spring and dashpot models presented in Fig. 2.11*

The relations for the Maxwell representation is

$$\varepsilon + \frac{\eta(E_1+E_2)}{E_2E_1}\dot{\varepsilon} = \frac{\sigma}{E_1} + \frac{\eta}{E_2E_1}\dot{\sigma} \tag{2.42}$$

Where the spring constants E_1 and E_2 are as represented in Fig. 2.12. And for the Kelvin representation

$$\varepsilon + \frac{\eta}{E_2}\dot{\varepsilon} = \frac{E_1+E_2}{E_1E_2}\sigma + \frac{\eta}{E_1E_2}\dot{\sigma} \tag{2.43}$$

There also exists Anti-Zener models of standard linear viscoelasticity, which comprise of one spring and two dashpots in the same configuration as for the Zener cases. As they are not used in this work and are similar in form to the Zener models they will not be approached in detail here.

Burges models are four component systems consist of two springs and two dashpots, with the added complexity incorporating viscous flow into the creep behaviour, whereby instead of approaching a constant asymptote as in the standard linear model, the asymptote increases linearly under stress. More complex again is the generalized Maxwell model, which uses the standard linear model in a Zener Maxwell configuration, adding in further linear Maxwell elements to represent that relaxation occurs over a distribution of timescales. This is represented schematically in Fig. 2.13.

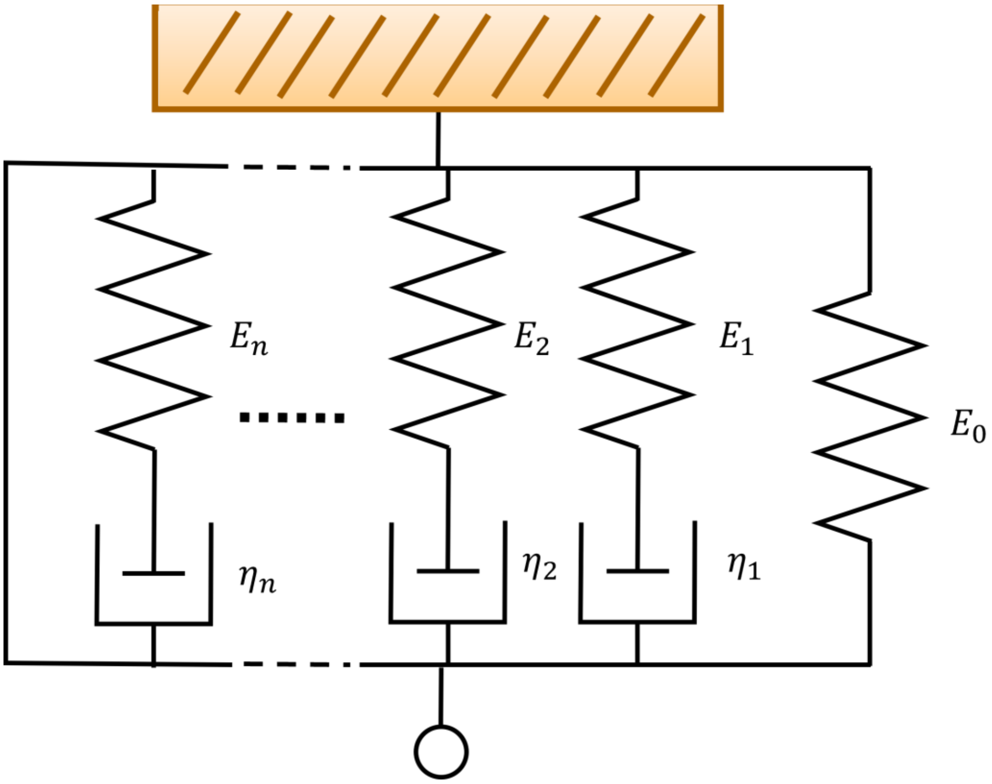

Fig. 2.13, *Generalized Maxwell model, incorporating n linear Maxwell elements into a standard linear model to describe viscoelastic behaviour with several time dependencies*

Incrementally increasing complexity by adding components allows for increasingly more accurate representations of viscoelastic behaviour as demonstrated above. The standard linear viscoelastic model is the most generally utilised of these in systems where it is applicable, as it offers a good trade-off between accuracy and complexity.

Ch 3 : Nanoindentation

In this chapter I review the experimental nanoindentation techniques used for a large portion of the presented work. I introduce the principles of conventional nanoindentation practice using self-similar sharp tips as developed by Warren Oliver and George Pharr [8], based on instrumented indentation co-developed with John Pethica, that is still used as the nanoindentation standard to this day. This includes the working principles of a nanoindentation system and the analysis required to convert the measured quantities into quantifiable material properties. I will also approach the case of a spherical indentation used for probing densification of polymer thin films. Of particular interest for this work, however, is a recent advance in nanoindentation testing of supported films dubbed the Layer Compression Test (LCT) [31]. This test utilises an aligned flat punch with diameter far exceeding the film thickness and allows for separate quantitative characterisation of elastic and plastic effects beyond current nanoindentation standards. The modifications to a standard indentation system to allow for the implementation of the LCT in our work, and the work done in the course of this thesis to forward the understanding of the technique will be detailed.

3.1 Device Principles

The latter half of the 20th century saw significant advances in the manipulation of matter on the micron scale, with the semiconductor industry in particular launching a ‘race to the bottom’ in terms of device fabrication [210], and new microscopy techniques allowing for determination of processes at these new length scales [211]. This necessitated new mechanical testing techniques to keep up with these technological advancements, and nanoindentation was developed to probe the mechanical nature of thin films materials and small volumes at this scale. When introduced in its currently most recognisable form in 1992, nanoindentation allowed for the mechanical nature of such systems to be explored for the first time and has become the de-facto technique for measuring mechanical properties of nano and micro scale solid matter.

Nanoindentation functions via measuring the displacement of a tip of known geometry into the material of interest, as well as the load required for that displacement. The nanoindentation system used primarily in this work is the MTS Nanoindenter XP, for which a simple schematic of the working components is shown in Fig. 3.1. Tip motion is monitored in the loading direction by a capacitance gauge consisting of three plates, allowing measurement resolution sub 0.01nm. The system is fundamentally one dimensional, with a series of support springs attached in parallel to the loading cell ensuring compliance in the loading direction, but with high stiffnesses in all other directions. The Loading cell is controlled by an electromagnetic coil actuator and allows for loads up to 500mN, and a high load module allowing additional loads of up to 10N. Fidelity is in the range of ~50nN, and the tip displacement range is 1.5mm. The sample and indenting unit are contained within the load frame, which is designed to be stiff so as to minimize unwanted strains when indenting, which would be measured as displacement into the sample and would need to be corrected for after indentation.

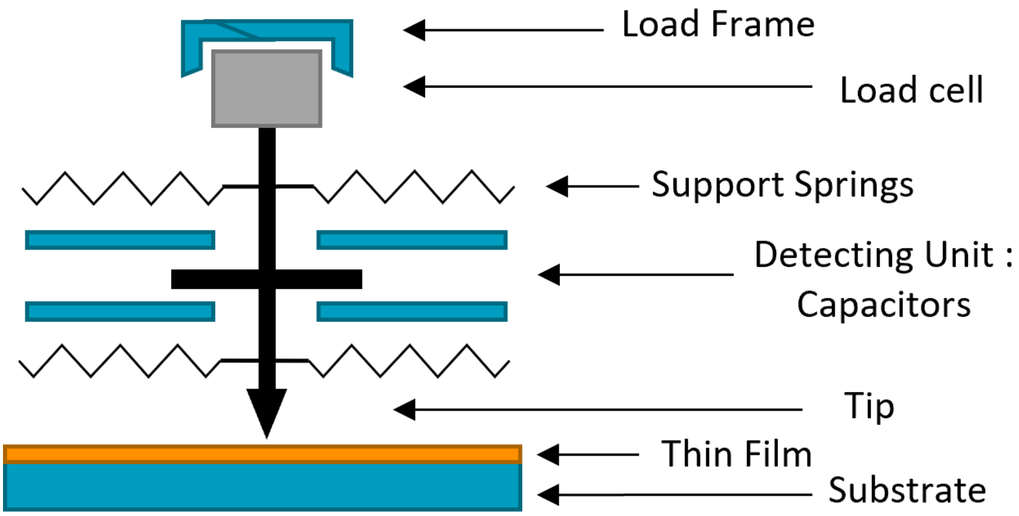

Fig. 3.1, *Schematic of the operating components of a one dimensional nanoindenter unit used to probe the mechanics of thin film materials*

3.2 Berkovich Tip Based Instrumented Indentation

Typical nanoindentation is performed using the Oliver-Pharr method [8] and allows for the determination of Hardness and Young's modulus of the sample of interest. This is done by indenting to a required depth and measuring the load applied to reach this depth, the resulting data typically being plotted in a load vs displacement curve as in Fig. 3.2. Measurement of both Hardness and Modulus require the contact area to be known, so tips with known contact area functions are typically used. The most popular tip geometry for this purpose is the Berkovich tip, which is a geometrically self-similar three sided pyramid that imposes a fixed strain on a half-space sample [212]. Typically, this is constructed with half angle of 65.3 degrees and included angle of 142.3 degrees. Importantly, it has a known area function that allows knowledge of the contact area with indentation depth on smooth surfaced, non-porous samples. Additionally, it has benefits over other tips with such features (such as conical tips, or the four sided pyramidal Vickers tips) by being easier to grind to a sharp and controllable point during production, granting it favour for nanoindentation applications [213]. A schematic of a Berkovich tip and corresponding load vs displacement curve is shown in Fig. 3.2.

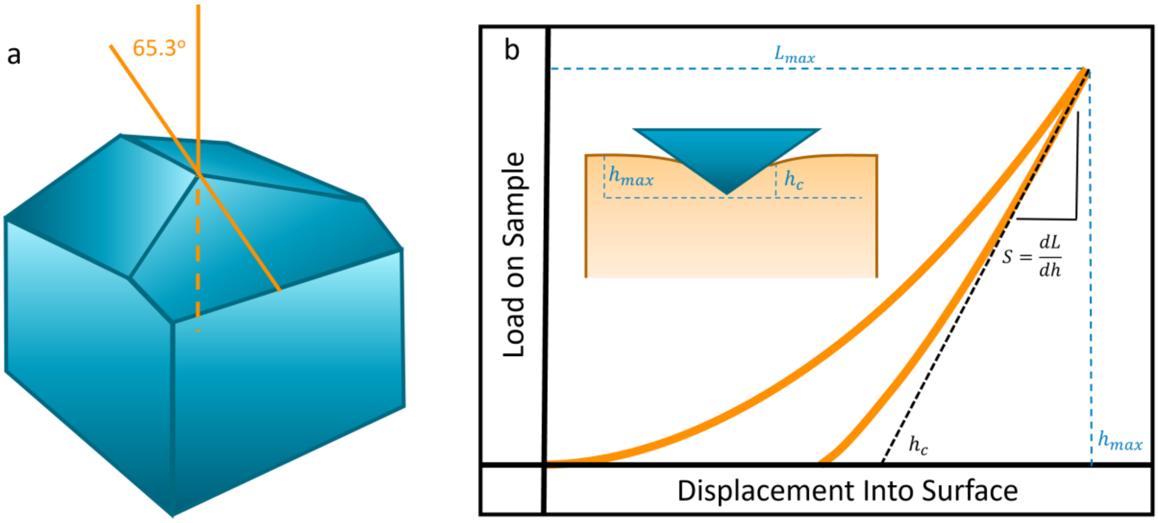

***Fig. 3.2, (a)** Berkovich indenter tip showing half angle of 65.3°, and **(b)** load vs displacement curve for Berkovich indentation into a halfspace, showing maximum load and displacement L_{max} and h_{max}, respectively. Also shown is the initial unload slope S which is used to determine Young's modulus, and h_c, the residual contact depth when sample compliance is accounted for*

The Hardness can be determined if the load and displacement are both known, provided the tip area function is known to allow conversion from depth to contact area

$$H = \frac{L_{max}}{A_p} \tag{3.1}$$

Where H is the hardness, L_{max} is the max load of the indent, and A_p is the projected area of the indent at peak load, specific to the tip geometry, and for a Berkovich with half angle of 65.3 degrees is

$$A_p = 24.5h_c^2 \tag{3.2}$$

Where h_c is the residual contact depth when compliance of the surface is accounted for.

For calculating the Young's modulus, we may consider the stiffness of the initial portion of the unload, as this stiffness is determined by the elastic recovery of the sample.

$$S = \frac{dL}{dh} = \beta \frac{2}{\sqrt{\pi}} E_r \sqrt{A_p} \tag{3.3}$$

Where S can be seen in the load vs displacement curve in Fig. 3.2. β is a correction factor specific to the tip geometry which can be calculated experimentally on samples with known Young's modulus (typically for well manufactured tips $\beta \approx 1$), and E_r is the reduced Young's modulus which is a function of the Young's modulus of the tip and sample as follows

$$\frac{1}{E_r} = \frac{1-v_i^2}{E_i} + \frac{1-v_s^2}{E_s} \tag{3.4}$$

Where v is the Poisson's ratio and the subscripts i and s refer to the indenter tip and the sample, respectively. Indenter tips are usually made of diamond, so for soft samples, $E_r \approx E_s$, but for stiffer samples the relation in Eq. 3.4 should be used.

3.3 Continuous Stiffness Measurement (CSM)

The Oliver-Pharr method described above allows for a single measurement of Young's modulus and hardness per indent. This may necessitate several indents if an average value is required, or if depth dependent measurements are required. An oscillatory continuous stiffness measurement (CSM) method was proposed by Warren Oliver and John Pethica in 1989 and is often employed for continual measurements of stiffness and hardness [214] throughout indentation. This is done by applying a small scale oscillation to the indenter tip (typically of the order of 1 to 5 nm amplitude and ~45Hz frequency) and treating the indenter as a damped one-dimensional harmonic oscillator. This is represented schematically in Fig. 3.3 [215]

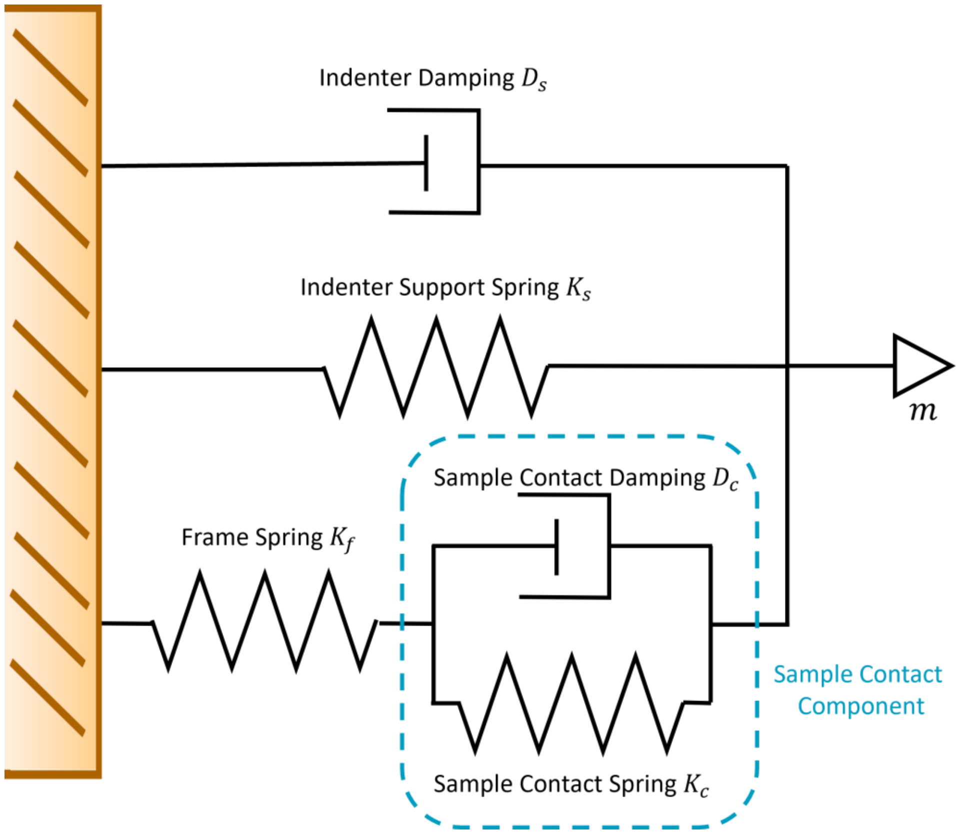

Fig. 3.3, *Indenter in contact with sample represented as a damped simple harmonic oscillator*

An oscillating force with a frequency ω is applied as

$$F(t) = F_0 e^{i\omega t} \tag{3.5}$$

With a resulting displacement

$$h(t) = h_0 e^{i(\omega t - \phi)} \tag{3.6}$$

With a phase lag of ϕ between the driving load and the displacement measurement. This phase angle will be used more directly for a surface determination method later in this chapter. As a damped oscillator, this can be inserted into the equation

$$m\ddot{h} + D\dot{h} + Kh = F(t) \tag{3.7}$$

Where m is the mass, D is the damping parameter, and K is the spring parameter. The solution of this has a real and imaginary part that results in the damping and stiffness solutions

$$D\omega = \frac{F_0}{h_0}\sin(\phi) \tag{3.8}$$

$$K = m\omega^2 = \frac{F_0}{h_0}\cos(\phi) \tag{3.9}$$

This can be analyzed for both for a free-standing indenter (ie. with no sample present) and for an indenter in contact. The total damping components are

$$D = D_s + D_c \tag{3.10}$$

Where the subscript s represents the indenter support springs, and c represents the component of contact. The total stiffness component is

$$K = \left(\frac{1}{K_f} + \frac{1}{K_c}\right)^{-1} + K_s \tag{3.11}$$

Where subscripts c and s are as before, and f is the indenter frame. Rearranging for the sample stiffness gives

$$K_c = \frac{K_f(K - K_s)}{K_f - K - K_s} \tag{3.12}$$

We can substitute in Equ (3.9) for both the contact case and free-standing case giving

$$K_c = \frac{K_f\left(\frac{F_0}{h_0}\cos(\phi) - \left[\frac{F_0}{h_0}\cos(\phi)\right]_{free}\right)}{K_f - \left(\frac{F_0}{h_0}\cos(\phi) - \left[\frac{F_0}{h_0}\cos(\phi)\right]_{free}\right)} \tag{3.13}$$

This relation allows for the continual measurement of stiffness throughout indentation via oscillating harmonic contact and relies only on the frame stiffness, and the difference between the amplitude ratio before and after sample contact. This can be used to probe depth sensitive stiffnesses of samples via a single continuous indentation.

3.4 Spherical Indentation

Indentations performed with spherical tips can be analysed with classical contact mechanics. In 1882, Hertz solved the problem of contact between two spherical elastic bodies, hoping to apply the results to optical lenses in close contact to characterise the distortion. He extended this work to the problem of elastic contact between a sphere and a half space, which can be applied to the contact of a spherical indenter tip on a flat sample [216, 217].

For a perfect sphere on a perfectly flat half-space, the contact begins as a point contact, which grows in size as load is applied as the sphere and sample deform. The contact area is

$$a = \sqrt{Rd} \tag{3.14}$$

Where R is the radius of the sphere and d is the displacement into the surface. The Force for this displacement is given by

$$F = \frac{4}{3} E_r R^{\frac{1}{2}} d^{\frac{3}{2}} \tag{3.15}$$

Where E_r is the reduced modulus as described in Eq. 3.4. This contact gives an uneven pressure distribution where the maximum pressure is given by

$$p_o = \frac{3F}{2\pi a^2} \tag{3.16}$$

And the distribution of pressure a distance r from the centre of the contact is

$$p(r) = p_o \left(1 - \frac{r^2}{a^2}\right)^{\frac{1}{2}} \tag{3.17}$$

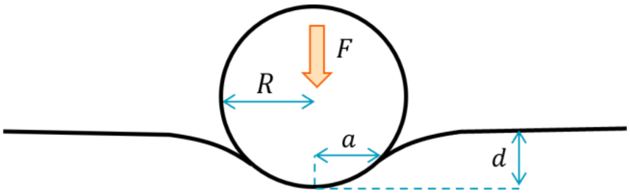

Fig. 3.4, *Contact parameters for spherical contact with a halfspace for Hertzian contact*

Spherical indentation can allow for large contact area indentation of a surface with known contact parameters and without the need for complicated sample setups requiring sample face alignment. This is at the cost of uniformity which generally precludes easy extraction of material properties.

Hertz's theory examines the contact between a sphere and half-space, but neglects any adhesive forces between the two. For this we may consider the Johnson-Kendall-Roberts (JKR) [218] or Derjaguin-Muller-Toprov (DMT) [219] models introduced much later in the 1970's. DMT is generally used for very hard spheres or where the contact area is kept small by a small tip radius. JMR is more suitable for softer elastic materials. With this in mind JMR is more suitable for the contacts explored in this thesis. The contact radius in adhesive contact by JMR theory is given by

$$a = \left(\frac{3R}{4E^*}\left(F + 3\gamma\pi R + \sqrt{6\gamma RF + (3\gamma\pi R)^2}\right)\right)^{\frac{1}{3}} \tag{3.18}$$

where γ is the adhesive energy of the surfaces and E^* is the reduced elastic modulus of the system. With adhesion of the system being considered, it is also important to note the pull-off force required to separate the two bodies after contact

$$F_c = -\frac{3}{2}\gamma\pi R \tag{3.19}$$

3.5 Thin Film Nanoindentation

Many indentation methods, including those explored above, are used to determine the mechanical nature of materials. Fundamentally, the analysis that is used to extract mechanical properties for these tests (such as the Oliver-Pharr method as in Equ. 3.3 to 3.4) rely on a continuous stress field propagating in a singular material of interest, and as such assume a monolithic material geometry that can be assumed to be a half space. Nanoindentation has also been extended as a means of examining the mechanical properties of supported thin films, key to many technologies ranging from opticelectronic layers for communication, computational, and energy devices to coatings in biological medical devices. It remains very challenging and sometimes impossible to accurately separate out the mechanical properties of a supported thin film when the proximity of the substrate contributes substantially to the overall contact mechanics [9-12]. Minimizing the substrate influence on film property measurement is handled by limiting indentations to low penetrations depths into the film and/or using complex corrections [12, 220-227]. These corrections are often unreliable and so indentations depths are generally limited to approximately one tenth of the film thickness to avoid significant interference from the supporting material.

The thickness of thin film materials utilised in technological spaces continues to shrink with the advent of new technologies with many films being measured in tens of nanometres or being deposited in atomically controllable layers [228], which causes significant problems for measurement of their mechanical properties via nanoindentation as defects in the tip geometry, sample surface topography, and sensor sensitivity limit the minimal depth from which accurate results can be obtained from an indentation [229]. With great experimental effort on ideal films, results can be extracted with penetration depths as low as ~20nm (necessitating a film of > 200nm thickness to effectively avoid the influence of the substrate), though this requires very careful experimentation with pristine tips. Current testing technologies are therefore insufficient to properly determine the mechanical nature of thin films as they exist today and new advances are required to tackle the needs of this key technological space.

3.5.1 Layer Compression Test

The Layer Compression Test (LCT) is a novel advance in thin film indentation testing that allows for quantitative analysis of the compressive mechanical response of supported thin film materials to significant indentation depths. Central to the LCT is a cylindrical flat punch tip that establishes a large contact area that remains constant with indentation depth. The load vs displacement behaviour of the LCT can be understood by considering the geometry and constraints imposed on the deformed region during indentation. If the tip face is assumed to be in perfect alignment to the film surface, and the contact area over the film is allowed to approach infinity (ie, with a tip with infinite diameter and so contact aspect ratio $\alpha \to \infty$, with α being the ratio between punch diameter and film thickness), combined with a perfectly rigid supporting substrate, all lateral strain vanishes by necessity. In this instance uniform deformation confined to a longitudinal direction normal to the film occurs in a uniaxial strain (US) state. This state can also be achieved with finite size samples, provided the compressed region is confined in the lateral direction by perfectly rigid sidewalls as depicted in Fig. 2.3. Such a state produces a compressive stress vs strain response as presented in Fig. 2.9, with Poisson's ratio v, Young's modulus E, and yield stress Y extractable from isotropic materials in a single compressive step by utilising the confined modulus M, bulk modulus K,and confined yield stress Y_c as in Eq. 2.15, 2.17, and 2.35. The LCT approaches this idealised state to approximate US for films provided with a stiff support.

With these considerations in mind, our implementation of the LCT approximating a US strain state is realized by utilising a diamond flat punch indenter with a diameter many times the film thickness to limit the degree of lateral strain generation in the compressed region [31, 33]. The punch face is precisely aligned to the surface of a thin film supported on a substrate with a much higher modulus than the film (for example a polymer film mounted on a Si substrate, for a Young's modulus ratio of ~20:1), in order to approximate rigid support. In this geometry the diamond indenter and stiff substrate act as stiff confining walls above and below the compressed puck of material, and the surrounding film jacket acts as the lateral confinement. Though less stiff than the rigid confinement in the longitudinal direction, the limitation of lateral strains via the large contact aspect ratio limits the need for perfect rigidity in this direction and allows confinement using only this surrounding material jacket. This approximation to uniaxial strain allows the direct analysis of stress vs strain behaviour in thin film samples even to large penetration depths.

This makes the LCT ideal for studying the mechanical response of supported thin films with Young's modulus approximately < 50 GPa (as the stiffest substrate available is diamond with $E \approx 1000$ GPa) to maintain a suitably high stiffness ratio. Even with a stiff substrate utilised, substrate deformation does occur and contributes to the overall deformation response of the indent. This can be accounted for simply by performing an equivalent indent to the one of interest on a bare section of substrate and subtracting the resulting displacement from that of the film indent. The accuracy of this correction and the stiffness ratio requirement will be explored in detail in Chapter 4.

A demonstration of the LCT is shown in Fig. 3.5 consisting of a stress vs strain curve of indentation by a 2μm diameter diamond flat punch on a 270 nm thick film of PMMA polymer which was prepared on a Si substrate via a standard spin coating method. Due to the US approximation of the LCT, the load applied to the sample can be converted to stress by dividing by the contact area of the punch, and the displacement into the surface can be converted to strain by dividing the indentation depth by the film thickness. The later of these two processes requires a substrate correction to be applied to account for 'parasitic strains' due to substrate bending. As discussed above this can be performed experimentally, and can also be performed analytically, which is approached in more detail in Chapter 4 which will assess the accuracy of the LCT to the US condition with and without an analytical substrate correction. The data presented in Fig 3.5 has a suitable substrate correction applied.

At low strain there is an initial linear region of elasticity, whereby all deformation is elastic in nature. For standard isotropic homogenous materials, like glassy PMMA, the slope of the curve in this region is represented by the confined elastic modulus M (see Eq. 2.17), here being ~5.2 GPa. A distinct kink is then observed as the curve transitions to a second, lower-valued constant slope. This kink is the confined plastic yield point, occurring at confined yield stress Y_c (which is higher than the unconfined yield Y due to the confined geometry as per Eq. 2.35), here at ~0.4GPa. Beyond this, further deformation is elastic-plastic in nature and the slope corresponds to the bulk modulus K (Eq. 2.15), here being ~4 GPa. As the equation for M and K contain only E and v, we can combine them to determine v with the following

$$v = \frac{3-(M/K)}{3+(M/K)} \tag{3.20}$$

As such, the Young's modulus, Poisson's ratio and Yield Point can be determined by a single continuous indention loading curve. This example in Fig. 3.5 gives a Poisson's ratio of 0.4 and a Young's modulus of ~2.4 GPa, both of which lie within literature values for glassy PMMA [50]

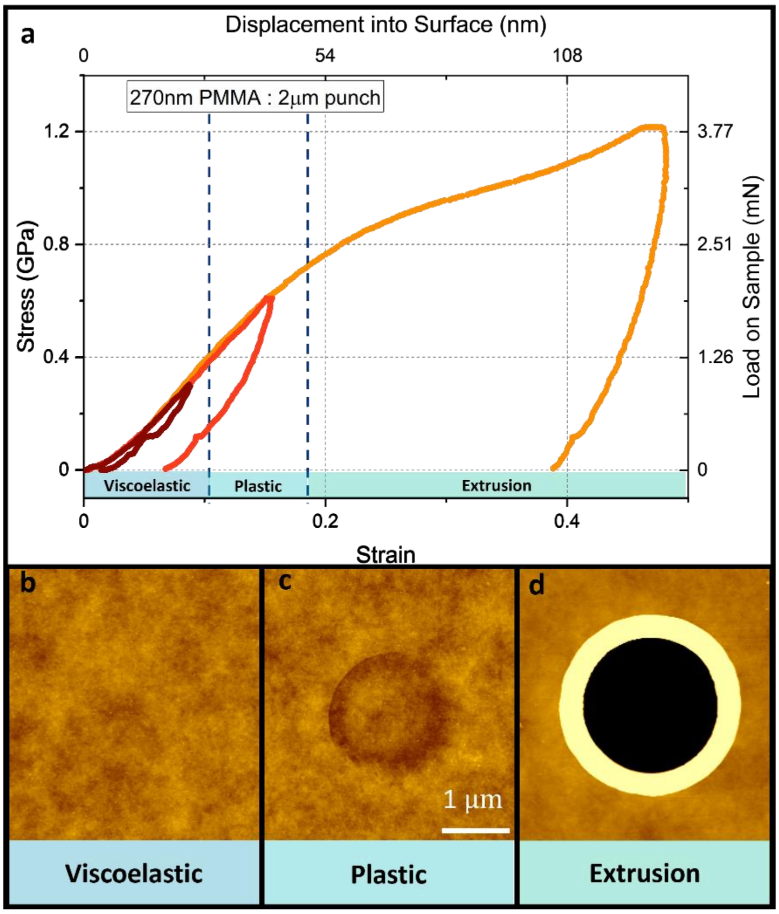

Fig. 3.5, (a) *LCT indents on 270nm thick PMMA film prepared on a Si substrate via spin coating. Shown are indents to three depths with corresponding AFM surface topographies after each indent in* ***(b-c)****; below the yield point in the elastic regime (maroon), beyond the yield point in the plastic regime (orange), and beyond the extrusion point during confinement failure (yellow)*

The purely elastic vs. elastic-plastic nature and sharp separation of these two regimes at the kink is confirmed by the residual strain of the stress vs strain curve, with purely elastic indents performed to a max load lower than Y_c returning to 0 strain after unload with no residual strain present (the maroon curve in Fig. 3.5). Indentation beyond this point shows residual strain and permanent plastic deformation (the red curve in Fig. 3.5). The uniaxial strain approximation of the LCT holds to ~20% strain on amorphous materials such as polymers. At strains beyond this, the confining effect of the surrounding film is no longer sufficient to contain the large lateral stresses applied to it, causing the puck of material to begin a process of extrusion outwards from under the punch into the surrounding material. This is characterised by a further downward inflection in the stress vs strain curve, and a subsequent extremely large residual strain, as can be seen in the yellow curve in Fig. 3.5. This confinement failure causes a ‘ring’ of extruded material (“pile-up” in nanoindentation parlance) to build up around the edge of the indent. Fig. 3.5 show AFM traces of the indented surface after indents to a max load below Y_c (elastic), above Y_c (plastic), and above the extrusion point, showing the elastic recovery, plastic deformation, and extrusion ring, respectively.

The LCT is thus a powerful tool for the examination of thin film mechanics. Later sections in this thesis will focus heavily around its development and implementation for amorphous films such as amorphous polymer glasses and nanosheet network films.

3.5.2 Flat Punch Surface Alignment

As discussed above, careful alignment of the punch face to the film surface is a requirement for the LCT. Particularly, higher aspect ratio contact geometries used to better approximate true US conditions require high quality alignment as even small misalignments will lead to severe or catastrophic artefacts in the data. For this, a dual axis tilt stage upon which samples are mounted, and AFM system are incorporated into the nanoindenter system. The setup is shown in Fig. 3.6. The Physik Instrumente M-044 tilt stage utilises piezo controlled x and y direction tilt, allowing for acutely controllable tilt of the sample stage. Initial misalignment before a tilt correction is determined by performing an initial indent to plastic strains on the sample, in order to leave a measurable indent trace from which misalignment can be calculated. The incorporated Semilab DME DS-95 AFM allows for in situ AFM measurements of the sample surface. AFM traces of the misaligned indent can be used to determine the degree of tilt needed in the x and y controllers to align the sample to the punch face.

Provided that the AFM scanning direction is aligned with the tilt axis, the degree of tilt required with the x and y controllers can be determined by the residual wall depth $h_{x/y}$ of the crescent indent in the x and y directions as in Fig. 3.6, combined with the radial length of the indent in that same direction $r_{x/y}$. This can be used to find the tilt required in the x and y direction

$$\alpha_{x/y} = \tan^{-1}\left(\frac{h_{x/y}}{r_{x/y}}\right) \tag{3.21}$$

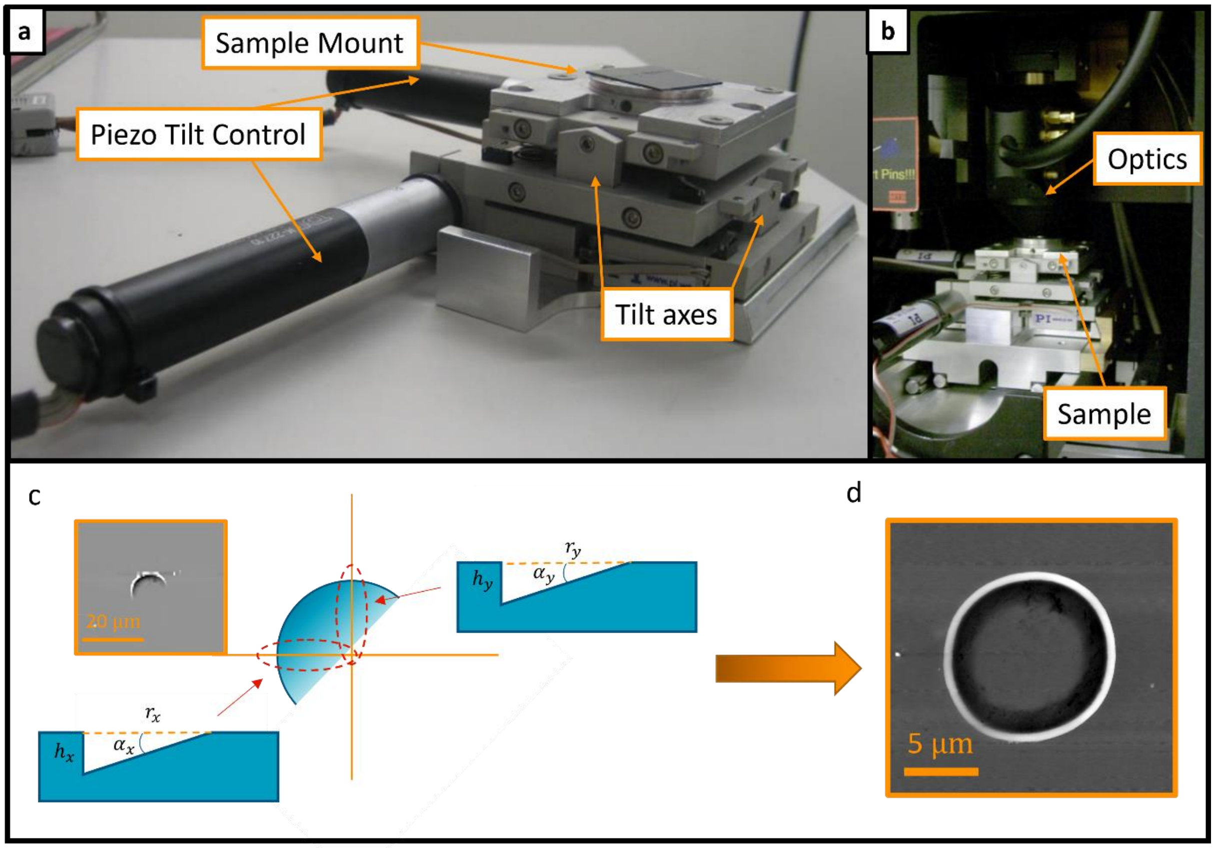

***Fig 3.6, (a)** Dual axis tilt stage with integration in the indenter chassis shown in **(b). (c)** AFM image of misaligned indent of a 10 μm punch on a PS film, and schematic of the parameters usedto determine the degree of tilt correction required in the x and y direction. **(d)** AFM trace of an indent using the same punch and sample, well aligned to the surface*

This tilt correction is sufficient to mostly correct for the misalignment, however small inaccuracies in the tilt controller, AFM tip sharpness, h and r (from elastic recovery of the sample) necessitate a series of smaller corrections to reach higher fidelity alignments. As indent AFM traces are insufficient for these small perturbations, this can be performed with a combination of small tilt corrections and indent load vs displacement curves. Small misalignments will result in a curvature in the initial portion of a load vs displacement curve before linearisation to the confined modulus M. Small corrections can be performed in the x and y direction until this curvature is reduced to the required fidelity. The residual misalignment can be determined by the degree of curvature and extrapolation of the slope M to zero load, as shown in Fig. 3.7. Typically, we can present the degree of misalignment as a percentage of the tip diameter. For example, a 80nm misalignment on a 4μm diameter punch would be referred to as a 5% misalignment.

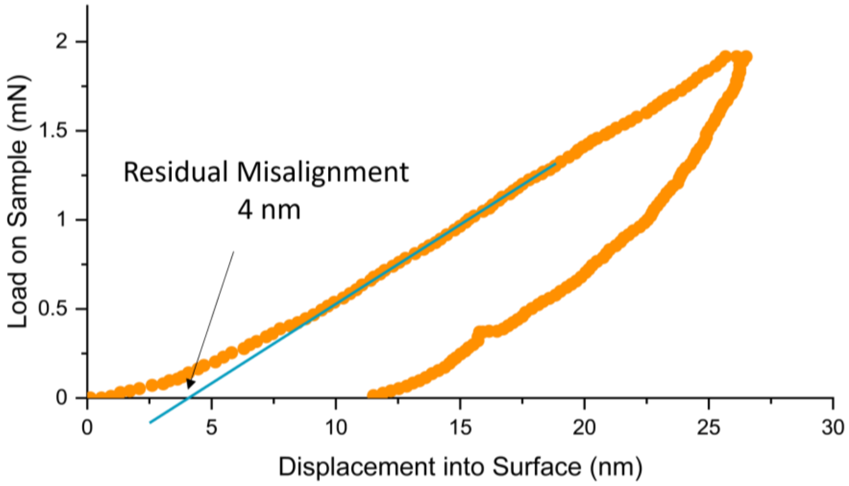

Fig. 3.7, *Residual misalignment of a 2 μm diameter flat punch tip on a 170 nm thick PMMA film on a Si substrate. The curvature at the start of the load vs displacement curve can be used in conjunction with the linear slope* M *to determine the degree of misalignment*

3.5.3 Surface Detection

Accurate detection of surface contact is important for determination of accurate strain measurements. On stiff samples such as metals, simple stiffness based surface detection methods may be utilised even with sharp tipped indenters. These rely on a continuous measurement of the load required to displace the tip a given distance during approach to the surface. This value will see a sharp increase upon contact with a stiff sample and be detectable as the point of surface contact after a user-defined stiffness threshold. The measured increase will be gradual in the case of a sharp indenter such as Berkovich which has a gradually increasing contact area. The stiffness threshold to define such contact can be tailored for softer films, such as polymers, to allow for a less severe stiffness increase to determine contact with the surface.

For a theoretical perfect alignment of a flat punch to a perfectly smooth film, the stiffness increase on contact will be a sharp discontinuity. In practice, however, and as discussed above, alignment to the surface can only be made with a certain degree of accuracy, and initial contact will be a crescent increasing to full circular contact, and therefore initial surface contact may not be sufficiently stiff on prohibitively soft films. Compounding with this for nanosheet network films are orders of magnitude lower stiffness than polymers, and a degree of surface roughness inherent to the deposition techniques that reduce initial contact area even further [37, 230]. This necessitates a more sensitive method of surface contact detection.

For this I utilise the oscillatory capabilities of the indenter as described above in Section 3.3. The oscillatory contact used for CSM measurements is maintained during approach to the surface and has a constant value of phase angle in air. For our system, this value is ~155 degrees. Upon contact with a solid surface, the phase angle drops sharply to 0, and does so for any material with sufficiently high stiffness compared to air, as shown in Fig. 3.8 for contact with a sputtered gold surface with a 55 μm tip with $< 0.5\%$ tip to surface misalignment. There is a region of settling after surface contact which is a mixture of tip misalignment and the feedback loop in the indenter adjusting to a sudden density change, after which the phase angle settles to a constant value of 0 for the remainder of the indent. In practice I define a phase angle threshold for surface contact, typically being the point where phase angle drops below 50 degrees in our system, although this value may be adjusted further to deal with surface roughness considerations of a particular sample in question.

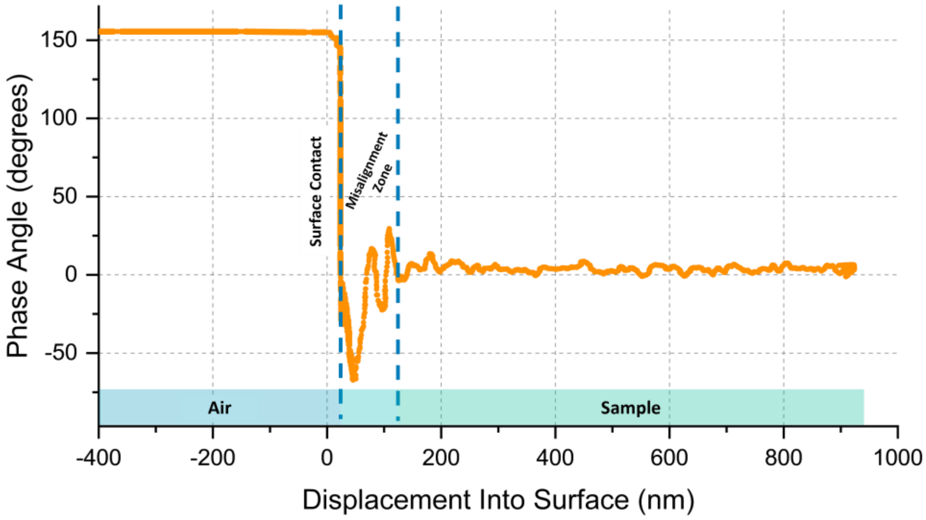

Fig. 3.8, *Phase angle between an oscillatory tip displacement and the load required to maintain such an oscillation, for an oscillation magnitude of 2.5nm during tip approach to sample surface. The tip diameter is 55 µm, contacting a sputtered gold layer on a glass microscope slide. The phase angle maintains a constant value in air and drops rapidly to zero upon contact with the surface. After a brief feedback settling time it maintains a value of zero for the remainder of the indent*

Ch 4 : Finite Element Analysis for the LCT

Preface : The work presented in this chapter has in places been integrated into the chapter based on, and adapted from, work published by the author in *The effect of contact aspect ratio and film to substrate elastic modulus ratio on stress vs strain up to the point of yield during flat punch thin film indentation of an elastic-plastic film,* Frontiers in Materials, 2022 [33]

As discussed above, the layer compression test (LCT) is a powerful tool for exploring the mechanical properties of supported thin films, even to significant penetration depths. So far, attempts to characterise the mechanical properties of soft, compliant films with vastly lower stiffness compared to the substrate have focused on low strain elastic properties [12, 220-227]. Even for the case of aligned flat punch indentation, analysis has not extended beyond this low strain limit. Notably, Wald et al. [220] investigated the problem of analysing the reduced elastic modulus of a purely elastic, elastically supported film indented by an aligned flat punch at the limit of zero-strain. Work investigating this flat punch indentation on a supported thin film beyond the zero strain exists [231-233], but generally it fails to consider the high contact aspect ratio limit, which as we have established above, renders the deformation highly uniform and creates a uniform strain throughout the compressed geometry, as explored by the layer compression test [31, 35]. As such, though the LCT appears to well approximate a state of uniaxial strain (US), and is backed up by experimental characterisation of polymer films in line with literature values, such as that presented in Chapter 3, a direct analysis of such a contact geometry to a pure US state has not been performed.

In this Chapter, I use finite element modelling to explore to what degree the LCT approximates a state of US in the elastic regime. Namely, I use finite element analysis to explore the effect of varying contact aspect ratio, α (cylindrical, flat ended punch diameter to film thickness), and film to substrate modulus ratio, S, during flat punch indentation of an elastic simple-plastic film supported by a purely elastic substrate, and to what extent variations in these approximate uniform uniaxial strain in the elastic, pre-yield regime of material deformation before the onset of significant plasticity.

4.1 Finite Element Analysis for Nanoindentation

Finite element analysis (FEA) is a numerical technique useful for obtaining solutions to problems that are impractical or impossible to obtain analytically. While this technique may be used to determine solutions for problems involving fluid flow, heat transfer, magnetic fields, and more, I will utilise it here for mechanical deformation problems related to the LCT. FEA works via discretisation of the given problem, decomposing it into a series of more manageable bodies (finite elements) which are connected to one another at points of common spatial location between elements (nodes), which form a mesh. For example, a 2D rectangular body may be decomposed into a mesh consisting of square elements, each with 4 nodes at each corner. In the case of modelling elastic deformation of the body, the connection between each node may be considered a simple spring, from which the deformation of each node can be calculated under the given force to determine the overall deformation. For a linear series of spring elements, the elastic nodal displacements can be composed simply by

$$(l) = [K]^{-1}(F) \tag{4.1}$$

Where (l) and (F) are arrays with a size equal to the number of degrees of freedom (dof), and $[K]$ is the global stiffness matrix of size dof^2 connecting the two.

Finite element allows for the approximation of solutions for complex geometries, even with multiple components and materials. Limitations can be set on the system through boundary conditions (which assign set values to specified nodes, such as anchoring a set of nodes by holding their displacement at zero or tied to other nodes), and meshing can be arbitrarily defined such that higher density meshing may be employed in regions experiencing higher degrees of deformation. The system can be solved explicitly or implicitly. Both calculate the evolution of the system at discrete time steps, with the difference being that the former calculates the new state based on the current state from the initial conditions and resulting accelerations, while the later recalculates after each increment and so requires an equilibrium after each time increment. Because of this implicit solving is usually used for lower complexity systems due to increased computations demands, and/or for slower applications of deformation, while the explicit solver is best used for more complex analysis or high speed events such as impact analysis.

FEA will be utilised in this chapter to analysis the LCT, and as such requires a degree of elastic-plastic deformation to properly model the deformation of a soft supported film on a substrate during indentation with a stiff punch. Because of this the differential equations solved will be the Prandtl-Reuss equations (Eq. 2.34) from Chapter 2 for stress-invariant analysis.

4.2 Experimental Parameters

Finite element simulations of the layer compression test were performed using the Abaqus 2019 explicit solver [234] as follows. The substrate and film were prepared using radially symmetric elements in two separate parts. A variable scale mesh was constructed in order to assign a high density of elements in regions expected to experience high stress gradients, such as close to the contact between the film and punch edge. This meshing is shown in Fig. 4.1. I represented the punch as a stiff flat ended cylinder surface (also radially symmetric), with radius 1000 nm. The corners of the punch were rounded with a 50 nm radius of curvature (ie, 5% curvature). This edge rounding was implemented to represent typical manufacturing tolerances in punch microfabrication, but also served to improve simulation stability at larger indentation strain for which stiff sharp corners introduce instability. The approximation of an ideally stiff punch was used as indenters are typically diamond, which deform little in contact with the soft films explored here.

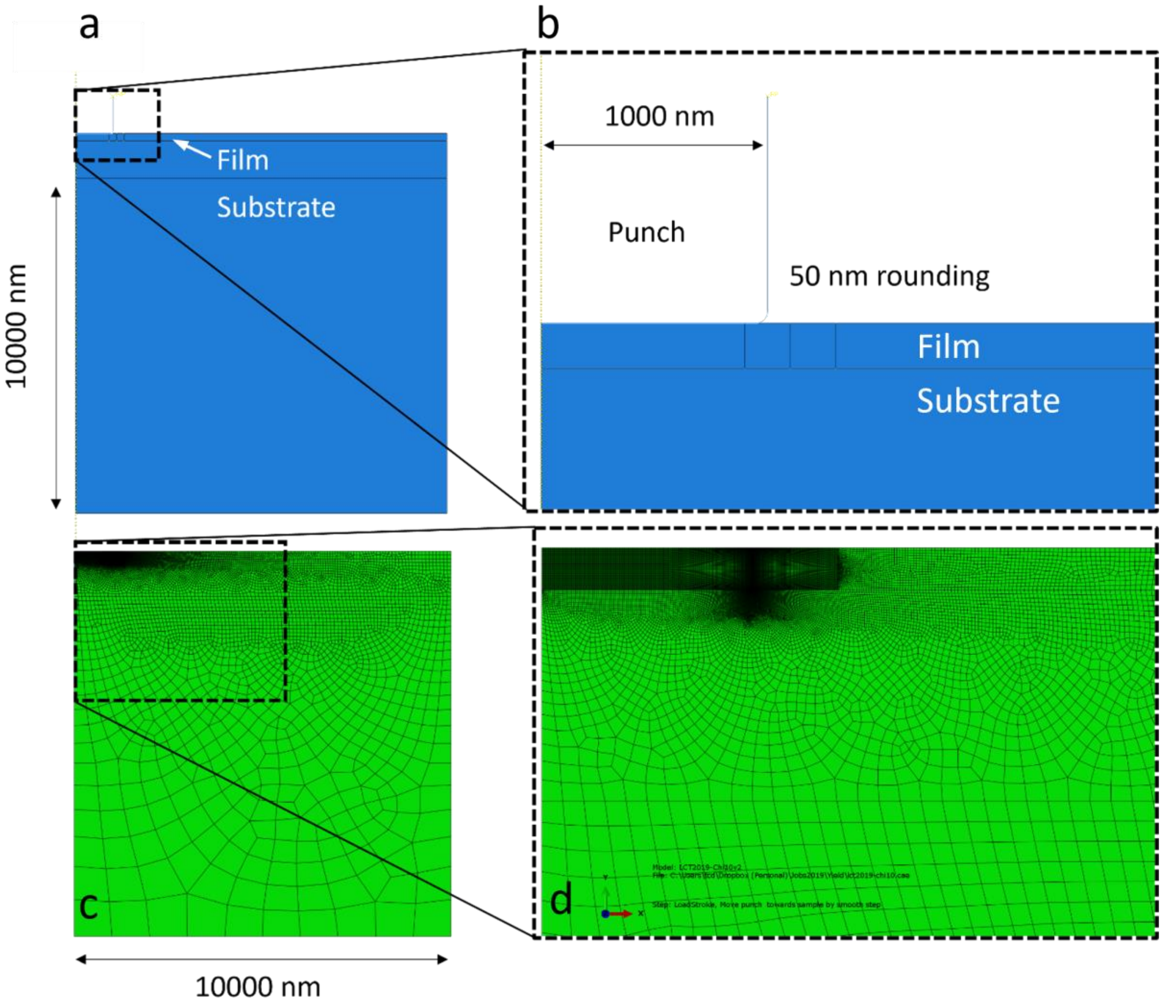

Fig. 4.1*, Radially symmetric LCT model for Finite Element analysis.* ***(a-b)*** *show the construction of a an elastic simple plastic film supported on an elastic substrate, with* ***(c-d)*** *showing the meshing of the same. Higher mesh density was used for the film, particularly near the rounded punch corners, as these were expected to receive higher deformations than other regions. The punch was approximated as a perfectly rigid structure, with a 5% rounding of the corner representing manufacturing tolerances. Film thickness was varied to alter contact aspect ratio* α*, and substrate modulus was varied to alter film to substrate modulus ratio,* S

Five films were prepared to a width of 10000 nm. The thickness of each film was varied, with each being 400, 200, 100, 40 and 20 nm to simulate various contact aspect ratios of α = 5, 10, 20, 50, and 100 with the punch. These films were simulated as an elastic, simple plastic material as follows; They were given a mass density 1000 kg m^{-3} and a Young's modulus of 1 GPa, Poisson's ratio of 0.35, and von Mises yield stress of 0.1 GPa for a Y_{film}/E_{film} of 10. These parameters are typical of amorphous solids such as polymer glasses [174]. The substrate was given dimensions 10000 by 10000 nm, and was prepared as an elastic material with a mass density 2000 kg m^{-3}, Poisson's ratio of 0.25, and a variable

Young’s modulus of 10, 20, 50, 100, 200, 500, and 1000 GPa to explore film to substrate modulus ratios, *S,* of 10, 20, 50, 100, 200, 500, and 1000. The film was treated as perfectly bonded to the substrate by using Abaqus element node ties to entwine elements across the shared film-substrate interface, while the punch contact was treated as frictionless. These parameters are presented in Table 4.1.

Sub:Film modulus ratios S	**Contact aspect ratios α**	**E/Y ratio** (Film Modulus / Yield point)	**Punch Diameter**	**Punch Corner Radius**	**Substrate : Film contact**	**Film : Punch contact**
5, 10, 20, 50, 100, 200, 500, 1000	5, 10, 20, 50, 100	10	1000nm	50nm	Bonded	Frictionless

Table 4.1. *Varied and held parameters for the variation of punch diameter to film thickness ratio α and substrate modulus to film modulus ratio S in the FEA simulation*

4.3 Substrate Correction

In displaying the results of these simulations, I use “effective true strain” ε_T which is a more accurate representation of finite strain than simple engineering strain as presented in Chapter 2, h/h_0 . This quantity is given by

$$\varepsilon_T = -\ln\left(\frac{h_0 - h}{h_0}\right) \tag{4.2}$$

where h is the indentation depth and h_0 is the initial film thickness. I treat this as being representative of the strain of the entire compressed puck of material under the puck. This assumes a level of compressive uniformity that is well maintained in the simulations. I treat the mean contact stress on the film surface as normal, $\sigma_T = L/A,$ where A is the contact area of the punch to film (calculated simply from the punch radius), and L is the load applied to the punch during indentation. I assume a degree of uniformity in the contact stress throughout the film as well, which is also well maintained throughout the simulations. The effect of these assumptions of uniformity are made clear in the results later.

Fig. 4.2 shows results of the finite element simulations of the layer compression test described above combined in a single mean stress vs. effective true strain graph, for all contact aspect ratios α ranging from 5 to 100 and modulus ratios S ranging from 10 to 1000. In Fig. 4.2(a) the results are presented unmodified, while in Fig. 4.2(b) a simple analytical correction described below has been applied to the effective true strain to account for substrate bending. α is represented by different colours as in the legends, with lighter shades of a given colour corresponding to lower values of S tested at that aspect ratio α. While the number of plots present complicates these graphs, the trend is as follows : for high values of α and S which more closely present the ideal case of perfect confinement and infinite aspect ratio, the curves in Fig. 4.2(a) follow the expected uniaxial strain slope M (black dashed line) closely. A kink in the curve near the confined yield point Y_c also appears as expected for US. As the aspect ratio and modulus ratio are reduced, the slope of the stress-strain curves reduce, showing still a linear slope, but being further from the case of US as we move away from the ideal case of high α and S. This downward spread in the curves is a result of lower overall system stiffness due to poorer lateral confinement and a more compliant substrate support.

With this, it is clear that substrate compliance affects the results greatly. As such, I attempt to correct for the compliance with a simple analytical correction. This is done by subtracting an estimate of the direct punch-substrate contact stiffness k_{sub} from the stress vs strain curves. This estimate can be made experimentally by indenting an exposed portion of the aligned substrate and subtracting the resulting stiffness measurement from that of the LCT indent on the film (as has typically been done in the past experimentally [31]), or alternatively, using an analytical estimate of the substrate stiffness which I perform here. This analytical case is less experimentally intensive, provided the substrate properties are known. The parasitic bending can be subtracted directly from punch indentation displacement h to correct the effective true strain as

$$\varepsilon_T = -ln\frac{h_o-(h-\frac{L}{k_{sub}})}{h_o} \tag{4.3}$$

$$k_{sub} = 2a\frac{E_{sub}}{1-v_{sub}^2} \tag{4.4}$$

where E_{sub} and ν_{sub} are the Young's modulus and Poisson's ratio of the substrate, and a is the radius of the punch. I applied the correction to the data in Fig. 4.2(a) by simply estimating $k_{sub} = 2aE_{sub}$. The effect on the stress vs strain curves was substantial as can be seen in Fig. 4.2(b): After this correction, a significant fraction of the curves collapsed around a locus line closely following the expected uniaxial strain slope. The furthest deviatory cases are now high α and S combinations that have become overcompensated by the correction, in some cases severely.

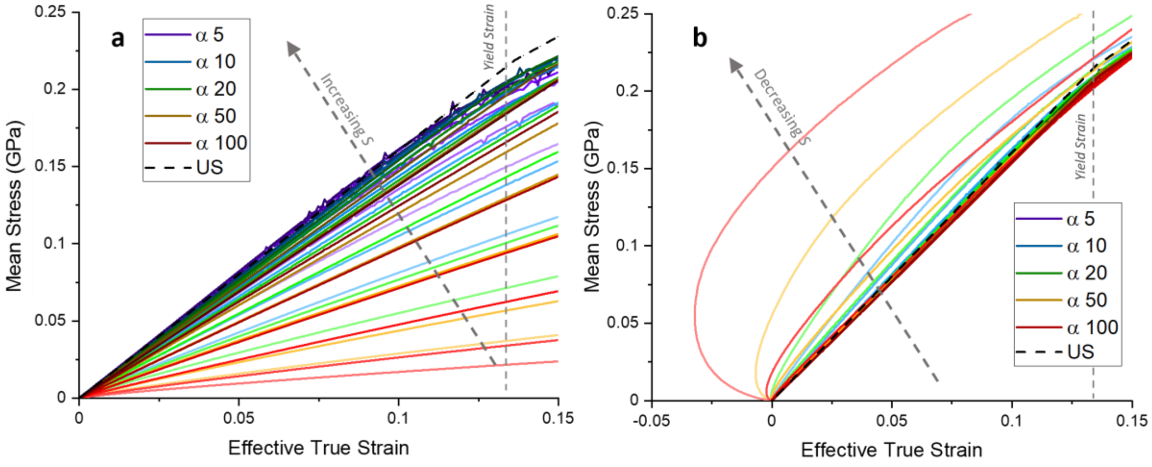

Fig. 4.2**. Effect of varying contact aspect ratio α and substrate-to-film modulus ratio S on mean stress vs. effective true strain in the layer compression test simulated for a 1 μm radius flat punch in frictionless contact with thin elastic-plastic films bonded to an elastic substrate.* ***(a) *Mean stress vs. effective true strain ε=-ln((h$_0$-h)/h$_0$) values for all S and α simulated, with no correction for elastic substrate deformation. The legend shows colour trend of α values, and the trendline insert shows the trend of S within the α subgroups, with darker shades of a given colour representing higher values of S. Numerical artefacts from the FEA simulation cause a slight sawtooth pattern in some curves, though this does not correspond to a physical effect.* ***(b)*** *Data of* ***(a)*** *with simple correction to remove effect of substrate bending (see main text)*

The slope of the stress vs. effective true strain curves in this region of interest is given in Fig. 4.3(a-f) for the cases of uncorrected (a to c) and substrate corrected (d to f) for a selection of aspect ratios (5, 20, 100). The complete set of all 5 aspect ratios in this study can be found in a full page spread at the end of Section 4.5, Fig. 4.6, with only three presented here for clarity. While our simple substrate bending compensation fails to account for non-uniform deformations (such as the substrate deforming more towards the centre of an indent [235], which we nominally call a 'pincushion' effect), which introduces inaccuracies particularly for low substrate stiffness at higher contact aspect ratio, the correction is overall very accurate for all but these most extreme outliers and can allow for close analysis of elastic deformation in thin films that would be largely indeterminable without the correction. In the uniaxial strain case the slope in this region is constant up to the point of yield, and is equivalent to the Confined Modulus M as outlined in more detail in Chapter 2. There is more variation in the slope of the LCT indents in the elastic region than in the case of pure uniaxial strain (particularly as we approach yield), but there maintains large regions of the elastic deformation from zero strain onwards that give very accurate determination of M with the substrate correction applied. As we approach the yield point, the accuracy begins to worsen. I attribute this to the early onset of plasticity in the film compared to the traditional confined yield event in uniaxial strain. This manifests as a gradual 'roll-off' of the slope in the region around yield as the material yields in a more gradual manner than in the idealistic and fully determinable single yield event in US. However, even for the α = 5 case which is the shortest-lasting uniformity before this yield-point roll-off, we maintain an accurate determination of M up to 50% of the yield strain before this occurs, and further still at higher aspect ratios, allowing determination of M for all contact aspect ratios explored.

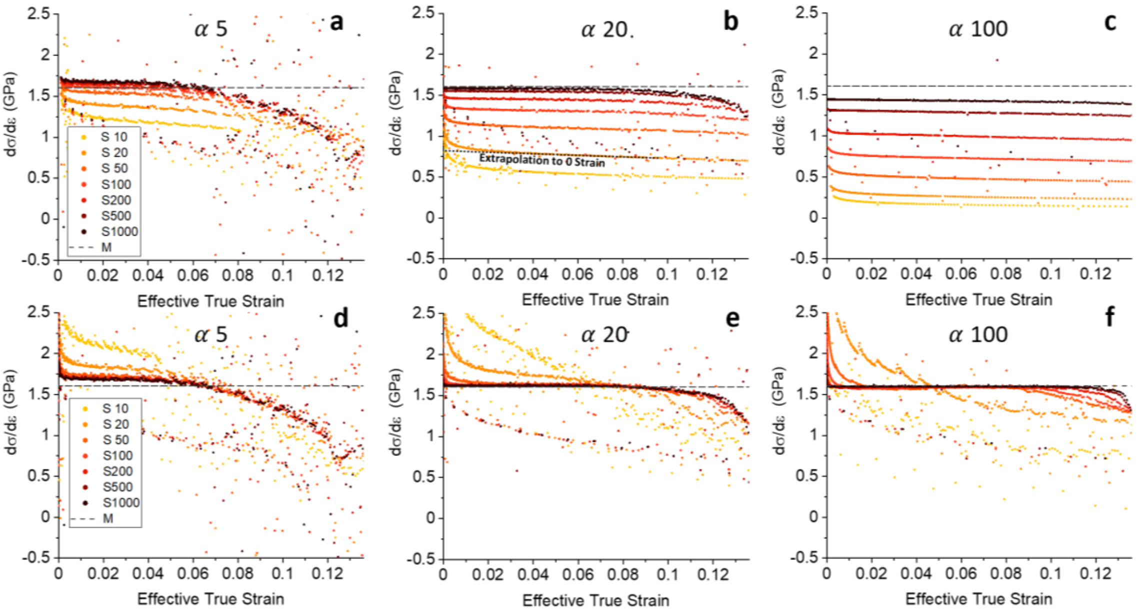

Fig. 4.3, (a-c) *Calculated slope $d\sigma/d\varepsilon$ vs. effective true strain of data in Fig. 4.2(a) up to the yield strain, showing scaling with S for a selection of aspect ratios. A good approximation to the confined modulus M is found at low strain for experimentally accessible aspect ratios (α = 5 to 20) when on stiff*

substrates. This breaks down however at high aspect ratios, or if S is not sufficiently high. If a lower S is used, a substrate correction step should be considered for more accurate results. ***(d-f)*** *provides $d\sigma/d\varepsilon$ curves as in* ***(a-c)*** *but with substrate correction of Fig. 4.2(b). Residual deviations from the expected M value at low S (particularly 10 and 20) are due to limitation of the simple substrate correction which does not account for non-uniform substrate bending strains or effects of the rounded punch contact area. Overall, the simple correction for substrate bending allows for excellent determination of M with values of α and S (eg. α=20 and S=50) that are generally experimentally feasible*

It should be noted that there are some artefacts from the simulation present in this data. In Fig. 4.3 there exists a brief but significant deviation around the zero strain limit in all datasets manifesting as a sharp upwards spike at zero strain. This was found to be due to a discontinuity at zero strain in our simulations and does not represent a real effect in experimental indentation [31], and so can be discounted as a zero strain artefact. There also exists larger deviations from the confined modulus M for low substrate stiffness values S in the substrate corrected data (Fig. 4.3 (d-f)), which are a result of some further limitations: Firstly, our simple substrate correction cannot account for secondary effects such as non-uniform substrate bending (the “pin-cushion” type effect mentioned earlier, whereby the substrate deforms more in the centre of the indent than at the edges, more pronounced at low S and high α) [235]. Secondly, there exists slight variations of true contact area between the punch and film due to punch edge rounding, not captured by Eq. 4.3 which assumes constant punch contact area. Direct measurement of the required substrate correction via indentation into an exposed region of substrate can mitigate some of these effects, although at extremely low S this too can fail to account fully for the pin-cushioning effect. Despite these limitations, Fig. 4.3 establishes that highly accurate values can be extracted from LCT indentations experimentally even at reasonably low S values with a simple analytical substrate correction step.

4.4 Comparison to Zero Strain Analysis in Previous Literature

As mentioned above, work by Wald et. al. has previously explored flat punch indentation of a supported film in the limit of zero strain [220]. I use this as a means of comparison with our own simulations in the elastic limit. Wald’s work utilised finite element analysis to study the mechanics of rigid flat punch indentation of an elastically supported, elastic thin film. Key differences to this work are the lack of punch rounding (ie the punch was modelled with sharp 90° corners), an elastic film (as opposed to elastic-plastic in this work), and the analysis not extending beyond the zero strain limit. In their work they performed a fitting procedure to their simulated indentation data using a simple analytical model, which approximated contact to the film-substrate system as two linear springs in series: One of which representing the compressed film region and the other representing compression of the substrate. This model allowed a fit to uniform contact to an elastic half-space as opposed to a separate film – substrate system. This was done for a large range of contact aspect ratios, substrate to film modulus ratios, Poisson's ratios and contact friction conditions, with effective scaling constants C_1 and C_2 extracted for each spring constant to account for the particular complexities of the differing conditions. To compare our results to theirs, we recast their semi-analytical model in terms of our uniaxial strain confined modulus M. We then extract our own confined modulus estimate at zero strain directly from our mean stress vs. effective true strain curves from our own fully elastic-plastic film simulations.

The zero-strain semi-analytical model developed by Wald et. al relates the intrinsic film modulus E_{film} to an effective contact modulus E^*_{eff} extracted from standard Oliver and Pharr [8] analysis of the unloading slope of flat punch indentation, $\Delta L/\Delta h = k_{film-sub}$ as

$$\frac{k_{film-sub}}{2a} = E^*_{eff} = E_{film} \times \frac{\pi C_1 C_2}{2\left(2C_1 \frac{E_{film}}{E_{sub}} + C_2 \frac{h_0}{a}\right)} \tag{4.5}$$

where E_{film}/E_{sub} is equivalent to $1/S$ using our definition of the Young's modulus ratio of film to substrate, C_1 and C_2 are finite element derived fitting parameters introduced above, and h_0 and a are the initial film thickness and radius of the indenting punch respectively [220]. The large fractional term containing C_1 and C_2 arises from series combination of the two springs described above, scaled by C_1 and C_2.

To convert Wald et. al.'s results to a confined modulus, we consider flat punch load L vs. displacement h curves and form an estimate of the uniaxial strain confined modulus M as that described in Eq. 2.17

as the stress vs strain slope in the elastic region, converted from L and h by considering punch contact area and initial film thickness

$$M = \frac{\Delta\sigma_{zz}}{\Delta\varepsilon_{zz}} = \frac{\Delta\left(\frac{L}{\pi a^2}\right)}{\Delta\left(\frac{h}{h_0}\right)} = \frac{h_0}{\pi a^2}\frac{\Delta L}{\Delta h}. \tag{4.6}$$

For simplicity here I have used engineering strain h/h_0 which asymptotically approaches true strain at the zero strain limit. I can then form a confined modulus from Wald's expression by combining Eq. 4.5 and 4.6 as follows

$$M^W = \frac{2h_0}{\pi a}E^*_{eff} = E_{film} \times \frac{C_1 C_2}{\alpha\left(C_1\frac{1}{S}+C_2\frac{1}{\alpha}\right)} \tag{4.7}$$

where I have incorporated our own α and *S* ratio definitions into the final expression. I note that within this elastic regime, loading and unloading slopes are equivalent and in principle either can be taken to determine $k_{film-sub}$.

Fig. 4.4 compares our simulated LCT results to those found by Wald et. al. using this estimate of *M* at zero strain described above. The comparison is made with our own data by extrapolating our uncorrected dσ/dε slope curves in Fig. 4.3(a-c) to zero strain as shown by example in Fig. 4.3(b). Doing so, we avoid the small strain artefact in our data mentioned above. The results of Wald et. al. are plotted as dashed lines using Eq. 4.7 and are found in good agreement with our results both qualitatively and quantitatively. It is clear from both that a stiffer substrate and higher aspect ratio increases fidelity to the US condition, with stiffer substrates required as higher aspect ratios are used, as the substrate has a greater degree of deformation at these high aspect ratios. For the configuration where our results overlap best with Wald's (α = 20), the deviation between our results are small and can be attributed to secondary variations in geometry between our two simulations (most prominently, our 50 nm curved edge vs their sharp punch corners, which play a significant role in the contact area at zero strain), slight inaccuracies in our extrapolation of the constants C_1 and C_2, and our use of Poisson's ratio 0.35 vs. their 0.3.

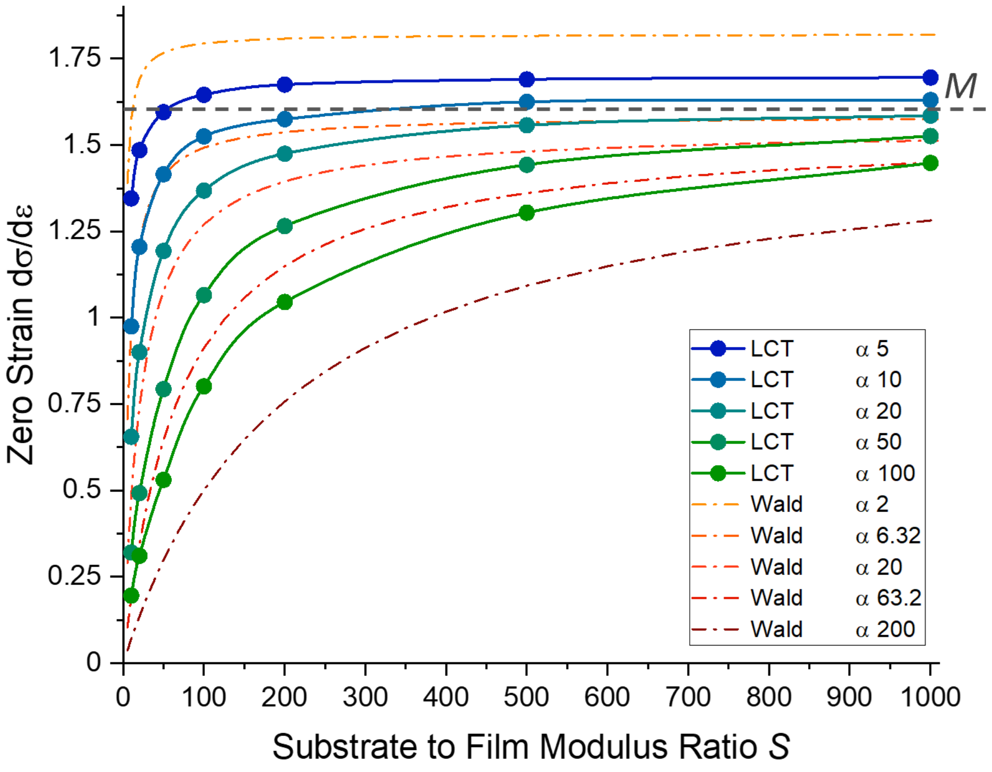

***Fig. 4.4**. Mean stress vs. effective true strain slope of the LCT evaluated at zero strain for the elastically supported, elastic-plastic film for all simulated values of α and S (using uncorrected data from Fig. 4.2). The theoretical confined modulus M = 1.6 GPa for the film material under uniaxial strain is shown by the dotted grey line. For each aspect ratio the slope asymptotically approaches a constant value with a set offset from M. The results of Wald et. al [220] using Eq. 4.7 are plotted as dashed lines and show excellent agreement with our results (eg. the most comparable case of α = 20)*

It is clear from Fig. 4.4 that for all aspect ratios the zero strain confined modulus M plateaus to separate constant levels as we increase *S* (and possibly converges to a single value at *S* = ∞). In the limit of small *S*, where the substrate and film approach an identical elastic response (ie an elastic halfspace as opposed to a film-substrate system), the value is grossly underestimated. The plateau to a constant value is approached more quickly for lower contact aspect ratios, with much higher substrate stiffnesses required to reach the plateau at high aspect ratio. The approached level of the calculated confined modulus from the true value is a function of the aspect ratio of indentation, with higher aspect ratios having a higher offset than lower aspect ratios. For the limiting case of a system with infinitely high *S* (ie ideal longitudinal confinement) and infinite aspect ratio (ideal lateral confinement), our results suggest that we will asymptotically approach the expected M = 1.6 GPa uniaxial strain value, though limitations in computational resources prevent us from exploring these extreme geometries as the number of elements would increase significantly. Significantly, the results in Fig. 4.4 show that for a given contact aspect ratio and a sufficiently high S, M can be accurately estimated with a single correcting value.

4.5 Deviation from Uniaxial Strain

It is important to more closely understand how the LCT deviates from pure uniaxial strain. To this end, Fig. 4.5 investigates the deviation of our measured confined modulus M from that in the US case for the range of contact aspect ratios explored already in Fig. 4.2, and all seven S values utilised in this work. This is done for the case of uncorrected data (a to c, representing data from Fig. 4.2(a)) and with the substrate correction applied (d to f, representing data from Fig. 4.2(b)). The full dataset is provided in a full page spread at the end of this section, Fig. 4.6, with only three presented initially in Fig 4.5 for clarity. Typically, aspect ratios between 5 and 20 are utilised in LCT indentations, depending on the tip size and fidelity required. The higher case of α = 100 represents a limiting value for the technique that would require significant instrumentation improvement and experimental redesign to approach.

We first consider the uncorrected, high aspect ratio data in Fig. 4.5 (c). As is expected, the LCT slope underestimates the confined modulus as the substrate stiffness ratio, S, is decreased, as the compliant substrate deforms more readily and introduces non ideal deviations from US. This approaches the true value of M as we increase S, but an underestimate is present even for extremely large S outside of experimental capabilities for many real world systems. For the stiffest substrate with S=1000, the LCT underestimates US with by -10% consistently from near zero strain to the yield point of 0.136 strain. I attribute the slight downward trend in all the curves to elastic relaxation of the confining surrounding film to be discussed below. At very low strain below 0.005, the abrupt upward swing in the data is due to a minor numerical artefact of the spline-fitting procedure used to allow noise-free differentiation of the simulated data and does not represent a real deviation near zero strain, and so should be ignored.

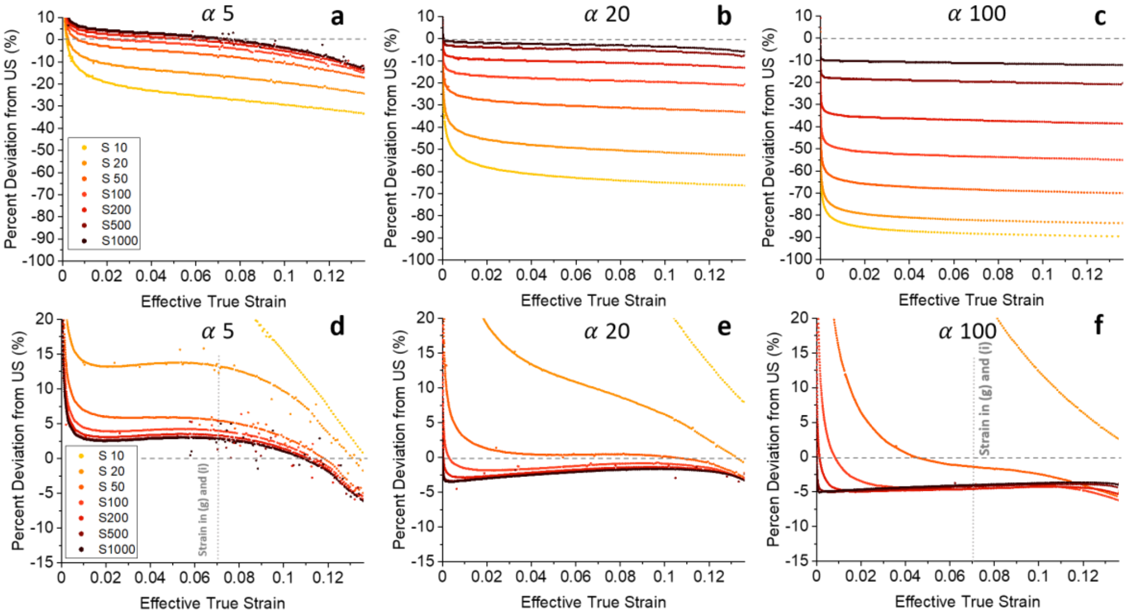

Fig. 4.5, *Results of Fig. 4.2(a-b) expressed as a percentage deviation of LCT mean stress vs. effective true strain relative to pure uniaxial strain up until yield strain without* ***(a-c)*** *and with* ***(d-f)*** *the substrate stiffness correction applied. The analytical substrate correction step (as per Eq. 4.3 and 4.4) reduces this error to that shown in* ***(d-f)****. As discussed earlier, this simple substrate correction grossly over-compensates at low S as described for Fig.4.3 (d-f), but can otherwise reduce the error from US to less than ±5% for all cases, with more experimentally approachable α and S being more favourably represented once the correction is applied*

Moving to lower, more experimentally approachable aspect ratio 5 (Fig. 4.5 (a)), there is a shift from negative to positive deviation for the full curves. There is also significantly less spread with *S* as substrate deformation is a lower consideration at the lower aspect ratios. This general upwards trend in deviation as we approach lower aspect ratios is likely due to lack of confinement of the stress at low aspect ratio, which causes a downward spreading of the strain field to a larger volume of material resulting in increased overall stiffness felt by the punch (see further discussion on this below.) There also exists a slightly steeper downward slope as strain increases for each set of curves for these lower aspect ratios, which also corresponds to weaker lateral confinement of the puck at low aspect ratio. In addition, the negative roll-off discussed earlier can be observed near the yield point, for example at α = 5 and high *S* around 0.08 effective true strain onwards. Examination of the simulated strain fields in a later section show this is due to early onset of plasticity in the outer radial regions of the puck near the corner before yielding of the bulk puck material. This roll-off has the effect of producing a less sharp kink but still distinct in the stress vs. strain curves as can be seen in Fig. 4.2 (a), but with an increasing shift away from the theoretical confined yield stress and strain point as the roll-off becomes more severe at low aspect ratio. Premature plasticity generally affects only lower aspect ratios as can be seen by its delayed (Fig. 4.5 (b)) or almost non-existent (Fig. 4.5 (c)) presence.

Applying the substrate compliance correction has a large effect on the trend with *S*, inverting the deviation to an overestimation compared to US with decreasing *S* while also creating large variance in the deviation with strain for small *S* values. The effect of the correction is smallest for larger *S* values, manifesting as a decrease in the α = 100 error from approximately -10% to -5% and from +5% to +2.5% for α = 5 when comparing the uncorrected and corrected datasets for high *S*. For high *S*, the correction results in a mostly constant deviation that rises gradually and peaks before yield for all aspect ratios. In the case of α = 5, we see an initial gentle upwards trend which peaks around 0.05 to 0.06 effective true strain before the onset of the sharp roll-off as the yield strain is approached. While the roll-off is a result of premature plasticity mentioned above and discussed later, the gentle increase beforehand is attributed to the rounded corners of the punch coming into contact with the film gradually. This results in gradual small increase in the contact area with indentation depth that acts in opposition to an initial underestimate of the true contact area from assuming a punch radius more accurately than would typically be assumed during experiment. This contact area effect is more pronounced for lower α indentation as the punch corners come into contact at lower strain in this geometry, but is then cut short by the premature plasticity earlier for lower α than for higher α, and gets masked by the resulting roll-off. At low *S* values, the correction leads to significant overcorrection of the stress vs. strain curves especially at high aspect ratio.

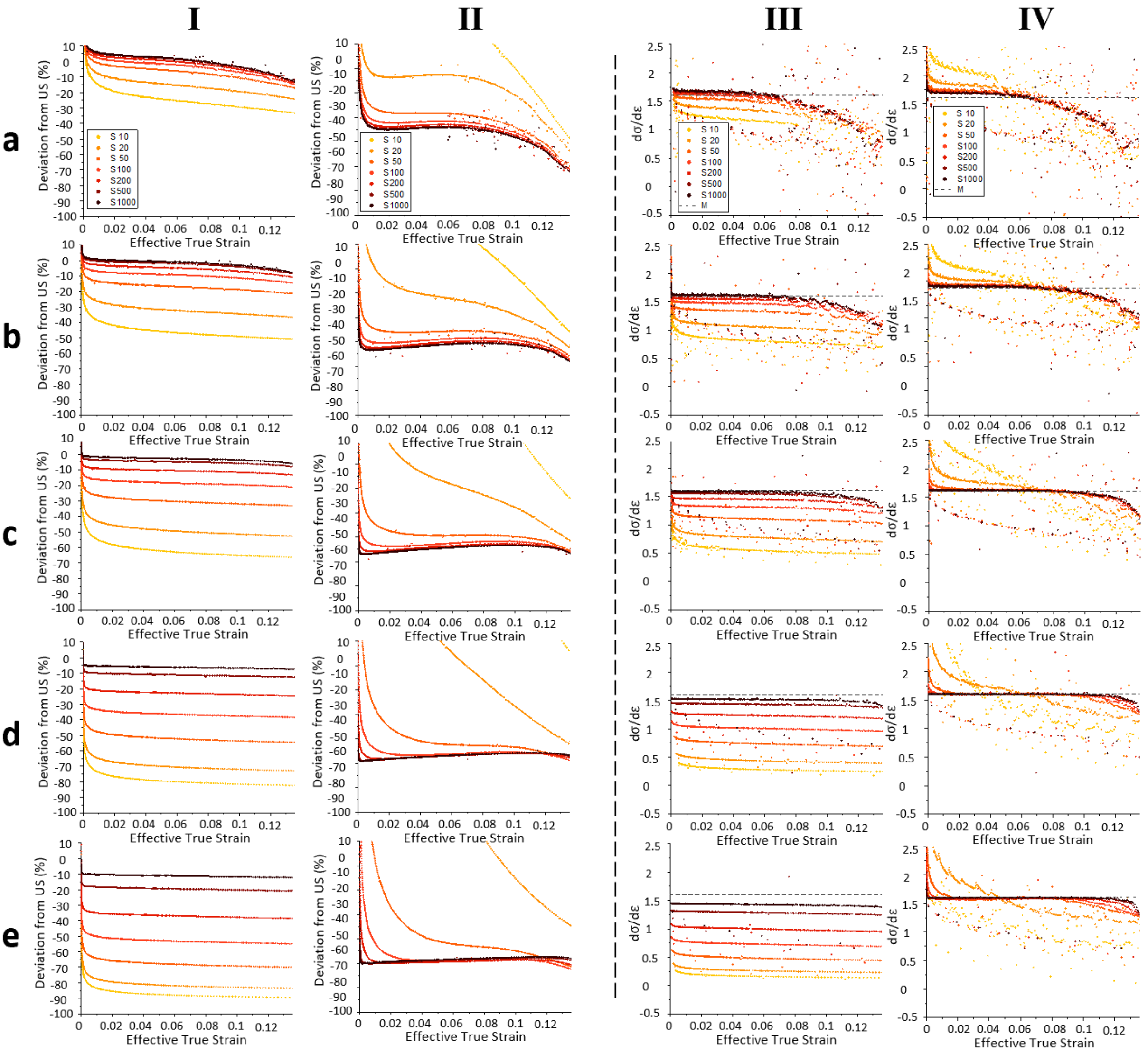

Fig 4.6. *The complete set of data for Percent Deviation from US (columns **I** and **II**), and $d\sigma/d\varepsilon$ (columns **III** and **IV**) vs True Strain for all α and S explored (α 5, 10, 20, 50, 100 represented by rows **a** through **e** respectively)*

4.6 Competing Error Effects

So far, we have seen deviations from pure US that in the substrate corrected dataset can both over and underestimate the M. We have alluded to strain field effects and premature plasticity that affects these deviations. In order to visualise these effects, we examine in Fig. 4.7 the detailed strain fields within the compressed puck and surrounding film calculated within the finite element simulations. In pure US, the puck material experiences uniform longitudinal strain parallel to the loading direction

[236]. In a FEA simulation this would manifest as every element within the compressed region experiencing the same longitudinal strain magnitude, and zero lateral strain. In the LCT, non-uniform strains develop in the film at stress riser locations such as the punch corner. Deviations from the US ideal of homogenous, longitudinal compression of a perfectly confined puck, and the effect these have on the LCT comparison to US, were analysed numerically by first considering the size of a given strain divergence compared to the entire compressed puck region (taking into account radial effects on the area occupied by each divergence), and then adjusting for the magnitude of the strain in that divergent region compared to the magnitude of strain within the puck volume. This gives a fractional consideration of how much of the overall strain experienced in the puck at any one instant is governed by the US-like longitudinally compressed puck, and how much is deviatory strain behaviour.

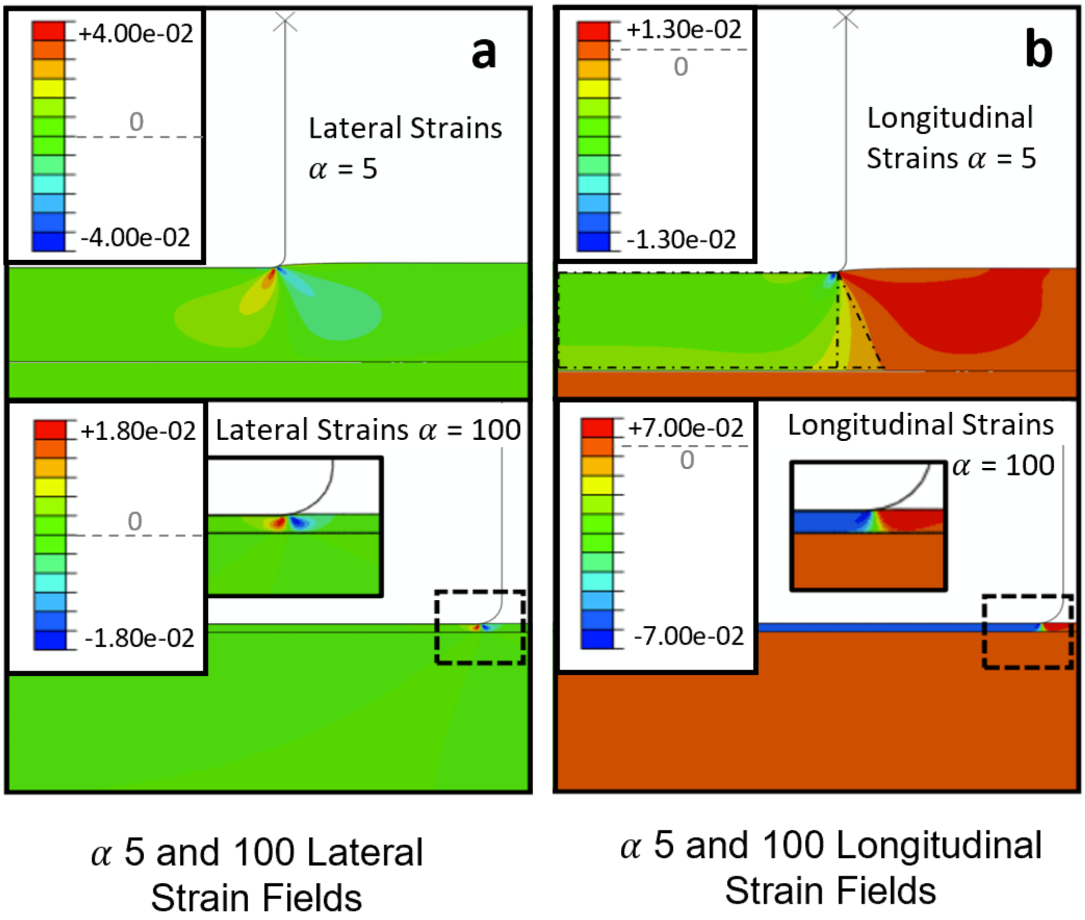

***Fig. 4.7**, Deviations from uniform strain of the puck under the punch are analysed via the strain fields extracted from the finite element simulations, shown for the edge cases of α 5 and 100 with S 1000 in both cases. Propagation of lateral strains caused by imperfect confinement by the surrounding films*

*are visualized in **(a)** and spreading of normal stress through the finite film thickness from the punch contact zone to the substrate below is visualized in **(b)** as gradients in vertical strain spreading with depth in the film beyond the punch periphery. The spreading of lateral stresses constitutes a more compliant film than for pure US, while the spreading of the normal strains constitute a stiffer response as a greater portion of material is being compressed*

In Fig. 4.7 (a), radial cross-sections show the concentration of lateral strain gradients at both low aspect ratio contact (α = 5 and 100 in the upper and lower panels, respectively, with S being 1000 in both cases) with the punch being at a penetration depth of 0.05 effective true strain. In both geometries these lateral strains propagate from the punch corners downwards and laterally into the film as two opposing lobes: Under the punch in the puck region, a lobe with positive radial displacement develops that is mirrored by a second lobe with a negative radial displacement in the surrounding film right outside of the compressed region. At high aspect ratio the spreading is prohibited by close proximity of the stiff substrate and thus these non-uniform lateral deviations constitute a far lower fraction of the overall deformed volume, resulting in a lower deviatory component from US by these lateral lobes.

A second deviation arises from spreading of normal (longitudinal) stress from the punch through the film to the substrate. This is shown in Fig. 4.7 (b) (under the same contact conditions as in (a)) as the distribution of longitudinal strain in the film, which reveals a spreading effect beyond the punch contact periphery. Ie, while the longitudinal strains in the puck itself remain uniform, there is a spread of lower magnitude longitudinal strains to higher radii outside the punch radius with deeper indentation depths. This effect is clearly more pronounced for low aspect ratio contact (upper panel vs. lower panel).

We propose that the net effect of these non-uniformities is to cause deviations of the LCT stress vs. strain curve from pure US in opposing directions. For the lateral strain lobes, a more compliant puck volume is created by the allowance of lateral deformations, which translates to a lower value of stress for given strain and therefore a negative error effect from the US slope. Conversely, the spreading of normal stress to a wider region of the substrate renders both the effective diameter of compressed puck and area of the compressed substrate higher, creating an overall stiffer response. In both cases, non-uniform regions represent larger fractions of the deformed volumes at lower aspect ratio.

Taking stock of our results as presented in Fig. 4.8 below, which shows deviation from US for all aspect ratios explored, we see that at the presumed best case scenario of high α and high *S,* which should act to minimise the strain field effects discussed above, we find a ~-5% deviation from the expect value of *M* at zero strain, rising to approximately -3.5% just before rolling off at yield. The overall mean offset of this curve can be accounted for from the way the mean stress was calculated from the punch load given by the finite element analysis. In order to more closely adhere to experimental conditions during these simulations, mean stress was calculated by dividing the load by a constant punch face area assuming a contact radius of $a - r/2$, where r is the punch corner rounding. Such a mean value might be determined via, for example, optical characterization of the punch dimensions, which may not be able to easily resolve nanoscopic rounding.

Examination of the strain field during contact reveals that pre-yield, the punch to sample contact radius remains very close to the initial contact radius of $a - r$, in our case 950 nm for a 1000 nm radius punch with *r* = 50 nm corner rounding radius, for large aspect ratios such as $\alpha = 100$. A simple analysis shows we should expect a ~5% relative underestimate of the US stress due to an overestimate of the contact area in this case, where other deviations are minimal, which is what we find in our data for these high aspect ratio contacts (such as in Fig. 4.5 (f) and 4.8 (a)). For all aspect ratios explored, this ~5% underestimate slowly reduces through the course of the indent as the punch comes into contact more fully, manifesting as a gradual upwards slope in the data in Fig. 4.5 (d-f). This self-correction of the contact area underestimate is more pronounced at lower α (until rolloff caused by premature plasticity) as more of the punch comes into contact at lower strains in this geometry. This is visualised more clearly in Fig. 4.8 (b-e) below which compares punch corner contact for α 5 and 100 up to 0.9 strain.

As a result of the presence of these competing error effects (from the incomplete tip contact, and from the propagation of inhomogeneous lateral and longitudinal strains), at aspect ratio α = 5 typical of current experiment, we find *M* to be uniformly overestimated by 3-4% for reasonable values of *S* to strain up to approximately two thirds the yield strain before sharp roll-off occurs under premature plasticity, and varies from -2% to 0% deviation for α = 10. Contact aspect ratios typically used in the rest of this work range between α 5 and 10 and so deviations from the pure US case are within the range of a few percent.

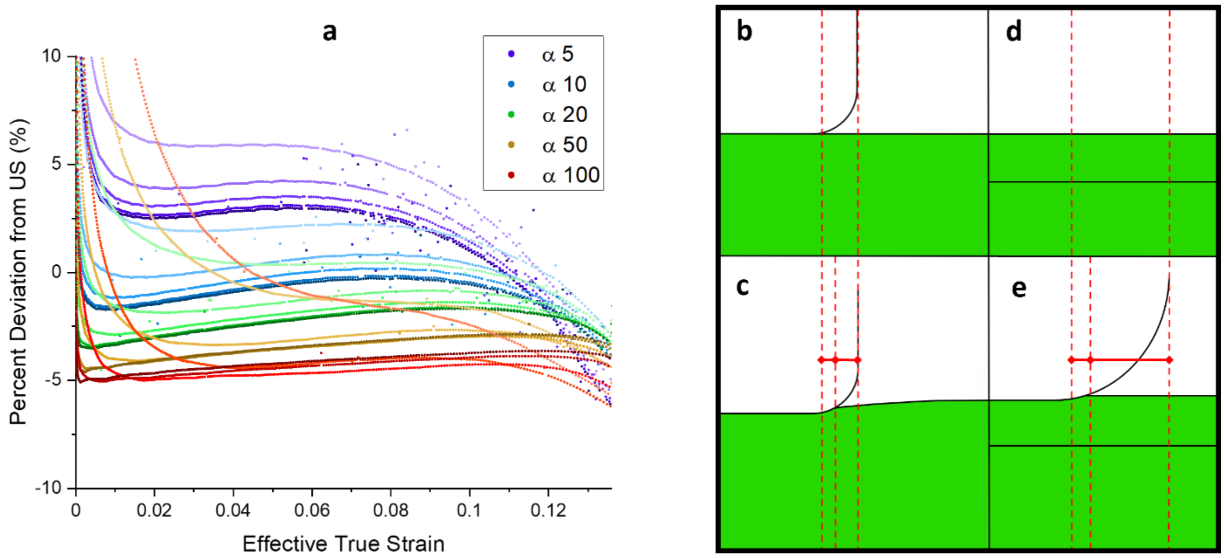

Fig. 4.8, (a) *Amalgamated percentage deviation from US slope for all α and S explored in this work (excluding S = 10 and 20 for clarity). Darker shades of a given colour represent higher S values. Competing error effects cause lower values of α to produce more accurate results than may otherwise be expected. There competing error effects are inhomogeneous strain fields (as presented in Fig. 4.7), and incomplete contact area due to rounded corners.* ***(b-c)*** *shows incomplete contact at true strain 0 and 0.9 respectively for $\alpha = 5$, compared to the same for $\alpha = 100$ in* ***(d-e)****, revealing the higher impact of incomplete contact on the results to higher indentation depths for larger contact aspect ratios*

4.7 Experimental Aspect Ratio Analysis

To explore the effect of contact aspect ratio experimentally, I present in Fig. 4.9 experimental LCT results performed with an $a = 2050$ nm radius diamond flat punch indenting atactic polystyrene (aPS) layers of thickness 190, 240, 300 and 470 nm spin coated onto flat Si(100) substates. This polymer features a low E/Y ratio of ~10, close to the simulated value of 10 and typical of soft amorphous materials most appropriate for the LCT. This sample gives a value of S ~ 22 when considering an expected aPS modulus of 3.1 GPa and Si(100) modulus of 70 GPa with a range of aspect ratios α = 8.8, 13.6, 17, and 21.6. Load vs. displacement measurements for each film Fig. 4.9(a) show the kink expected for a confined yield event, while the overall slope of each curve increases with decreasing film thickness (ie, increasing aspect ratio) as expected from our simulations The upward curvature at very small displacements is due to a small misalignment between punch face and film [31], as discussed in Chapter 3. In Fig. 4.9 (b), conversion of load and displacement to mean stress and effective strain with a substrate correction applied collapses the data to a common locus throughout the pre-yield kink regime. The slope of the data agrees well with the typical range of confined modulus slope of aPS found in the literature from M = 4 to 5.46 GPa slope (represented by green dotted lines, based on the range of Poisson's ratio for aPS from ν = 0.32 to 0.35 and Young's modulus E from 2.8 to 3.4 GPa used to calculate M as per Eq. 2.17) Effects of aspect ratio predicted by the simulations can be seen even over this relatively small range: At high strain, the lower aspect ratios start to roll off, indicative of premature plasticity. This demonstrates the accuracy of the LCT to the predicted confined modulus using a simple substrate correction.

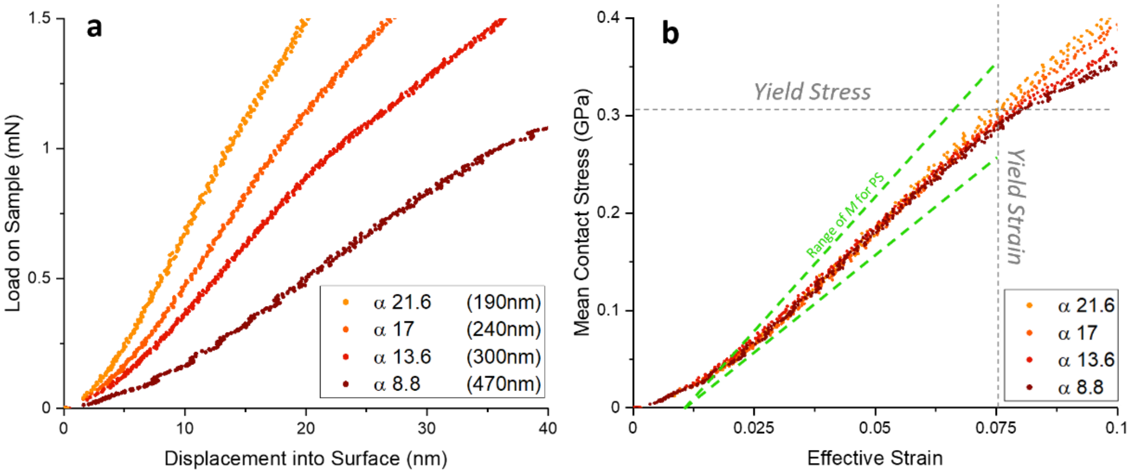

Fig. 4.9, (a-b) *Experimental LCT results using a 2.05 µm radius diamond flat punch on atactic polystyrene films of various thicknesses, with a compliance correction applied for the Si(100) substrate (E = 70 GPa). This S ~ 22 configuration is in good agreement with the simulated results and gives a reasonable estimate of the expected Young's modulus of polystyrene, once a substrate correction is applied as shown in* ***(b)****. The green dotted lines in (b) denote the range of expected possible values of confined modulus M for PS (based on typical literature values of ν ranging from 0.32 to 0.35 and E from 2.8 to 3.4 GPa). These are offset from 0 strain to account for the initial inflection in the stress-strain curve caused by punch-film misalignment*

4.8 Conclusion

In this Chapter I have presented a finite-element numerical analysis of the effect of punch radius to film thickness contact aspect ratio α and substrate to film elastic modulus ratio S on the accuracy of the layer compression test to uniaxial strain within an elastic-simple plastic, elastically supported film in the elastic regime up to the nominal confined yield true strain of 0.136. The film was given an E/Y ratio of 0.1 typical of amorphous materials. Results are most consistent for high S values for all tested α in this region of strain, though the results are most uniform from zero strain to yield when high α are also used. This combination of high S and α that produce the most uniform results underestimate the true value of confined modulus M by ~10%, an error that is a complex but explainable function of α, S that influence strain inhomogeneity in the compressed material, and geometric defects like punch edge rounding. Because of this, results benefit greatly from a simple analytical substrate correction, that allows accurate determination of M with only minor deviations for the typical range of α and S used in experiment.

Results match well with previous reports of elastically supported elastic films using different analytical techniques. Experiments conducting over a limited range of α and at S ~ 20 for a polymer film on silicon substrate agree with the deviations I find in the simulations and the trends observed within. These results add further credence to the LCT as a means of accurate determination of the elastic mechanical properties of thin films that is used for the analysis of materials in further chapters of this thesis.

Future work may explore larger strains in order to encompass an analysis the yield point and beyond into the zone of confined plasticity, or explore a range of Poisson's ratio and high E/Y ratio materials like metals and ceramics. This study, and the comparison to polymer data that is generally highly influenced by sample preparation history, highlights an important issue of identifying a calibration sample for the layer compression test. The LCT requires reasonably high value of substrate stiffnesses to maintain a required S ratio, a value that will be fundamentally capped by diamond. The modulus of engineering materials like silicon, sapphire or diamond likely limits the test to films with stiffness not exceeding those of soft metals. Moving to much softer films like polymers, biomaterials, nanocomposites etc. as a reference presents the problem of their non-equilibrium state and typically amorphous nature that is often strongly dependent on sample preparation history as evidenced in the range of values presented in Fig. 4.9 (b). This limits the potential candidates for a reference material quite significantly. The candidate must also possess a Poisson's ratio that is not prohibitively high as high lateral expansion in the film will also cause large deviations from uniaxial strain by complicating the confining nature of the surrounding film jacket. Some exotic materials like Europium (E = 14.5 GPa, ν = 0.2) show some promise, but may suffer from rapid oxidation in ambient conditions, which also brings into light the expectation that the material be chemically inert in ambient conditions. Potential candidates are being considered and finding such a reference material may be the subject of a further study.

Ch 5 : Pressure Dependent Mechanics of Amorphous Thin Films

Preface : The work presented in this chapter has in places been integrated into the text based on, and adapted from, work published by the author in *Pressure Dependent Mechanical Properties of Thin Films under Uniaxial Strain via the Layer Compression Test,* Journal of Materials Research*,* 2023 [237], and co-authored in *8Li Spin Relaxation as a Probe of the Modification of Molecular Dynamics by Inelastic Deformation of Glassy Polystyrene,* Journal of Physics : Conference Series, 2023 [207]. The author's contribution to this co-authored piece was the preparation and patterning of the polymer films, with the β-NMR analysis being performed by collaborators in the University of British Columbia.

As discussed in Chapter 1, the mechanics of amorphous materials with excess free-volume is complicated by pressure dependant effects as the material densifies. While such pressure effects have been reported for some time in a range of bulk materials [196-199], how these may manifest in thin film geometries remains poorly explored. The quasi-two dimensional nature of thin films, along with their higher surface contributions and unique production methods compared to bulk materials are known to affect their morphological characteristic [238-240], which may also necessitate different treatment for pressure induced effects. In this chapter I present combined finite element and experimental exploration of uniaxial strained amorphous films (including polymers and nanosheet networks), exploring changes in their mechanical response to uniaxial compression utilising the Layer Compression Test (LCT). I also report on a highly novel probe of the effect on molecular dynamics of large area compression via spherical indentation of polymer films using a specialized variant of nuclear magnetic resonance (NMR) called "beta-NMR", namely the rotation of phenyl sidegroups along the polymer chain, which may reduce with the reduction in available free volume. This beamline technique was invented by collaborators at the TRIUMF facility in Vancouver, Canada for thin film geometries and we show it can reveal molecular dynamics on compressed vs uncompressed amorphous films for the first time.

5.1 Pressure Dependency of Amorphous Films in the LCT

The confining conditions of uniaxial strain lead to the generation of significant hydrostatic stress per increment of total imposed strain compared to simple uniaxial stress. We thus expect a strong influence of pressure-dependent properties in free-volume amorphous materials tested via US. US also acts to limit the generation of shear stress vs applied stress compared to the unconfined uniaxial strain, which delays yielding to higher stress as discussed in Section 2.3.4, particularly surrounding Fig 2.8 and 2.9. Crucially, however, the LCT does not produce perfect uniaxial strain, with deviations arising from substrate deformation, inhomogeneous strains at the punch corners, and eventual failure of the lateral confinement (as detailed in Chapter 3). This can be demonstrated in Fig. 3.5 from Chapter 3 (and is shown again here in Fig. 5.1 with the regions of specific interest highlighted), which shows stress vs strain curves of LCT indents on a 270nm thick film of PMMA prepared with a standard spin coating method [60], mounted on a Si(100) substrate, and indented with a 2 μm diameter diamond flat punch (contact aspect ratio ~7.5:1). Indents were performed with a constant loading rate of 0.67 mN/s (0.2 GPa/s). Three indents are displayed for clarity, with maximum peak loads below the yield point (green curve), above the yield point (teal curve), and after the extrusion point (orange curve), displaying indents in the three strain regimes of interest. Previous work has shown that such indentations are highly repeatable on such polymer thin films [31]. There exists in these curves a clear slope transition around 0.1 strain, which has been established earlier in this thesis to be indicative of material yield. This is in contrast to Ravi-Chandar’s observation of a lack of compressive yield in confined uniaxially strained PMMA [205].

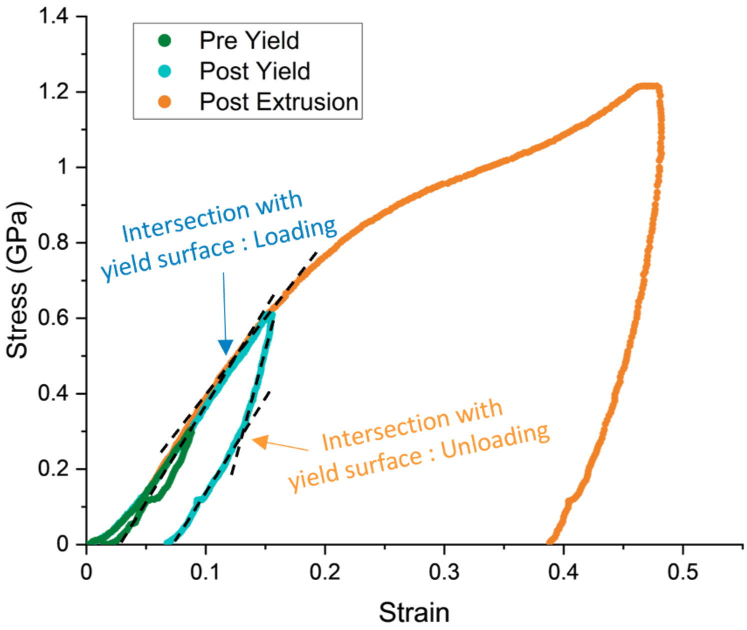

Fig. 5.1, *LCT indents on 270nm thick PMMA film prepared on a Si(100) substrate via spin coating. Shown are indents to three depths; below the yield point in the elastic regime (green), beyond the yield point in the plastic regime (teal), and beyond the extrusion point during confinement failure (orange). A kink during the loading portion is evident at ~0.1 strain, indicative of yield, and a second on unloading for indents performed sufficiently beyond the yield stress but before extrusion, indicative of a second intersection with the yield surface caused by the confinement. Other features such as the inflection at extrusion and creep under a held load are described in detail in Chapter 3*

There exists also a second kink in the unloading portion of the post yield curve indicating potentially a second intersection with the yield surface caused by the confinement, as described in more detail in Chapter 2, note that this unloading yield is not evident in the post extrusion curve, as the confinement has failed in this case). It is also not clear if this kink is simply a doming of the unload curve, as it does not coincide with the expected stress level below peak stress as expected from the analysis of confined shear generation in Chapter 2. As such it is not examined in detail here. This discrepancy between the LCT and pure US in describing a fundamental yielding phenomena in LCT highlights the need to more carefully understand the subtleties in pressure dependencies as explored by the LCT. In particular, it is important to understand in what ways it may be used to explore pressure effects and how this may lead to methodologies not easily attainable in idealised US experiments. To this end I utilise finite element simulations of a pressure dependent elastic-plastic material in a uniaxial strain system to explore pressure dependencies of the yield surface, as well as the features of the LCT that can facilitate yield in materials that otherwise exhibit yield surface pressure dependencies with a von Mises pressure coefficient of $\mu_{vm} > \frac{2\sqrt{2}}{3}\frac{G}{K}$ (See Eqt 2.39 in Section 2.4 for details) such as in PMMA. We also examine observed pressure dependency in compressive uniaxial strain of amorphous films using the LCT. This includes observations of pressure dependent stiffness of thin films of both polystyrene and sprayed graphene nanosheet films in Section 5.3.1 and 5.3.2, respectively. We do this using in situ continual stiffness measurements as described in Chapter 3. While ex-situ densification of polymer films after LCT compressions has been observed before [241], we detail instead in the later sections of this chapter observation of pressure dependant stiffness during compression.

5.2 Finite Element Simulated Pressure Dependent Solid in Uniaxial Strain

Finite element simulations of a pressure dependant material were used to explore the pressure dependant yield surface in amorphous materials. These were performed in a simulated confined uniaxial strain geometry as opposed to a simulated LCT as in Chapter 4 in order to keep complexity at a manageable level and better display the resulting yield surface. These were performed with the Abaqus 2019 implicit solver. In order to simulate a pressure dependant material, I consider that the means of altered mechanics with applied pressure in an amorphous material is primarily through densification and collapse of free volume. For example for polymer glasses, quenching within finite timeframes causes the polymer chains to settle in non equilibrium configurations characterised by large areas of available free volume. This free volume may be reduced thermally via long quenching times, or annealing near the glass transition temperature (as explained in further detail in Chapter 1), or via compressive pressure [206]. As such, a porous elastic material model with tailorable pressure dependent elastic parameters was used, adapted from Hughes and Kelly's work on second order elastic deformation [242]. The model uses the following to calculate Young's modulus as a function of pressure

$$E = E_{ref}\left(\frac{p+p_0}{p_{ref}+p_0}\right)^n \tag{5.1}$$

Where E is the Young's modulus, p is the pressure ($p > 0$), E_{ref} is the Young's modulus at a reference pressure of p_{ref}, and p_0 and n are material constants which may be derived empirically from known material stress vs strain response. The relation for the pressure dependent Poisson's ratio is as follows

$$v = v_0 + (v_\infty - v_0)(1 - e^{-mp}) \tag{5.2}$$

Where v is the Poisson's ratio, v_0 is Poisson's ratio at $p = 0$, v_∞ is that at infinite pressure, and m is an empirically derived material constant. In the case of tension rather than compression, a value f was used such that $E = fE_{ref}$ for $p \leq 0$

$$f = \left(\frac{p_0}{p_{ref}+p_0}\right)^n \tag{5.3}$$

Values for the material constants were selected to match the pressure dependant properties of polystyrene found in Hugh and Kelly's work [242], with values of n, m, and p_0 chosen to fit this known empirical pressure behaviour of bulk polystyrene to give a simulation of the porous elastic system. These are given in Table. 5.1 below. The resulting behaviour is consistent with that for polystyrene found in Hugh and Kelly's work for the pressure range explored here.

E_{ref} (GPa)	p_{ref} (Gpa)	p_0	v_0	v_∞	n	m
4.8	0.2	0.67E9	0.34	0.395	1	3E-9

Table 5.1, *Parameters used for the finite element simulation of the porous elastic model outlined in Eq. 5.1 through 5.3. These parameters are described in the above text*

For the plastic portion, a model of soft rock plasticity that incorporates pressure dependent variables was utilised to model deformation beyond the yield point [243, 244]. This model was prebuilt into Abaqus and was selected for the variable yield surface, with other effects such as strain hardening turned off. The referenced material gives a more comprehensive overview of this model, with quick explanations given below to explain the various parameters. The yield surface in this model is defined by the equation

$$\sqrt{((e_0 Y tan\beta)^2 + g(\sigma)q)^2} - (p - p_t)tan\beta\left(\frac{p-Y_c}{Y_t-Y_c}\right)^{\frac{1}{n_y}} - e_0 p_c^0 tan\beta = 0 \tag{5.4}$$

Where p is the pressure, q is the Mises equivalent stress, Y_c is the yield stress in hydrostatic compression, Y is the initial value of Y_c under no compression, Y_t is the yield stress in hydrostatic tension, β is the friction angle, n_y is a material property that controls the shape of the yield surface in the shear-pressure plane, and e_0 is the eccentricity parameter. As above, many of these parameters can be chosen to fit empirical behaviour of materials of interest. $g(\sigma)$ is a function that captures the transition of the yield surface in the octahedral plane from a rounded triangular shape to a circular shape as pressure is increased (see Fig. 2.7), and is given by

$$g(\sigma) = \left(\frac{1}{1-f(p)}\left(1 + f(p)\left(\frac{r}{q}\right)^3\right)\right)^{\alpha} \tag{5.5}$$

$$f(p) = f_0 \exp\left(f_1 p \left(\frac{Y}{Y_c}\right)\right) \tag{5.6}$$

Where r is the third stress invariant, α, f_0, and f_1 are material properties. The friction angle β is defined as the angle between the pressure axis and the shear surface in the p-q (shear-pressure) plane at $p = 0$. There also exists a dilation angle, ψ, which is the angle between the normal of the shear surface and the shear axis. If $\psi \geq 0$, the material will dilate.

While Eq. 5.4 through 5.6 may seem rather involved, much of the components that govern complex yield surfaces only take significant effect at high strains or for significantly complex yield surfaces. In the range we explore here, only small offsets from linearity are expected for typical amorphous solids, as such, many of the values are set to 0, or ≈0 in the case that a true value of 0 is not a valid input. With this in mind, much of the complexity is reduced, and the following parameters were used to fit to the known yield surface of polystyrene [245].

Y (GPa)	β	ψ	n_y	e_0	α	f_0	f_1
0.2	11.45	0	1	0.001	0	0	0.001

Table 5.2, *Parameters used for the finite element simulation of the soft rock plasticity model co-opted for its variable yield surface, as outlined in Eq. 5.4 through 5.6. These were utilised alongside those presented in Table 5.1 for the complete simulated pressure-dependent elastic-plastic behaviour presented in this section*

Fig 5.2 shows a contact stress vs strain curve of uniaxial compression of the simulated pressure dependent polymer described above. This is compared in the same graph to an identical linear polymer with no pressure dependence. This comparison reveals some key similarities and differences. In both cases two distinct loading regimes can be observed, corresponding to elastic and plastic deformation, separated by a kink denoting yield transition between the two. The inclusion of pressure dependency introduces some key differences aside from this, however. Firstly is the increase in the stress value at the yield transition, with the pressure dependent material exhibiting a yield transition that is 44% higher than for the identical linear material. This is not unexpected from pressure dependent yield surfaces as discussed in Chapter 2, and will be demonstrated in more detail for this case later. The second difference of note is the nonlinearity of the slopes of the stress vs strain response in the pressure dependant material in both the elastic and plastic regime. In contrast to the linear case that experiences slopes in these regions of the confined modulus M (in the elastic regime), and the bulk modulus K (in the plastic regime), the pressure dependent case shows a clear upward curvature in both regimes, indicative of an increasing stiffness as the pressure increases and the material densifies.

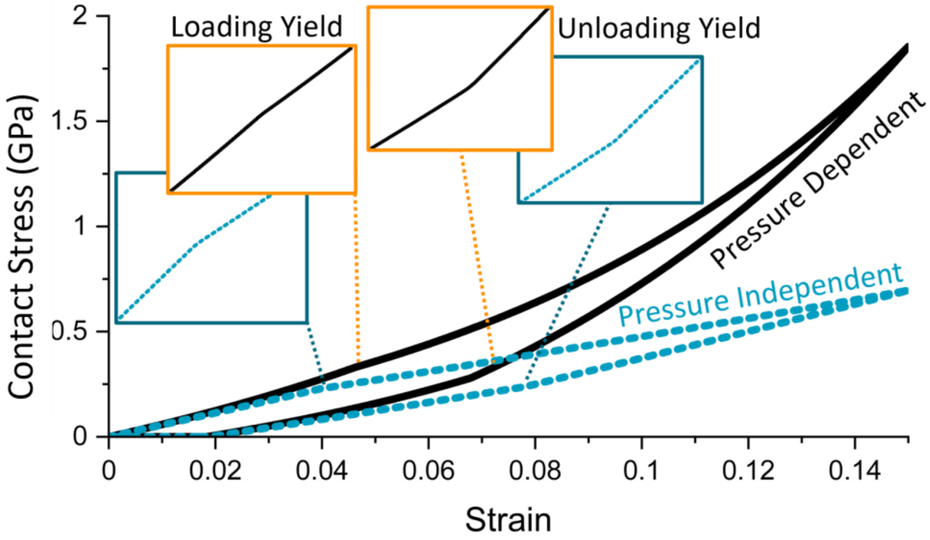

Fig. 5.2, *Finite element analysis simulation of stress-strain curve (applied punch stress) of a rigidly supported film under uniaxial strain compression. The material has properties emulating glassy polystyrene as described in Section 5.2. The graph displays the change in modulus (curvature), as well as yield point on loading and unloading*

There exists also in the unloading portion of both curves a kink in the stress vs strain curve indicative of a second intersection with the yield surface as shear is increased in unloading due to the confinement of the stiff surrounding jacket (see Chapter 2). The differences displayed in the pressure dependent case can be best explained by plotting the evolution of shear vs pressure during the compression and unloading in this case, as is shown in Fig. 5.3. This shows the internal shear increasing rapidly through elastic loading before the intersection with the yield surface, beyond which the material can sustain the generation of no further shear and will yield. The yield surface continues to increase however, so the material maintains a shear value equivalent to this surface until the unloading point. The shear then reduces back to zero, before growing in magnitude in the opposite direction due to the confining walls and intersecting with the yield surface again.

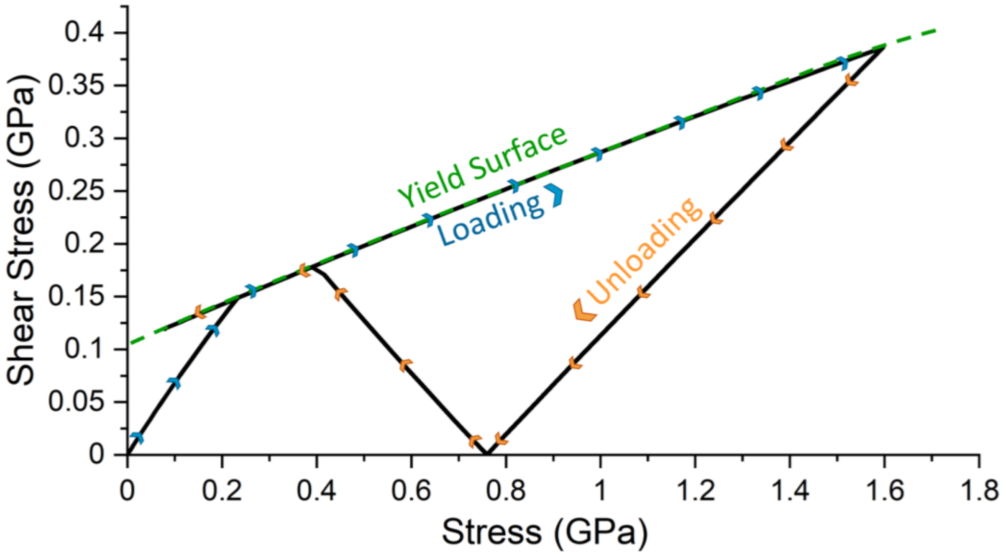

Fig. 5.3, *Shear vs compressive hydrostatic stress during the same finite element simulation as in Fig. 5.2, revealing the intersection with the yield surface at ~0.2 GPa on loading, and second intersection at ~0.4 GPa on unloading caused by the wall confinement*

All of these features are expected from uniaxial strain of an amorphous material and therefore the model can be used to explore how the LCT may alter the response from the pure US case and allow yielding at lowered stresses in materials such as PMMA.

5.3 Pressure Dependent yield and the Layer Compression Test

It is interesting to note that the yield surface for some amorphous materials may increase under confined compressive stress faster than the generation of shear within the material, in principle precluding the system from ever reaching yield. In this case the material may never fail plastically due to the greater magnitude of hydrostatic pressure generation over shear in uniaxial strain experiments, as can be seen in Ravi-Chandar's PMMA experiments. This is a problem for materials testing due to the range of valuable information extractable from such US measurements. While the LCT well approximates the US condition, LCT indents on a thin film PMMA sample show clear indications of uniform yielding behaviour, as in Fig. 5.1 and discussed above.

In order to reconcile the existence of a yield transition in the LCT compressions of PMMA with Ravi-Chandar's results, we consider the effect of introducing excess shear into a compressed material on the yield stress. The dotted orange and yellow lines in Fig. 5.4 demonstrate how pressure dependencies can increase the yield surface in such a way that greater shear stress is needed to induce a yielding event as per Eq. 2.39, compared to the case of zero pressure dependency (plotted with a horizontal dashed line) [242]. The solid blue line represents the evolution of octahedral shear stress with applied pressure in an ideal US geometry, and the dashed yellow line represents the case of $\mu > \frac{2\sqrt{2}}{3}\frac{G}{K}$ where the evolution of the yield surface outpaces the generation of shear in US as per Eq. 2.38. This shows that for a material with a yield surface of high enough pressure dependency, yielding may be delayed indefinitely in compressive loading geometries. In materials with such highly pressure dependant yield surfaces, uniaxial tension has been shown to introduce yielding more readily than uniaxial compression. This has been explored in bulk high contact aspect ratio experiments and pressure dependant analysis by Caruthers et al. [201, 246]. Fig. 5.4 allows this to be visualised by the intersection of the yield surface in the tensile direction (negative pressure values), whereby the pressure dependency facilitates intersection with the yield surface at lower pressures than for compressive loading. Caruthers noted that for confined uniaxial compression, intersection with the yield surface may not be plausible for certain polymer glass systems [201]. However, introducing excess shear (effect shown by the shaded spread accompanying the solid line in Fig. 5.4) can increase the generation of octahedral shear stress enough to allow the exploration of material yield in otherwise difficult to yield materials while maintaining a largely uniaxial strain state [31, 33].

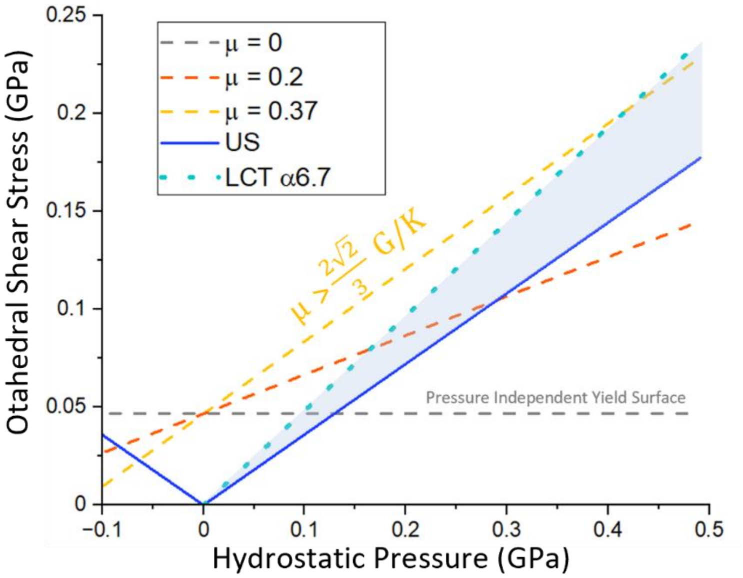

***Fig. 5.4**, Octahedral shear stress vs applied pressure for an arbitrary pressure dependent system, detailing the increasing shear needed to cause yield in a material with a pressure sensitive yield surface as the yield surface increases with applied pressure. Example materials with yield surface pressure dependency $\mu < \frac{2\sqrt{2}}{3}\frac{G}{K}$ (orange) and $\mu \geq \frac{2\sqrt{2}}{3}\frac{G}{K}$ (yellow) are both shown by dotted lines, with the shear generation in US demonstrated by a solid blue line, and the effect of additional shear by the shaded blue region, which may allow intersection with a steep yield surface at reduced pressures*

For the case of PMMA, a similar increase in the shear surface slope can allow for intersection with the yield surface where normally the increase in the yield surface with applied pressure would outpace the generation of shear, as PMMA has a Von Mises pressure coefficient μ_{vm} of 0.23 [245]. Taking a pressure dependent *G* and *K* into consideration explains Ravi-Chandar's result of being unable to yield PMMA in a uniaxial strain geometry, as shown in Fig. 5.5 [247] which shows the evolution of the pressure dependent surface in PMMA. The differences in geometry between LCT indentations and a pure US case can be examined to explain the yield behaviour observed in contrast to these experiments. I attribute increased shear generation in the LCT to the observed yield behaviour in Fig.

5.1, which may allow exploration of yield in a closely approximated US system where one may not exist in a pure US configuration.

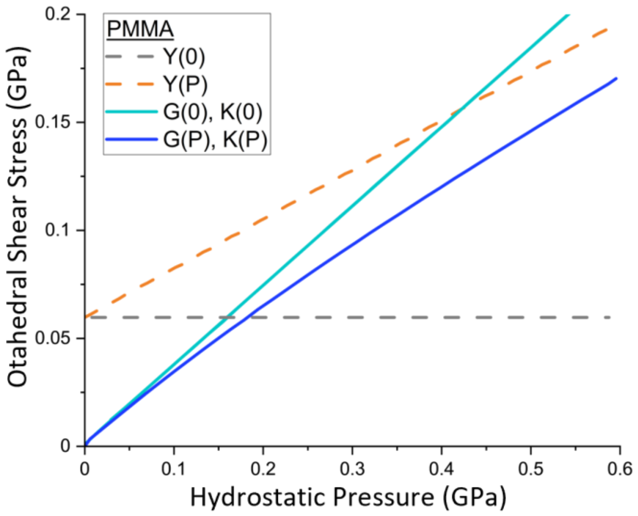

Fig. 5.5, *Pressure dependant yield surface and shear generation in US for PMMA. Y(0) is the shear value for yield at zero pressure, Y(P) is the case when pressure dependency is taken into consideration. G(0), K(0) represents the evolution of shear in US if not taking pressure dependency of G and K into account, and G(P), K(P) show how taking into consideration pressure dependent G and K can alter the shear surface such that yielding in a US geometry becomes challenging in PMMA*

The most influential of these differences are the rounded punch corners, from which lateral strains propagate throughout the compressed puck [33], a non-perfectly stiff confining substrate, and elastic confining walls. The influence of these features to direct approximation to US is approached in detail in Chapter 4. These work to introduce more highly sheared regions in the compressed puck of material, and greater overall propagation of shear strains throughout the compressed puck, propagating primarily from the puck corners. This increases the slope of the shear – stress surface, and allows the material to approach the yield surface quicker, as demonstrated analytically above in Fig. 5.4.

While these influences were identified in detail in Chapter 4, it is instructive to gain a more concrete sense of the magnitude of shear propagation in US here. Fig. 5.6 shows shear stress vs applied pressure in a FEA LCT indentation compared to the case of US for the same simulated elastic simple plastic material as in Chapter 4. For clarity, the two extreme cases are shown, one with the highest examined aspect ratio (α) and substrate to film modulus ratio (S) (100 and 1000 respectively) representing the more idealised case, and a lower bound of contact aspect ratio α = 5, and substrate to film stiffness ratio S = 50, representing conditions further from US and more indicative of typical experimental parameters. In this figure, the shear present in all elements under the punch were examined. The spread in these values is large, attributable to the majority of highly deviatoric elements being situated near the puck corners. To display the true extent of shear generation more clearly, the shear value of all elements under the punch were averaged, represented by the solid blue and red lines. The shaded regions represent the spread present in the data values. Although the spread is large, the average line reveals that this spread is dominated by a comparably low number of deviatory elements.

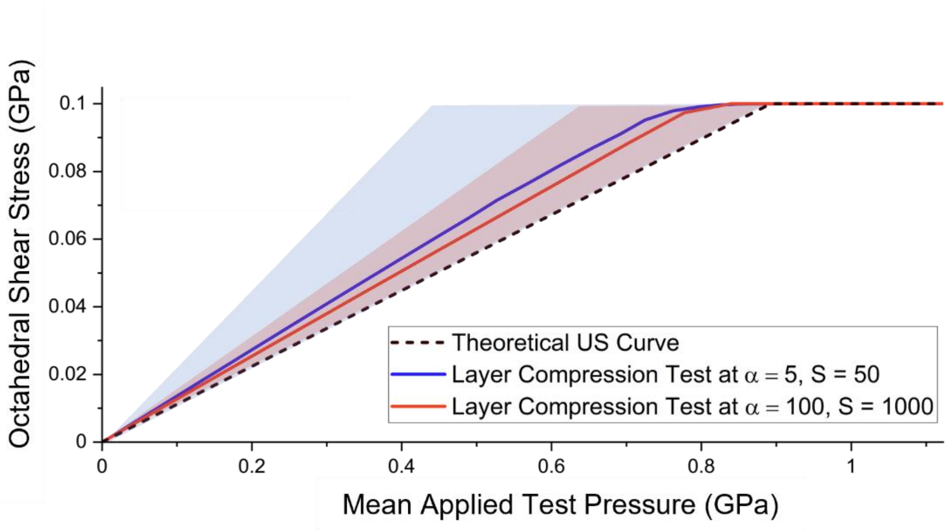

***Fig. 5.6**, The accelerated generation of shear stress in a LCT indentation compared to pure US from finite element simulation of the LCT that can allow for intersection with the yield surface at lower pressure. The extreme cases of high contact aspect ratio (α) and substrate : film modulus ratio S (100 and 1000, respectively), and low α and S (5 and 50, respectively) are shown, with parameters between these extremes lying within these bounds. The solid lines represent the average shear within all elements under the punch for each case, and the shaded regions represent the degree of deviation from this average for all puck elements, largely determined by deviatoric elements surrounding the puck corners*

As can be seen, the case of higher α and S which more closely approximates the US condition in terms of deformation uniformity, limits the generation of shear stress and more closely resembles the case of shear in US, while lowering the contact aspect ratio combined with the substrate stiffness takes us further from this case and facilitates the generation of shear stress more readily. With this effect in mind it can be important to consider the extent of shear stress generation in a confined flat punch geometry such as the LCT when considering using the technique as a comparison to US. Compared to more typical indentation techniques, the shear generation is small, but must still be considered as this study has demonstrated.

It can also offer useful insights into the processes controlled by introducing shear into an otherwise largely uniaxial compression and how this might affect and allow exploration of the mechanics of thin film materials (such as surrounding the yield transition). While shear may typically be introduced to such a system via lateral oscillations via, for example, a small amplitude oscillating piezo underneath the substrate, this introduces further experimental and instrumentation complexity. It also may affect the confining effect of the surrounding material in unforeseen ways and cause additional analytical complexity. As such the LCT can be considered an effective and tailorable tool for the exploration of pressure dependant yielding in approximated US compressions, allowing for controllable generation of shear and observation of yield using single dimension indentation on thin film materials.

5.3.1 Pressure Dependent Stiffness of Polystyrene Thin Film

The FEA analysis presented above provides understanding around the yielding phenomena in homogenously compressed amorphous materials during the LCT. However, the stiffness increases expected during elastic and plastic deformation in this approximated US test condition have gone unexplored in experimental thin films testing so far. I present here observation of these effects on thin film PS during LCT indentation.

Fig. 5.7 shows three LCT indents on a 191nm thick film of PS supported on a Si(100) substrate, prepared via spin coating. Indents were performed with a constant loading rate of 0.67 mN/s (0.2 GPa/s) with a punch of diameter 2μm (contact aspect ratio of ~10:1). Fig. 5.7 (a) displays the load vs displacement curve for these indents, which displays the typical features expected of a LCT indent on a supported polymer, including the yield kink, with the initial misalignment inflection and extrusion zones shaded for clarity. Congruently with the load vs displacement curve, I measured the instantaneous small amplitude dynamic stiffness via continual stiffness measurement discussed in Chapter 3 (ie, the harmonic stiffness). This oscillation was maintained at 45Hz with an amplitude of 1nm via feedback to a force to maintain this amplitude, and from this was determined the continuous stiffness throughout the indentations. An averaging of the three curves is also presented as a blue line for clarity. The resulting harmonic stiffness vs displacement graph is shown underneath the load vs displacement curve in Fig. 5.7 (b).

Initial stiffness at the onset of the elastic region in the load vs displacement curve is ~80 kN/m, resulting in a Young's modulus E of approximately 4 GPa, consistent with that expected for glassy polystyrene. Stiffness as measured using the harmonic technique is approximately 20% higher at this point (~100 kN/m). This small difference can be attributed to a rate dependence of the material response to the differing loading conditions. The load vs displacement slope is a quasi-static indentation performed over the course of 100s, whereas that observed in the harmonic channel is measured from a small amplitude 45 Hz oscillation as described above. This corresponds to a loading rate difference of approximately two orders of magnitude that accounts for the small discrepancy in measured stiffness between the two.

One other discrepancy is at the yield intersection, where the stiffness drops in the load vs displacement dataset as expected, whereas in the harmonic channel the stiffness drop is less pronounced and quickly recovers to a rising stiffness. There are several potential causes for this. A rate dependency as discussed above could be introducing significant differences, as well as creep differences introduced by the rate difference and/or friction effects. Significantly, material response under plastic compression in the layer compression test has yet to be analysed in detail, though it is clear it presents noticeable variation from pure uniaxial strain behaviour that requires correction, as has been done for the elastic region as detailed in Chapter 4. Notably, plasticity commences in a rapid but not fully discrete event in the LCT, with dependencies on contact aspect ratio. As well as this, the accuracy to the uniaxial strain condition reduces throughout plastic deformation with a gradual transition to confinement failure and extrusion. These can both be seen in for example Fig 4.8 (a). As such it is likely that complex deviations from uniaxial strain behaviour could be the cause of the observed discrepancy when comparing a rapid 45 Hz oscillation and a quasi-static loading. Namely, the quasi-static case could be susceptible to effects such as material creep and 'leakage' to the surrounding uncompressed film in ways rapid small amplitude compressions are not, compounding with traditional rate dependencies and creep behaviour internal to the compressed region. A more comprehensive analysis of plastic deformation of the layer compression test in comparison to uniaxial strain is currently being considered for future exploration.

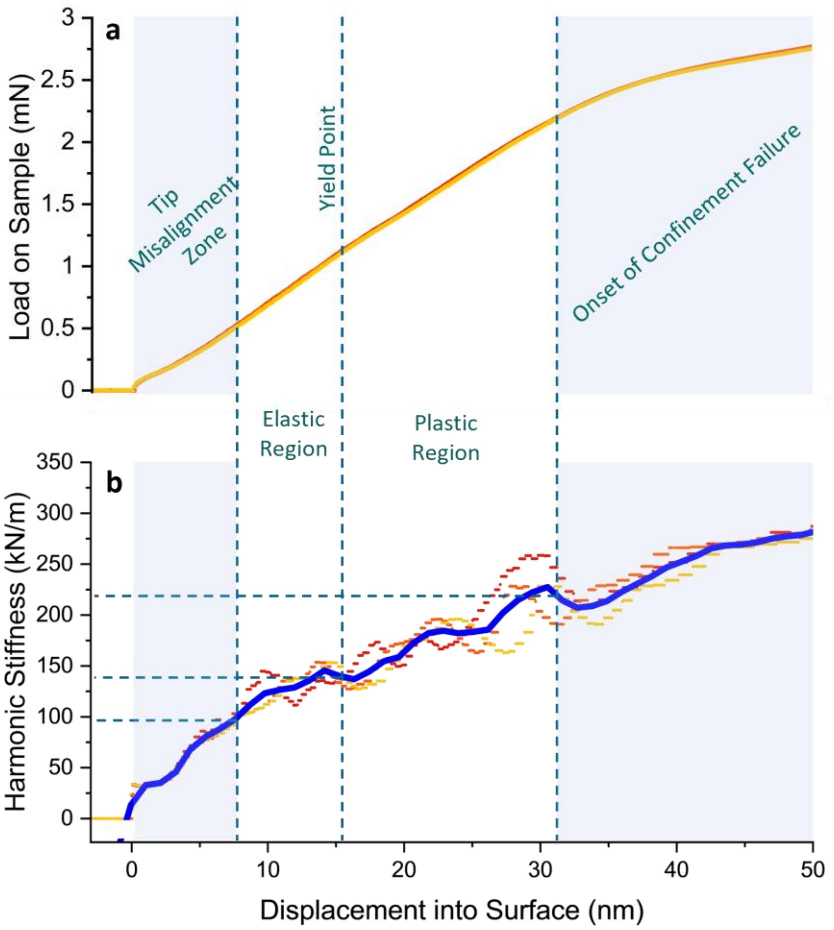

*Fig. 5.7, **(a)** Load vs displacement and **(b)** continual harmonic contact stiffness (CSM) data of LCT indentations on a 191nm polystyrene supported on a Si(100) substrate with a 2μm diameter punch. Between the region of full contact and plastic yield, we observe a 45% increase in the stiffness, as well as an upwards curvature in the elastic regime of deformation, both indicative of the modulus of the*

material being altered by applied pressure. The dark blue line in ***(b)*** *represents an averaging of the three curves presented for clarity*

While the stress vs strain curvature associated with pressure dependent confined modulus is clearly defined in the FEA simulations (Fig. 5.2), it is instructive for the experimental case to refer to the harmonic stiffness for increased clarity. While we can dismiss the increasing stiffness around zero strain resulting from incomplete punch contact, beyond this there exists a clear increase in the contact stiffness. From onset of full punch contact to the yield strain there is a ~45% increase in the harmonic stiffness from 97kN/m to 140kN/m. The corresponding curvature change in the load vs displacement curve expected from such an effect is also present. This is in contrast to a non-pressure-dependant response, whereby the harmonic contact stiffness plateaus to a constant value after the region of initial punch misalignment.

Beyond the yield point into the region of plastic deformation, the harmonic stiffness continues to increase due to the continued densification, the stiffness beginning to plateau only during the onset of material extrusion. This is expected due to the halting of densification at the extrusion point in favour of plastic flow. This clear increase in stiffness demonstrates a change of the material response with compression, which we attribute to collapse of free volume and densification of the material as it is compressed due to the constraints imposed by the layer compression test. Substrate stiffness and contact aspect ratio are both in line with that required for close uniaxial strain approximation as demonstrated in Chapter 4, with a correction added to the displacement to account for substrate deformation. As well as this, confined compression has been demonstrated in detail for this contact condition on glassy polymers in the past [31, 35]. This demonstration of pressure dependency in LCT indentations on thin film PS show clearly the presence of such effects on amorphous films and calls into question the degree to which such affects can manifest in thin films of other amorphous materials.

5.3.2 Pressure Dependent Stiffness of Graphene Nanosheet Network

While demonstrated above on PS, similar effects are expected to manifest in a range of amorphous films that have large degrees of free volume, owing to the densification process. While glassy solids such as polymers experience pressure dependent effects due to a reduction in internal free volume between entangled polymer chains, nanosheet network films exhibit void spaces many order of magnitudes larger. As well as this, the fundamental nature of a vdW bonded platelet system is quite different to that of long entangled polymer chains. To what extent the pressure dependent nature of the nanosheet networks can be compared to the PS case is presented in this section.

Analysis is presented here on graphene sample *II* (6.3 µm film thickness, average sheet length 300nm, average 8 layers thick), which was indented with a 55 µm diameter diamond punch (contact aspect ratio 8.7:1). Unlike atomic polymer chains that may thermally rattle in their free volume cages, these large flakes are expected to have negligible thermal motion relative to void sizes between the flakes owing to the large component of the attractive vdW forces compared to $k_B T$ (see Section 1.3, Chapter 1). Sprayed nanosheet networks present many challenges to rigorous nanomechanical testing, with two effects in particular causing significant difficulty for the LCT. Firstly, the high surface roughness of these networks interferes with the required uniform stress field applied by the LCT and also introduces local plastic deformation of surface roughness peaks before full punch contact. Secondly, the soft granular platelet nature of this system means it can experience both solid behaviour (in this case attributed mostly to the bending of individual flakes), and more liquid like deformation at longer timescales as the flakes can slide and rearrange within the compressed volume [63]. This viscoelastic behaviour will be explored in more detail in Chapter 6. This is exacerbated by surface roughness where initial deformation can be dominated by rearrangement of flakes on the rough surface, masking the bulk response of the puck. While more in depth characterisation of the mechanical nature of the films under out of plane compression is presented in Chapter 6, here I describe only the methodology required to observe the evolution of stiffness with pressure in a similar manner to that presented for PS.

To avoid the issues described above and to reduce the response of the network to a more clearly definable state, a series of irreversible pre-conditioning indentations were performed on the region of interest. This was done by performing 4 iterative indentations in the same location to a maximum load of 5 mN (2.1 MPa) with a constant loading rate of 0.05mN/s and a holdtime of 5s at max load, the load vs displacement curves of which are presented in Fig. 5.8. This evolved the network to a steady state in which uniaxial compression may be isolated without interference of surface roughness and a minimisation of granular flow. This establishes a well-defined geometry and framework for mechanical analysis while maintaining the qualitative nature of a porous flake network. It also has the added benefit of ‘delaying’ material extrusion until 5mN (as opposed to ~2.5mN on unpatterned film), which allows for a clearer examination of the pressure/density dependent stiffness to higher strains. While I acknowledge that this pre-patterning has some effect on the films mechanical properties compared to unpatterned film, more careful analysis of mechanical effects will be instead explored in Chapter 6. Of interest here is clarifying the densification process and isolating the response of the network to a uniaxial compression.

In the first of these curves can be seen the inflection caused by extrusion, as well as a large inflection following contact that is indicative of surface roughness. We can discount this inflection being a result of tip misalignment via indentation on exposed gold substrate, which shows a misalignment in the order of ~50 nm. The result is also consistent with surface roughness found via FIB-SEM tomography of the networks (see Chapter 6 and 7).

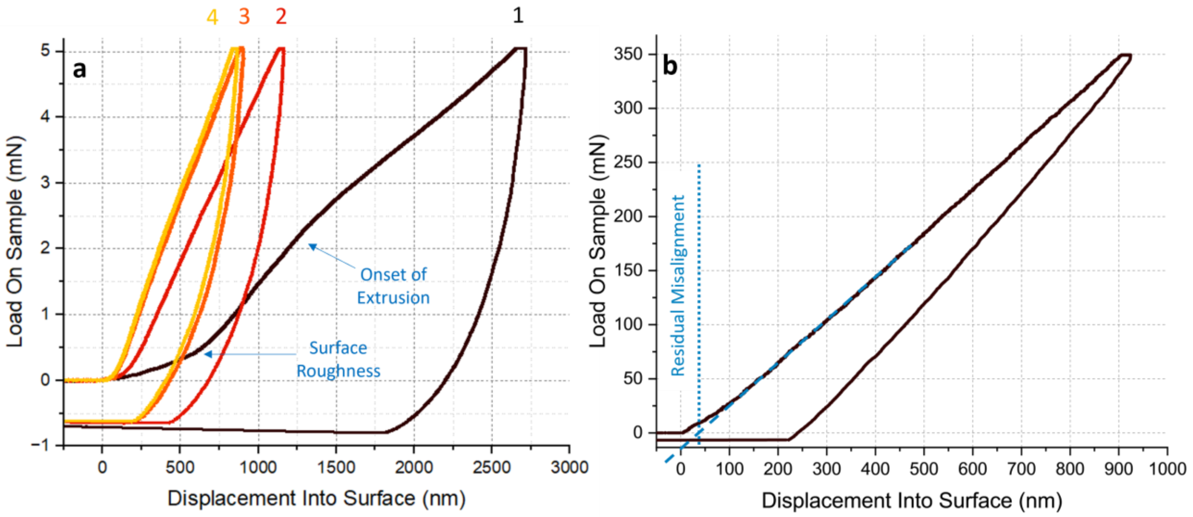

Fig. 5.8, (a). *Pre patterning of graphene Sample I to probe pressure dependent effects, consisting of four successive indentations to 5mN in a single location to remove surface roughness and evolve the system to a steady state with minimal granular motion. Indentation order is numbered and 'displacement into surface' is measured from the zero strain point of each individual indentation. The initial inflection on the first indentation is indicative of surface roughness and not tip misalignment, as* ***(b)*** *shows an indentation on the gold substrate, revealing sub 50nm misalignment*

Following the pre-patterning indentations, a single further indentation was performed to peak load 6 mN (2.52 MPa) with a loading rate of 0.06 mN/s. The simultaneously collected load vs. displacement and harmonic contact stiffness vs. displacement curves for this are shown in Fig. 5.9 in the same manner as for the PS sample. The same procedure for Harmonic Stiffness as outlined earlier is followed, with the exception that oscillation amplitude was increased to 2.5nm for clearer data collection on such a disordered and granular system. Due to the pre-patterning, there is no tip misalignment zone present in this instance. Instead there exists a small zone proceeding zero strain where the indenter adjusts to sudden contact with the pre-patterned surface and resulting large stiffness discontinuity from free space, manifesting as a settling time in the harmonic stiffness channel. Beyond this there exists a clear increase in the harmonic stiffness with applied pressure, increasing in a linear manner with strain from 20 kN/m up to 29 kN/m, a 45% increase. Similar to that observed in polymers in the LCT and other elastic-plastic materials in US geometries, there is then a clear kink in the load-displacement and harmonic stiffness data, which I nominally label yield here, although the exact interpretation of this transition in this material, and its relation to a traditional elastic to plastic yield point will be explored in Chapter 6. Similar to what we see for polymers, this kink demarks a second region of stiffness increase with a lower constant slope. The rise continues until the onset of material extrusion at 5mN, which is defined by the pre-patterning conditions as opposed to the fundamental confinement parameters of the material and contact geometry.

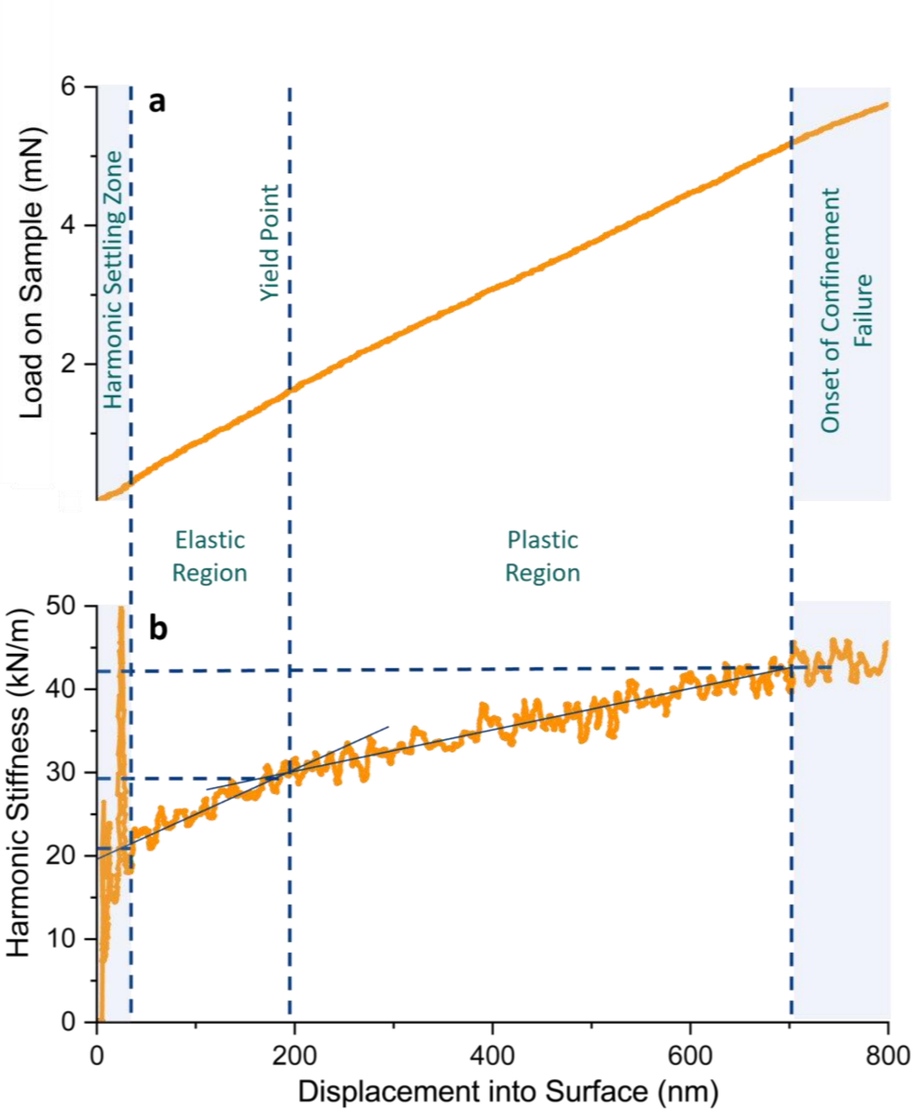

***Fig. 5.9**, **(a)** Load vs displacement and continual harmonic contact stiffness (CSM) data **(b)** of an LCT indentation on a 6.3 μm thick graphene network film indentation on a glass substrate with a 55μm diameter punch. Between the region of full contact and plastic yield, we observe a 45% increase in the stiffness, indicative of the modulus of the material being altered by applied pressure.*

As with the case of PS, I interpret this increasing stiffness as a signature of a pressure dependent modulus of the compressed puck caused by densification. In polymer glasses, this is caused by collapse of free volume existing between polymer chains that was left according to the specific preparation history of the sample. In the nanosheet network, the stiffness increase is also caused by a densification, but through collapse of much larger void space between flakes, with molecular changes only manifesting in the folds of the bending sheets and contributing little to the overall density. This increase in stiffness may originate from increased contact number between particles in a densified film [74], or from altered bending angle of sheets in a less porous system [248]. The means of deformation in these films will be explored in Chapter 6.

We note the similarity in pre-yield stiffness increase in both PS and the graphene network despite very fundamental differences in material and morphology (~45% increase from contact to yield). This is in line with other elastic – yield relations between otherwise very different amorphous materials, such as a universal relation between the ratio between yield stress and Young's modulus for otherwise very different amorphous materials [174]. In addition to this there is traction behind the idea that disordered solids share a mechanism of plasticity nucleation even between fundamentally different systems [172, 174]. Because of this, while this study represents only two systems of a polymer glass and a spray coated nanosheet network, the similarity in the stiffness increase preceding yield may demonstrate a dependence on densification and free volume collapse fundamental to amorphous media, as opposed to the effect such densification has on more complex processes such as close molecular interaction and chain motions which are not ubiquitous between these materials.

5.4 Probing Densification of Polymers using β-NMR

5.4.1 Nuclear Magnetic Resonance as a Probe of Densification of Polymer Glasses

Nuclear Magnetic Resonance spectroscopy (NMR) is a technique that can be used to observe the local magnetic fields around nuclei [249, 250]. Standard NMR operates under the principle that nuclear spins will orient in an applied magnetic field (B_0). If the field fluctuates at a specific frequency, the nuclei will absorb energy and the spins may flip in resonance with the field. The difference in the spin ½ and –½ energy states can be measured by the absorbed energy and therefore the nuclear environment may be identified (ie, that from the nucleus itself and the surrounding bonding environment).

In this Chapter, we are more concerned with the special case of β-NMR, which relies on measuring the anisotropy in the β decay from polarised nuclei (being that polarised nuclei will not decay in all directions equally and will instead have orientation based on the direction of spin polarisation) [251]. This does not measure a change in the energy as in standard NMR, but instead on measuring the anisotropy in intensity of decay in each direction using scintillator detectors. This gives far higher signal strength than for typical NMR. It is also generally performed by implanting highly orientated isotopes into the host material, which increases the signal strength further. In total, the signal can be many of orders of magnitude stronger than for typical NMR, which allows for measurements in more challenging materials and geometries such as thin films.

In this work ^{8}Li is used due to its low atomic weight and ease of polarisation. Here we investigate the densification of high molecular weight glassy polystyrene using β-NMR analysis. ^{8}Li is quadrupolar (spin I = 2), so in a nonmagnetic host such as PS, the largest term in the spin Hamiltonian aside from the Zeeman interaction with B_0 is the quadropolar interaction with the local field gradient. For implanted ^{8}Li this interaction fluctuates based on the surrounding molecular motions and results in nuclear spin relaxation. In a polymer glass, even though the molecular chain backbone is frozen, spin lattice relaxation of the implanted ^{8}Li may still occur due to a fraction of the phenyl sidechains making ~180^o rotations at sufficiently high frequencies [252, 253] (typically one in ten phenyl rings experiencing such motion [254, 255]). With densification, the available free volume in the PS will reduce, and somewhat limit such sidechain motion. As such, densification should be observable from the decay asymmetry.

5.4.2 Polymer Sample Preparation

Two atactic polystyrene samples of 300nm thickness (1.13 MDa, polydispersity 1) were prepared via spin coating on a sapphire substrate (prepared using a 2.5% wt. PS/Toluene solution). The samples were annealed at 393 K (20 K above the glass transition) for 30 minutes, with a subsequent rapid quench at room temperature. One sample was left unprocessed as a reference, whilst the other was processed via densification described below. The implantation beam size of the β-NMR technique requires a large patterned area, and as such flat punch compression was not feasible with the equipment available. Instead, indentation was done via a polished Si sphere of diameter 1mm and ~2 nm surface roughness (measured via AFM). A 36 x 36 array of indentations were performed with ~83 µm distance between the centre of each indentation for a total patterned area of 3 x 3 mm. Indentations were each performed rapidly to 9N load over the course of 6s, with residual plasticity visible in a ~45 µm radius from each indentation centre, giving a 91.6% plastic deformation coverage of the total 3 x 3 mm region. Fig. 5.10 shows a load vs displacement curve of one such indentation, as well as an AFM trace showing the distance between indentations.

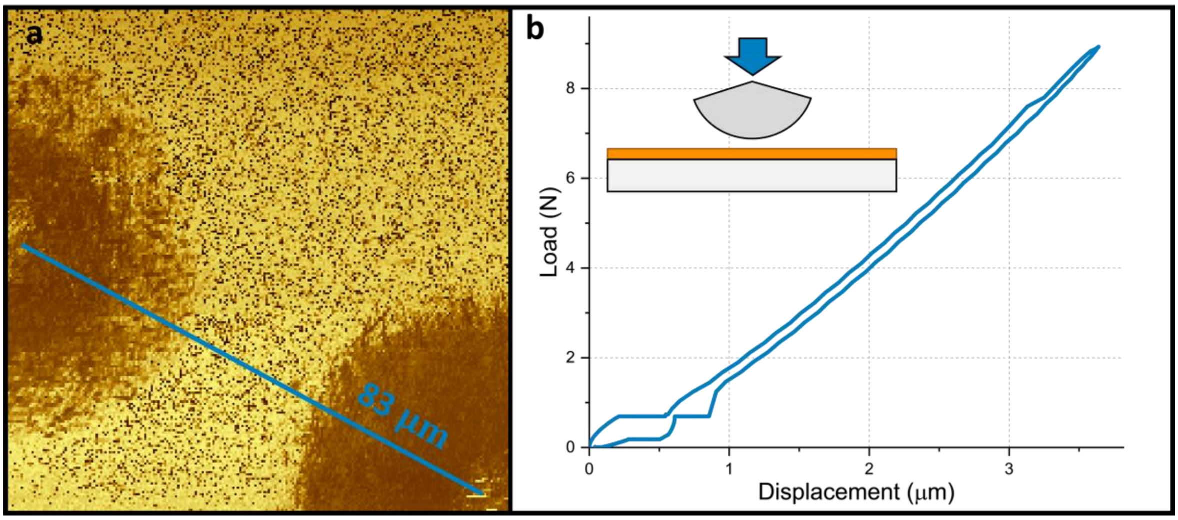

Fig. 5.10, (a) *AFM phase trace of 1mm diameter Si sphere indentation on 300nm Ps on a sapphire substrate, showing distance between indentations in the array. Phase instead of topographical trace is used here for increased clarity. Load vs displacement curve for one such indentation is shown in* ***(b).*** *The large creep portions around 0.65 N in the load and unload are due to the time taken to initialise the high load system, and measurement of thermal drift, respectively. Residual strain is a small fraction of the overall indentation depth due to the large elastic deformation present*

While the load vs displacement curve in Fig. 5.10 displays little residual strain compared to indentation depth, this is in large part due to the large deformation of the Si sphere compared to the low compressive depths reached on the PS sample. The resulting plasticity of the indentations was therefore measured with AFM analysis of the indented region, as shown in Fig. 5.11. The residual depth of the indentation reveals the degree of excess plasticity in each indentation which is in large part due to densification of the film. Estimating the degree of densification of the entire 3 x 3 mm region can be done by estimating a volumetric strain. The shaded orange triangle in Fig. 5.11 represents an area on that graph equivalent to the integrated area between the 0 nm height and the topography line (ie, the compressed area). This can then be integrated around the centre line to estimate the compressed volume, V as follows

$$V = \int_0^{8.2} \pi \left(\frac{45000}{8.2}\right)^2 y^2 dy \tag{5.7}$$

Accounting for the total indented area volume and the 1296 indentations within that area, we can approximate a volumetric strain (V_c) of the region to be tested

$$V_c = \frac{(1296 \times V)}{((3\times10^6)^2 \times 300)} \tag{5.8}$$

This gives a total volumetric strain of 0.00835, or just under 1% volumetric compression.

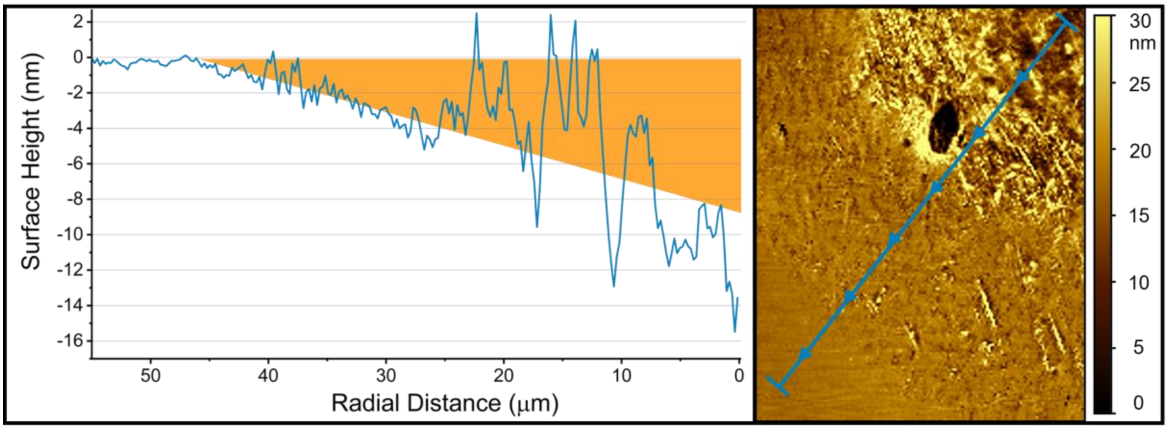

Fig. 5.11, *AFM topography image and trace of an indentation in the array. The shaded orange triangle represents an area equivalent to the integrated area of the depth profile for ease in estimating a volumetric strain*

5.4.3 β-NMR Probing

β-NMR experiments were performed by collaborators at the Isotope Separator and Accelerator facility at TRIUMF, Vancouver. A ~1 mm beam spot of ^{8}Li ions were implanted into the sample with a flux of 10^6 ions/s. Implantation energy was decided based on Stopping Range of Ions in Matter (SRIM) simulations for PS [256]. From this it was found that average implantation depth, z, varied with energy E (in keV) as $z \approx 11.4E$ + 1.4 nm. This allows for implantation depth to be varied and therefore the molecular dynamics at different depths to be explored. A range of implantation energies were used to probe the relaxation as a function of depth. A static magnetic field of $B_0 = 6.55$ T was applied perpendicular to the surface (ie, in parallel with the beam), for an NMR frequency of 41.275 MHz, such that the decay would be in parallel or antiparallel with the field and beam direction. Both these directions were monitored to observe the anisotropy. Measurements were performed at 300 K, and the beam pulse was 4s in duration. Measured spin lattice relaxation data on the unpatterned control sample was typical of PS, with a difference in the decay asymmetry present in the patterned film as a function of time as evidenced in Fig. 5.12, which shows the asymmetry at an implantation energy of 12 keV (corresponding to ~140 nm depth, or approximately half the film depth).

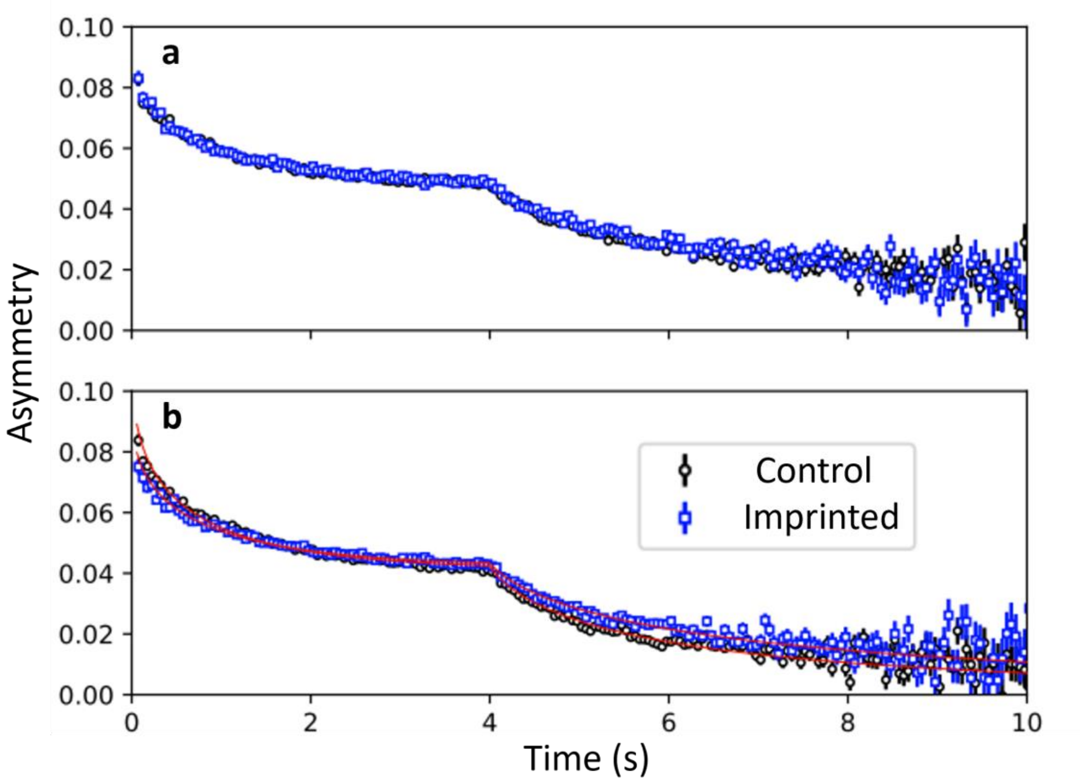

Fig. 5.12, *Spin lattice relaxation asymmetry for imprinted and control PS samples using 4s pulsed of implanted ^{8}Li at 300 K in a 6.55 T magnetic field.* ***(a)*** *shows relaxation data for the control film only (blue and black) at two 10 keV runs separated by 8 hours to show reproducibility of the results.* ***(b)*** *shows a comparison between imprinted (blue) and control (black) runs at 12 keV, which displays a small but clear difference in the decay asymmetry of the imprinted sample*

The polarisation of the implanted ^{8}Li as a function of time $t > t'$, where t' is the implantation time, is assumed to follow the following stretched exponential

$$p(t,t') = p_0 e^{-\left(\lambda(t-t')\right)^{\beta}} \tag{5.9}$$

Where λ is the inverse of the average relaxation time, T_1, and β is the stretching exponent typical of any stretched exponential function and ranging typically between 0 and 1. The average relaxation time can then be expressed as [257]

$$\frac{1}{\langle T_1 \rangle_\beta} = \lambda \frac{\beta}{\Gamma(1/\beta)} \tag{5.10}$$

Where Γ is the gamma function. This allows the plotting of the relaxation rate $1/\langle T_1 \rangle_\beta$ as a function of the implantation depth for the range of implantation depths explored, which is shown in Fig. 5.13. The sharp rise at low depths is due to enhanced mobility at the surface, which is expected from previous measurements of PS as shown by the green curve representing work by McKenzie et al. [252]. The differences between this work and McKenzie's we attribute to differences in sample preparation and history, which as discussed in Chapter 1 has a large influence on amorphous material morphology.

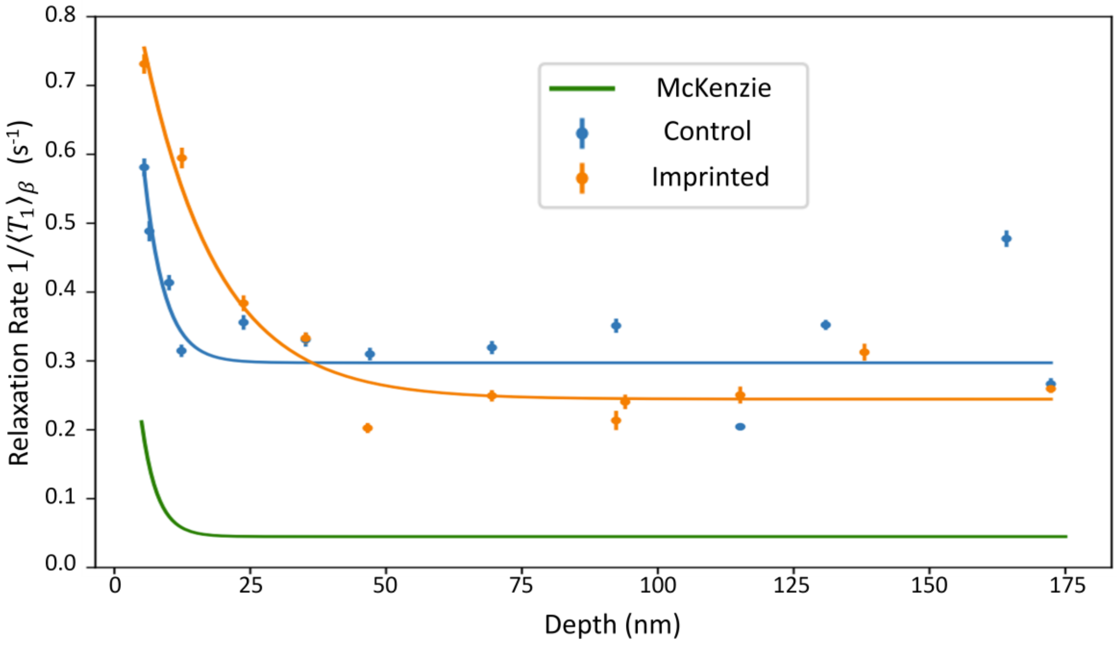

Fig. 5.13, *Relaxation rate as a function of implantation depth for the range of implantation energies tested. An initial high value region associated with increased surface mobility rapidly plateaus to a constant value beyond the first ~10 nm. This is consistent with previous work by McKenzie et al. [252] shown here in green. The difference between this work and McKenzie's is likely due to differences in sample preparation that can have profound effects on polymer glass morphology. The surface peak is extended for the patterned sample due to the surface roughness introduced by the sphere indentations. Beyond this region there is a clear ~16% difference in the relaxation rate between the patterned and control samples, indicative of reduced sidegroup mobility*

This surface related phenomena is starker and continues to higher depths for the imprinted sample which is to be expected given the degree of surface roughness introduced by the imprinting process, as evidenced in the AFM trace in Fig. 5.11. Accounting for this roughness is beyond current capabilities and so inferences about the densification cannot be made in these surface regions. At deeper indentation depths, however, where the data (fit with a least-squares method) has plateaued beyond surface effects, there is a clear difference in the relaxation time between the patterned and control samples, which regress to 0.244 s^{-1} and 0.297 s^{-1}, respectively. This corresponds to a ~16% reduction in the relaxation rate caused by the patterning of the sample, which we attribute to densification of the material and reduction in phenyl ring motion caused by reduced free volume.

5.5 Conclusion

We have presented observation and means of probing pressure dependent mechanical and molecular dynamic nature of deformed thin film amorphous materials, through both the layer compression test, and through β-NMR spectroscopy of imprinted films. The uniaxial strain state approximation imposed by the LCT allows for the exploration of pressure dependant mechanical effects in amorphous thin films, and we have explored this through analytical and finite element exploration of pressure dependant mechanical properties on amorphous materials in true uniaxial strain, and through experimentation of amorphous thin films through the layer compression test as follows.

Using the layer compression test, I report the observation of increasing material stiffness with densification in both elastic and plastic deformation for two amorphous thin film materials with largely differing morphologies; polystyrene and an exfoliated graphene sheet network. Similarities were found between these materials in the degree of stiffening before plastic yield, despite their large morphological differences. This may suggest some shared characteristic between strain hardening and yield for amorphous media, in line with previous observations of a shared modulus / yield relation in such systems.

We also report observed yield in thin film PMMA, a material which has previously been found not to yield under bulk compressive uniaxial strain conditions. I attribute this to the generation of additional shear during the layer compression test propagating primarily from the punch corners, allowing for the shear generation to surpass the yield surface criteria despite a strong pressure dependency of the yield criteria for PMMA. The non-uniformity in strain, introduced by shear injection in the LCT, does not mask the collective yield behaviour typical of a US yielding event, allowing analysis of confined yield in materials such as PMMA where this may otherwise be challenging. As the degree of shear generation is tailorable via the contact aspect ratio and substrate stiffness, as explored in Chapter 4, the LCT may allow for explorations of the elastic – plastic transition in other such materials that are difficult to yield in such confined geometries.

Densification of amorphous polymer glass (atactic PS) was probed via large area patterning via spherical indentation, and subsequent probing using β-NMR spectroscopy. This was performed by implantation of ^{8}Li ions, aligned in a magnetic field, and observing asymmetry in the decay of the ions, which is influenced by phenyl side group motion in polymer glasses. This revealed a ~16% reduction in the relaxation rate with a > 1% volumetric densification of the film, attributed to lowered free volume resulting in reduced side group mobility.

These results show the promise of probing densification effects in small thin film geometries and open the way for further exploration into the morphological characteristics that influence mobility and mechanical properties of amorphous films.

Ch 6 : Compressive Mechanical Properties of Nanosheet Networks

Preface: The work presented in this chapter has in places been integrated into the text based on, and adapted from, work published by the author in *Mechanical Properties of Conducting Printed Nanosheet Network Thin Films Under Uniaxial Compression,* Advanced Materials, in press.

The dependence of the electrical response to nanosheet network films, as well as their potential use in wearable electronics, necessitates a strong understanding of their compressive mechanical nature that has been sorely under explored in the current literature. This is in no small part due to the difficulty in performing conventional nanomechanical testing on these very soft thin films. The surface roughness, anisotropy, granular nature, locational inhomogeneity and thin film geometry each individually constitute extreme challenges for established nanoindentation techniques, and combined present a material for which analysis via standard indentation techniques would require extreme analytical and experimental progress to overcome. Many of these issues are mitigated (or at least reduced) by the large contact area and uniform strain field induced by the LCT. This opens up the possibility of exploring the low strain compressive mechanical response of such materials for the first time. In this chapter, I utilise this technique to explore out-of-plane elastic, plastic, and creep deformation in these systems. Doing so I extract properties such as elastic modulus, plastic yield, viscoelasticity, tensile failure and sheet bending vs. slippage under both out of plane uniaxial compression and tension. I approach these for the range of graphene networks *I* through *IV* utilised in this thesis, as well the effect chemical cross linking of MoS_2 networks has on the response.

6.1 Berkovich Indentation of Graphene Nanosheet Networks

For demonstration of the incompatibility of these networks with traditional nanoindentation techniques, initial indents were performed with a Berkovich tip. Such indents on an anisotropic film may not be solved analytically due to the Oliver-Pharr method for extracting Young’s modulus assuming an isotropic material [8] (see Chapter 3). Adapting a model to account for the anisotropy and allow for extraction of Young's modulus using a Berkovich tip would involve significant theoretical complexity, given that the groundwork for the Oliver-Pharr method extend as far back as Hertzian contact mechanics of elastic isotropic half spaces in the 19th century [216]. Such an undertaking was quickly ruled out given the nature of the networks incompatibility with sharp indentation testing even if anisotropy could be accounted for, owing to the geometric complexity discussed above. To demonstrate and verify this, initial Berkovich indents were performed on a sprayed graphene sample. The sample used was a precursor sample, prepared via the LPE method discussed in Chapter 1, with a mean nanosheet length of 620nm, average sheet thickness of 15 layers, and film thickness of 6.8 µm. This sample was not utilised for further testing due to issues with available indent area and deposition issues, as such it is not included in the LCT tests of sample *I* through *IV,* though was prepared using the same technique and is functionally comparable.

Load vs displacement curves of three Berkovich indents to a depth of 3000nm are shown in Fig. 6.1 (a) below. Indents were performed in the same sample locality (within ~500 µm of each other) with a constant loading rate over the course of 100s and a hold time of 5 s at maximum load. As can be seen, there is extreme variance between the indents due to location dependant morphological differences between sample locations, even within the same locality. This alone would preclude mechanical analysis without significant statistical averaging. The degree of morphological variance can be seen also in the step-like patterns throughout the load vs displacement curves (for example most prominently at ~1200nm depth on the orange curve), which I attribute to large collapsing void space as the tip encounters large porous regions.

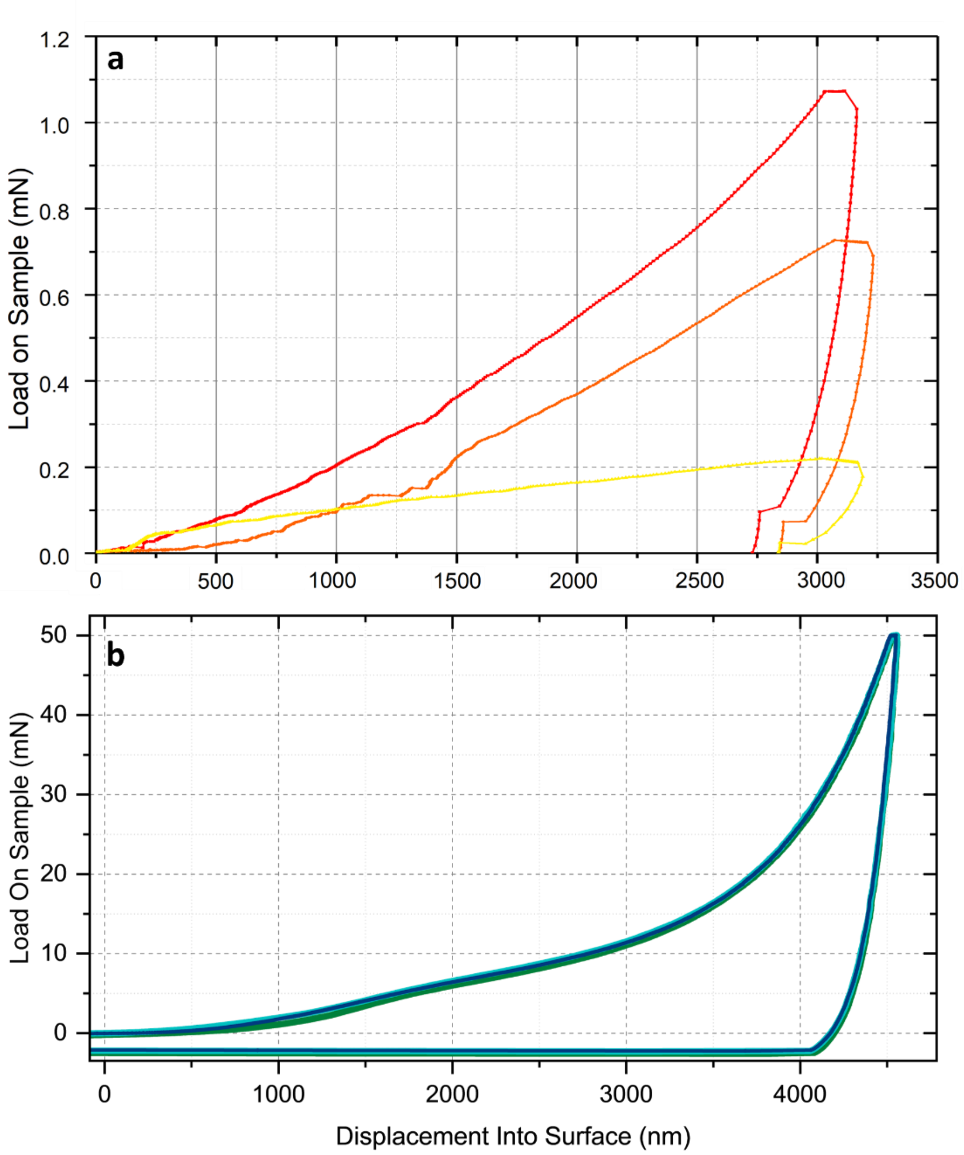

Fig. 6.1, (a) *Load vs displacement curves for three Berkovich indents on a 6.8µm graphene network thin film. Each of the colours presented (red, orange, and yellow) represent a separate Berkovich indentation in the same sample locality of the graphene network described in the main text. Large locational inhomogeneity is clearly evident, as well as influence from porosity which can be seen in the step patterns particularly at lower indentation depths.* ***(b)*** *Displays the load vs displacement curves for three indents on Sample II with a 55 µm diameter flat punch using the layer compression test technique. The large compression area averages out much of the inhomogeneity allowing for repeatable mechanical analysis.*

As well as this, the surface roughness makes a fractional depth difficult to determine with sharp indentations, as well as complicating the surface area contact between the tip and sample needed for mechanical analysis. With this in mind it was determined that LCT indentations would be better suited to probe the mechanical nature of these networks, removing or reducing the influence of many of these issues.

Fig 6.1 (b) displays three indents to a maximum applied load of 50 mN performed on different sample locations on Sample *II* using a 55 μm diameter flat punch and the layer compression test technique. As can be seen, the large compression area averages out much of the mechanical inhomogeneity, resulting in repeatable load vs displacement behaviour that can be used to extract mechanical properties representative of the bulk network. There exists some small deviations still at low loads caused by the high degree of surface roughness present in these networks, which will be approached in a later section.

6.2 LCT of Nanosheet Networks

Layer Compression Test experiments were performed on nanosheet networks *I* through *IV* as well as the MoS_2 samples outlined in Table 1, using the same 55 µm diameter diamond flat punch tip utilised in Chapter 5. Unless otherwise stated, all indents were performed with a constant loading rate over the course of 100s, with a 5s hold time at maximum load, utilising the phase angle surface determination technique as outlined in Chapter 3 for determining surface contact. After the held peak load timeframe, the tip retracts off the surface at a constant rate of ~ 0.2 mN/s until detachment from the surface. As mentioned above, traditional nanoindentation techniques struggle to accurately examine supported thin films, and nanosheet networks present a particular set of new challenges compared to traditional hard materials. Much of these challenges may be somewhat mitigated by the LCT but it is important to be aware of the limitations that still exist in comparison to more homogenous traditional films.

A typical indent on a sprayed LPE graphene sample (Sample *I*) is shown in Fig. 6.2 (a). As discussed briefly in Chapter 5, the features of the stress vs. strain curve are comparable to those seen in LCT results for solid polymers and other soft supported films: an initial compression with minimal lateral strains to large indentation depth followed by extrusion of material as the surrounding film fails to confine the material under the punch [33, 258]. In our nanosheet samples, material extrudes outwards from under the punch and a ring of extruded material becomes visible around the indent at ~0.13

strain. Fig. 6.2 (b) and (c) display indents without and with this ring of extruded material before and after this inflection point. As extrusion is still characterised by a distinct inflection in the stress-strain curve and a subsequent ring of extruded material as is the case for other amorphous materials, I can conclude that extrusion still occurs in a defined event and 'leakage' into the surrounding film is low over short timescales.

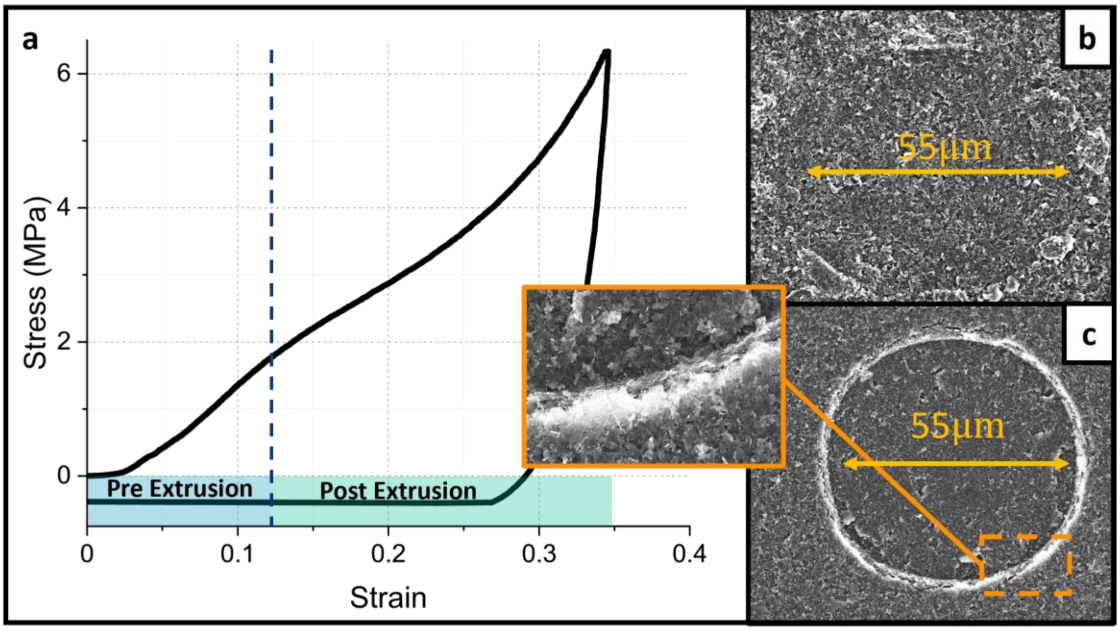

Fig 6.2, (a)** Contact stress vs strain for an LCT indent with a 55 μm punch on Sample II, showing clearly an extrusion inflection. SEM images on the networks reveal that ring of extruded material is not present for indents with a maximum load below this inflection, shown in **(b)**, but is present for indents above this point as shown in **(c)

Understanding the features present in this stress-strain curve is the first step to understanding the mechanical behaviour of these films, particularly in the pre-extrusion regime, where the comparison to a uniform compressed puck of material in a uniaxial strain geometry still holds. It should be noted that although the x-axis displays strain, this only holds for indentation depths below the extrusion point. A stress vs strain curve of a lower strain indent on Sample *II* is shown in Fig. 6.3 to highlight this pre extrusion region, with the features outlined below.

In the region between zero-strain to ~0.06 strain is a concave inflection. On flat, smooth surface samples such an inflection is often the result of initial incomplete punch-sample contact due to a residual misalignment between the tip face and sample surface [259]. We can determine that this is not the case here however, as indents on regions of bare gold substrate on each sample determined that sample misalignment corresponds to < 0.01 strain only (see Fig. 5.8 (b)). Thus, I attribute this curved region to innate nanosheet surface roughness, which causes increasing contact area and therefore stiffer contact as the surface roughness portion is compressed. While the large contact area of the punch helps to mitigate the effect of local surface roughness, variations still exist at the lowest strains due to the high degree of inherent surface roughness. SEM inspection shows average surface roughness in the range of 10% of the total thickness, shown in Fig. 6.3 (b), with modest local changes.

As the contact area increases throughout the portion of surface roughness, we stabilize to a near-linear rising slope typical of LCT indentations after this portion has been bypassed and the tip is in full contact with the sample. The kink in this slope indicative of inelastic yield in amorphous systems such as polymers is largely masked by this surface roughness portion for a large portion of indents on the nanosheet networks explored. Regions with lower surface roughness show the typical features of a LCT indent on an amorphous film beyond the initial surface roughness portion, as shown in Fig. 6.3. These include a linear region beyond zero strain of constant slope indicative of elastic deformation, a distinct change to a new slope (here at 1.08 MPa) typical of the yield point in elastic-plastic films followed by a second linear region of plastic deformation, followed finally by the extrusion event where the confinement of the technique breaks down. These regions are highlighted more clearly in Fig 6.3 (a).

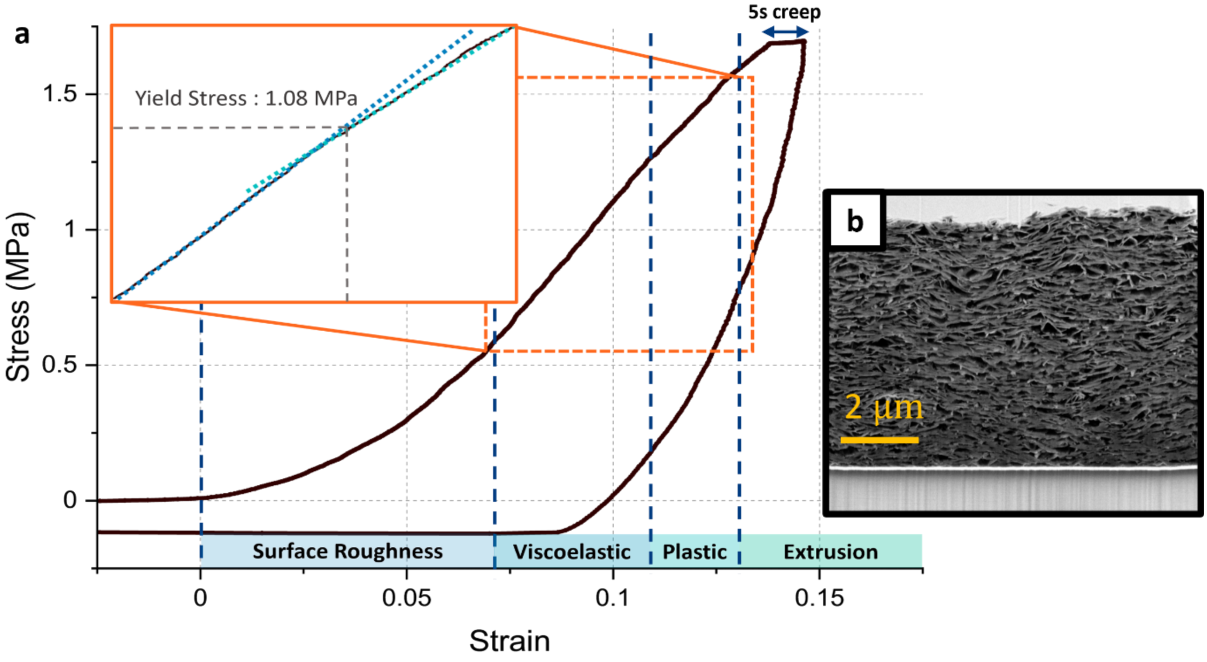

Fig 6.3, (a) *Stress vs strain curve for an LCT indent with a 55 μm punch on Sample I, demonstrating regimes of interest including a significant surface roughness effect, as well as a kink at 1.08 MPa reminiscent of a yield transition on elastic-plastic films. Surface roughness inflection is in line with the surface roughness observed in SEM cross sections of the same sample, as shown in* ***(b)***

Following loading, we observe a mild creep behaviour over 5 s hold at peak load (observable from the flat portion of increasing strain with no corresponding stress increase at the end of the loading portion), which is a significant feature I will discuss later. Towards the end of unloading, the residual strain as we cross back over zero stress during unloading represents the degree of inelastic deformation present, here at ~0.1 strain (purely elastic processes resulting in zero residual strain). At the end of unloading, we observe a negative tensile force rather than a return to zero stress, indicating significant adhesion between the diamond punch and compressed graphene nanosheets, which will be used for tensile measurements in a later section. While I have compared the regions present here to elastic and plastic deformation separated by a yield kink as has been explored previously on polymers, it is prudent to demonstrate such elastic-plastic behaviour on these networks more rigorously.

6.3 Demonstrating Viscoelastic-Plastic deformation

While these features seem to mirror typical elastic – plastic behaviour observed in amorphous solid films such as polymers, for a system of granular vdW bonded platelets, a determinable singular yield point as in more traditional materials has not been a foregone expectation, with a more continuous plasticity mediated around weaker, more disordered flake centres being a distinct possibility [260].

Disregarding artifacts of initial incomplete punch face contact, the initial portion of LCT indentation around zero strain will be dominated by recoverable elastic or viscoelastic processes in solid materials. However, this is reliant on uniform surface contact, which is possible on flat films deposited, for instance via chemical vapour deposition or spin coating. On the sprayed nanosheet networks, the large degree of surface roughness and creep (large relative to typical viscoelastic solids) complicates this low strain response. Initial contact with surface roughness peaks causes small scale local plasticity in the lowest strains, as the punch plastically deforms the local peaks before making full contact with the film at large. In low peak stress load-unload curves this results in immediate plastic hysteresis and residual strain associated with this local geometry, masking any global pre-plastic processes of the full compressed puck under the punch that may be present. As discussed above, in regions of extensive surface roughness, the curvature from zero strain associated with surface roughness may also be extensive enough to mask the yield kink entirely.

For these reasons, in order to best display the nature of the yield transition and demonstrate the viscoelastic-plastic nature of the networks, removal of surface roughness is required. This is done by pre-patterning the region of interest with a series of initial indents performed at the same load in a singular location, as shown in Fig. 5.8. Reiterating the benefits here from Chapter 5, such a strategy is exploited for several reasons:

- Firstly, it removes surface roughness that would cause local surface plasticity and mask viscoelastic deformation.

- Secondly, it evolves the film to a mechanical steady state which allows for demonstration of pre and post yield behaviour through successive in place indents after the shakedown, free from the effect of further strain hardening and excess sheet slippage between subsequent indents. It allows this in a single sample location which is of benefit due to mild inhomogeneities in surface thickness and morphology between locations that may obscure the finer details of viscoelasticity and yield.
- Lastly, it delays the onset of material extrusion to the max stress of the pre-patterning step in order to better show the plastic response post-yielding and pre-extrusion.

Though the patterning has benefits for demonstrating the low strain and yield behaviour as described above, it also causes other mechanical / morphological changes such as strain hardening, which is evident in the increasing slopes between indents in Fig. 5.8. This is expected from the degree of densification involved in such a process. While the same constitutive features exist in the stress vs strain curves for unpatterned regions of the film, this no longer represents an as-received film. It is therefore important to note that the extensive pre-patterning as described here is used only to demonstrate the viscoelastic – plastic nature of the networks in this section and is not used for the determination of properties such as modulus or yield stress in later sections. Any pre-processing that is applied for determining such properties is employed only when necessary and is kept minimal to avoid evolving the film away from the received state, and will be made clear in the relevant section.

This pre patterning was done on Sample *II*, and following the pre-patterning step, a series of incremented indents, starting with an indent at 1mN (0.42 MPa) with subsequent indents successively increasing the peak load by 0.5 mN, was performed on the patterned location. This gradually increases the applied load between each indent on a singular location, generating a stress vs strain curve for each. This technique can be used to probe an elastic to inelastic transition in the LCT by observing the residual strain after each indent and observing if a change in behaviour is observed at a key stress / strain. For elastic materials, low strain indents will exhibit zero residual strain, which will then grow for indents proceeding the yield point, accompanied by a yield kink in the stress vs strain curve [31]. The stress vs strain curve for these indents is shown in Fig. 6.4 (a) with the lightest initial indents shown in yellow, trending through orange and red as load is increased for subsequent indents. The corresponding residual strain for each indent is shown in Fig. 6.4 (b-c) for two definitions of residual strain; the point where the unload crosses zero stress, and the point where the tip detaches from the sample. Both give consistent results. The colour of the datapoints in Fig. 6.4 (b-c) correspond to that extracted from the corresponding coloured curve in (a), though they may also be related by the peak strain as plotted on the x-axis.

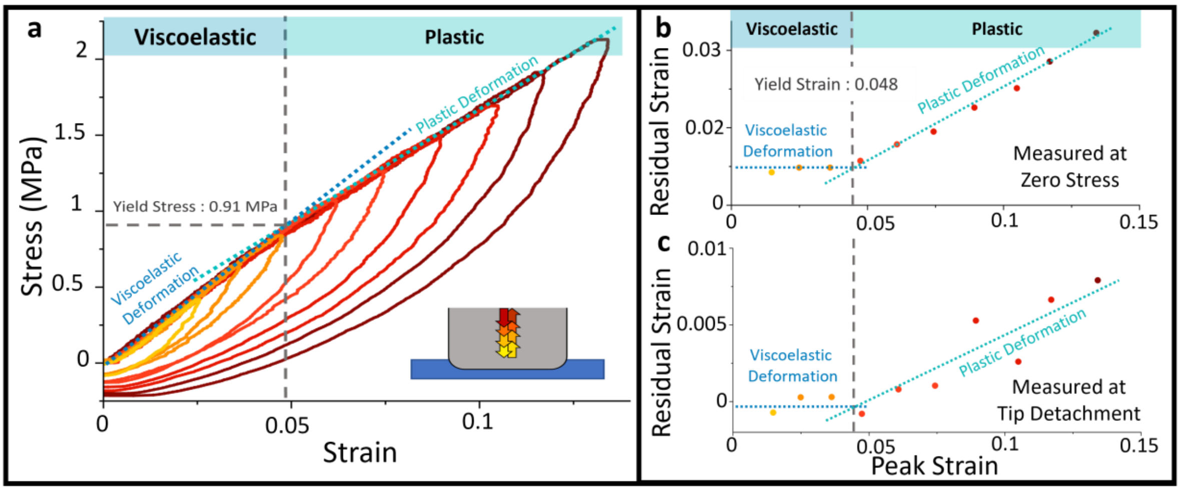

Fig 6.4, (a) *Stress vs strain curve for the incremented LCT indents on the patterned region of Sample II. A kink is apparent at 0.91 MPa. Indents beyond this maximum load display a sharp change in the residual strain behaviour from a constant value to a gradually increasing residual strain, indicative of an elastic-plastic transition*

For the lowest stress indents, the network displays viscoelastic behaviour. This manifests as a hysteretic unload with a constant residual strain value independent of applied stress. The viscous portion of the response manifests as the non-zero residual strain in low strain indent. Creep behaviour when holding the load constant is also observed, another feature of viscoelasticity which will be explored in more detail later. For indents beyond a certain critical stress, the response is observed to switch sharply, whereby increasing maximum stress imposed on the sample results in a steady increase in residual strain post unload, and is indicative of material yield. As such we can conclude that the sample exhibits viscoelastic behaviour under uniaxial compression as performed here.

The precise effective yield stress and strain of the yield transition can be determined by a visible kink in the stress strain curve that accompanies this change in residual strain response. As discussed above, this is a feature of uniaxial strain and is observed in LCT indents for amorphous elastic-plastic materials and we can conclude that this determinable kink does represent a point of distinct inelastic yield in these films, and that the slope of the stress vs strain curve before this yield transition therefore represents an effective viscoelastic modulus. This slope change has also been observed to be accompanied by a change in material stiffness with compression in the same manner as amorphous polymer glasses as demonstrated in Chapter 5. As the material is morphologically and mechanically anisotropic, this must be accounted for before a comparison between the measured modulus and Young's modulus may be made.

6.4 Anisotropic Considerations

While Eq. 2.17 and 2.35 describe the confined modulus and yield point for amorphous films, they hold only for homogenous, isotropic materials. These networks composed of semi-aligned 2D nanosheets are subject to transverse linear isotropy, whereby the semi aligned nature of the sheets causes a difference in mechanical properties between the orthogonal in-plane directions, and the third out of plane direction in a standard cartesian coordinate system. This requires that the elastic analysis of strain for the LCT to be re-approached with this in mind. Our analysis for this has been presented in Section 2.2 in Chapter 2, which deals with the effect of this form of anisotropy on the elastic response to confined uniaxial compression. It concludes that the stress in the loading direction reduces to

$$\sigma = \varepsilon \frac{(\nu-1)(E')^2}{(\nu-1)E'+2E(\nu')^2} \qquad (6.1)$$

Where $E = E_{22} = E_{11}$ is the in-plane Young's modulus, $E' = E_{33}$ is the out of plane Young's modulus. $\nu = \nu_{12} = \nu_{21}$ is the in-plane Poisson ratio, and $\nu' = \nu_{31} = \nu_{32}$ is the out of plane Poisson ratio (see Chapter 2 for more detailed definition of these parameters).

While for an isotropic material we can extract Young's modulus E and Poisson ratio ν from a single loading curve by measuring M and K through the pre and post-kink slope respectively (see Chapter 3), this is not possible for an anisotropic material like this, due to the splitting of these parameters in the anisotropic planes and the presence therefore of two moduli E and E', and two Poisson's ratios ν and ν'. Even though the stress vs strain curves appear to be similar once surface roughness is accounted for, the slope of the stress vs strain curve in elastic compression for this anisotropic case is presented by the more complex parameter in Eq. 6.1, as opposed to that presented in Eq. 2.17. It remains beyond the capabilities of current mechanical testing techniques to accurately determine both the in and out of plane Poisson ratios and Young's moduli needed to characterise this parameter in a thin film material.

In the absence of a means of direct measurement of these parameters, we observe that the deviator term in this expression is the denominator term $2E(\nu')^2$, whereby as this approaches zero, the expression approaches $\sigma = E'\varepsilon$. While ν' is not measured in this work, there are expectations on its value based on closest analogues. Materials with high porosity tend to have low Poisson's ratios [261], with materials with more elliptical pores (as in this material) being lower again than for circular pores [262]. Closest experimental comparison can be found with semi aligned clay/shale stackings, which share in the semi aligned sheet network nature with the same anisotropic condition. For these, it is found that $E \approx 0.5E'$ (depending on alignment) and ν' is low in the regime of alignment interest for this work [263]. With these as reference, we may expect the deviator term to be small compared to the other terms due to its squared power scaling, resulting in a measured effective modulus from a stress-strain slope being within an acceptable range of the true Young's modulus (≤15% deviation using conservative values from these geomechanical systems [263]).

In support of this is the relationship between measured modulus and yield point in this work, shown in Fig. 6.5, which displays an Ashby chart of the universal relation between Young's modulus and yield point for amorphous solids. The position of our measurements (E' and yield stress) of nanosheet networks on this chart supports the measurements being within a reasonable range of Young's modulus, as it lies along the relation known for amorphous solids.

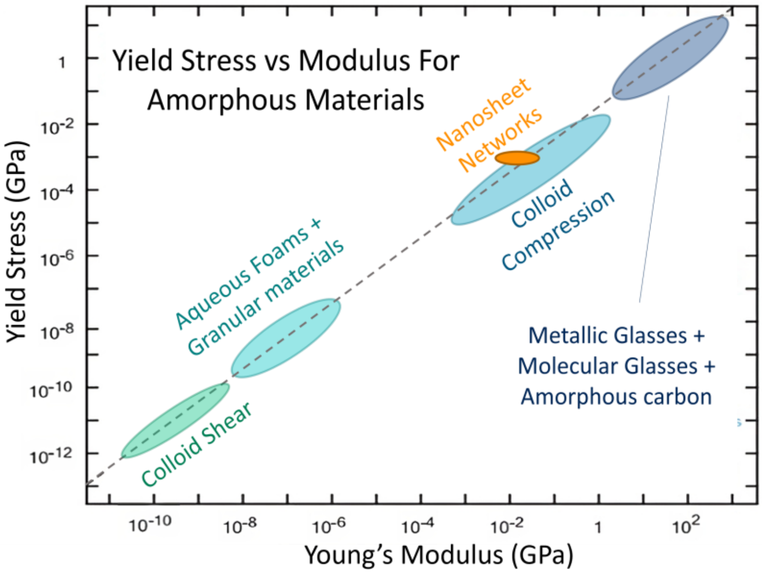

Fig. 6.5, *Ashby chart displaying the universal relation between yield stress and Young's modulus for amorphous materials, for which our measured nanosheet networks show good agreement. This data was adapted from work by Cubuk et al. [174]*

Considering the large degree of variance within such sprayed structures due to spraying differences, sheet size selection, drying effects, and location differences due to inhomogeneity, we may assume variance between two films prepared under similar conditions is of equal or greater consideration as that given by this approximation [131] (for comparison, even well studied amorphous materials vary in Young's modulus by ~30% depending on sample history [50, 51], as discussed in more detail in Chapter 1). As such we can consider our measurement of an effective contact modulus as a reasonable approximation of the out of plane Young's modulus (E'), while we accept that accurate measurement of the out of plane Poisson's ratio is needed for more prudent analysis of specific films.

6.5 Modulus Measurements

6.5.1 Performing Modulus Measurements

As discussed above, the linear pre-kink portion of the stress vs strain curves represents an effective confined modulus that is likely to be within a reasonable estimate of the out of plane Young's modulus,

E'. The residual strain present in the viscoelastic regime I attribute to a sheet sliding (a dissipative process), and the recoverable elastic portion of this regime I attribute to amalgamated sheet bending behaviour within the compressed puck, which is backed up by analysis in this section, but also by comparison with cross linked networks presented in Section 6.9.

In the case of a sample with sufficiently low surface roughness, the modulus may be measured directly from the pre kink slope of an indent excluding the surface roughness inflection (for example the stress vs strain curve in Fig 6.3). For networks of much larger sheets (such as Sample *IV*), surface roughness is typically higher due to spraying limitations and the modulus cannot be measured from a single indent on an un-patterned film. In this case a single pre-patterning indent to remove the surface roughness is performed beforehand, typically to < 0.1 strain. This light pre patterning of the single indent contrasts with the heavier shakedown process used to demonstrate viscoelastic – plastic behaviour in Section 6.3, and represents only minor correctable morphological changes to the network morphology. The pressure dependent study on these networks in Chapter 5 revealed that stiffness increases as the network is compressed, and because of this the strain at which the modulus is measured, as well as any light single indent pre patterning required, must be accounted for. For example, in Fig. 6.3 the strain would be measured only after the surface roughness inflection tapers away at ~ 0.7 strain. This is done by considering a commensurate change in porosity with compression at that point. The measured compressive modulus E' of the graphene networks is in the range of 0.3 MPa to 15 MPa for the graphene films *I* through *IV* explored in this work, with networks of larger sheets displaying lower moduli. As such, factors like porosity and sheet size play a large role in the modulus of the networks. Moduli values can be seen in Fig. 6.6.

6.5.2 Modulus Scaling With Network Parameters

We can explore how the modulus is affected by network parameters by considering how the network deforms under compressive stress. Section 1.9 in Chapter 1 explores the similarity between crumpled sheet mechanics and the deformation of nanosheet networks, which I use here to formulate an expectation of modulus scaling with sheet size and porosity. The work in bending a thin sheet is given by [157, 158, 264]

$$W \approx \kappa N \left(\frac{\chi}{h}\right)^{\frac{1}{3}} \tag{6.2}$$

Where κ is the bending stiffness of the sheets, *N* is the number of folds, χ is the length of the folding ridge, and h is the sheet thickness. For our nanosheets the ridge length is equal to the sheet length; $\chi = l$. As our consideration will be volumetric, and that the nanosheets are likely to form only a single ridge each owing to their size and aspect ratio, we can take N = 1. The bending stiffness of graphene sheets scales with the sheet thickness as a function of the bending angle. For small bending angles the scaling is in the range of $\kappa \propto h^2$ [248], though this will change somewhat as the network is compressed and the bending angle changes. It is however a reasonable estimate for low strain compression. The pressure to bend a sheet will depend on the work divided by the compressed volume and will be directly related to the modulus E' of the network based on the strain contribution of each fold to the network compression

$$P \propto E' \propto W/V \tag{6.3}$$

As we considered this for $N = 1$, we consider the volume occupied by each nanosheet, which depends on the sheet length *l,* thickness *h*, and nanosheet volume fraction ϕ as follows

$$V = \frac{l^2 h}{\phi} \tag{6.4}$$

For liquid phase exfoliated sheets, the average length of sheets scales with the thickness, so we can approximate for simplicity [111]: $l \propto h$, and combining Eqt 6.2 to 6.4 with these considerations, it gives

$$E' \approx \alpha \frac{\phi}{h} \tag{6.5}$$

where α is a constant of proportionality that will depend on the nanosheets. For example, liquid phase exfoliated sheets of graphene will share a comparable α if prepared similarly, but networks of different materials that have different bending stiffness scaling, or different exfoliation techniques will have a different scaling constant. This constant captures several relations, including the scaling constant between κ and h, that from P to fold a single sheet to E' for the network, l to h, and other proportionalities.

The liquid phase exfoliated graphene networks *I – IV* have known zero strain porosities [37] and as such we can plot the measured modulus vs ϕ/h for these networks, shown in Fig. 6.6. The influence of surface roughness inflections, and any required light pre-patterning to remove it, can be accounted for here by considering an equivalent change in ϕ with strain for the corresponding strain where E' is measured from. The relation is appreciably linear as predicted, with small offsets likely due to subtle differences in bending angle (and therefore bending stiffness) between networks of different porosities and sheet thicknesses, or by smaller energy considerations for bowing of sheets separate from the ridge formation approximation in Eq. 6.2 which could suggest a slight power law relation in contrast to the main linear response presented in Eq. 6.5. Should an analytical relation between these parameters be found we could likely improve the fidelity of these results.

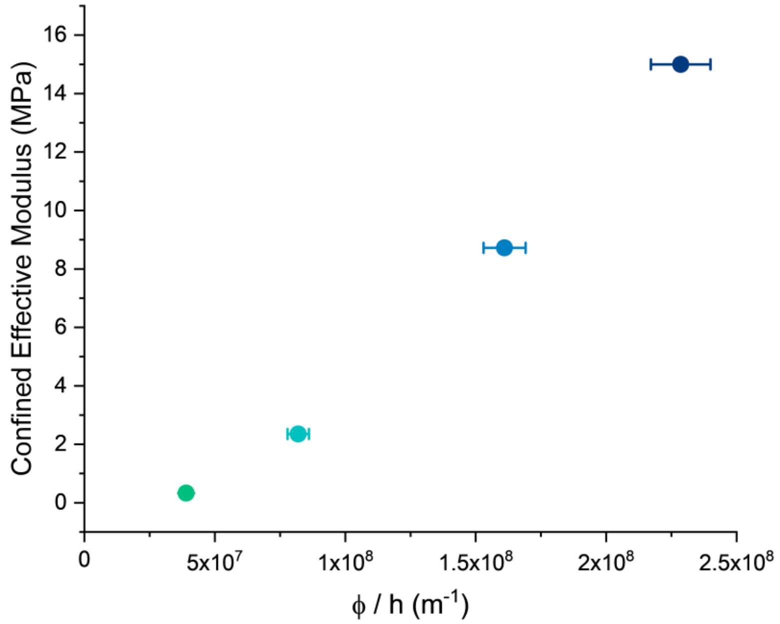

Fig. 6.6, *Measured confined effective modulus of graphene networks I through IV plotted against ϕ/h as per Eq. 6.5. Potential influences that affect a change from linearity are outlined in the text*

Our relation holds well in the range of porosities and sheet thicknesses measured here (volume fraction ~0.5 to ~0.64, with zero strain volume fraction given in Table 1.1 for each graphene sample), but may break down in more extreme regimes. For example, a regime of low porosity may limit sheet bending, as would a network of very low aspect ratio sheets, or for very thick sheets that a ridge based model may not accurately represent. Extremely low porosities may also affect the modulus as per Eqt 6.1 via altered Poisson ratios. At the other end of the spectrum, a regime of sufficiently high porosity approaches a material more closely resembling a disconnected foam or net system, though some similarities may remain. For example, recently studied low ϕ colloidal graphene sheets attribute compressive response beyond the gelation point to a similar bending/crumpling mechanism, though with a different scaling with ϕ [265]. Therefore, while this linear relation holds within this range, more considerations may have to be made for networks with parameters sufficiently outside the explored range.

6.5.3 Effect of Compression on Modulus

Chapter 5 showed that reducing porosity via compression has an effect on the stiffness of these networks, and Equ. 6.5 models the same. Cycled indentation testing can explore the effect of increased compression on the modulus experimentally. This can be realized by performing a series of indentations with successively higher peak stress at a single location of the film. Each indent produces a stress-strain curve with a measurable yield point and pre-kink slope, and also compresses the film such that the porosity is decreased for the next indent in the series. As we cannot account directly for the degree of material extrusion after confinement failure, and there is no known means of in-situ porosity measurement that can compensate for this, the modulus measured at high compressions cannot be matched directly to a porosity, but serves as a basis for the degree of modulus increase with compression in the MPa range.

A series of such indents on graphene Sample *II* is shown in Fig. 6.7, revealing that the modulus in a given network increases significantly with compression, but remains within the same order of magnitude. On this sample, ranging from 15 MPa with no compression to 41 MPa for the most compressed portion of the network. Without a means of in situ porosity measurement, plotting these as a function of indentation depth is not constructive, but is instead plotted for Sample *I* in Fig. 6.7 against applied maximum stress of the previous indent. While the highest datapoint in this set may at first appear to be an outlier against a tapering trend set by the previous values, it is a steepening of the response caused by a morphological effect discussed in Chapter 7 and is consistent with further observations in that chapter. The degree of modulus increase with compression reveals a strong dependence on porosity. Networks of MoS_2 sheets exhibit higher moduli compared to graphene of comparable sheet length, owing to the much larger bending stiffness of the flakes (~5-11x higher for monolayer MoS_2 compared to graphene) [248, 266]. The MoS_2 sample ranged in modulus from 36.75 MPa to 107 MPa depending on the degree of compression.

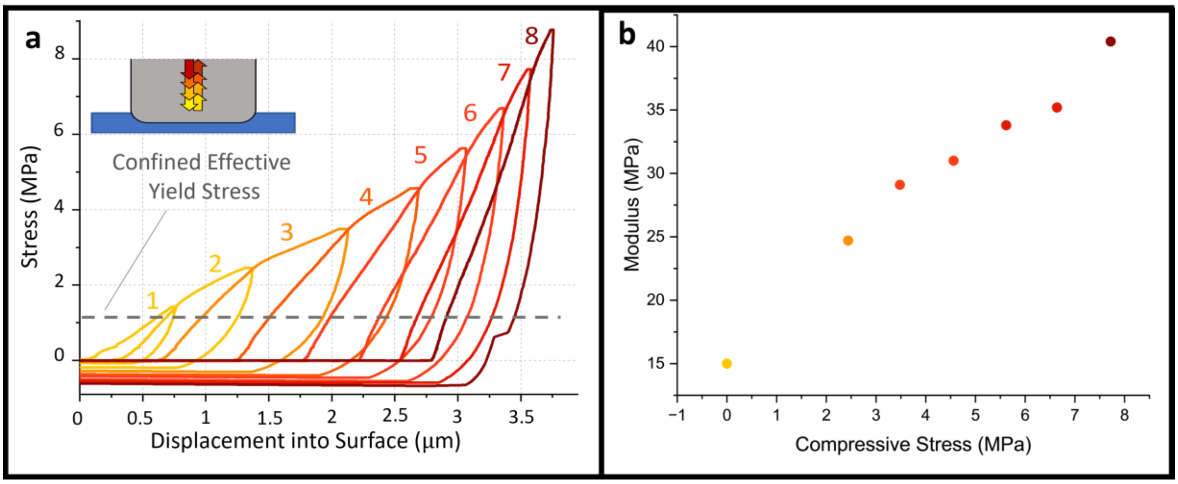

Fig. 6.7, (a) *Incremented in place loading on a previously unpatterned location of Sample II, displaying the increase of modulus with compression ~3x after ~8MPa compression.* ***(b)*** *Displays the increase of modulus with applied compressive stress for this dataset*

6.6 Yield Point

The specifications of material yield have distinct implications for device manufacturing, being fundamental to the mechanical tolerances of a given device. Understanding the mechanisms of such yielding can allow for both greater understanding of the deformation pathways fundamental to the material class as a whole, and with further implications for post processing parameters in mass-scale device manufacture, such as roll-to-roll processing [110, 267]. Both the stress and strain at which yield occurs, as well as how this evolves with densification, are important considerations and are explored here for these networks.

6.6.1 Evolution of Yield Stress and Strain with Compression

Incremented indentation testing is used to explore the effect of porosity on the yield point in the same manner as for modulus in Section 6.5.3. The increment set on Sample *I* shown in Fig 6.7 allows for analysis of the yield point as a function of compression by observing the yield kink in each stress vs strain curve. This reveals that the yield stress in a given network does not change appreciably with sample compression. We can conclude from this that the yield stress is largely independent of the network porosity (at least in the range of porosities explored here, ranging from ~0.4 to >0.2 during this incremented compression on Sample *I*), or only weakly dependent upon it. This implies that the yield stress is governed more strongly by the properties of the individual flakes, and by sheet deformations such as folds and ridges, as opposed to conglomerate network processes such as sliding which would be more influenced by porosity and free volume that would be required to facilitate such processes. This reliance on local mechanisms is further supported by examination of covalently cross – linked MoS_2, discussed in Section 6.9.

Although the effective yield stress is independent of network compression, the effective yield strain is not. Fig 6.8 (a) shows the effective yield strain for the same set of incremented indents as in Fig. 6.7, defined relative to the new film thickness after each indent. This reveals a decreasing yield strain for more highly compressed networks. As the yield stress was unaltered by the compression, it is unlikely this is due to strain hardening, and is instead likely intrinsic to the change in network parameters such as porosity, nanosheet alignment, or sheet morphology. For example, given the folding model already put forward, it is reasonable that pre compressed networks may already have folds present in the sheets which would reach a yielding strain at lower additional deflection than unfolded sheets. While this has not been measured as a function of these network parameters due to aforementioned problems quantifying extrusion accurately, and elastic recovery making post – indent analysis unreliable to extract these properties, it is evident that the yield strain reduces noticeably as the film is compressed.

The effect of sheet size on the yield stress is plotted in Fig 6.8 (b) and reveals that the yield stress reduces with increasing sheet size. While it may initially seem counterintuitive that networks comprised of larger, thicker sheets yield at lower stresses than those of thinner sheets, it is important to consider that the length and thickness of LPE sheets is intrinsically connected [111]. Thicker sheets are also longer, and the network pore size is increased also [37]. This allows more space for sheet deformation, and increases the length between individual bending moments and their fulcrum (both being located at contact points between sheets) which may reduce the overall network stiffness. This is further supported by the fact that the MoS_2 sample has a measured effective yield stress of 2.1 MPa, which is significantly higher than graphene Sample *I* which has a comparable sheet length and an effective yield point of 1.08 MPa, likely owing to the increased stiffness of MoS_2 sheets compared to graphene [248, 266, 268, 269], showing that stiffer sheets form networks with higher yield points when nanosheet length is accounted for.

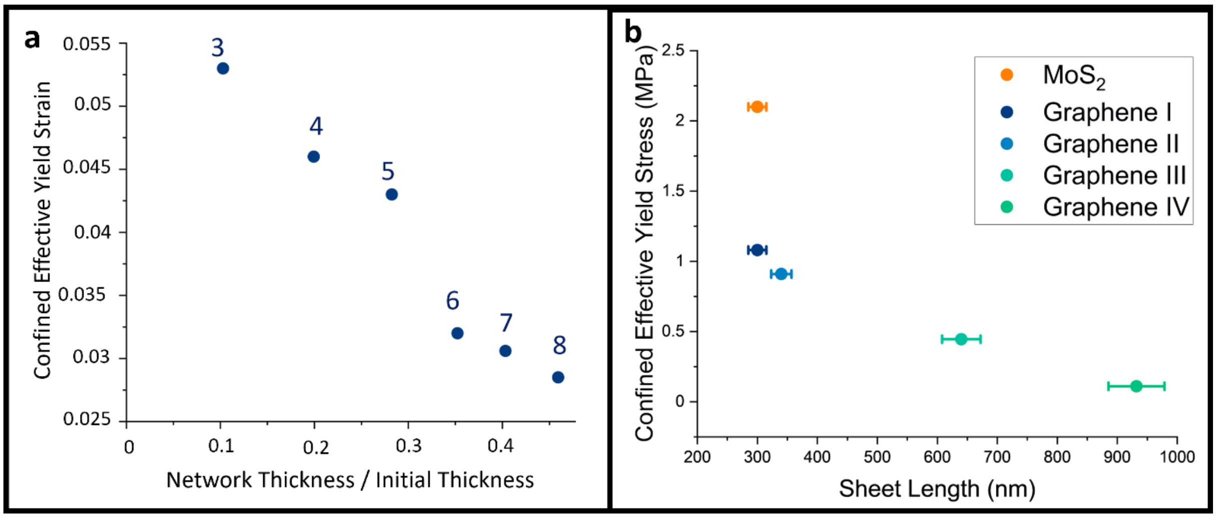

***Fig. 6.8, (a)** Decreasing yield strain plotted against network compression in Sample I for the increment dataset in Fig. 6.7. **(b)** Displays the constant yield stress for all networks explored in this work. Though*

networks of larger (thicker) sheets have lower yield stress, this is likely due to network rather than sheet properties such as bending moments evidenced by the increased yield stress in MoS_2 networks of comparable sheet length

6.6.2 The Role of Shear in Network Yield

The role of shear in the onset of plasticity in these networks deserves some discussion, as it is fundamental to the onset of plastic yield in solid materials [183]. The LCT is fundamentally an approximation of a uniaxial strain geometry and as such lowers the ratio of shear to hydrostatic pressure compared to unconfined geometries or shear-based loading. The porous and granular nature of these samples is likely to readily facilitate lateral sheet movement as a means of plastic deformation in the event of a large amount of shear injection in the network [260]. This build-up of shear and the resulting large scale lateral movements of the network are observed also in our geometry upon failure of the confining influence of the surrounding film at high pressures, which sees mass ejection of the confined material into the surrounding film jacket. While I attribute yield and viscoelasticity to sheet bending processes in this confined uniaxial compression, other loading geometries may facilitate lateral motions more readily via increased shear, and therefore alter the mechanical response. The effect of shear injection on the compressive mechanical response of such networks is currently being explored, utilising small amplitude piezo oscillations underneath the substrate to probe the effect of both shear amplitude and frequency [270].

6.7 Creep and Viscosity

As discussed above, a dissipative deformation component is present in these networks. This is unsurprising given that amorphous solids can experience viscoelasticity [208, 217, 271], as well as the granular nature of the network which often exhibit flow-like behaviour [63], as discussed in Chapter 1. The degree of the flow response generally depends on the material and on a complex combination of factors such as grain size, shape, stress rate, cohesive forces, and many more [66, 272-275]. Fig. 6.4 (a) shows stress vs strain curves of a graphene nanosheet network exhibiting hysteresis in the pre-yield portion of the curve, a feature of viscoelastic materials. As well as this, the nanosheet networks also experience a noticeable creep response when load is held constant, as seen in the continuing displacement into surface with a held constant load in stress strain curves such as Fig. 6.3 (a), 6.4 (a), and 6.7 (a).

6.7.1 Measuring Effective Viscosity

To quantify this further, Fig. 6.9 shows the evolution of punch displacement at a held constant 1 MPa stress applied over the course of 1 s on graphene Sample *II,* with the zoomed in section displaying the portion of constant held load*,* clearly displaying significant creep behaviour. Both creep and pre-yield hysteresis are indicative of an appreciable viscous response to the deformation. This can be visualised as a slippage or sliding of sheets past one another, either as a bulk motion or individual sheet slippage into void space. This is in contrast to deformation via sheet bending as described in the previous sections which constitutes a solid response [264].

To quantify this viscous component of the deformation, I leverage the uniform stress – strain state imposed by the LCT with comparison to a viscoelastic Zener model in the Kelvin representation (see Chapter 2 or the inset of Fig. 6.9 (b)). The prediction of this model is that upon application of instantaneous stress, the material instantly deforms to a constant displacement defined by E_1 and creeps towards a constant value defined by the spring E_2 in parallel with the dissipative dashpot with viscosity η. The strain response is typically expressed as follows [209]

$$\varepsilon(t) = \sigma_0 \left[\frac{1}{E_1} e^{-t\left(\frac{E_2}{\eta}\right)} + \frac{E_1+E_2}{E_1 E_2}\left(1 - e^{-t\left(\frac{E_2}{\eta}\right)}\right)\right] \tag{6.6}$$

Where ε is strain and t is time after application of stress σ_0. E_1 is the spring constant of the first spring, in series with a spring and dashpot in parallel defined by E_2 and viscosity η. We can rearrange this to

$$\varepsilon(t) = \sigma_0 \frac{E_1+E_2}{E_1 E_2} - \frac{\sigma_0}{E_2} e^{-t\left(\frac{E_2}{\eta}\right)} \tag{6.7}$$

Where the first term describes the total displacement of the punch with an offset for the creep response defined by the exponential term. The behaviour is shown in the insert of Fig. 6.9 (a).

By applying a known stress over a very short timescale (~1s) and fitting the resulting creep behaviour to the exponential term in Eq. 13 we can extract a value for the viscosity of high viscosity thin films. Performing this with a 55μm diameter flat punch tip on a 5 μm thick Polystyrene (PS) thin film (1,000,000 Mw, 21^{0}C) on a silicon substrate (with a substrate correction performed as standard for LCT indents) gives a value of η = 1.2 x 10^{12} Pa·s, which is within expected values for glassy polymers. This may be used as a point of comparison between nanosheet thin films and viscoelastic solids. This PS creep response and the fitting is shown in Fig. 6.9 (c).

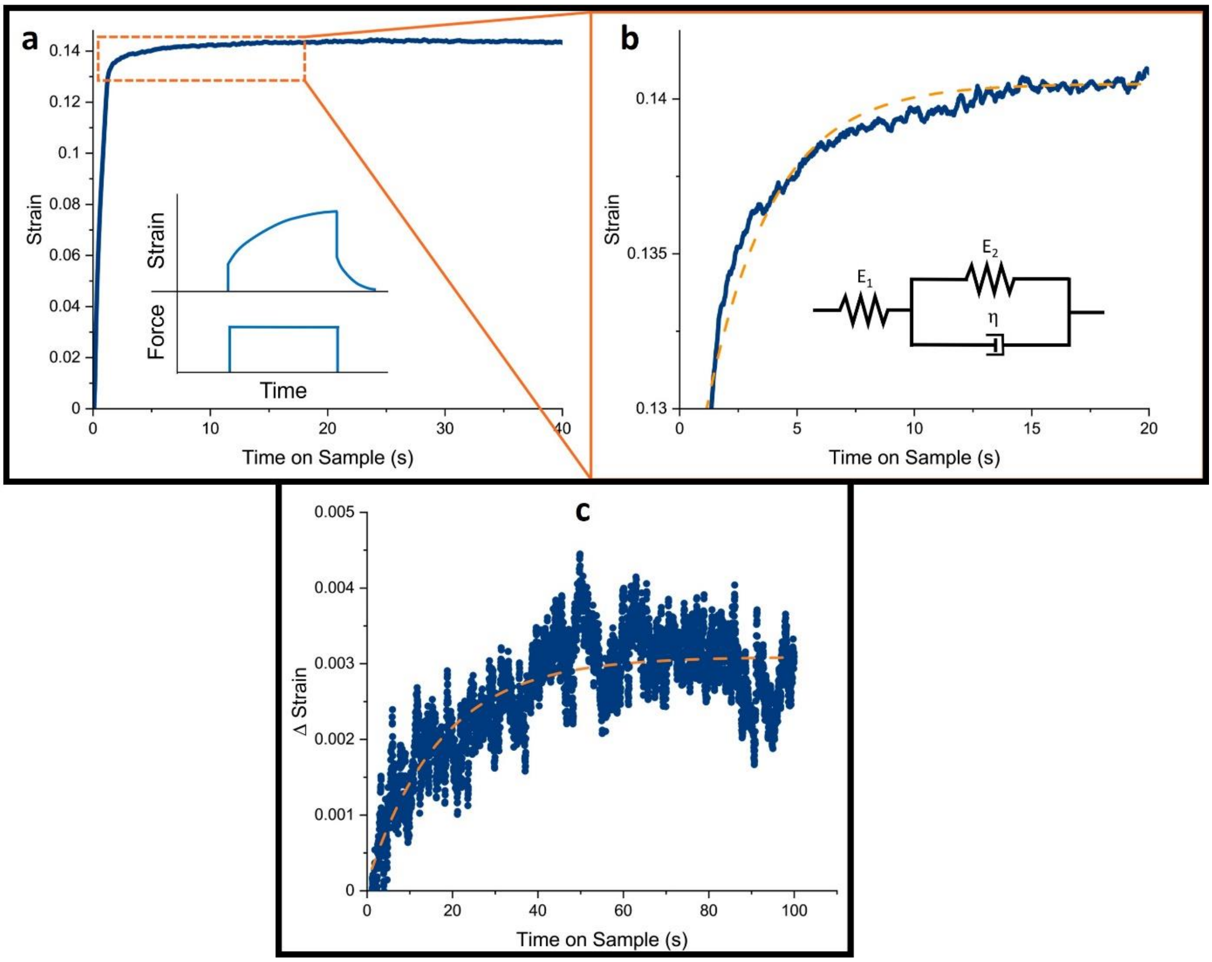

Fig. 6.9, (a) *Creep behaviour of graphene sample II after a held constant 1 MPa stress applied over 1 s.* ***(b)*** *Shows the region of creep, cropping out the application of the stress and showing only the held portion. The orange dotted line shows fitting of the creep data to a Zener model as shown in the inserts of* ***(a)*** *and* ***(b)*** *used to extract an effective viscosity.* ***(c)*** *Shows the same procedure on substrate adjusted*

indent on a 5 µm thick PS thin film indentation, which results in a viscosity value within the known range for amorphous viscoelastic polymer glasses

6.7.2 Viscosity Change with Compression

As we have attributed creep response in the nanosheet networks primarily with dissipative flow of sheets, we would expect the process to be limited by the available void space and friction between sheets, and therefore dependant on morphological parameters such as sample porosity and sheet alignment. It may also be facilitated by the recovery of folded sheets, which under compression would apply stress to nearest neighbours and facilitate further dissipative deformation [148], and as such sheet stiffness may also be expected to play a role. Exploration of viscosity at different degrees of applied stress (and therefore compression), and on networks of varying sheet stiffness but similar sheet size is therefore of interest. Measurements to this effect were performed on graphene network Sample *II* as well as the MoS_2 samples. While the measured value of viscosity depends on the method of measurement and applied strain (e.g., shear vs creep experiments), wide order of magnitude comparisons to other materials can be made.

Low strain kinematic viscosity (measured at an applied stress of 0.42 MPa) for graphene network Sample *II* was measured to be 9.5 x 10^7 Pa·s, which is over four orders of magnitude lower than the measured polystyrene film (1.2 x 10^{12} Pa·s), and several orders of magnitude below typical viscoelastic solids [276]. This value is also several orders of magnitude higher than is typical for cohesive granular systems [273], and measured materials that occupy viscosities in this range tend to be highly thermally dependent such as polymer melts or petroleum based polymers such as pitch [277]. Measurements were performed at room temperature (21°C), though large thermal variation is not expected in these nanosheet networks owing to their granular, non-molecular nature that is arrested by vdW interactions. This is also higher than explored high viscosity graphene polymer nanocomposites (with ex silly putty), that have been shown to increase viscosity with higher graphene content and have viscosities in the order of 10^6 Pa·s [278]. It should also be noted that the measured viscosity is a measurement of creep under applied stress, and little to no thermal rearrangement is expected in ambient conditions, due to the large grain size and their cohesive properties (see Chapter 1). Fig. 6.10 shows the kinematic viscosity range of the MoS_2 and graphene samples from low to high strain alongside some common materials for reference, showing the unique viscosity range occupied by these networks.

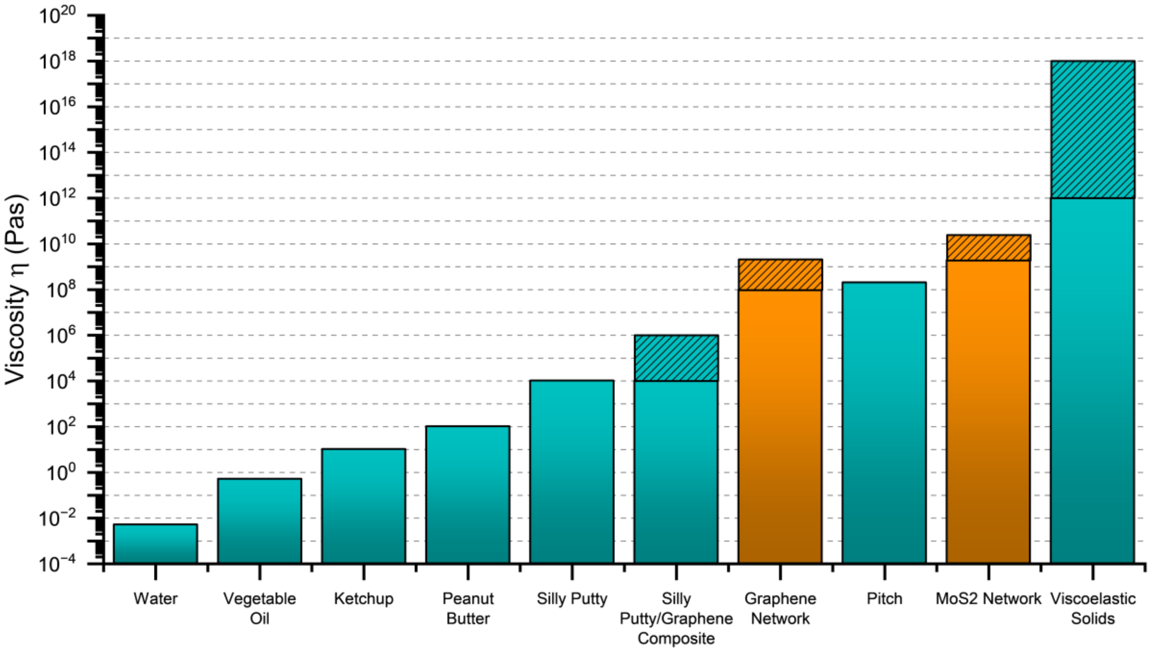

Fig. 6.10, *Comparison of the measured kinematic viscosity of networks used in this work (orange) with some other commonly known materials (teal). Shaded regions for the nanosheet networks represent the range found with compression (ie porosity decrease), for the silly putty / graphene composite represents increasing graphene volume fraction, and for viscoelastic solids represents a range for various materials (eg low* M_w *polymer vs silica glass)*

While MoS_2 shows reduced flake: flake cohesion than graphene counterparts (see Section 6.8), the MoS_2 network shows a viscosity of 2.16 x 10^9 Pa·s at 0.42 MPa, over an order of magnitude higher than a graphene network of comparable sheet lengths, under the same applied stress. This is likely owing to the larger sheet thickness making sheet flow more difficult. This may demonstrate a greater reliance on sheet size, stiffness, and network morphology than inter-sheet interaction in the viscosity of the networks. While porosity differences owing to reduced compression of the stiffer MoS_2 network compared to graphene counterparts at 0.42 MPa may account for some of this, it is a smaller effect than that of sheet parameters (adhesion, sheet size etc). This is supported by higher strain viscosity measurements on the graphene samples. The viscosity of Sample *II* increased from 9.5 x 10^7 Pa·s when measured at a held stress of 0.42 MPa to 1.08 x 10^9 Pa·s when measured at 3.37 MPa, an ~11x increase of effective viscosity with a large reduction in porosity in this range. While we can't measure the porosity change directly, this change in porosity is much larger than that between Sample *II* and the MoS_2 sample at 0.42 MPa, which displayed a ~23x higher viscosity. This demonstrates that factors other than porosity have a large influence on the creep response. A more in depth look at the viscosity scaling with compressive stress will be explored in Chapter 7, as it is subject to other effects that are the focus of that chapter.

The viscosity of the graphene network Samples *II, III,* and *IV* measured at 0.42 MPa were 9.5 x 10^7 Pa·s, 1.35 x 10^8 Pa·s, and 1.97 x 10^8 Pa·s respectively, showing viscosity to increase with nanosheet size despite also increasing zero strain porosities [37]. Careful analysis of viscosity vs porosity for the networks is unavailable in absence of a means of in situ porosity measurements at high strains. Post compression porosities may be measured using FIB – SEM tomography [37, 230], however any strain recovery would interfere with such measurements and make the results unreliable. If such a technique for in situ porosity measurement could be developed, it may allow for more acute determination of the role of network morphology on the effective viscosity. It should also be noted that these viscosity values are taken during LCT indentations along a singular axis. This may be affected by the contact aspect ratio of the indentation, and is likely strongly affected by the direction of applied stress. Such studies are beyond the scope of this work but offers interesting avenues of further exploration.

6.8 Out of Plane Tensile Testing

At the end of unloading in a standard LCT indentation on the nanosheet networks as in Fig. 6.2, 6.3, 6.4 and 6.7, we observe a negative tensile force indicative of significant adhesion between the diamond punch and compressed graphene nanosheets. This manifests as a negative stress after unloading in contrast to a return to 0 stress which would be the case for zero adhesive force. The measured adhesive force increases with the maximum load applied by an indentation, evidenced clearly in Fig. 6.7 (a). This increase is likely due to a reducing porosity increasing the contact area between sheets and increasing alignment of surface sheets to the punch face.

For very high peak loads we can observe this adhesion overcoming the internal film cohesion. Removal of a layer of flakes from the surface can be seen after indentation by subsequent contact to exposed gold substrate, and observing material transfer to the gold as redeposit of nanosheet contamination from the diamond tip. This is made possible by the adhesion energy between graphene/MoS_2 and gold/diamond compared to inter-flake cohesion [279, 280]. The inset of Fig. 6.11 shows significant flake deposition onto the substrate even with three successive depositions after indentation on a graphene network. The extent of the transferred flakes after high-load indentation reveals that the primary separation on unload must occur via inter-flake separation. I exploit this pull-off force as a comparative measurement of out-of-plane cohesive tensile strength of the network after high peak strain indentation. I also use this to explore the change in tensile strength imposed by cross linking of MoS_2 sheets, and how altering sheet size affects the out of plane tensile strength of the networks.

Comprehensive analysis of cohesive strength with porosity would require an in situ means of porosity analysis. In absence of this, we can display dependence on sheet size by representing a spread of values around compressions of a given strain range. This value is shown to be dependent on both material and sheet size, with networks of smaller sheets showing larger cohesion. Cohesive failure for Samples *I* through *IV* after indentations with maximum strain between 0.3 and 0.5 are shown in Fig. 6.11. This is attributed to greater available surface area for smaller sheets, as well as less severe surface roughness for smaller liquid phase exfoliated sheets allowing larger contact areas between sheets. The *MoS₂* network exhibits a much lower cohesive strength than equivalent graphene Sample *II* (0.12 vs 0.44 MPa at an indentation strain of 0.45).

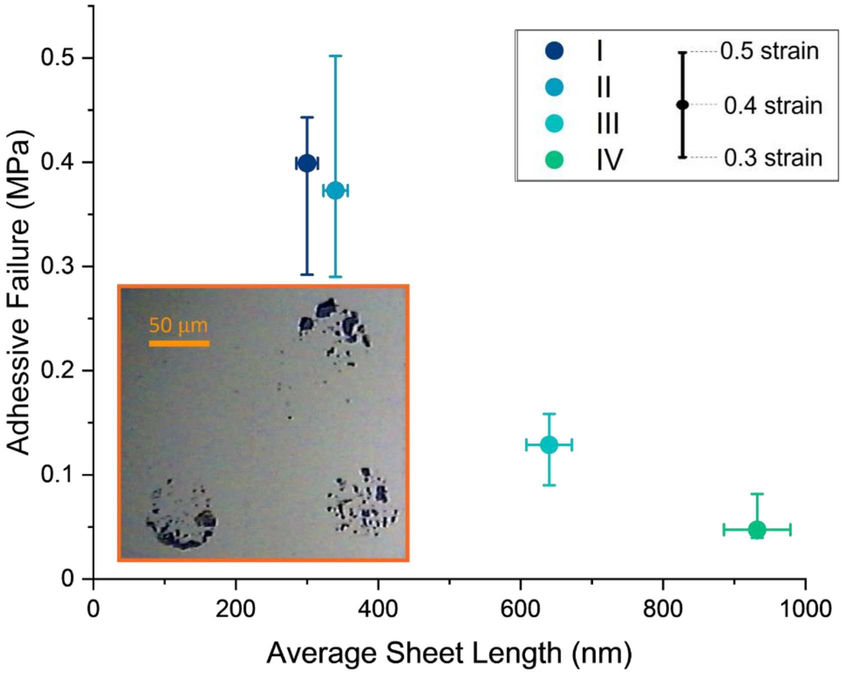

Fig. 6.11, *Adhesive failure stress for graphene samples I through IV, measured for indentations with maximum strain between 0.3 and 0.5, with the value measured at strain 0.4 represented by a dot in each case. This represents the range wherein interflake cohesive forces fail before the adhesion between the flakes and tip, representing a tensile failure point of the sample. The insert shows the transfer of graphene flakes to gold substrate after such a test, showing the degree of tip contamination after the cohesive failure*

6.9 Cross linked MoS_2

As discussed above, two identical samples of MoS_2 were produced from the same ink and spraying parameters, with one undergoing chemical cross linking via sulphur vacancy healing by using 1,4-benzenedithiol molecules [161, 162]. This allows the effects of chemical cross linking (CL) on the compressive mechanical properties to be explored. The tests described above in Sections 6.4 through 6.8 were performed on the cross-linked MoS_2 sample as well as the unprocessed sample. The results are presented here rather than in those sections above as a more comprehensive overview of the effect of cross linking on the network mechanics and what can therefore be inferred. The results are as follows in comparison to the unlinked MoS_2 sample:

- CL did not noticeably alter the compressive modulus of the network

- CL did not noticeably alter the compressive yield stress or strain of the network
- CL increased the measured creep viscosity > 2x at a held stress of 0.42 MPa, from 2.2 x 10^9 to 4.8 x 10^9 Pa·s.
- CL increased the stress required to reach extrusion by ~25% (evident in Fig. 6.12)
- CL increased the cohesive strength of the sample, increasing the stress required to reach out of plane tensile failure 5x (evident in the inset of Fig. 6.12)

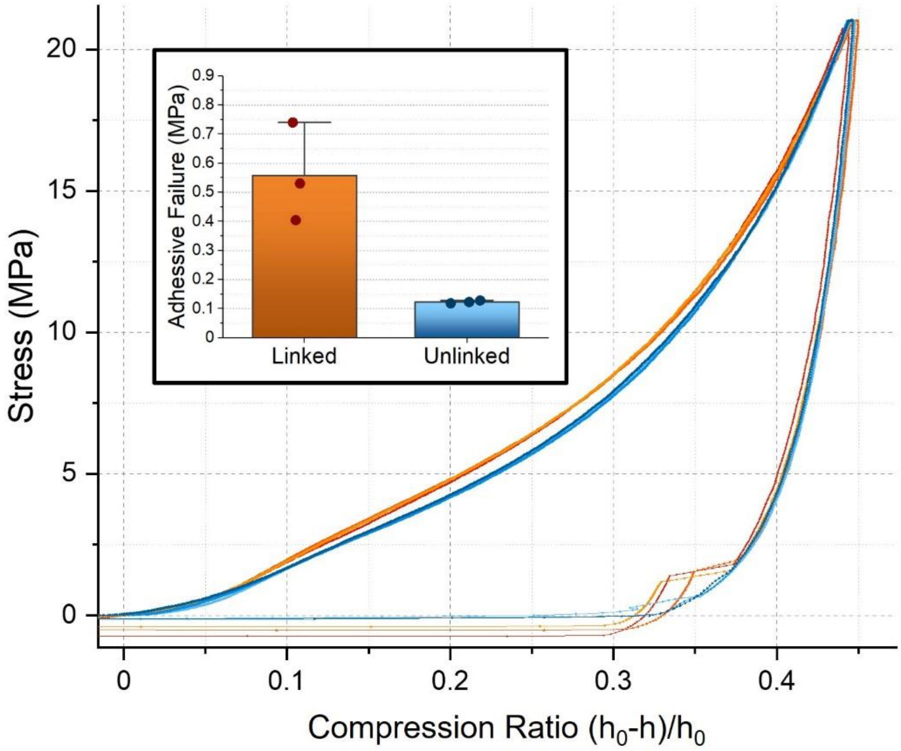

Fig. 6.12, *Three stress vs strain curves for each of unprocessed* MoS_2 *(blue), and otherwise identical crosslinked* MoS_2 *(orange) networks. The insert shows the point of adhesive failure upon unload for these three tests, with the points representing the individual tests and the bar representing the average value*

This reveals that cross linking has little influence on the uniaxial compressive properties of the networks, but noticeably inhibits long range movement between flakes such as during creep, tensile strength, and resistance to the extrusion process. It therefore adds credence to the supposition that low strain compressive effects such as the viscoelastic response and yield are determined by short range processes such as sheet bending and folding, as opposed to longer ranged sliding processes. Altering the degree of cross linking in a sample may therefore allow for a degree of tuneability in lateral and tensile stability with little change to compressive stiffnesses, which may have implications for strain sensing applications.

6.10 Conclusions

In this chapter the out of plane mechanical properties of spray coated nanosheet network thin films were investigated via the layer compression test. A viscoelastic response was discovered, with the resulting effective elastic modulus characterised for networks *I* through *IV* and both MoS_2 networks via careful consideration of the effect of network anisotropy on the stiffness compared to an elastic modulus value. For the graphene networks, compressive moduli were in the region of 0.3 to 78 MPa depending on sheet size and network porosity. MoS_2 networks were found to have moduli over 2x higher than graphene networks of comparable average sheet lengths and porosity, owing to increased bending stiffness of the flakes. The modulus measurements on the graphene networks were compared to a folding sheet model in the range of volume fractions from ϕ = 0.54 to 0.64 which is typical of sprayed networks, finding favourable comparison to the model predicting modulus directly proportional to volume fraction and inversely proportional to sheet thickness in this range. Slight deviations to the linearity of this model can be attributed to smaller considerations such as the change of sheet bending stiffness with bending angle or contributions from sheet bowing rather than bending. Current knowledge of sheet and network deformation does not allow the incorporation of such processes, and investigation of such effects is outside the scope of this work. If such effects could be characterised, the potential small offset from linearity in our prediction could likely be accounted for.

A yield transition to plastic deformation was characterised, with the yield stress being dependent on sheet size but independent of porosity, with networks of smaller sheets exhibiting higher yield stresses. Yield strain on the other hand was found to be reliant on porosity. The relationship between yield stress and elastic modulus was found to be consistent with other amorphous solids, and yield stress was higher for MoS_2 networks than for comparable graphene networks. The existence of a yield transition from viscoelastic to apparently plastic deformation does not preclude longer time scale recovery processes after supposedly plastic deformation as observed in crumpled sheet experiments (see section 1.9 in Chapter 1), and this will be explored more in Chapter 7.

Creep behaviour attributed to sheet rearrangement within the networks was fit to a standard linear viscoelastic model and compared to a polystyrene film of comparable thickness as a means of comparison with known viscoelastic solids. Extracted effective viscosity was over four orders of magnitude lower for graphene networks than for the polystyrene, and over three orders of magnitude lower than polystyrene for the MoS_2 network. Both networks increased by an order of magnitude with significant compression, displaying a strong dependence on porosity. The viscosity range occupied by these networks is unique among non-thermally active materials, and likely relies heavily on the mode of applied stress due to anisotropy of the networks.

Out of plane tensile failure of the networks was tested via adhesion to the large contact area indenter tip and subsequent tension testing until failure. Tensile failure was found to occur at higher stresses for graphene networks of smaller sheets and was dependent on porosity. The MoS_2 network exhibited tensile failure at lower stresses than for comparable graphene networks. Chemical cross linking of MoS_2 was found to increase network resistance to lateral motion and tensile stress, but did not alter the compressive modulus or yield stress / strain, demonstrating that these properties are largely determined by the elastic properties of the flakes rather than the interaction between them. Cross linking was associated with a 5x increase in out of plane tensile failure and a 2x increase in viscosity compared to a pristine MoS_2 network.

This represents the first comprehensive exploration of the compressive mechanical properties of nanosheet network thin films. As such, the work presented here has focused largely on quantifying a vast range of properties and developing the techniques to do so. There exists a range of potential further research avenues opened up by this work to explore these properties individually in more intense detail that was foregone in this project in favour of establishing a more comprehensive overview of the network properties. This includes the role of shear in deformation, extending the modulus vs porosity/sheet size model to incorporate changing sheet bending stiffness during compression and sheet bowing, extending to other materials and exfoliation techniques (with vastly different sheet aspect ratios such as for electrochemical exfoliation), a technique to more closely monitor porosity during indentation, and more.

Ch 7 : High Strain Morphological Changes and Strain Recovery in Nanosheet Networks

While the low strain mechanical properties of nanosheet network films explored in Chapter 6 elucidates some of their fundamental mechanical nature, it is high strain compression that is of most immediate technological interest to facilitate tailored electromechanical properties. In Chapter 6 we revealed how the networks increase significantly in modulus and decrease their degree of creep deformation with compression, correlated to a decrease in network porosity. As well as this, it is known that the electrical properties of these films rely heavily on their morphology and porosity [37, 131, 133, 144, 281], as reviewed in detail in Chapter 1 and demonstrated by the models of Eq. 1.9 and 1.10. As these equations show, the conductivity of the network can be improved significantly by decreasing the junction resistance and also by increasing the volume fraction of nanosheets within the film. Increasing volume fraction improves the conductivity by both creating new sheet contacts to decrease electron path length, and by improving alignment and thereby decreasing junction resistance in existing contacts. Controlling these parameters directly during network production can be challenging and often limited to small variations from varying spraying and annealing parameters; mechanical compression offers a means to do this post-production. This potentially allows for tuneable conductivities if the alignment and volume fraction can be controlled in a post processing stage.

The promise of tailorable improvements to morphology and conductivity via mechanical post processing is ultimately dependant on how well the networks maintain compressive strains after load is removed. Morphological changes induced by compression may be undone by any long term strain recovery that the networks exhibit. It is therefore important to quantify to what degree compression induced morphological improvements are maintained over long time periods.

In this chapter, I explore mechanically induced morphological changes on printed nanosheet network thin films. Through high strain layer compression test (LCT) nanoindentation, I monitor the morphological changes induced via compressive pressure, and the degree of energy dissipation / storage associated with such high strain compressions. I report how morphological parameters known to influence network conductivity such as sheet alignment and pore parameters change with compression. I also explore the degree of long-term sample recovery present post uniaxial compression, which can re-introduce significant porosity into the networks, as well as means of reducing this recovery significantly. A critical motivation for this chapter's work is that the compression states applied via LCT indentation are representative of deformation occurring in techniques such as Roll-to-Roll (R2R) calendaring which may facilitate mass-scale mechanical postprocessing of printed nanosheet devices [110, 217]. While this chapter provides a range of carefully measured data critical to the morphological tailoring of nanosheet networks, it remains primarily an empirical exploration in this thesis, with a theoretical framework encompassing the observed effects currently in development.

7.1 Energy Dissipation and Storage in Compressed Networks

Understanding the potential energy stored in the nanosheet network during large strain compression can give insight into long term recovery mechanisms to applied strain. Materials with ordered lattice structures like metals and crystals tend to dissipate the majority of large strain elastic-plastic deformation energy as heat [282], whereas free voluminous amorphous materials like polymers can store a large (up to 50%) portion of the deformation as potential energy in the form of an altered morphology that settles in a local energy minima [172, 207]. In folded sheet structures, energy may be stored in folded ridges and in crumpled sheets this can lead to significant slow long term recovery after the initial elastic recovery process, even after large strain compressions [148]. In order to determine means of morphology change in a compressed system, examining the dissipation / storage of energy in mechanical compression is considered.

The degree of energy dissipation / storage per unit volume can be explored by examining the degree of hysteresis in the load – displacement curves of individual LCT indentation experiments. Morphology changes induced by sheet sliding will manifest most strongly as frictional dissipation through heat (with smaller storage contributions plausible through surface energy decrease), whereas inelastic sheet bending will have a larger potential storage contribution as bond stretching in the sheet folds may result in energy storage through enthalpic processes [283-286] (with some frictional dissipation through bond movement and stretching also). As such, distinguishing deformation dominated by sheet bending mechanisms from sliding processes as best as possible can help determine the means by which energy is expended in the system upon compressive deformation.

We expect that high strain LCT indentations that exceed confinement and lead to extrusion are dominated by sliding and longer range sheet motion, which will dissipate energy primarily through friction. Loss of confinement can be minimised through a preconditioning or "shakedown" indention series to better isolate local deformation processes. This shakedown procedure has been described previously in Sections 5.3.2 and 6.3 with benefits of

- Removal of Surface Roughness: Removes excess dissipative plasticity during deformation of surface roughness peaks
- Delayed onset of extrusion: Removes excess dissipation from friction during long range sheet motion in the extrusion process
- Reduces the system to a steady state: The repeated deformations allow the network explore a local energy minima through minor morphological changes (in this case small local sheet motion into available void space) which is the current understanding of such behaviour of repeated indentation processes on amorphous free-volume systems [287-289]

A similar procedure was utilised in this Chapter. Over the course of these indentations a number of morphological changes that help isolate bending mechanisms within the compressed material are produced. These were also discussed in detail in sections 5.3.2 and 6.3.

Using shakedown conditioning, frictional dissipations via long range sheet motion is reduced to a smaller consideration, and the remaining energy cost can be more heavily weighted towards bending mechanisms. Mechanisms such as viscous creep remain observable in the system even after shakedown, eg. as in Section 6.3 which shows creep behaviour even after such a shakedown process. When considered with other minor dissipative processes (such as tip to sample interfacial slip [217]) not all frictional motion within the system is removed. The resulting energy dissipation however remains an approximate 'upper bound' for the energy that may be stored and dissipated by sheet bending on uniaxial compression, and the difference between the hysteresis before and after shakedown gives a lower bound on frictional dissipation.

Fig. 7.1(a-c) shows a series of indentions performed at the same location of the sample to realize shakedown conditioning at maximum applied loads of 4 mN, 7.5 mN, and 15 mN on sample *I*. Three different values of maximum load were chosen to show the evolution of energy storage and energy dissipation pre- and post-shakedown at different degrees of compression. The indentations were performed with a constant loading rate over the course of 100 s with a 5 s hold-time at maximum load, consistent with those in previous chapters. All indentations presented in this chapter follow these parameters unless otherwise stated. The associated energy storage/dissipation extracted from the hysteresis to zero load is shown in Fig. 7.1 (e) for the first and last indentations in each shakedown series, showing energy expenditure for both the steady state of minimal sheet sliding, and the unperturbed state dominated by extrusion processes (post and pre shakedown, respectively). The isolated first and last indent in the series presented in Fig 7.1 (a) are shown in Fig 7.1 (d) as well as the integrated area. This reveals the extent of energy dissipation in sliding friction processes compared to local deformations such as sheet bending in the steady state. There is still significant hysteresis in the steady state case, showing that these local deformations still contribute to significant energy storage or dissipation in the network. Energy stored in this bending process can facilitate the large degree of long term sample recovery through individual sheet recovery.

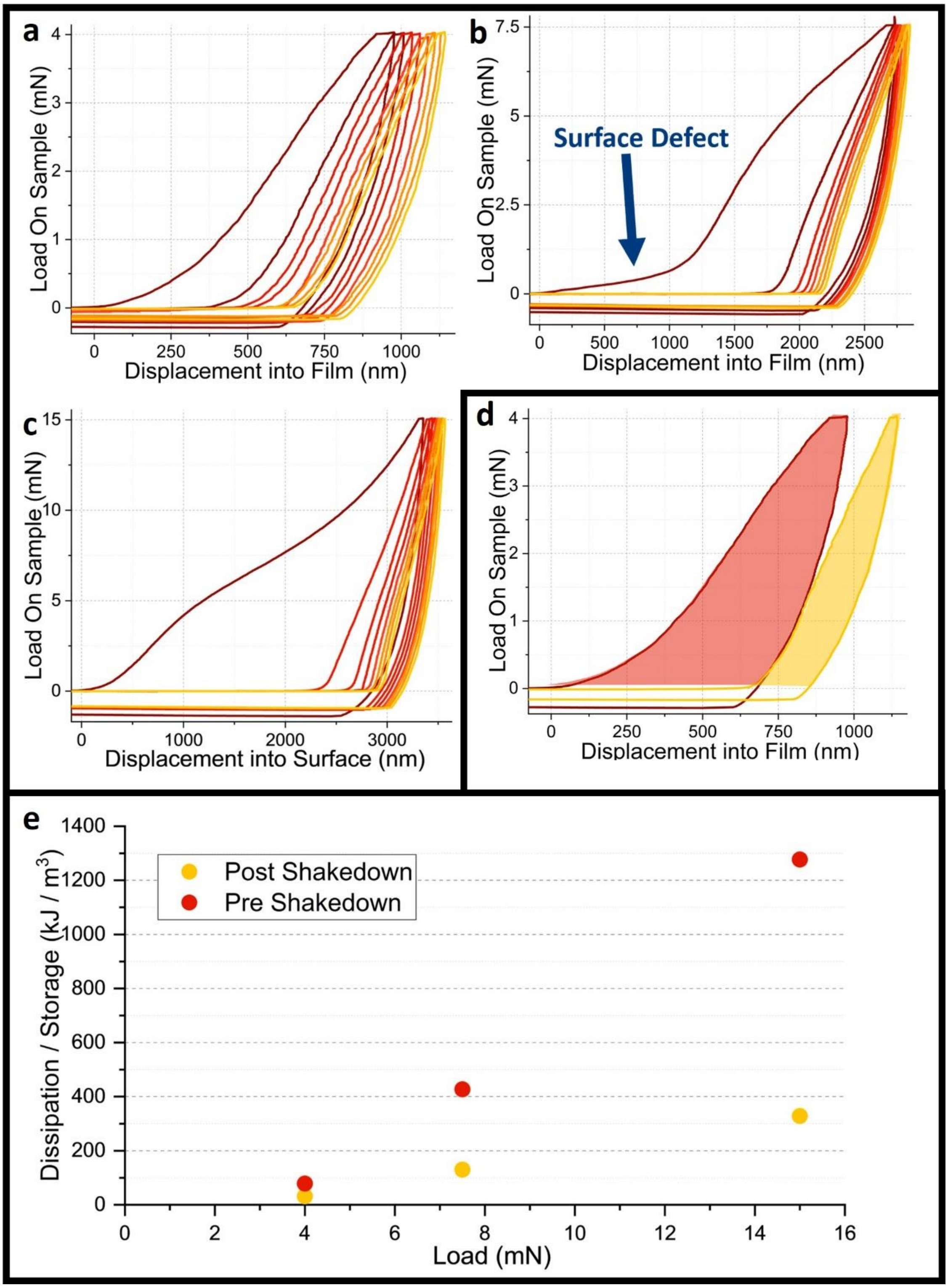

Fig. 7.1, (a-c) *Shakedown indentations to three maximum loads (4, 7.5 and 15 mN) on graphene Sample I, with the darkest red being the first indentation in each series and yellow being the final.* ***(d)*** *shows the hysteresis extracted from the first and last indentation from* ***(a)*** *with the same process used for the other two also. A mild surface defect in the first indentation of* ***(b)*** *was corrected for via extrapolation of the curve excluding the defect portion.* ***(e)*** *Shows the degree of dissipation / storage for each of these tests between the unprocessed films (red) and steady state after the shakedown (yellow). The*

difference between the two is an upper bound for dissipative processes at this load, and the yellow points are an upper bound for storage processes

7.2 Strain Recovery Post Compression and vdW Lock-in

Due to the viscoelasticity discovered already at low strain in Chapter 6, we expect some degree of sample recovery. At high strain, more significant and perhaps long timescale recovery may be present given the potential for energy storage in these networks. This becomes a more significant consideration given the relatively low sheet aspect ratios compared to those obtained from more complex techniques such as electrochemical exfoliation [101, 290] for which sheet folds strain a lower portion of the sheet length.

7.2.1 Long Term Recovery Measurements via FIB-SEM Tomography

We analyse long term recovery by considering both LCT load-displacement data and post-facto cross sectional microscopy analysis. A series of high strain indentations were performed on Sample *I* to a maximum load of 10, 25, and 40 mN (4.2, 10.5, and 16.8 MPa, respectively), with the corresponding load - displacement curves given in Fig. 7.2. Samples were kept at ambient lab conditions for a period of three months to allow for any long term recovery before cross sections of indented regions were taken using focused ion beam-scanning electron microscopy (FIB-SEM) nanotomography [37]. Porosity and film thickness can be extracted from the resulting images and compared to an undeformed region of the film as a means of comparison. The degree of sample recovery can be determined by comparing the thickness measured in the FIB-SEM cross section with the thickness measured at the point where the indenter tip detached from the sample at the end of the unloading portion of the load – displacement curve. A cross section for each indentation and the control region is given in Fig. 7.2 (c-f).

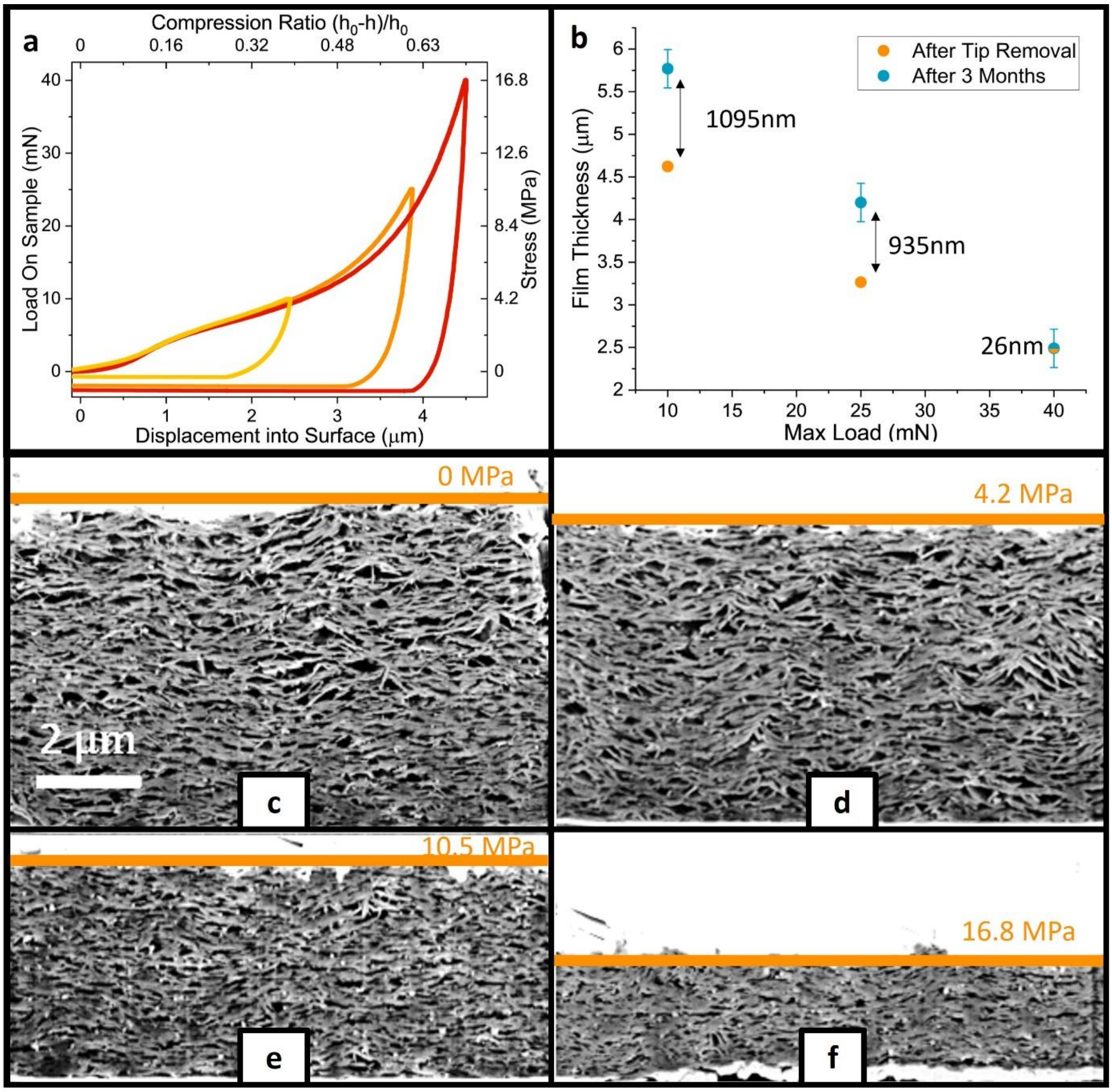

Fig. 7.2, (a) *Load vs displacement curves of 10, 25, and 40 mN max load indentations used to determine sample recovery over the period of two months, performed on Sample I. The tip detachment point of these curves gives the film thickness at the end of unload.* ***(b)*** *shows the film thickness measured both after tip removal and after the three-month period for each indent, revealing a significant drop in recovery for the 40mN indent. Recovery after the three month period was determined from FIB-SEM cross sections of each region, as shown in* ***(c-f)***

The degree of recovery measured for each indentation is plotted in Fig. 7.2 (b), and shows significant sample recovery for even high stress indentations far beyond the effective confined yield stress of 1.08 MPa (corresponding yield load here is 2.57 mN). The degree of recovery is in the range of 1 μm for indentations at 4.2 and 10.5 MPa. However recovery is only 26nm for the indentation at 16.8 MPa, a colossal decrease in recovery when compared with the lower load compressions. While we may expect the extent of recovery to be affected by the loss of material to extrusion at higher indentation strains (and this is noticeable in the slight decrease in recovery between 4.2 and 10.5 MPa) it does not explain the drop to near zero recovery exhibited in the indentation performed at 16.8 MPa. To explore this further, short term recovery was measured using the nanoindenter for which a recovery drop is also observed. While the FIB cross sections also offer a means of probing pressure induced morphology changes closely, this will be explored in a further section.

7.2.2 Short Term Recovery Measurements via Indentation

The MTS XP nanoindentation system controls and measures the position of the indentation punch to nanometre precision over a 1.5 mm travel range. Short term recovery experiments were performed via LCT by performing a full indentation load-unload cycle at a region of interest over a period of 100 seconds, waiting for a period of five minutes and then re-detecting the surface position with the punch. The difference between the detachment position after the initial unload and the subsequent surface contact point on the second approach gives the distance the film has recovered in this timeframe. Determining the surface contact on the second approach is complicated by the existence of surface artefacts caused by adhesion between the diamond tip separating from the surface after the initial indent. Adhesion is revealed in unloading curves by presence of a negative loading excursion before the sharp separation signal (see Chapter 6). These adhesion artefacts often manifest as small disruptions to the surface flakes as can be seen in the insert of Fig. 7.3. In rare cases, adhesion can be more extreme causing light film delamination from the substrate.

We can overcome surface detection artefacts due to minor adhesive flake displacements by using an oscillatory method. A rapid 45 Hz oscillation maintained at 2.5 nm amplitude via feedback control is applied to the tip on approach, with the phase angle between the applied harmonic force and the resulting displacement being continuously measured during approach. This method is similar to that used to determine surface contact in general (see Section 3.3), relying on the constant phase angle value in air and sharp drop to zero for the duration of the indentation upon surface contact. Surface roughness and adhesion artefacts introduce small and soft initial contacts that manifest as a slower drop to zero phase angle as the tip gradually comes into full contact. I correct for these by determining full contact as the point where the phase angle settles to zero, instead of first material contact. A comparison of the phase angle signal as contact is made with a typical nanosheet surface with minimal, moderate, and major surface detection artefacts is shown in Fig. 7.3.

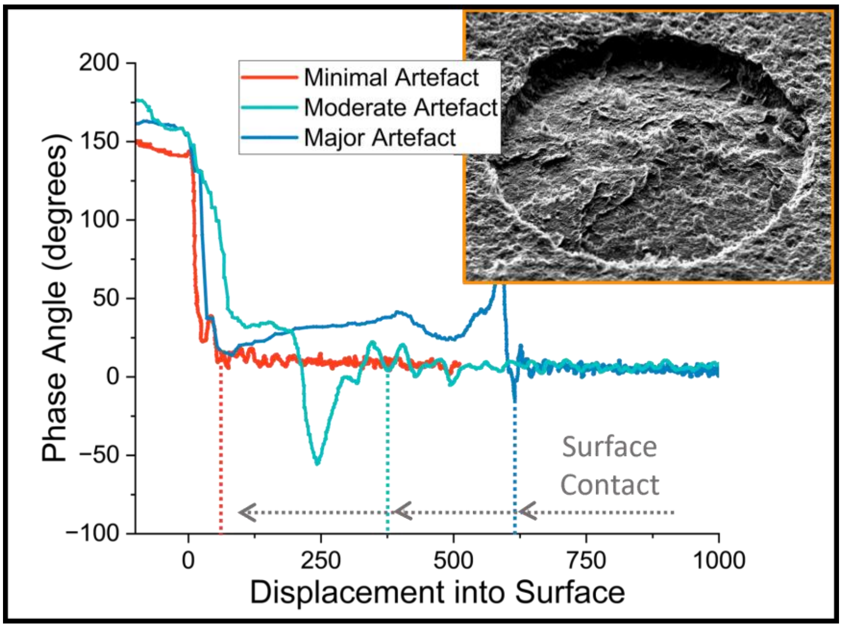

Fig. 7.3, *Determining surface contact correcting for surface artefacts caused by adhesion between the tip and sample. Shown are examples of the phase angle response when encountering minimal, moderate, and major artefacts, with the surface determination point market by dotted lines. Insert shows an SEM image of an indentation on sample II displaying adhesion artefacts*

Measurements were performed on Samples *I* through *IV* via incremented in place testing (ie performing the series of loading and probe indentations in a single location by increasing the load between each indent, as in Fig 6.7). The results of this are shown in Fig 7.4, with average nanosheet size increasing from sample *I* through *IV* as detailed in Table 1.1. The most complete dataset is for Sample *II,* which is plotted individually in Fig 7.4 (a). This sample most clearly displays the trends that are nevertheless present in all the samples. Two distinct drops in the recovery are seen here, one at ~1.7 MPa, and a more severe drop to near zero at ~4.5 MPa. The second drop will be explored here, with the first addressed in the following section. The reduction to zero recovery was observed for all graphene samples over a range ~3-5 MPa, shown in Fig 7.4 (c), slightly decreasing with sheet size. , I refer to this sharp recovery drop as "lock-in" with an associated lock-in stress-strain point. I remind the reader here that networks of smaller sheets have been shown to be stiffer than larger sheets in Chapter 6.

Incremented in place-testing was shown to give the same lock-in point as fresh location testing (ie performing only one indentation and recovery probe per location so that each test is on as-produced sample), and so compressive history below the lock-in point appears to have little effect on the lock-in stress. The fresh location testing data for sample *II* is shown in Fig 7.4 (b), revealing that the reduction to near zero recovery occurs at the same stress for both testing methods. While results are consistent regardless of performing the test on a single location with incremented indentations or on fresh locations each indentations, incremented indentation allows for more complete datasets with smaller data spread by avoiding the effect of variable sample thickness, roughness, and inhomogeneity between locations. There remains some spread in the data for incremented indentations at the highest loads due to inaccuracies in surface detection (eg surface artefacts, or the tip contacting the indentation walls on approach to the surface etc), however the trend is clearly observable. The spread is larger for samples *III* and *IV* due to increased sample inhomogeneity and rough morphological features present with larger average sheet size. For these reasons sample *II* most discernibly displays the features present, though the same trends are observable on all samples.

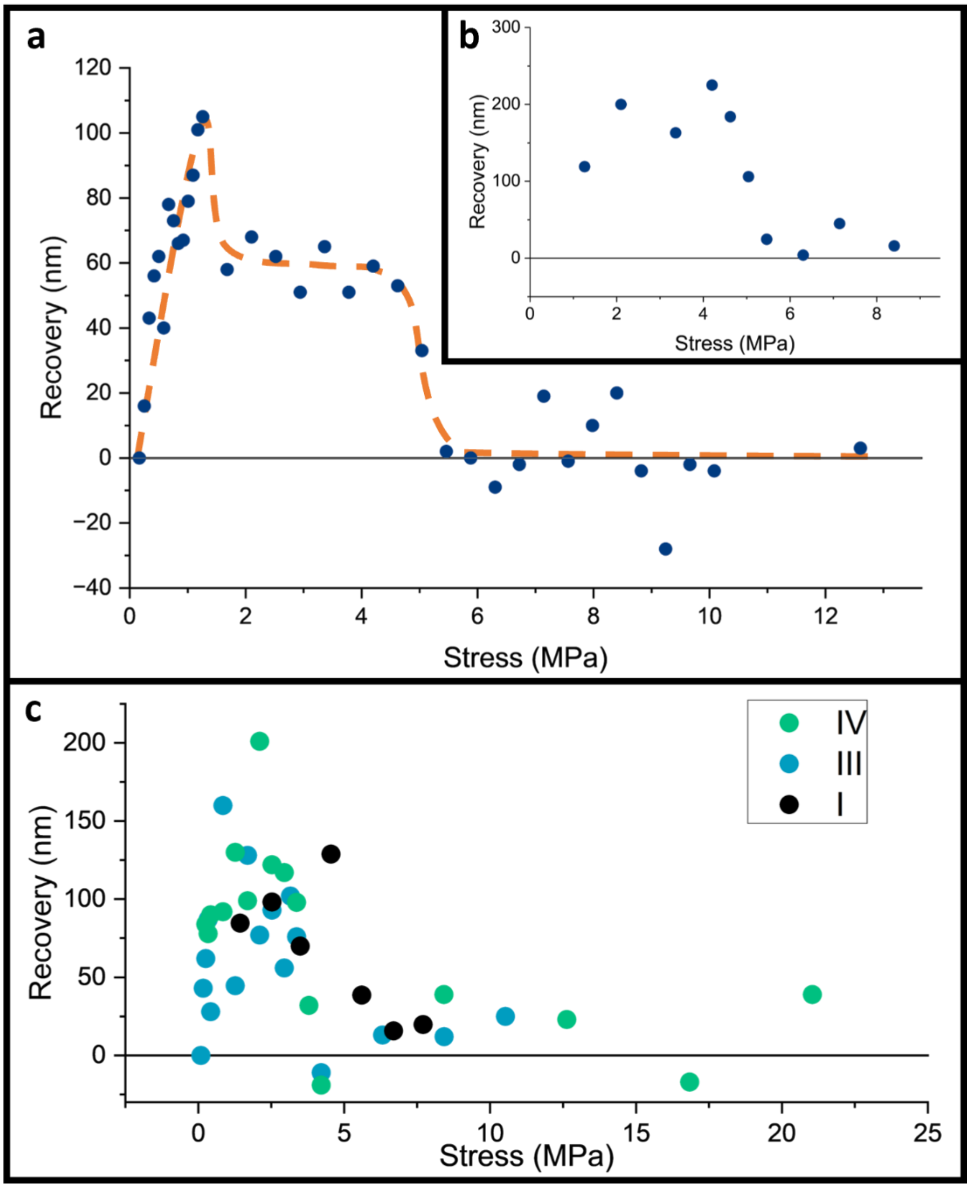

Fig. 7.4, *5 minute recovery time for incremented in-place indentations on graphene Samples I – IV. Sample II is shown in* ***(a)*** *as the most complete dataset, with the other graphene samples plotted in* ***(c)****. A sharp drop to near-zero recovery is observable on all samples at a critical stress, attributed to vdW lock-in of nanosheets. The lock-in effect and associated lock-in stress is consistent with single location testing as shown in* ***(b)*** *for Sample II, demonstrating that mechanical history has little influence on the lock-in stress. A smaller recovery drop at lower stresses is associated with the onset of extrusion (at 1.7 MPa in* ***(a)****)*

It is also instructive to consider the recovery geometrically as a function of the peak compression ratio $(h_0 - h)/h_0$ of the network, where h_0 is the initial film thickness and h is the thickness at a given compression. Although initially equivalent to uniaxial compressive strain of the puck of film below the punch, this parameter eventually becomes an average strain quantity due to the loss of material for indentations beyond the extrusion point. Nonetheless, it can provide a useful geometric comparison of a degree in compression when compared to plotting the recovery vs the maximum applied stress. The results shown in Fig 7.4 (a) and (c) are reproduced in Fig 7.5 (a-d), showing Samples *I-IV* in the same order but with compression ratio plotted on the x-axis. Beyond the lock-in point, further compression of the network becomes much more difficult, with large increases in applied stress corresponding to much smaller increases in compression. This can be seen for example for Sample *II* in Fig 7.4 (a) and 7.5 (b), where the first 5 MPa of compression preceding lock-in result in a compression ratio of ~0.45, whereas compressions after the lock-in stress in the range of 5 MPa to 12 MPa correspond only to an increase in compression ratio of ~0.12. This could be solely due to a fundamental change in the material properties, or also be affected by confinement being reintroduced into the highly compressed film. Changes in mechanical properties at this point will be explored in a further section.

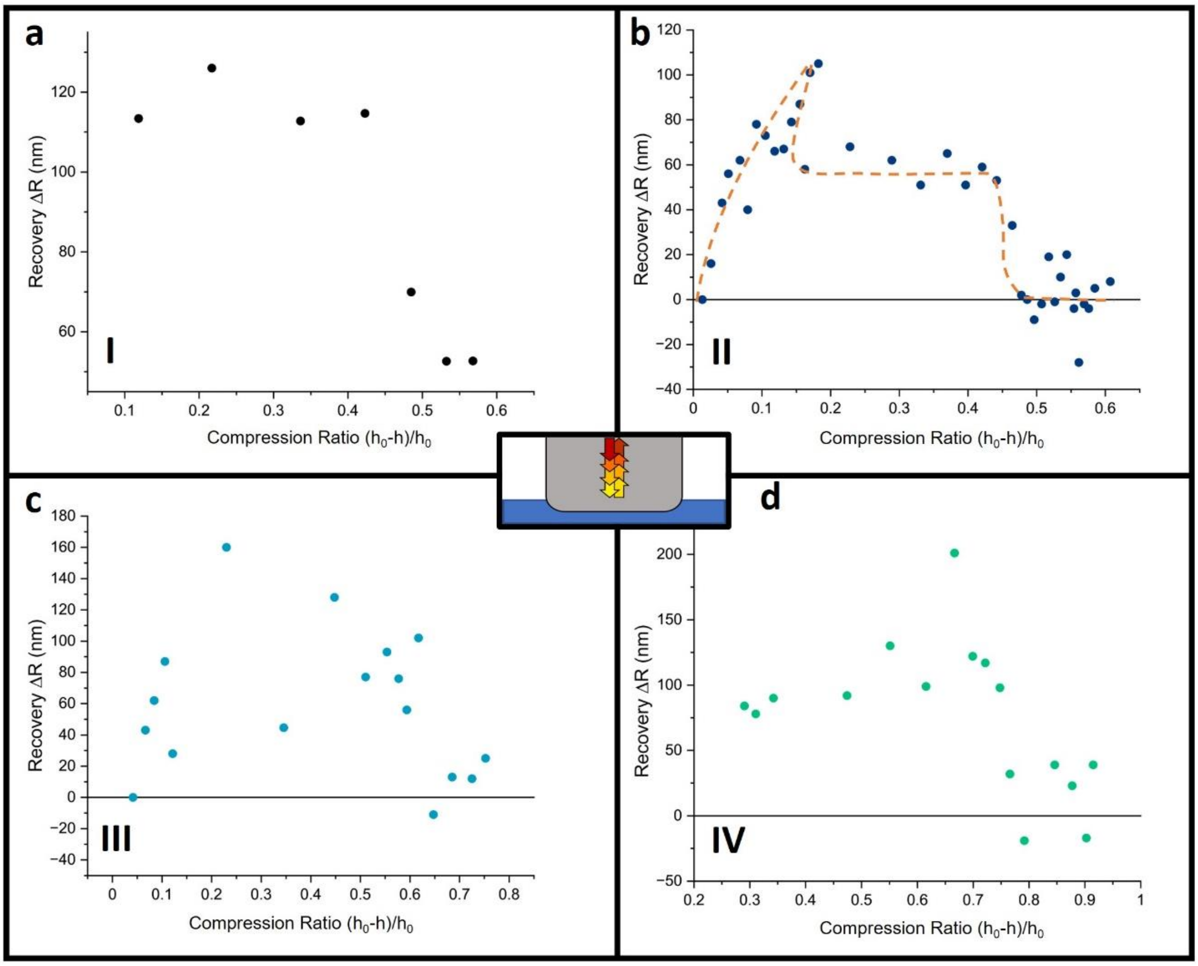

Fig. 7.5, *5 minute recovery time for incremented in-place indentations on graphene Samples I – IV in* ***(a-d)*** *respectively, plotted vs compression factor. The same dataset is utilised as in Fig. 7.4*

7.2.3 Recovery Drop with Shear Deformation

At strains lower than the lock-in point, a lower magnitude recovery drop is noted, most clearly displayed in Fig. 7.4 (a) and 7.5 (b) at ~1.7MPa and ~0.18 compression ratio, respectively. This point is the same as that which material extrusion from the indented region commences, and marks a transition between uniaxial compression dominated deformation, to a regime consisting of a mix of compression and lateral movement of flakes into the surrounding film periphery. At this point, there is an immediate and noticeable drop in the recovery rate of the sample. The immediate drop in recovery magnitude over a very small strain range, and the subsequent plateauing of the recovery magnitude in the following region, both suggests that this is not an effect of sample thinning due to the extrusion process which would manifest as a more gradual transition (as the material extrudes from under the punch gradually over several MPa, as evidenced by the associated smooth curvature in the stress vs strain curves throughout Chapter 6). As such I attribute this to the onset of lateral sheet movements within the puck and can infer that inducing shear deformations in the network during compressive loading facilitates a reduction in recovery rate at stresses below the lock-in stress. This is likely a result of greater ease of sheets exploring available free volume and sheet rearrangements that facilitate greater sheet to sheet contact.

Shear stress is known to induce plastic yield and drive plastic flow in amorphous materials including confined film geometries [183, 205]. Of more recent note, shear flow under a background of large hydrostatic pressure after the point of confinement failure in the LCT has been shown to produce significant densification of polymer films beyond what would be expected by residual elastic stresses in confined compression alone [241]. Crucially, the polymer densification experiments observed a sharp discontinuity to an increased density deep into the extrusion regime. This is not dissimilar to the recovery discontinuity observed at a key stress deep into the extrusion regime in this work. This may suggest a key role of shear stress in the densification or morphological nature of amorphous films in general; more specifically, it could suggest a role in the ratio between hydrostatic stress and shear deformation, as the densification is observed only far into the extrusion regime as opposed to the onset of extrusion where shear generation is expected to be highest. With this consideration, it is perhaps less surprising that such shear flow has an effect on the recovery of these nanosheet network, for which attractive potential between sheets is largely dependent on their proximity and alignment to nearest neighbours.

Future work may examine the role of shear deformation in the recovery process and morphological evolution of these networks via controllable small amplitude piezo oscillations beneath the sample substrate during indentation, which may shine light on the role of shear and its relation to hydrostatic pressure in densification and morphological changes.

7.2.4 Lock-in Stress vs Network Sheet parameters

The magnitude of recovery over the 5-minute period between indentations varies for each network *I* through *IV*, and so may depend on several parameters such as sample thickness, average sheet size and bending stiffness etc. However, the reduction to near zero recovery at the lock-in point is clearly determinable in all graphene network samples tested regardless of the degree in recovery beforehand, with the lock-in stress varying with the network sheet parameters. The trend in lock-in stress shows an inverse relation to the average nanosheet thickness in each network as shown in Fig. 7.6. I postulate that the lock-in phenomenon is due to the establishment of van der Waals like bonds as sheets are brought into close contact overcoming the recovery forces in the network. Other adhesive forces might play a role either, such as attractive forces from residual surfactant contamination. Further work may explore this via changing annealing times to control residual surfactant in the network, or vacuum/humidity conditions. In this thesis I focus on the effect this lock-in phenomenon has on the network properties, with future work potentially exploring the root cause of the increased adhesion. Analysis of network mechanical properties before and after this lock-in point suggest it occurs as a discrete event, as opposed to being a gradual increase of attractive forces overtaking recovery forces, to be explored in more detail in Section 7.4.

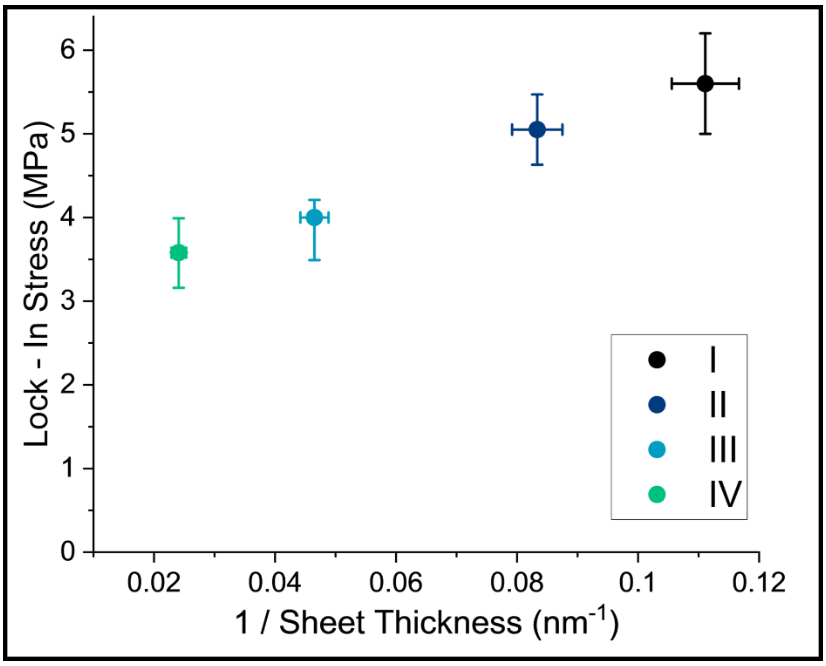

Fig. 7.6, *Lock-in stress as a function of 1/h, where h is the average thickness of nanosheets in the network, for graphene samples I – IV, revealing an inverse relation between sheet thickness and network lock-in stress*

We note that while the lock-in point for sample *I* follows the same trend as the other graphene networks, long term recovery as viewed with FIB-SEM cross sections (as in Fig. 7.2) on this particular sample reveals that this state was only maintained over the three month period for higher load indentations. Lock-in is observable for 5 minute recovery times for indentations above ~5.7MPa for this sample, however three month recovery viewed in FIB-SEM sections show that the same network compressed at 10.5 MPa showed significant recovery, where the indentation to 16.8 MPa maintained near zero recovery in this extended period. The cause of this could be due to many factors. The indentation location for the 10.5 MPa indentation may have been on a region of extreme inhomogeneity that precluded lock-in (though unlikely given the large indentation contact area and otherwise repeatability of the effect on various sample locations). It may be that the lock-in effect does not hold to such long timescales unless higher compressions are reached such as that for the 16.8 MPa indent. It could be that gas expansion in the pores during vacuum pumping for the FIB-SEM imaging compromises the lock-in unless sufficiently low porosity is reached. In a complex amorphous granular system there are many potential variables that could conceivably affect this, and while in depth long timescale studies and parameters that may allow tuning of the vdW lock-in effect warrant further study, they are beyond the scope of this thesis.

7.2.5 vdW Lock-in for MoS_2 Networks

The reduction in recovery via the lock-in process relies on adhesion between flakes overcoming the recovery forces of the flakes. This makes the effect highly reliant on the attractive potential between the sheets in comparison to the recovery force. As such, not all materials may experience the reduction of recovery at this point. In support of this, the same incremented testing as described above was performed on the MoS_2 sample, for which no recovery drop was observed (Fig. 7.7). This is consistent with the tensile failure measurements in Chapter 6 which showed that internal adhesion between flakes in such MoS_2 networks are much lower than for equivalent graphene systems. The lock-in point is also shown to effect network properties beyond thickness recovery however, which are observable in both MoS_2 and graphene samples. These effects will be discussed in more detail in Section 7.4. This suggests that the MoS_2 network does undergo lock-in in a discrete event but that this state is undone by the internal recovery forces when load is removed.

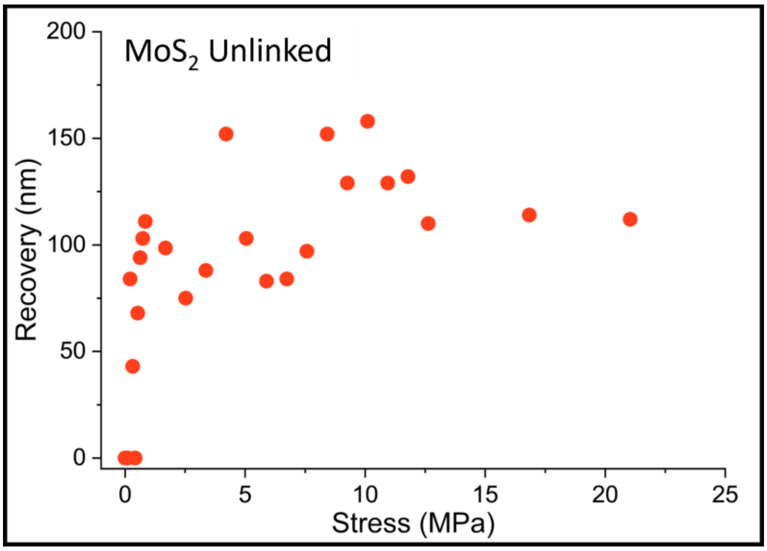

Fig. 7.7, *5 minute recovery time incremented indentations on the unprocessed* MoS_2 *sample. Methodology is the same as for the graphene samples as in Fig 7.4. No recovery drop associated with vdW lock-in is observed for* MoS_2 networks

7.3 Morphology Changes With Compression

As detailed in Section 1.7 and 1.8, morphology changes have the potential to allow for tailored conductivities on nanosheet network films. As well as this, reduced porosities induced by compression have been shown in Chapter 6 to greatly increase the effective compressive modulus of the networks and so also allow for tailored mechanical properties. Analytical analogues to define morphology such as Philipse random contact equation [139, 140] are insufficient due to assumptions that preclude comparison to nanosheet networks (stiff disks, independent contacts, random orientation, etc). Because of this such analytical expressions underestimate packing fraction significantly and so experimental explorations of morphology are required to characterise this with compression.

7.3.1 Extracting Pore Parameters via Cross Section Binarization

FIB-SEM tomography techniques have been shown to allow for the characterisation of morphological parameters in these systems [37]. While this has been examined before as a function of small porosity changes from altered spraying and sheet parameters, I use this technique to explore morphology changes induced via high compressive loads with a larger porosity range.

The same indentations and FIB-SEM cross section analysis to determine long term recovery in Sections 7.1 and 7.2 are used here to determine morphological changes on compression. Eight cross sections, each 12 μm wide, were taken in each indented region. Pores vs. nanosheets were identified via image contrast binarization (Fig. 7.8) using the Image-J software. The pores and sheets were then analysed for a range of morphological characteristics. As the four regions analysed with FIB-SEM cross sections are the same as in Fig 7.2, it is the final most compressed sample (ie the highest volume fraction) that has exhibited zero recovery in the datasets in the following sections.

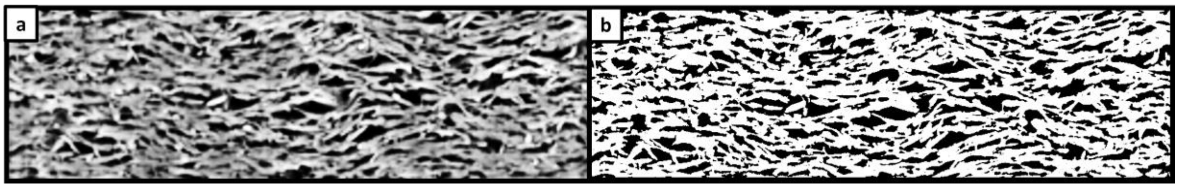

Fig. 7.8, *Unprocessed* ***(a)*** *and binarized image* ***(b)*** *for a cross section of Sample I as received. Binarization allows for analysis of sheet and pore parameters for compressed networks as outlined in the text*

7.3.2 Nanosheet Alignment

The angle of nanosheets identified in the binarized images was determined relative to the x-axis (lying in an in-plane direction, ie the horizontal direction in the cross sections presented in Fig. 7.8 and 7.9) using the Orientation-J package, as shown in Fig 7.9. This groups the nanosheets into bundles and gives a distribution of angles to which a simple gaussian was fit. The FWHM of this gaussian was used to determine Herman's Orientation Factor

$$S = \frac{3\cos^2(\varphi) - 1}{2} \qquad (7.1)$$

where φ is the FWHM of the angle distribution. A value of 1 would be for perfect orientation of each sheet with the horizontal x-axis while 0 represents a fully disordered network. This gave a value for unprocessed film as S = 0.49 at a volume fraction of ϕ = 0.61, which is lower than values previously reported with a similar technique of S = 0.61 [37]. This is likely due to variations in the sheet parameters (average sheet length is 300 nm here vs 238 nm in the referenced material), and also small variations in the alignment determination procedure. The alignment factor increased linearly with volume fraction to a maximum value of S = 0.68 at ϕ = 0.82, induced via compression at 16.8 MPa. The slope of the relation was calculated as 1 $\pm$ 0.25. No apparent discontinuity was observed due to lock-in outside of standard error. The orientation factor is shown for each indentation in Fig. 7.9.

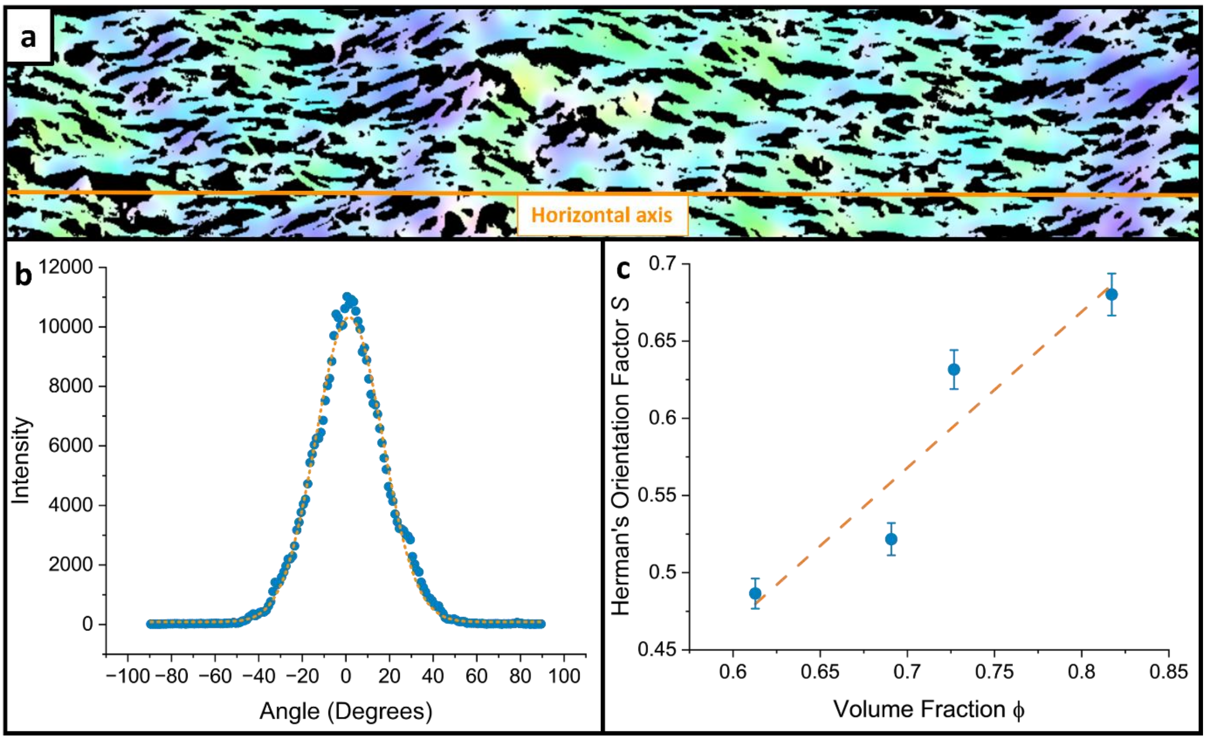

***Fig. 7.9**, Determination of nanosheet orientation to the horizontal axis. **(a)** shows the orientation analysis performed in Image-J for uncompressed Sample I, with turquoise representing perfectly aligned sheets, and colours tending towards purple and white for each direction of misalignment. The horizontal axis of ideal alignment is represented by an orange line. **(b)** Shows the distribution of angles for a single cross section on the same sample. This was averaged over 8 slices in order to determine the FWHM for Herman's orientation factor, S, which is shown in **(c)** for each of the four compressions as a function of nanosheet volume fraction*

7.3.3 Pore Size

The binarized images were inverted in order to isolate pores instead of nanosheets, and the cross-sectional area of each pore was analysed. Pores were separated by size into 50 bins , and the total area occupied by pores of a given size was found by multiplying the number of pores N_{bin} by area A_{bin}.

The smallest pores are attributable to statistical noise in the SEM images (constituting only few pixel datapoints), an artefact that will skew the distribution significantly. Because of this, pores with a size smaller than 10 pixels (with each pixel representing an area of 25 nm^2) were removed and an average characteristic pore area was found from the remainder. The characteristic pore area was converted to a characteristic pore size, $\zeta_{char} = \sqrt{A_{char}}$, for better readability and clarity (representing a pore ‘length scale’ as opposed to a less intuitive cross-sectional area). This is plotted as a function of volume fraction via compression in Fig. 7.10 (a). The average pore size is shown to appreciably decrease in a linear fashion with compression induced volume fraction increase, although there may be some tapering off of this trend at higher volume fraction values, potentially due to tensile processes during unload at punch pull-off. The linear relationship with volume fraction suggests that it is a decrease of pore size, and not pore number (from complete collapse of only the most unstable pores), that is responsible for the majority of the increase in volume fraction in this compressive range.

To show this, the characteristic pore size of the three largest pores in each dataset was averaged and plotted as a function of volume fraction, shown in Fig. 7.10 (b). This reveals that the average size of the largest pores in the network decreases linearly with volume fraction in a similar manner to the average pore size: The difference in the average pore size between the uncompressed and most compressed network is ~2x, while the difference between the size of the largest pores is ~2.4x. The close agreement between the two values further shows that complete collapse (ie, annihilation) of the largest pores is not a significantly more favourable condition than that of gradual homogenous pore size decrease.

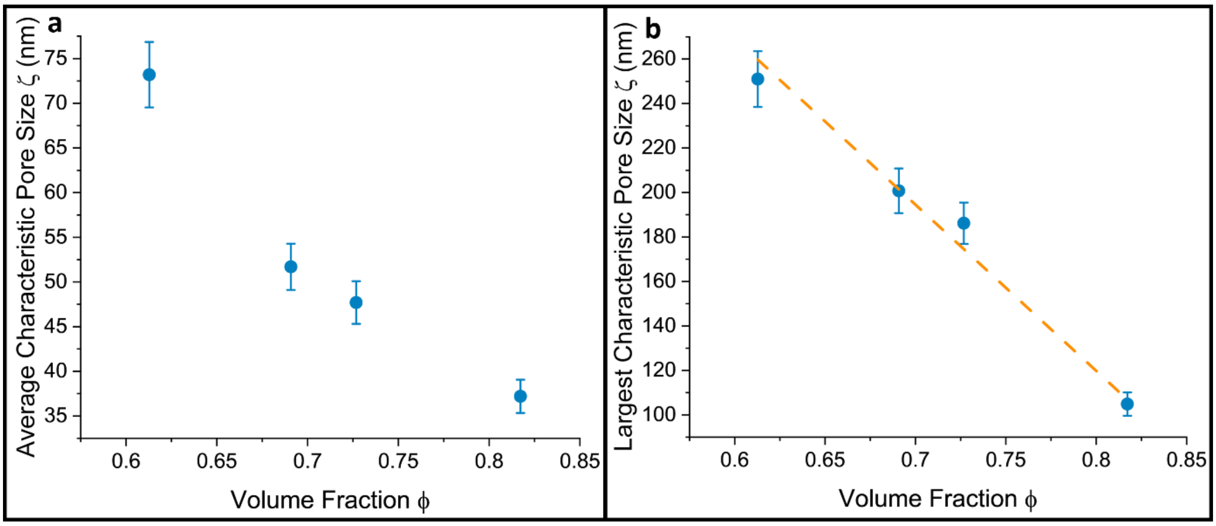

Fig. 7.10, (a) *Characteristic pore size (square root of the characteristic pore area), plotted as a function of volume fraction induced by network compression.* ***(b)*** *Displays the average size of the largest three pores in each dataset, revealing that the largest pores reduce linearly only marginally more rapidly than the overall average pore size as in* ***(a)***

It should be noted that the significant adhesion present between the tip and sample that seems to develop at high peak compression may have an appreciable effect on the pore size distribution, as porosity may be re-introduced via tensile strains upon unload. Passivating the interface between the indenter punch and network surface is currently being explored to see what changes this has to the morphology after high load compressions, and if passivating steps should be considered in mass output techniques such as roll to roll.

7.3.4 Pore Aspect Ratio

The aspect ratio (width : height ratio) of the as-deposited pores remains around a constant value of ~2.4 regardless of porosity, even as the average pore size decreases, and is shown in Fig. 7.11. For a locked – in network this appears to reduce slightly to ~2.2, however with the spread in data values and small variation this cannot be discounted as a statistical effect. While the aspect ratio doesn’t change much with porosity, the spread of aspect ratios around a mean value decreases somewhat. After exploring the quality of fit for several functions, this was determined by fitting the spread in measured aspect ratios to a lognormal distribution and reporting the FWHM. Values for this are shown in Fig. 7.11 (b), with the FWHM reducing linearly with volume fraction. This reveals that during compression, pores with aspect ratios further from the mean value are collapsed primarily, or are changed by the compression to group the distribution closer to a mean value. This trend does not change for the locked-in indent, indicating that these pores are not regenerated during the recovery process.

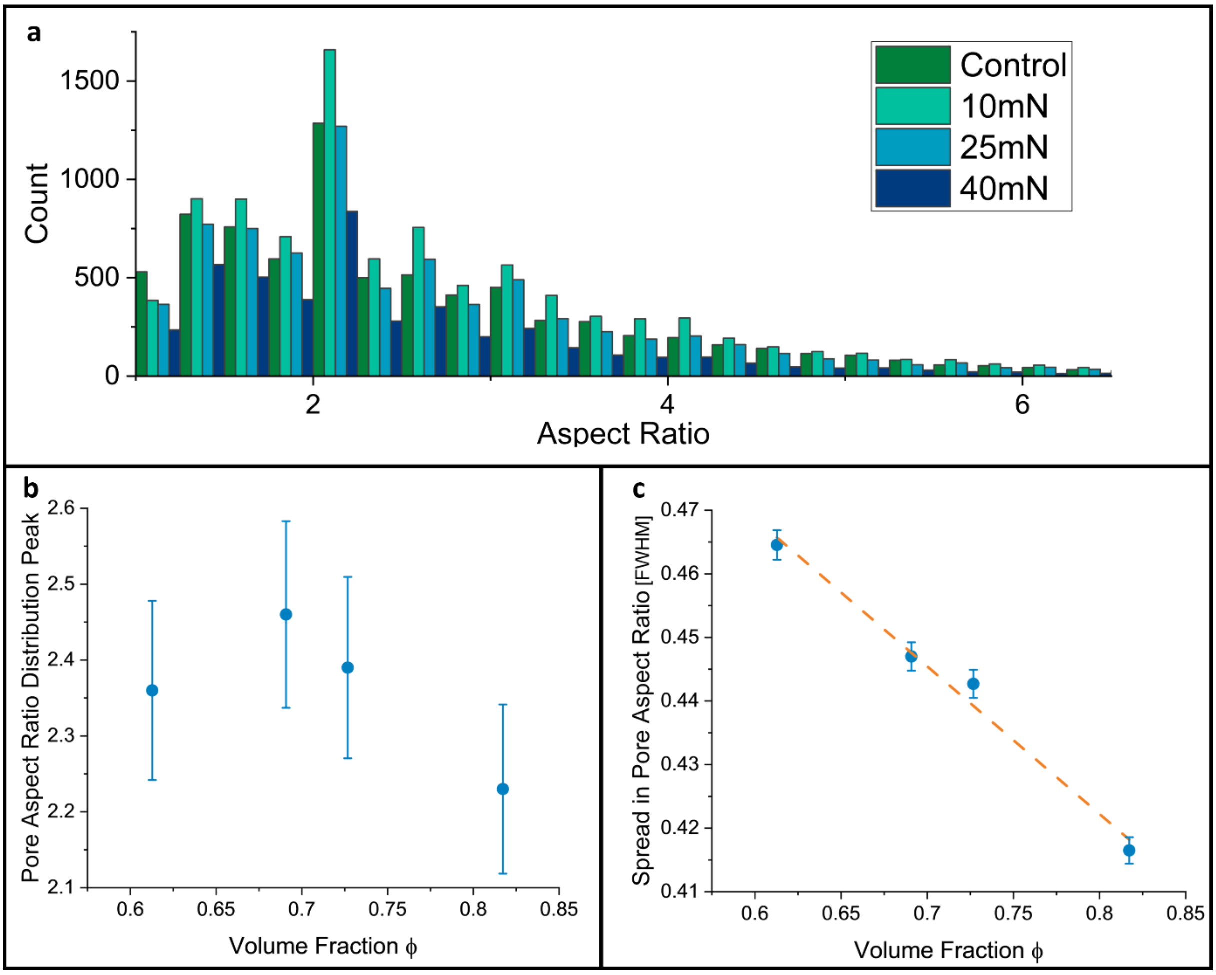

Fig. 7.11, (a) *Aspect ratio histograms of the four regions examined* ***(b)*** *Average pore aspect ratio plotted as a function of volume fraction increase induced by compression. There may be small drop from ~2.4 to ~2.2 after the lock-in point, but is also likely due to a statistical affect given the small decrease and spread in values.* ***(b)*** *reveals the spread in the average aspect ratio around the mean value represented by the FWHM of the aspect ratio gaussian for each dataset. This reveals that although the average aspect ratio does not reduce significantly with compression, pores further from the mean aspect ratio are more predominantly removed by compression than those around the mean*

7.3.5 Pore Circularity

Circularity measures the degree of deviation of the perimeter of a pore from a perfect circle of the same area. It is defined as $C = \frac{4\pi A}{P^2}$ where C is the circularity, A is the pore cross sectional area, and P is the pore cross sectional perimeter. The value of circularity is 1 for pores with a circular shape, while values tending towards 0 have increasingly distorted perimeters. The distribution of pore circularities in the compressed regions is shown in Fig 7.12 (a), with the peak of the distributions shown in Fig 7.12

(b). I find that the circularity of the pores increases linearly as the porosity decreases, ranging from 0.52 to 0.65 over the range of porosities explored. There is no discernible difference in this trend for locked – in regions, indicating it has little effect on the pore circularity.

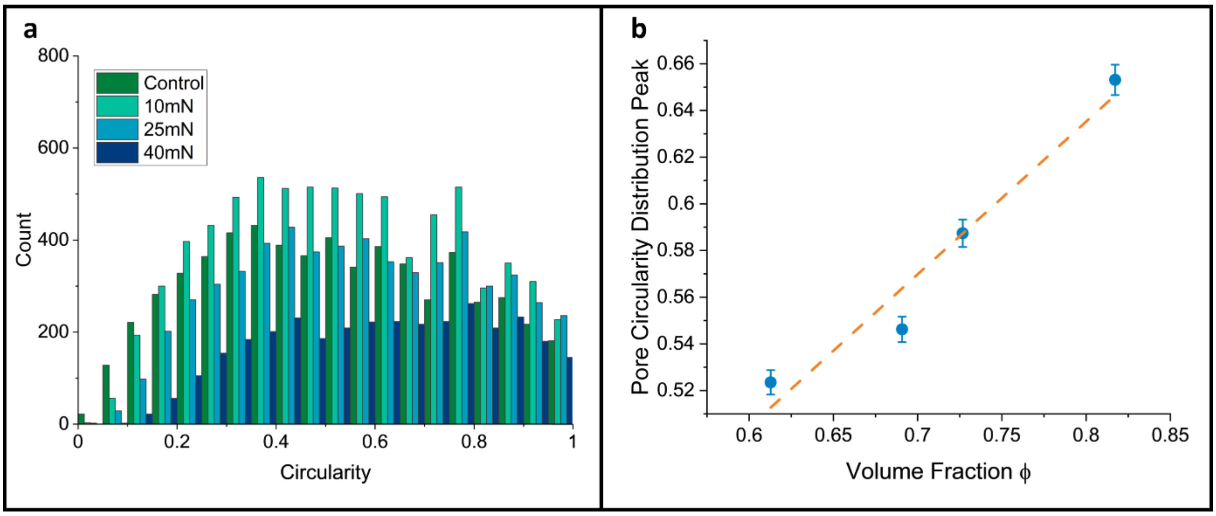

Fig. 7.12, (a) *Distribution of pore circularity in the compressed and control regions of Sample II* ***(b)*** *Pore circularity at the peak of the distribution as a function of volume fraction increase induced by compression. The trend of increasing circularity is appreciably linear, with no apparent change at the lock-in point*

7.3.6 Morphology Summary

The above datasets show that several morphological changes occur with compression. In summary, compression reduces the average pore size with compression, reducing pore size rather than annihilating the largest or smallest sheets by fully collapsing them. As this occurs there is little change in the average pore aspect ratio, but the spread in pore aspect ratios is reduced linearly with volume fraction. Pore circularity increases noticeably linearly with volume fraction but does not see a change in the spread around a mean value with compression alone. Nanosheet alignment also increases linearly with compressed volume fraction.

The lock-in point has no appreciable effect on the majority of these parameters, except for potentially a small decrease in pore aspect ratio. It must be noted again that the adhesive forces between the tip and sample at high loads may influence the final morphology of the networks after high compressions, and passivating the interface to remove this influence is currently being explored. While models of network deformation and conductivity as a function of pore and sheet parameters are in their infancy, such morphological information will help enlighten future work in developing such models and monitor transitions in behaviour from eg, a regime dominated by bending processes at high porosity to alternate compressive modes at reduced porosity.

7.4 Effect of Lock-in on Material Mechanical Properties

The lock-in point is indicated by a sudden reduction in the recovery of the sample that occurs over a small range of strain. This suggests that it is a discrete event that occurs at a particular degree of network compression. It is both possible that the sharp transition to a locked-in state represents a discrete event and change in material behaviour due to increased vdW interactions over a small compression range (or potentially other adhesive forces), or that it is simply a case of increasing adhesive forces slowly overcoming recovery forces that manifests as a discrete event in recovery data but would otherwise show no significant mechanical discontinuity. To investigate if the locked-in state has an appreciable effect on the network aside from overcoming recovery forces, I measured mechanical properties as a function of applied stress and observe any behavioural changes present around the lock-in point. These included small amplitude harmonic stiffness and creep measurements as introduced in Chapter 5 and 6.

7.4.1 Strain Hardening Discontinuity after Lock-in

The most direct way to probe strain hardening effects and changes of mechanical stiffness/modulus with compression is with the oscillatory harmonic contact stiffness method, as introduced in Chapter 3 and utilised extensively in Chapter 5. Indentations performed to high loads on each of samples *II* through *IV* as well as unlinked MoS_2 were monitored continuously using a 2.5 nm amplitude, 45 Hz oscillation, measuring the load required to maintain this amplitude and extracting a harmonic contact stiffness (further details in Chapter 3). Fig. 7.13 shows the harmonic contact stiffness as a function of indentation depth on an indentation for each of these samples. Indentations were performed at a constant loading rate over the course of 100 s. While low strain features dominated by surface roughness and plastic yield as shown in Chapter 5 can be challenging to measure due to the relative speed of a linear loading rate at shallow penetration depths, the measurement becomes robust at deeper penetrations considered here.

The contact stiffness vs displacement appears linear in the plastic regime, denoting a constant stiffening of the material with increased compression. This can be most clearly seen in Fig 5.9 of chapter 5 which explored the increasing contact stiffness around the yield point in Sample *II*. Beyond the extrusion point, at ~0.1 compression ratio for sample *II* in Fig 7.13 (a), the contact stiffness is seen to plateau and then increase gradually to significant penetration depths. The first recovery drop occurs near the beginning of this extrusion region. However, there is an apparent rapid increase in the rate of stiffening around the second 'lock-in' recovery drop (indicated in Fig 7.13 by blue shaded regions), for example at 0.6 compression ratio in (a). We can see direct correlation of this stiffness scaling transitions to the ΔR short-term recovery parameter in the other samples tested, plotted in Fig. 7.13 (b-d) for graphene networks *III, IV,* and the unlinked MoS_2 network, respectively.

The changes in the stiffness slope around the lock-in point suggests that this point represents a change in regime of mechanical behaviour. The mechanisms of deformation in these high strain regions, and how they differ from the low strain response is a topic of interest for future exploration, but is unlikely to be governed by the same sheet bending processes as explored in Chapter 6 due to the higher compression and much lower porosity at this point.

It should be noted that the transition regions in the harmonic stiffness data as denoted in Fig. 7.13 show slight variation when compared to the recovery drop of the associated sample, with some minor compression factor ratio differences between them. This is unsurprising considering both the mild locational inhomogeneity in these samples that sees mild changes in film thickness and porosity etc from location to location, and also the viscous component of deformation; The recovery data was taken from a single location subjected to multiple indentations. This subjects the region to a combined time under stress significantly higher than for the single indentation used to extract harmonic stiffness.

As such the degree to which the sample has undergone creep will be different in both datasets, introducing mild compression factor inconsistencies between the two datasets. These factors together are sufficient to explain the minor difference in compression factor between the features in the harmonic stiffness and recovery datasets.

We see that MoS_2 experiences the same stiffness features as the graphene samples, despite not benefitting from reduced recovery once load is removed. This suggests that the MoS_2 network may undergo pore configuration changes similar to those leading to graphene lock-in, but cannot maintain this state when external loading is removed. This is likely due to the reduced cohesion between MoS_2 nanosheets as demonstrated in Chapter 6 that is not sufficient to maintain this state against the inherent recovery forces in the sheets. This is noted also in following section 7.4.2.

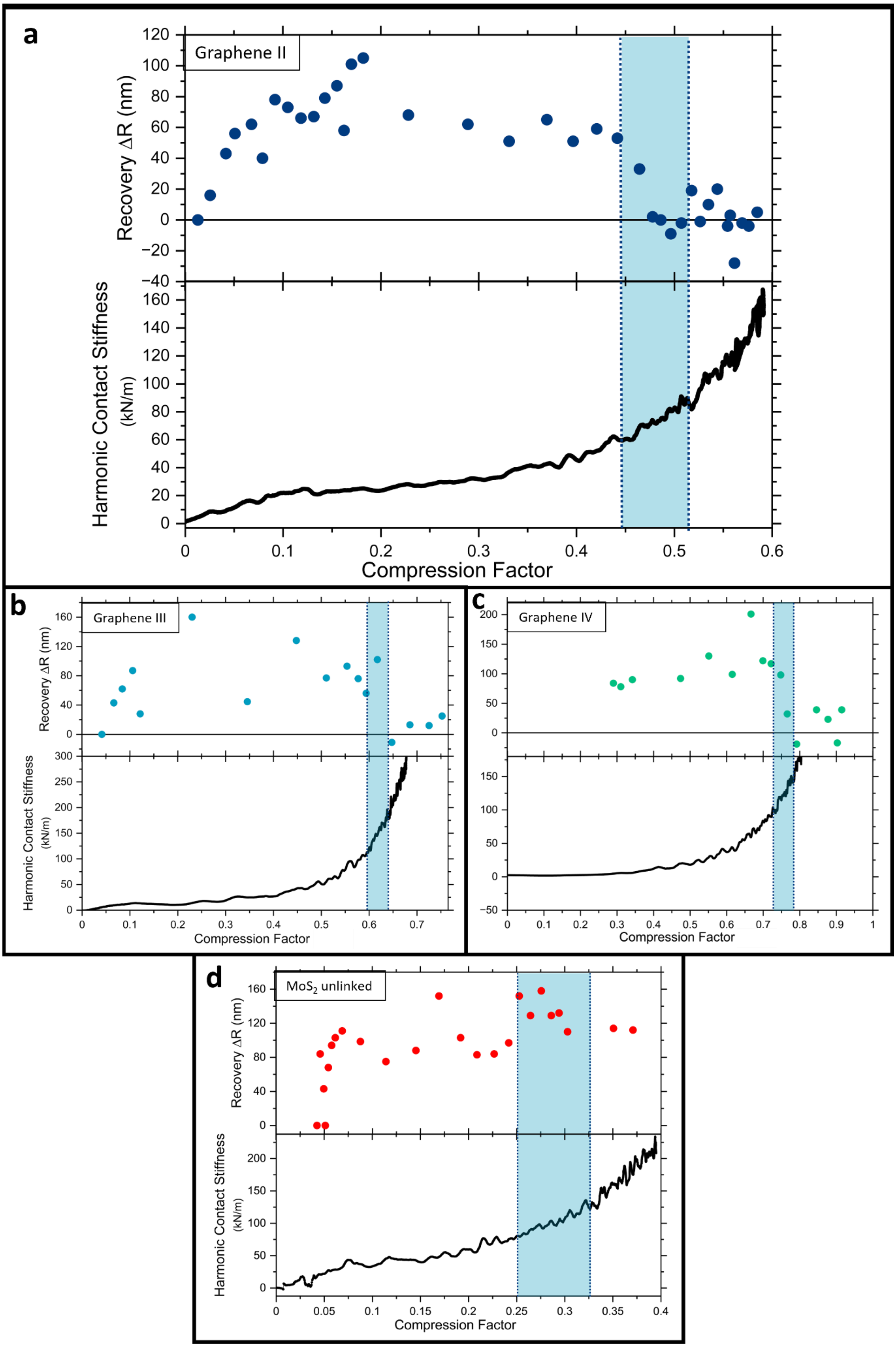
a
Graphene II
Recovery ΔR (nm)
120
100
80
60
40
20
0
−20
−40
Harmonic Contact Stiffness (kN/m)
160
140
120
100
80
60
40
20
0
0
0.1
0.2
0.3
0.4
0.5
0.6
Compression Factor
b
Graphene III
Recovery ΔR (nm)
160
120
80
40
0
Harmonic Contact Stiffness (kN/m)
300
250
200
150
100
50
0
0
0.1
0.2
0.3
0.4
0.5
0.6
0.7
Compression Factor
c
Graphene IV
200
150
100
50
0
150
100
50
0
−50
0
0.1
0.2
0.3
0.4
0.5
0.6
0.7
0.8
0.9
1
Compression Factor
d
MoS$_2$ unlinked
Recovery ΔR (nm)
160
120
80
40
0
Harmonic Contact Stiffness (kN/m)
200
150
100
50
0
0
0.05
0.1
0.15
0.2
0.25
0.3
0.35
0.4
Compression Factor

***Fig. 7.13,** Compression factor vs harmonic contact stiffness during a single indent, and vs recovery for the incremented probing method described in section 7.5.2 for graphene samples II **(a),** III **(b)**, IV **(c)** and the unlinked MoS_2 network **(b)**. Indicated on the graphs is the range of compression ratio over which lock-in occurs, with acceleration of the stiffness vs compression factor evident over this region for each dataset. Also evident is the initial drop in recovery at the extrusion point, as for example in **(a)** at ~0.1 compression ratio*

7.4.2 Creep Viscosity Discontinuity after Lock-in

The effective viscosity extracted from constant stress displacement vs. time behaviour (as in Section 6.7) can be used to determine if a difference in creep behaviour occurs at the lock-in strain. The same methodology from Chapter 6 was used here: Rapid application of stress over a 1 s period followed by a several minute hold at this stress to allow for creep behaviour. The creep behaviour is fit to a Zener model as per Eq. 6.7 to extract an effective viscosity, η, which I associate with sheet rearrangements to available void space.

Fig. 7.14 shows η plotted as a function of applied stress for samples *II -IV* and for the unprocessed MoS_2 sample. As can be seen, η increases with applied stress, which is expected as a reducing porosity limits the free volume available for a creep processes. A distinct rapid rise in viscosity ranging from 2x to 4x occurs over the lock-in stress for each sample, indicating that the lock-in process inhibits lateral sheet motion. This suggests that the lock-in point does not just represent a gradual overtaking of the internal recovery forces, but instead marks a distinct change in the network properties, manifesting here as increased inter-sheet interaction and therefore reduced sheet flow. This viscosity increase is also observed for the MoS_2 network at ~8 MPa, despite MoS_2 not exhibiting a change in recovery response associated with lock-in at this point. This also suggests that the MoS_2 network undergoes a “lock-in-like” morphological change under sufficient stress, but that the state is reversed by comparatively strong recovery forces when load is removed.

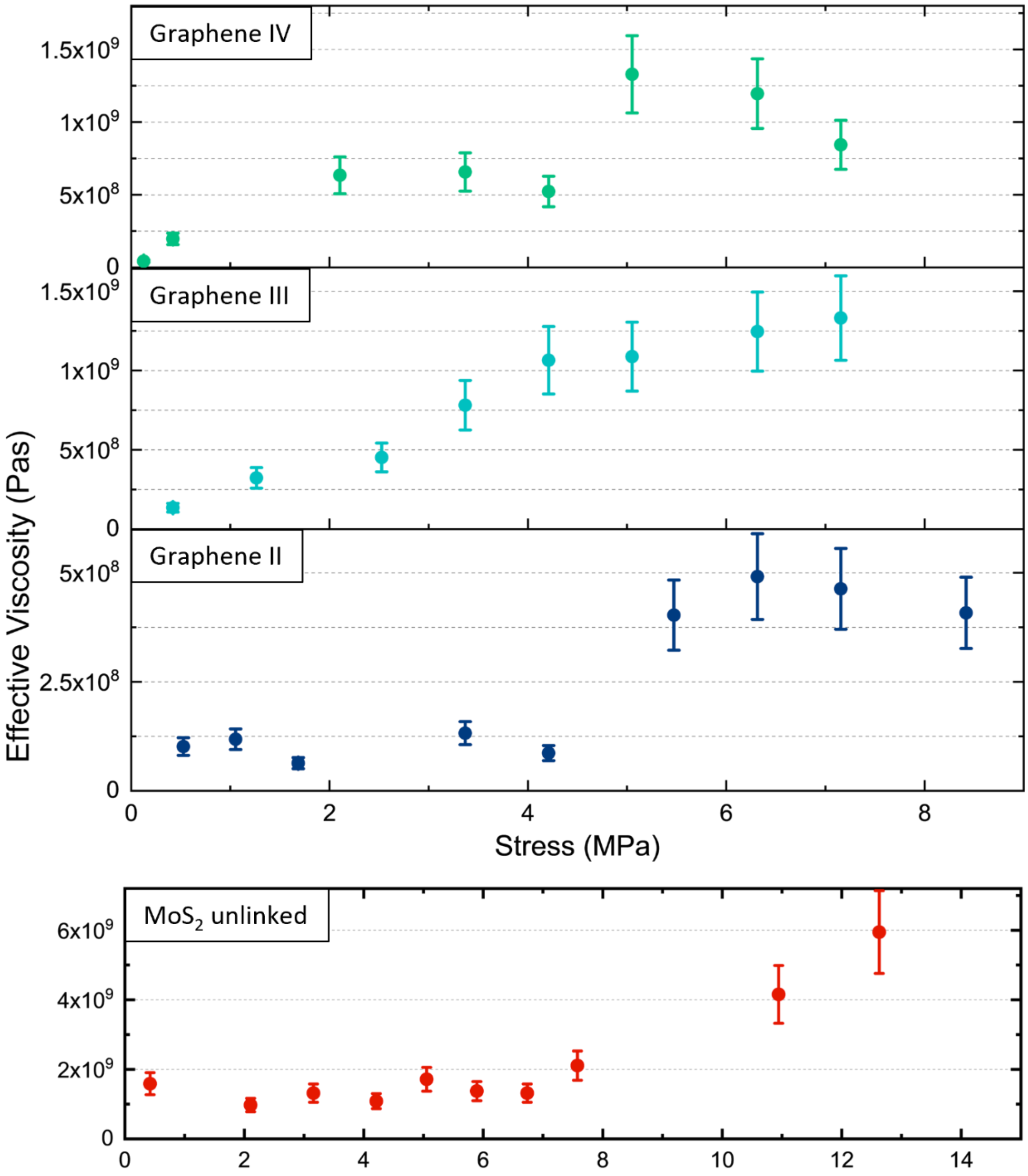

Fig. 7.14, *Measured relative viscosities for samples II – IV and the unprocessed* MoS_2 *sample, revealing for all samples a slowly increasing viscosity as porosity is reduced by compression. All samples display a significantly decreased creep behaviour (increased effective viscosity) at the lock-in stress, displaying a change in response to mechanical stress at lock-in*

We note that the viscosity jump for sample *IV* does not correspond precisely to that from the recovery data. This is likely due to the large amount of inhomogeneity and roughness associated with sprayed samples with such large flakes. As such I determined the lock-in point for this sample from the recovery data which is supported by more datapoints and is in line with the other results. The viscosity discontinuities are in exact agreement with the recovery data for all other samples.

Interestingly, while cross-linked MoS_2 has a higher viscosity pre lock-in compared to its unprocessed counterpart as seen in Chapter 6 (attributable to increased resistance to lateral sheet motion from the linking molecules), it was not observed to have an appreciable increase at the lock-in point, which may indicate some level of resistance to the lock-in effect compared to unprocessed networks. As the lock-in process appears to occur over a discrete compressive range, it is possible that the chain groups that constitute the cross linking inhibit the lock-in process either through resisting flake motion, or being an additional chemical 'impurity' that may inhibit vdW interaction between highly compressed sheets through steric hinderance. More testing is required to elucidate the mechanism behind this behaviour however.

7.4.3 Network Compression at Lock-in Stress

The abrupt appearance of the lock-in effect in the recovery vs compression data raises the potential of its direct observation as a distinct event in individual indentation curves. To investigate this, creep experiments were performed to examine if the discrete nature of the lock-in phenomenon could be observed at the lock-in stress. The same procedure used to determine effective viscosity was employed. I observed a sudden jump in the punch displacement for creep stress held around the lock-in point, shown for samples *II – IV* and the uncrosslinked MoS_2 in Fig. 7.15. This sudden displacement was not observed in creep tests that were performed at stresses other than the lock-in stress for each sample.

This sudden displacement varies in magnitude between samples but is in the order of 10 – 50 nm. It represents a sudden collective movement of the entire block of material below the 55 µm diameter punch in a single instance at (near) constant stress. The speed at which this occurs excludes conventional creep effects already described here, as well as collapse of inhomogeneities such as a singular large pore collapsing (which would manifest as a slower overall compression as the puck rearranges to accommodate sudden dislocation movement), and would thus seem to be a result of a collective behaviour within the entire puck of material.

The creep time (and thus amount of slow creep displacement) at which the sudden displacement occurs varies also, occurring as early as 50 s and as late as 400 s into the hold time. Our tests do not reveal a trend of this time dependence with network parameters. On rare occasions, the displacement can occur as a successive, two-stage process (as shown in Fig. 7.15 for sample *IV*). This two-stage process has been observed only on samples with larger nanosheet sizes such as sample *IV*.

The 2.5 nm amplitude harmonic stiffness signal collected during these tests also reveals a change in material properties at this point as also shown in Fig. 7.15. The harmonic contact stiffness is plotted against the time on sample (middle panels) and against the tip displacement (bottom panels), represented as a compression factor (see Eq. 1.11), for each sample. The harmonic stiffness increases at a gradual rate as the material creeps, which is expected as free volume reduces. At the compressive jump there is a sudden increase in stiffness which is larger for networks of larger sheets. The creep response then also changes, evidenced by a discrete change of slope in the harmonic stiffness with time. A similar change in slope in the harmonic stiffness with compression factor reveals a change in the material stiffness response with compression. And increase in harmonic stiffness, and decrease in the rate of creep are observed also at the lock-in point as discussed in the above sections, and are consistent with that expected from a sudden puck compression. The magnitude of these changes depend on the nanosheet parameters and as such is variable between samples.

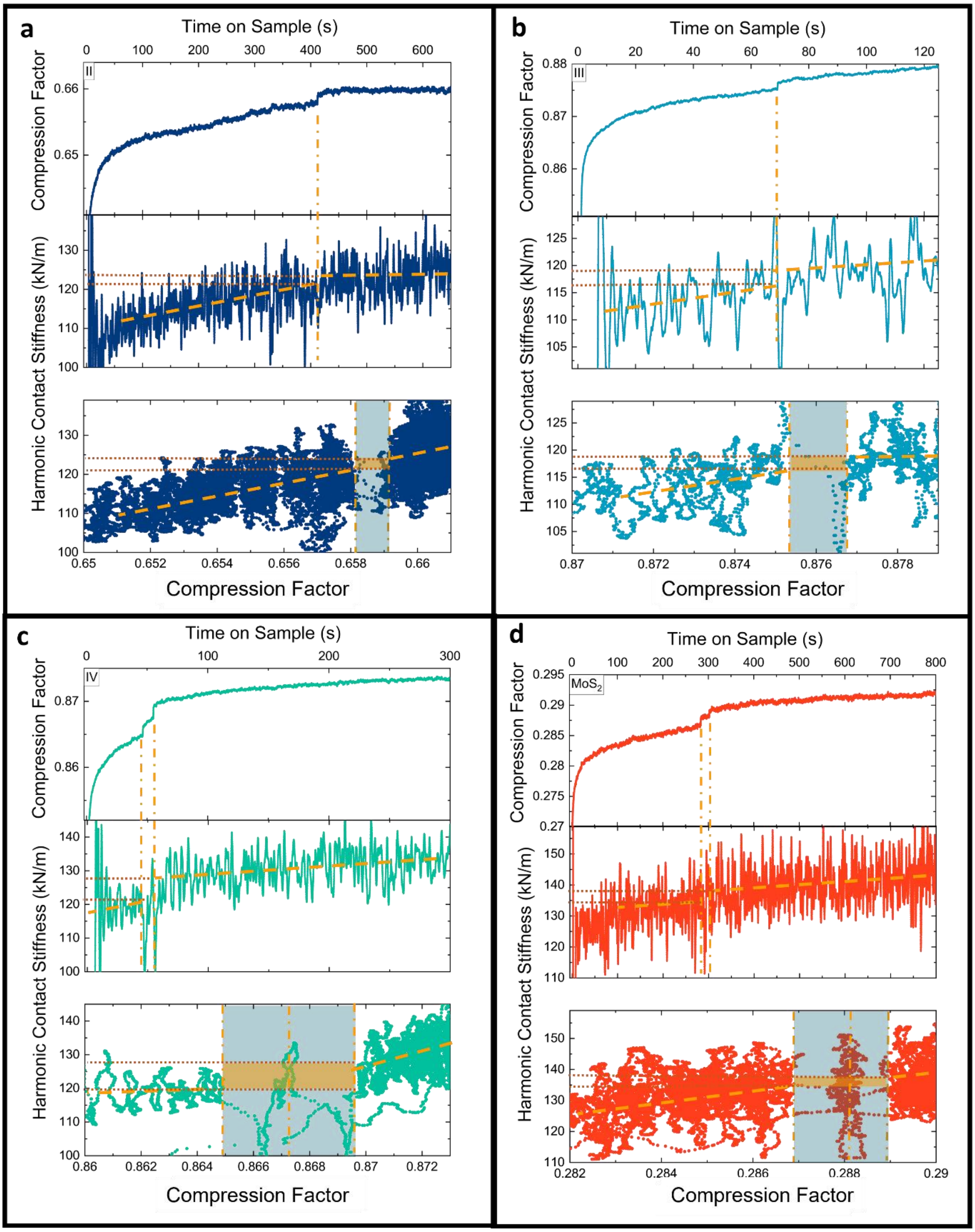

***Fig. 7.15**, Rapid compression of nanosheet networks at a held load at the lock-in point, shown for samples II through IV in **(a-c)** respectively, and the unprocessed MoS_2 sample in **(d)**. The upper panel shows the creep response as a compression factor vs time on sample. The middle panels show the corresponding harmonic stiffness vs time, and the bottom panels show the harmonic stiffness vs compression factor, displaying small but sudden jump in harmonic stiffness at this point. These effects are consistent with those observed at the lock-in point and with a sudden uniform network compression*

The precise cause of this creep-test jumps is as of yet to be determined. It's location at the lock-in stress might suggest a cascading avalanche of increased sheet interaction through small pore collapse, or of local wrinkling deformations to increase sheet conformity in low porosity regions. It could also be attributed to generation and extrusive propagation of a shear band within the compressed volume. Alternatively, the jump phenomena may arise from an interfacial effect. For example, a cohesive interface failure may occur as material starts to extrude from below the punch as has been observed previously for polymer films [291]. However, the existence of the compressive jump only at the lock-in stress (for both MoS_2 and graphene films which have very different lock-in stresses), the associated change in stiffness and creep response after the compressive jump (which is in line with that seen at lock-in), and the magnitude of stiffness increase trending with the size of sheets within the network, all suggest it to be fundamentally related to the lock-in phenomenon. In this case, it suggests that lock-in occurs as a discrete event at a certain stress threshold, and may manifest as a small instantaneous compression of the entire compressed network. Future work may explore this displacement further and more conclusively shine light on the mechanism surrounding this effect.

7.5 Conclusions

Large strain out of plane uniaxial compression was explored on thin film networks of sprayed liquid phase exfoliated graphene and MoS_2 nanosheet networks. Morphological changes that have an effect on electrical transport and mechanical properties of the networks were explored as a function of increasing nanosheet volume fraction induced by the compression, in the range of ϕ = 0.61 to 0.82. Parameters that are known to affect conductivity such as sheet alignment were shown to increase significantly in this range.

A large degree of long timescale strain recovery that undoes compressive morphological tailoring after high strain compression was observed and examined on these networks, showing to recover much of the applied compression over long time periods. Recovery was shown to reduce to near zero after an application of pressure exceeding a critical stress point. This was attributed to Van-der-Waals locking of the sheets when sheet contact is increased sufficiently. This lock-in was shown to be able to reduce strain recovery significantly even over long timescales, maintaining the effect over the entire three month timescale tested. The stress required to induce this lock-in effect was shown to be in the range of 5 MPa for graphene networks and 7.5 MPa for MoS_2 networks and lightly dependent on average sheet size within the network. Such uniaxial pressures are approachable with mass manufacturing techniques such as R2R processing.

Changes in network mechanical behaviour were explored at this lock-in point for both graphene and MoS_2 networks, evidenced by greatly reduced creep response, higher stiffness, and a distinct change in the strain hardening mechanism. I also note a lower reduction in recovery upon introduction of lateral sheet motion in the uniaxial compression, indicating recovery may be reduced at lower pressures than the lock-in point via the introduction of shear oscillations during uniaxial compression. Parallels with these findings may be drawn to similar confined geometry experiments on polymer films whereby the polymer was found to densify over a small compressive range deep into the extrusion regime beyond what is expected from hydrostatic pressure alone, in a similar manner to the lock-in behaviour presented here [241]. It is therefore important to consider the possibility of the lock-in effect being due to sudden morphological change induced by a combination of high hydrostatic pressure and shear flow that can manifest in amorphous solids in general. If so, it can help shine light not only on the deformation of nanosheet networks, but also on the response of non equilibrium solids under confined high pressure shear deformation.

Ch 8 : Conclusion and Future Work

8.1 Conclusion

In this thesis I have presented exploration of the mechanics of thin film amorphous materials predominantly through a unique nanomechanical testing framework dubbed the Layer Compression Test. This test utilises an indenting punch with diameter many times the film thickness, well aligned to a thin film supported on a stiff substrate, and allows for monitoring of compressive stress vs strain behaviour to significant penetration depths. The LCT allows for monitoring of a range of mechanical properties not easily extracted from traditional nanoindentation techniques, such as the yield transition from elastic to plastic deformation, and pressure induced stiffening. This can help shine light on the elusive mechanisms of plastic deformation in amorphous media, and opens up the possibility of rigorous mechanical exploration of supported thin film materials. On top of this, the large contact area allows for mechanical analysis of materials with high degrees of inhomogeneity and/or surface roughness, and is leveraged here to explore for the first time the compressive mechanical response of printed nanosheet network thin films. This granular nanoscale flake system offers exciting avenues of mechanical exploration owing to its unique morphological nature, while also having direct technological applications through compressive morphological tailoring for improved electromechanical properties.

In Chapter 4, I explored the stress and strain behaviour of the LCT in the elastic regime up until yield in an ideal elastic-plastic material using finite element analysis, for a range of contact aspect ratios, α, and film to substrate modulus ratios, S. I found that a simple analytical correction to the effective true strain largely corrects for deviations from true uniaxial strain behaviour for the range of explored parameters and allows for extraction of the confined modulus to within 5% deviation from that obtained from pure uniaxial strain testing. Furthermore, it was found that with this correction applied, competing error effects acted in favour of contact aspect ratios favourable for experimental testing, with deviations in the range of 2% achievable as α approaches 10.

Chapter 5 explored pressure dependent effects in thin film materials, and how these may manifest in confined uniaxial compressive testing such as the LCT. I also explored to what degree the LCT may deviate from ideal confinement in uniaxial strain testing via introduction of additional shear stress. I found that this can allow yielding of amorphous materials such as PMMA that have otherwise not shown yielding behaviour in confined uniaxial compression, while predominantly maintaining a compressive state comparably to uniaxial strain in the bulk of the compressed region. This may allow for exploration of plastic deformation under compressive pressure in highly pressure sensitive materials in a single uniaxial test. I explored also pressure dependent stiffening up to and beyond the yield point on thin film polystyrene, as well as the same for a nanosheet network thin film, and found similarity between the two despite vastly different morphological characteristics. Finally, I observed reduced chain motion in a compressed polystyrene thin film through β-NMR analysis of a patterned vs unpatterned film.

In Chapter 6 I provided a framework of mechanical testing of printed nanosheet network thin films using the layer compression test. I found a strong viscoelastic response on compression and characterised an effective modulus for graphene networks with a range of sheet sizes, finding modulus to decrease inversely to the constituent sheet thickness. I also characterised the yield stress and strain on compression, finding the yield stress largely independent of compression in the range explored, as well as characterising the viscous component of deformation through fitting to a viscoelastic model. I explored also the effect of chemical cross linking on the mechanical response by comparing otherwise identical cross-linked and pristine MoS_2 networks, finding that the cross linking increased resistance to lateral flake motion, as well as significantly increased the out of plane tensile strength and noticeably decrease the creep behaviour, with little to no change in the compressive mechanical properties.

Chapter 7 extended the analysis of uniaxial compression on nanosheet networks to high strain compressions, with particular focus on the recovery of the network after the removal of compressive load, and on morphological changes after high compressive strains. I found a large degree of strain recovery after even high strain compressions beyond the yield stress over long periods. This recovery was seen to reduce significantly at the onset of in plane confinement failure associated with large flake motion through the compressed puck, suggesting a strong role in shear deformation in the network recovery. More starkly, I found the recovery to reduce to near zero over a small strain range dubbed the lock-in point. This region was found to be associated with a region of rapid stiffening with applied stress, and with a noticeable decrease in the creep of the network. I characterised also several morphological parameters with applied compression through analysis of FIB cross sections, such as porosity, pore size, pore aspect ratio, pore circularity, and sheet alignment, which may help shine further light on the electrical and mechanical reliance on morphological parameters. While primarily empirical in nature as presented in this thesis, it opens the door for comparison to analytical models

8.2 Future Work

Recent work utilising the layer compression test, including that presented here, has made clear that it is a powerful tool for exploring the compressive mechanical characteristics of thin film materials with minimal required sample preparation. Much work remains to be done however to fully characterise the intricacies of the LCT compared to the uniaxial strain condition it emulates. While Chapter 4 of this thesis provided detailed finite element analysis of the LCT for a range of contact geometries, and the resulting relation to an idealised US compression, it did so for the elastic regime only. Similar studies surrounding the yield point and plastic deformation would further allow the LCT to be used to explore the complex plastic behaviour of amorphous films with a higher degree of fidelity. This would necessitate a comprehensive finite element study combined with analytical analysis to correct for imperfections in the confined plastic response such as at the punch periphery and for the bending substrate. Extending the FEA analysis to 3D from the radially symmetric 2D framework employed in Chapter 4 may also be of interest for exploration of plasticity.

As well as this, the problem of calibration remains an issue in the LCT. With fused silica often acting as a calibration sample for Berkovich tips, a similar standard should be adopted for the LCT to account for elastic deformation of the punch, misalignment between the applied load direction and the surface normal, and manufacturing inaccuracies in the punch. Such a calibration material would need comparatively low modulus to allow for a stiff supporting substrate, mechanical homogeneity and isotropy, be thermally stable over long time periods, and chemically stable in atmospheric conditions. This rules out polymeric materials for which ageing processes can often alter their mechanical response. Low modulus metallic or crystalline materials may be suitable but so far have presented other problems. Selenium is promising but difficult to manufacture, while Europium would be suitable if not for heavy oxidation in atmospheric conditions. Due to the large contact area of the LCT, atomic level homogeneity is not necessarily a requirement as long as the material experiences little to no aging effects. Future explorations will focus around alloys and compounds.

Analysis of nanosheet network mechanics leaves a host of potential research avenues available. Extending the empirical observations in Chapter 7 to analytical models is currently being explored. Of particular interest for future experimental work is the role of shear in compressive deformation. Shear has already been seen to reduce the recovery rate of the networks at the onset of extrusion in Chapter 7, and is known to be the key factor in the onset of plasticity in materials in general. The granular and semi aligned nanosheet structure of the networks is expected to be highly sensitive to shear deformation, and I plan to explore this in detail with injection of small amplitude oscillatory shear during confined compression by utilising a controlled shear piezo mounted underneath the supporting substrate [270]. This will allow for a comprehensive study of the effect of oscillation frequency and amplitude on the compressive network response, and help elucidate the role of shear in the recovery and yield in these systems. Finally, studies directly correlating mechanical processing and morphological changes to opto-electronic property outcomes has yet to be achieved. This is potentially a very large body of work with great promise both for fundamental understanding of the deformation mechanics as well as technology optimization.

Of immediate technological interest is extending the morphological improvements observed from uniaxial compression from local indentation zones to bulk film output. This will necessitate careful consideration of the role of compression on morphological changes. While this has been explored somewhat in Chapter 7, it is complicated by the adhesion present between the punch and sample surface, which acts to introduce tensile strains upon unload. Reducing the adhesion between the tip and surface should act to provide an understanding of compressive forces on the morphology of the system, without being as significantly altered by a subsequent tensile portion. I have begun exploring this, with large areas on Sample *II* (being the sample imaged with FIB-SEM technique in Chapter 7) being passivated with a thin ~30 nm layer of gold sputter coated on the surface. Indents to the same peak loads as explored in this thesis have been performed on this region and partially imaged using the FIB-SEM tomography technique, and while analysis is still ongoing, porosity in the region with 40 mN maximum applied load has seen porosity reduced to ~12%, as compared to ~20% in the non-passivated case presented in Chapter 7. This suggests a large role of the tensile unload on the network morphology that is to be explored. A comparison between the two cases is likely to make for an interesting study, given that full passivation, with for example a gold layer, may not be technologically feasible in all mass production applications, so limitations on morphological improvement with an unpassivated surface may be of interest.

With high technological interest surrounding nanosheet thin film networks, I ultimately plan on extending our morphological improvements to mass production techniques such as roll-to-roll compression. This is achievable with a variable pressure R2R system within the group, however some engineering challenges remain to reach the pressures required for high morphological improvement with this system. In absence of this, samples of sprayed graphene on flexible substrates such as Kapton and PET have been compressed in a hydraulic press to various high pressures in order to test the effect on conductivity ex-situ. An uncompressed and highly compressed (~175 MPa applied over 100s) sample are shown in Fig 8.1 (a) and (b) respectively. The network properties such as average sheet size and initial porosity are yet to be fully characterised but are expected to be similar to Sample *II* from the preparation methodology. The resulting sheet resistance measurements as a function of approximate applied pressure are shown in Fig 8.1 (c), and show greatly reduced sheet resistance with pressure, with significantly diminishing returns after a point, in line with the lock-in stress.

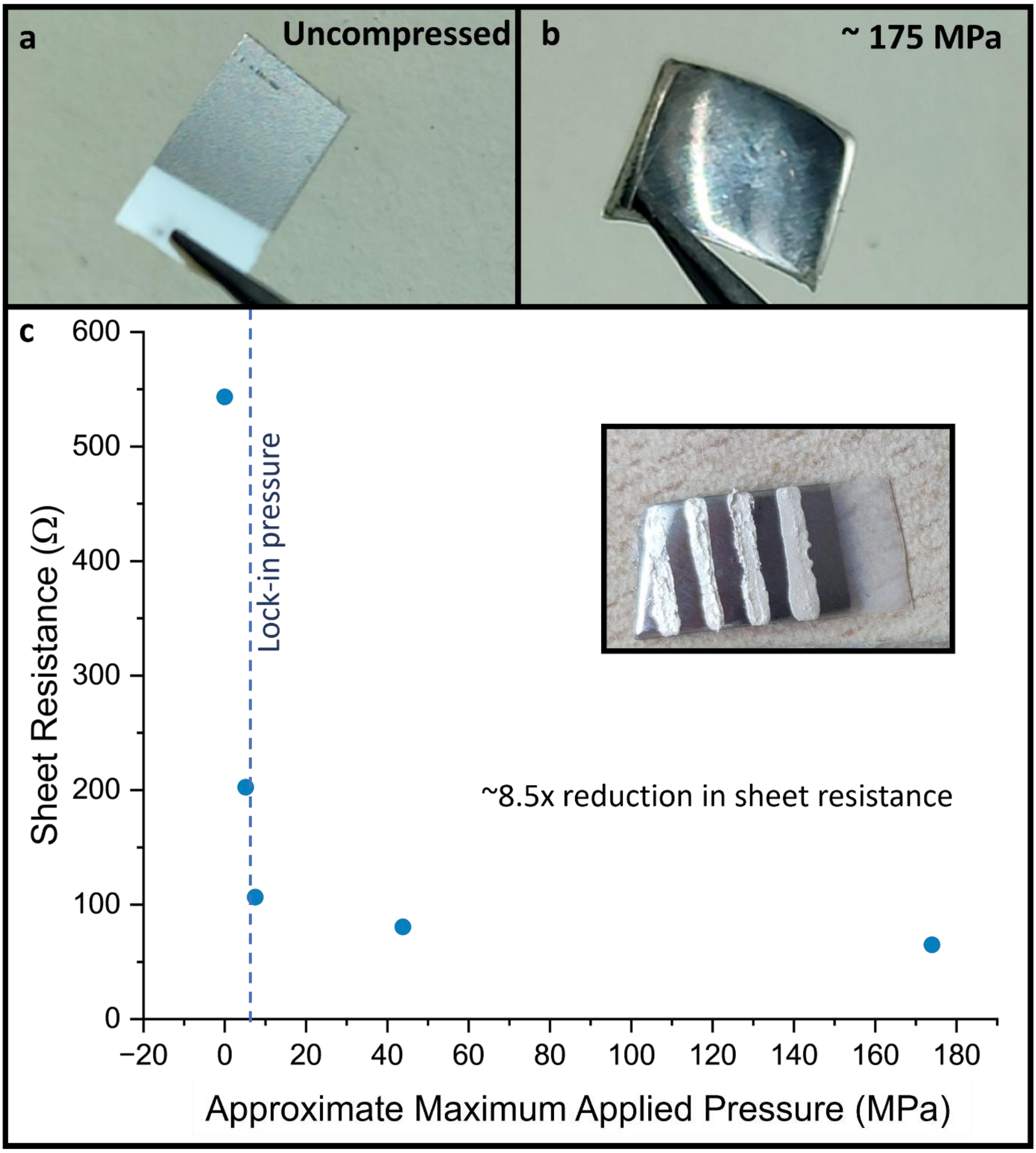

Fig 8.1, *The effect of uniaxial compression on the sheet resistance of printed graphene networks.* ***(a)*** *An uncompressed graphene sample on a PET substrate.* ***(b)*** *A sample from the same preparation batch compressed to ~175 MPa over the course of 100s in a hydraulic press.* ***(c)*** *sheet resistance as a function of approximate applied pressure. Inset shows a sample with silver paint electrodes applied for four point probe measurement*

Initial FIB-SEM images on these highly compressed networks reveal a highly packed morphology with porosities in the range of ~2%, and much decreased surface roughness, shown below in Fig 8.2. The decreased surface roughness is promising for tribological applications, and for device manufacture where surface roughness has been known to interfere with printed transistor manufacture and also is known to cause electrical shorts. This is to be explored further in the upcoming experiments. Of further interest are initial scratch testing measurements using a multi-dimensional iMicro indenter and sharp Berkovich tip that suggest a scratch resistance approaching two orders of magnitude higher than for the uncompressed network, largely mitigating the fragility of the sprayed network that is a known issue for devices produced with such printed networks. While all of these results are promising, they are preliminary in nature and will be explored more extensively in the coming months.

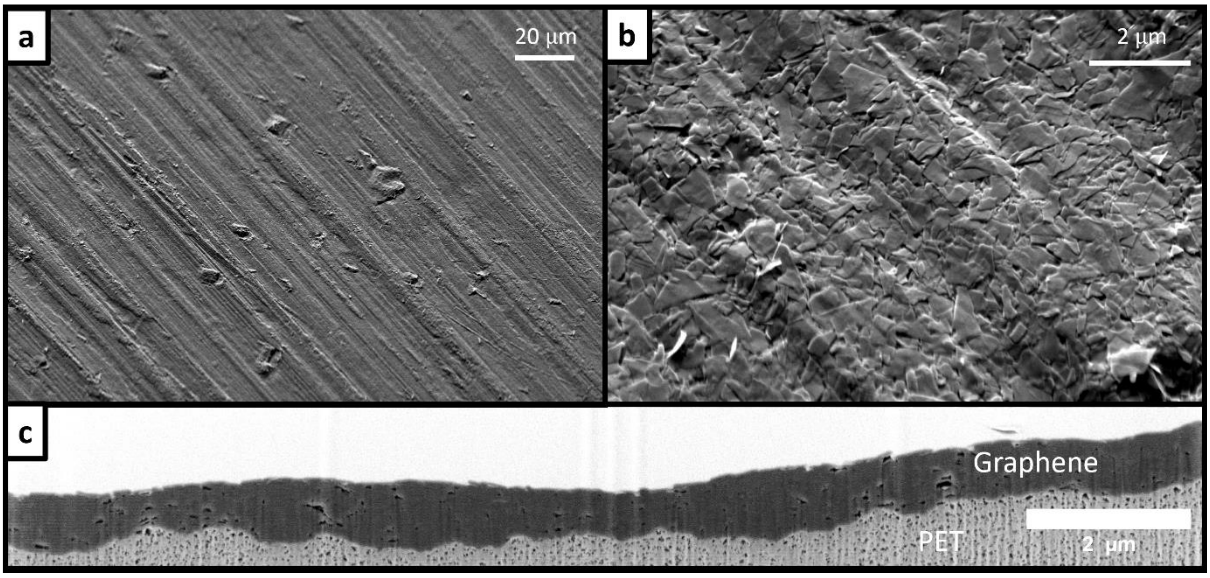

Fig 8.2, *FIB-SEM analysis of a sprayed graphene sample on PET polymer sheet compressed to ~175 MPa.* ***(a)*** *and* ***(b)*** *show top down images of the compressed network, with surface roughness manifesting from polishing imperfections of the stub used for compression.* ***(c)*** *A FIB-SEM cross section of the same network, revealing an extremely low surface roughness compared to uncompressed counterparts and porosity in the range of ~2%*

References

1. Echeverría, I., et al., *Enthalpy recovery, creep and creep–recovery measurements during physical aging of amorphous selenium.* Journal of Non-Crystalline Solids, 2003. **324**(3): p. 242-255.
2. Li, P., et al., *Toward Robust Macroscale Superlubricity on Engineering Steel Substrate.* Advanced Materials, 2020. **32**(36): p. 2002039.
3. Song, H., et al., *Self-forming oriented layer slip and macroscale super-low friction of graphene.* Applied Physics Letters, 2017. **110**(7): p. 073101.
4. Makhlouf, A.S.H. and N.Y. Abu-Thabit, *Advances in smart coatings and thin films for future industrial and biomedical engineering applications*. 2019: Elsevier.
5. Kelly, A.G., et al., *All-printed thin-film transistors from networks of liquid-exfoliated nanosheets.* Science, 2017. **356**(6333): p. 69.
6. Kelly, A.G., et al., *Highly Conductive Networks of Silver Nanosheets.* Small, 2022. **18**(14): p. 2105996.
7. Lee, K., et al., *Highly conductive and long-term stable films from liquid-phase exfoliated platinum diselenide.* Journal of Materials Chemistry C, 2023. **11**(2): p. 593-599.
8. Oliver, W.C. and G.M. Pharr, *An improved technique for determining hardness and elastic modulus using load and displacement sensing indentation experiments.* Journal of Materials Research, 1992. **7**(6): p. 1564-1583.
9. Tsui, T.Y. and G.M. Pharr, *Substrate effects on nanoindentation mechanical property measurement of soft films on hard substrates.* Journal of Materials Research, 1999. **14**(1): p. 292-301.
10. Chechenin, N.G., J. Bøttiger, and J.P. Krog, *Nanoindentation of amorphous aluminum oxide films I. The influence of the substrate on the plastic properties.* Thin Solid Films, 1995. **261**(1): p. 219-227.
11. Jönsson, B. and S. Hogmark, *Hardness measurements of thin films.* Thin Solid Films, 1984. **114**(3): p. 257-269.
12. Saha, R. and W.D. Nix, *Effects of the substrate on the determination of thin film mechanical properties by nanoindentation.* Acta Materialia, 2002. **50**(1): p. 23-38.
13. Anderson, P.M., J.P. Hirth, and J. Lothe, *Theory of dislocations*. 2017: Cambridge University Press.
14. Oleinik, E.F., et al., *Plastic Deformation in Disordered Solids: The State of the Art and Unresolved Problems*, in *Problems of Nonlinear Mechanics and Physics of Materials*. 2019, Springer, Cham. p. 313-332.
15. *Material Testing Market Size and Forecast*. 2021: Verified Market Research.
16. Zhang, C., et al., *Stamping of Flexible, Coplanar Micro-Supercapacitors Using MXene Inks.* Advanced Functional Materials, 2018. **28**(9): p. 1705506.
17. Li, H., et al., *Flexible All-Solid-State Supercapacitors with High Volumetric Capacitances Boosted by Solution Processable MXene and Electrochemically Exfoliated Graphene.* Advanced Energy Materials, 2017. **7**(4): p. 1601847.
18. Caffrey, E., et al., *Quantifying the Piezoresistive Mechanism in High-Performance Printed Graphene Strain Sensors.* ACS Applied Materials & Interfaces, 2022. **14**(5): p. 7141-7151.
19. Ren, J., et al., *Environmentally-friendly conductive cotton fabric as flexible strain sensor based on hot press reduced graphene oxide.* Carbon, 2017. **111**: p. 622-630.
20. Carey, T., et al., *Fully inkjet-printed two-dimensional material field-effect heterojunctions for wearable and textile electronics.* Nature Communications, 2017. **8**(1): p. 1202.

21. Li, J., et al., *Recent progress in polymer/two-dimensional nanosheets composites with novel performances.* Progress in Polymer Science, 2022. **126**: p. 101505.
22. Hang, G., et al., *Review of MXene Nanosheet Composites for Flexible Pressure Sensors.* ACS Applied Nano Materials, 2022. **5**(10): p. 14191-14208.
23. Ndieyira, J.W., et al., *Nanomechanical detection of antibiotic–mucopeptide binding in a model for superbug drug resistance.* Nature Nanotechnology, 2008. **3**(11): p. 691-696.
24. Fritz, J., et al., *Translating Biomolecular Recognition into Nanomechanics.* Science, 2000. **288**(5464): p. 316-318.
25. Gindl, W., et al., *Mechanical properties of spruce wood cell walls by nanoindentation.* Applied Physics A, 2004. **79**(8): p. 2069-2073.
26. Hayot, C.M., et al., *Viscoelastic properties of cell walls of single living plant cells determined by dynamic nanoindentation.* Journal of Experimental Botany, 2012. **63**(7): p. 2525-2540.
27. Vettiger, P., et al., *The "millipede" - nanotechnology entering data storage.* IEEE Transactions on Nanotechnology, 2002. **1**(1): p. 39-55.
28. King, W.P., et al., *Atomic force microscope cantilevers for combined thermomechanical data writing and reading.* Applied Physics Letters, 2001. **78**(9): p. 1300-1302.
29. Davis, Z.J., et al., *AFM lithography of aluminum for fabrication of nanomechanical systems.* Ultramicroscopy, 2003. **97**(1): p. 467-472.
30. Landis, S., *NanoImprint Lithography*, in *Nano-Lithography*. 2013. p. 87-168.
31. Brazil, O., et al., *In situ measurement of bulk modulus and yield response of glassy thin films via confined layer compression.* Journal of Materials Research, 2020. **35**(6): p. 644-653.
32. Brazil, O., et al., *Extrinsic Plastic Hardening of Polymer Thin Films in Flat Punch Indentation.* arXiv, 2020.
33. Sinnott, A.D., O. Brazil, and G.L. Cross, *The effect of contact aspect ratio and film to substrate elastic modulus ratio on stress vs. strain up to the point of yield during flat punch thin film indentation of an elastic-plastic film.* Frontiers in Materials, 2022. **9**: p. 906204.
34. Cross, G.L.W., et al., *Variable temperature thin film indentation with a flat punch.* Review of Scientific Instruments, 2008. **79**(1): p. 013904.
35. Brazil, O., et al., *Extrinsic plastic hardening of polymer thin films in flat punch indentation.* Philosophical Magazine, 2021. **101**(11): p. 1327-1342.
36. Hernandez, Y., et al., *High-yield production of graphene by liquid-phase exfoliation of graphite.* Nature Nanotechnology, 2008. **3**(9): p. 563-568.
37. Gabbett, C., et al., *3D-imaging of Printed Nanostructured Networks using High-resolution FIB-SEM Nanotomography.* arXiv preprint arXiv:2301.11046, 2023.
38. Kaufman, J.D. and C.M. Klapperich, *Surface detection errors cause overestimation of the modulus in nanoindentation on soft materials.* Journal of the Mechanical Behavior of Biomedical Materials, 2009. **2**(4): p. 312-317.
39. Jiang, W.-G., J.-J. Su, and X.-Q. Feng, *Effect of surface roughness on nanoindentation test of thin films.* Engineering Fracture Mechanics, 2008. **75**(17): p. 4965-4972.
40. Epshtein, S.A., F.M. Borodich, and S.J. Bull, *Evaluation of elastic modulus and hardness of highly inhomogeneous materials by nanoindentation.* Applied Physics A, 2015. **119**(1): p. 325-335.
41. Swadener, J.G., J.-Y. Rho, and G.M. Pharr, *Effects of anisotropy on elastic moduli measured by nanoindentation in human tibial cortical bone.* Journal of Biomedical Materials Research, 2001. **57**(1): p. 108-112.
42. Ward, I.M. and J. Sweeney, *Mechanical properties of solid polymers*. 2012: John Wiley & Sons.
43. Rouse, P.E., Jr., *A Theory of the Linear Viscoelastic Properties of Dilute Solutions of Coiling Polymers.* The Journal of Chemical Physics, 1953. **21**(7): p. 1272-1280.
44. Roth, C.B., *Polymer Glasses*. 1 ed. 2016, Boca Raton: CRC Press. 572.
45. Doi, M., S.F. Edwards, and S.F. Edwards, *The theory of polymer dynamics*. Vol. 73. 1988: oxford university press.

46. Wang, W.-H., C. Dong, and C. Shek, *Bulk metallic glasses.* Materials Science and Engineering: R: Reports, 2004. **44**(2-3): p. 45-89.
47. Hunter, G.L. and E.R. Weeks, *The physics of the colloidal glass transition.* Reports on Progress in Physics, 2012. **75**(6): p. 066501.
48. Angell, C.A., et al., *Relaxation in glassforming liquids and amorphous solids.* Journal of Applied Physics, 2000. **88**(6): p. 3113-3157.
49. Ngai, K.L. and M. Paluch, *Classification of secondary relaxation in glass-formers based on dynamic properties.* The Journal of Chemical Physics, 2003. **120**(2): p. 857-873.
50. Brandrup, J., et al., *Polymer handbook*. Vol. 89. 1999: Wiley New York.
51. Mark, J.E., *Physical Properties of Polymers Handbook* Springer. 2007, New York.
52. Hoggan, E.N., et al., *Spin Coating of Photoresists Using Liquid Carbon Dioxide.* Industrial & Engineering Chemistry Research, 2004. **43**(9): p. 2113-2122.
53. Pham, H.T., et al., *Ferroelectric/Dielectric Double Gate Insulator Spin-Coated Using Barium Titanate Nanocrystals for an Indium Oxide Nanocrystal-Based Thin-Film Transistor.* ACS Applied Materials & Interfaces, 2016. **8**(11): p. 7248-7256.
54. Tippo, T., et al., *The effects of solvents on the properties of ultra-thin poly (methyl methacrylate) films prepared by spin coating.* Thin Solid Films, 2013. **546**: p. 180-184.
55. Liu, C., et al., *Self-assembly of semiconductor/insulator interfaces in one-step spin-coating: a versatile approach for organic field-effect transistors.* Physical Chemistry Chemical Physics, 2013. **15**(21): p. 7917-7933.
56. Hong, Y.-K., et al., *Controlled two-dimensional distribution of nanoparticles by spin-coating method.* Applied Physics Letters, 2002. **80**(5): p. 844-846.
57. Xu, L., et al., *Transparent, Superhydrophobic Surfaces from One-Step Spin Coating of Hydrophobic Nanoparticles.* ACS Applied Materials & Interfaces, 2012. **4**(2): p. 1118-1125.
58. Liu, S.-W., et al., *Robust microscale superlubricity under high contact pressure enabled by graphene-coated microsphere.* Nature Communications, 2017. **8**(1): p. 14029.
59. Lin, Z., et al., *Solution-processable 2D semiconductors for high-performance large-area electronics.* Nature, 2018. **562**(7726): p. 254-258.
60. Danglad-Flores, J., S. Eickelmann, and H. Riegler, *Deposition of polymer films by spin casting: A quantitative analysis.* Chemical Engineering Science, 2018. **179**: p. 257-264.
61. Hall, D.B., P. Underhill, and J.M. Torkelson, *Spin coating of thin and ultrathin polymer films.* Polymer Engineering & Science, 1998. **38**(12): p. 2039-2045.
62. Herrmann, H.J., J.-P. Hovi, and S. Luding, *Physics of dry granular media*. Vol. 350. 2013: Springer Science & Business Media.
63. Jaeger, H.M., S.R. Nagel, and R.P. Behringer, *Granular solids, liquids, and gases.* Reviews of Modern Physics, 1996. **68**(4): p. 1259-1273.
64. Rao, K.K., P.R. Nott, and S. Sundaresan, *An introduction to granular flow*. Vol. 490. 2008: Cambridge university press Cambridge.
65. Walton, O.R. and R.L. Braun, *Viscosity, granular-temperature, and stress calculations for shearing assemblies of inelastic, frictional disks.* Journal of Rheology, 1986. **30**(5): p. 949-980.
66. Da Cruz, F., et al., *Viscosity bifurcation in granular materials, foams, and emulsions.* Physical Review E, 2002. **66**(5): p. 051305.
67. Lun, C.K.K., et al., *Kinetic theories for granular flow: inelastic particles in Couette flow and slightly inelastic particles in a general flowfield.* Journal of Fluid Mechanics, 1984. **140**: p. 223-256.
68. Lade, P.V. and R.B. Nelson, *Modelling the elastic behaviour of granular materials.* International Journal for Numerical and Analytical Methods in Geomechanics, 1987. **11**(5): p. 521-542.
69. Liu, Z., et al., *Interlayer binding energy of graphite: A mesoscopic determination from deformation.* Physical Review B, 2012. **85**(20): p. 205418.
70. Kou, B., et al., *Granular materials flow like complex fluids.* Nature, 2017. **551**(7680): p. 360-363.

71. Gnoli, A., et al., *Controlled Viscosity in Dense Granular Materials.* Physical Review Letters, 2018. **120**(13): p. 138001.
72. Hicher, P.-Y., *Elastic Properties of Soils.* Journal of Geotechnical Engineering, 1996. **122**(8): p. 641-648.
73. Liao, C.L., et al., *Pressure-dependent elastic moduli of granular assemblies.* International Journal for Numerical and Analytical Methods in Geomechanics, 2000. **24**(3): p. 265-279.
74. van Hecke, M., *Jamming of soft particles: geometry, mechanics, scaling and isostaticity.* Journal of Physics: Condensed Matter, 2009. **22**(3): p. 033101.
75. Donev, A., et al., *Improving the Density of Jammed Disordered Packings Using Ellipsoids.* Science, 2004. **303**(5660): p. 990-993.
76. Aharonov, E. and D. Sparks, *Stick-slip motion in simulated granular layers.* Journal of Geophysical Research: Solid Earth, 2004. **109**(B9).
77. Staron, L. and E.J. Hinch, *Study of the collapse of granular columns using two-dimensional discrete-grain simulation.* Journal of Fluid Mechanics, 2005. **545**: p. 1-27.
78. Holtzman, R., D.B. Silin, and T.W. Patzek, *Mechanical properties of granular materials: A variational approach to grain-scale simulations.* International Journal for Numerical and Analytical Methods in Geomechanics, 2009. **33**(3): p. 391-404.
79. Vescovi, D., et al., *Plane shear flows of frictionless spheres: Kinetic theory and 3D soft-sphere discrete element method simulations.* Physics of Fluids, 2014. **26**(5): p. 053305.
80. Coniglio, A., et al., *Unifying Concepts in Granular Media and Glasses: From the Statistical Mechanics of Granular Media to the Theory of Jamming*. 2004: Elsevier.
81. Walter, P., et al., *Early Use of PbS Nanotechnology for an Ancient Hair Dyeing Formula.* Nano Letters, 2006. **6**(10): p. 2215-2219.
82. Hull, A.W., *A New Method of X-Ray Crystal Analysis.* Physical Review, 1917. **10**(6): p. 661-696.
83. Wallace, P.R., *The Band Theory of Graphite.* Physical Review, 1947. **71**(9): p. 622-634.
84. Bernal, J.D. and W.L. Bragg, *The structure of graphite.* Proceedings of the Royal Society of London. Series A, Containing Papers of a Mathematical and Physical Character, 1997. **106**(740): p. 749-773.
85. Novoselov, K.S., et al., *Electric Field Effect in Atomically Thin Carbon Films.* Science, 2004. **306**(5696): p. 666.
86. Venables, J.A., G.D.T. Spiller, and M. Hanbucken, *Nucleation and growth of thin films.* Reports on Progress in Physics, 1984. **47**(4): p. 399.
87. Nelson, D., T. Piran, and S. Weinberg, *Statistical mechanics of membranes and surfaces*. 2004: World Scientific.
88. Hideo Aoki, M.D., *Physics of Graphene*. 2013: Springer Science & Business Media.
89. Lee, C., et al., *Measurement of the Elastic Properties and Intrinsic Strength of Monolayer Graphene.* Science, 2008. **321**(5887): p. 385-388.
90. Cao, K., et al., *Elastic straining of free-standing monolayer graphene.* Nature Communications, 2020. **11**(1): p. 284.
91. *2010 Nobel Physics Laureates Prize Announcement*. 2010.
92. Mayorov, A.S., et al., *Micrometer-Scale Ballistic Transport in Encapsulated Graphene at Room Temperature.* Nano Letters, 2011. **11**(6): p. 2396-2399.
93. Nicolosi, V., et al., *Liquid Exfoliation of Layered Materials.* Science, 2013. **340**(6139): p. 1226419.
94. Bryant, W.A., *The fundamentals of chemical vapour deposition.* Journal of Materials Science, 1977. **12**(7): p. 1285-1306.
95. George, S.M., *Atomic Layer Deposition: An Overview.* Chemical Reviews, 2010. **110**(1): p. 111-131.
96. Coleman, J.N., et al., *Two-Dimensional Nanosheets Produced by Liquid Exfoliation of Layered Materials.* Science, 2011. **331**(6017): p. 568-571.
97. Su, C.-Y., et al., *High-quality thin graphene films from fast electrochemical exfoliation.* ACS nano, 2011. **5**(3): p. 2332-2339.

98. Paton, K.R., et al., *Scalable production of large quantities of defect-free few-layer graphene by shear exfoliation in liquids.* Nature Materials, 2014. **13**(6): p. 624-630.
99. Coleman, J.N., *Liquid Exfoliation of Defect-Free Graphene.* Accounts of Chemical Research, 2013. **46**(1): p. 14-22.
100. Turner, P., et al., *Controlled Sonication as a Route to in-situ Graphene Flake Size Control.* Scientific Reports, 2019. **9**(1): p. 8710.
101. Xu, Y., et al., *Liquid-Phase Exfoliation of Graphene: An Overview on Exfoliation Media, Techniques, and Challenges.* Nanomaterials (Basel), 2018. **8**(11).
102. Bergin, S.D., et al., *Multicomponent Solubility Parameters for Single-Walled Carbon Nanotube−Solvent Mixtures.* ACS Nano, 2009. **3**(8): p. 2340-2350.
103. Schuld, N. and B. Wolf, *Polymer-solvent interaction parameters.* Polymer handbook, 1999. **4**.
104. Price, G.J. and A.J. Ashworth, *Prediction of thermodynamic properties of polymer solutions using the UNIFAC group-contribution method.* Polymer, 1987. **28**(12): p. 2105-2109.
105. Lindvig, T., M.L. Michelsen, and G.M. Kontogeorgis, *A Flory–Huggins model based on the Hansen solubility parameters.* Fluid Phase Equilibria, 2002. **203**(1): p. 247-260.
106. Clarke, C.J., et al., *Measurements of the Flory−Huggins Interaction Parameter for Polystyrene−Poly(4-vinylpyridine) Blends.* Macromolecules, 1997. **30**(14): p. 4184-4188.
107. Paolucci, V., et al., *Sustainable Liquid-Phase Exfoliation of Layered Materials with Nontoxic Polarclean Solvent.* ACS Sustainable Chemistry & Engineering, 2020. **8**(51): p. 18830-18840.
108. Kim, J., et al., *Direct exfoliation and dispersion of two-dimensional materials in pure water via temperature control.* Nature Communications, 2015. **6**(1): p. 8294.
109. Coleman, J.N., *Liquid-Phase Exfoliation of Nanotubes and Graphene.* Advanced Functional Materials, 2009. **19**(23): p. 3680-3695.
110. Large, M.J., et al., *Large-Scale Surfactant Exfoliation of Graphene and Conductivity-Optimized Graphite Enabling Wireless Connectivity.* Advanced Materials Technologies, 2020. **5**(7).
111. Backes, C., et al., *Equipartition of Energy Defines the Size–Thickness Relationship in Liquid-Exfoliated Nanosheets.* ACS Nano, 2019. **13**(6): p. 7050-7061.
112. Backes, C., et al., *Production of Highly Monolayer Enriched Dispersions of Liquid-Exfoliated Nanosheets by Liquid Cascade Centrifugation.* ACS Nano, 2016. **10**(1): p. 1589-1601.
113. Griffin, A., et al., *Spectroscopic Size and Thickness Metrics for Liquid-Exfoliated h-BN.* Chemistry of Materials, 2018. **30**(6): p. 1998-2005.
114. Perkampus, H.-H., *UV-VIS Spectroscopy and its Applications*. 2013: Springer Science & Business Media.
115. Harvey, A., et al., *Non-resonant light scattering in dispersions of 2D nanosheets.* Nature Communications, 2018. **9**(1): p. 4553.
116. Quate, C., C. Gerber, and C. Binnig, *Atomic force microscope.* Phys. Rev. Lett, 1986. **56**(9): p. 930-933.
117. Overney, R.M., et al., *Friction measurements on phase-separated thin films with a modified atomic force microscope.* Nature, 1992. **359**(6391): p. 133-135.
118. Vanlandingham, M.R., et al., *Nanoscale Indentation of Polymer Systems Using the Atomic Force Microscope.* The Journal of Adhesion, 1997. **64**(1-4): p. 31-59.
119. Costa, K.D. and F.C.P. Yin, *Analysis of Indentation: Implications for Measuring Mechanical Properties With Atomic Force Microscopy.* Journal of Biomechanical Engineering, 1999. **121**(5): p. 462-471.
120. Jones, J.E., *On the determination of molecular fields.—I. From the variation of the viscosity of a gas with temperature.* Proceedings of the Royal Society of London. Series A, Containing Papers of a Mathematical and Physical Character, 1924. **106**(738): p. 441-462.
121. Jones, J.E., *On the determination of molecular fields. —II. From the equation of state of a gas.* Proceedings of the Royal Society of London. Series A, Containing Papers of a Mathematical and Physical Character, 1924. **106**(738): p. 463-477.
122. Hu, G., et al., *Functional inks and printing of two-dimensional materials.* Chemical Society Reviews, 2018. **47**(9): p. 3265-3300.

123. Kelly, A.G., et al., *All-printed capacitors from graphene-BN-graphene nanosheet heterostructures.* Applied Physics Letters, 2016. **109**(2): p. 023107.
124. Li, J., M.C. Lemme, and M. Östling, *Inkjet Printing of 2D Layered Materials.* ChemPhysChem, 2014. **15**(16): p. 3427-3434.
125. Lu, S., et al., *Flexible, Print-in-Place 1D–2D Thin-Film Transistors Using Aerosol Jet Printing.* ACS Nano, 2019. **13**(10): p. 11263-11272.
126. Wilkinson, N.J., et al., *A review of aerosol jet printing—a non-traditional hybrid process for micro-manufacturing.* The International Journal of Advanced Manufacturing Technology, 2019. **105**(11): p. 4599-4619.
127. Ng, L.W., et al., *Printing of graphene and related 2D materials.* Cham (Switzerland): Springer International Publishing, 2019.
128. He, P., et al., *Screen-Printing of a Highly Conductive Graphene Ink for Flexible Printed Electronics.* ACS Applied Materials & Interfaces, 2019. **11**(35): p. 32225-32234.
129. Chang, Q., et al., *Water-Soluble Hybrid Graphene Ink for Gravure-Printed Planar Supercapacitors.* Advanced Electronic Materials, 2018. **4**(8): p. 1800059.
130. Akbari, M., et al., *Fabrication and Characterization of Graphene Antenna for Low-Cost and Environmentally Friendly RFID Tags.* IEEE Antennas and Wireless Propagation Letters, 2016. **15**: p. 1569-1572.
131. Kelly, A.G., et al., *The electrical conductivity of solution-processed nanosheet networks.* Nature Reviews Materials, 2022. **7**(3): p. 217-234.
132. Hauquier, F., et al., *Conductive-probe AFM characterization of graphene sheets bonded to gold surfaces.* Applied Surface Science, 2012. **258**(7): p. 2920-2926.
133. Nirmalraj, P.N., et al., *Nanoscale Mapping of Electrical Resistivity and Connectivity in Graphene Strips and Networks.* Nano Letters, 2011. **11**(1): p. 16-22.
134. Kim, J.-Y. and N.A. Kotov, *Charge Transport Dilemma of Solution-Processed Nanomaterials.* Chemistry of Materials, 2014. **26**(1): p. 134-152.
135. Richter, N., et al., *Charge transport mechanism in networks of armchair graphene nanoribbons.* Scientific Reports, 2020. **10**(1): p. 1988.
136. Halim, J., et al., *Variable range hopping and thermally activated transport in molybdenum-based MXenes.* Physical Review B, 2018. **98**(10): p. 104202.
137. Schießl, S.P., et al., *Modeling carrier density dependent charge transport in semiconducting carbon nanotube networks.* Physical Review Materials, 2017. **1**(4): p. 046003.
138. Ponzoni, A., *The contributions of junctions and nanowires/nanotubes in conductive networks.* Applied Physics Letters, 2019. **114**(15): p. 153105.
139. Philipse, A.P., *The Random Contact Equation and Its Implications for (Colloidal) Rods in Packings, Suspensions, and Anisotropic Powders.* Langmuir, 1996. **12**(5): p. 1127-1133.
140. Nardin, M., E. Papirer, and J. Schultz, *Contributiona`l'etude des empilements au hasard de fibres et/ou de particules sphe´riques.* Powder Technology, 1985. **44**(2): p. 131-140.
141. Zhai, P.-Y., et al., *Calendering of free-standing electrode for lithium-sulfur batteries with high volumetric energy density.* Carbon, 2017. **111**: p. 493-501.
142. Huang, X., et al., *Highly Flexible and Conductive Printed Graphene for Wireless Wearable Communications Applications.* Scientific Reports, 2015. **5**(1): p. 18298.
143. Arapov, K., et al., *Conductivity Enhancement of Binder-Based Graphene Inks by Photonic Annealing and Subsequent Compression Rolling* Advanced Engineering Materials, 2016. **18**(7): p. 1234-1239.
144. Barwich, S., et al., *On the relationship between morphology and conductivity in nanosheet networks.* Carbon, 2021. **171**: p. 306-319.
145. Habibi, M., M. Adda-Bedia, and D. Bonn, *Effect of the material properties on the crumpling of a thin sheet.* Soft Matter, 2017. **13**(22): p. 4029-4034.
146. Mirzaali, M.J., et al., *Crumpling-based soft metamaterials: the effects of sheet pore size and porosity.* Scientific Reports, 2017. **7**(1): p. 13028.

147. Lin, Y.C., et al., *Crumpling under an Ambient Pressure.* Physical Review Letters, 2008. **101**(12): p. 125504.
148. Cottrino, S., et al., *Mechanical properties of crumpled aluminum foils.* Acta Materialia, 2014. **81**: p. 98-110.
149. Bouaziz, O., et al., *Compression of crumpled aluminum thin foils and comparison with other cellular materials.* Materials Science and Engineering: A, 2013. **570**: p. 1-7.
150. Deboeuf, S., et al., *Comparative Study of Crumpling and Folding of Thin Sheets.* Physical Review Letters, 2013. **110**(10): p. 104301.
151. Matan, K., et al., *Crumpling a Thin Sheet.* Physical Review Letters, 2002. **88**(7): p. 076101.
152. Baimova, J.A., et al., *Mechanical properties of crumpled graphene under hydrostatic and uniaxial compression.* Journal of Physics D: Applied Physics, 2015. **48**(9): p. 095302.
153. Becton, M., L. Zhang, and X. Wang, *On the crumpling of polycrystalline graphene by molecular dynamics simulation.* Physical Chemistry Chemical Physics, 2015. **17**(9): p. 6297-6304.
154. Kuo, W.-S., N.-H. Tai, and T.-W. Chang, *Deformation and fracture in graphene nanosheets.* Composites Part A: Applied Science and Manufacturing, 2013. **51**: p. 56-61.
155. Wood, A.J., *Witten's lectures on crumpling.* Physica A: Statistical Mechanics and its Applications, 2002. **313**(1): p. 83-109.
156. DiDonna, B.A. and T.A. Witten, *Anomalous Strength of Membranes with Elastic Ridges.* Physical Review Letters, 2001. **87**(20): p. 206105.
157. Åström, J.A., J. Timonen, and M. Karttunen, *Crumpling of a Stiff Tethered Membrane.* Physical Review Letters, 2004. **93**(24): p. 244301.
158. Lobkovsky, A., et al., *Scaling Properties of Stretching Ridges in a Crumpled Elastic Sheet.* Science, 1995. **270**(5241): p. 1482-1485.
159. Tallinen, T., J.A. Åström, and J. Timonen, *The effect of plasticity in crumpling of thin sheets.* Nature Materials, 2009. **8**(1): p. 25-29.
160. Backes, C., et al., *Guidelines for Exfoliation, Characterization and Processing of Layered Materials Produced by Liquid Exfoliation.* Chemistry of Materials, 2017. **29**(1): p. 243-255.
161. Ippolito, S., et al., *Covalently interconnected transition metal dichalcogenide networks via defect engineering for high-performance electronic devices.* Nature Nanotechnology, 2021. **16**(5): p. 592-598.
162. Ippolito, S., et al., *Unveiling Charge-Transport Mechanisms in Electronic Devices Based on Defect-Engineered MoS(2) Covalent Networks.* Adv Mater, 2023. **35**(15): p. e2211157.
163. Luan, B. and M.O. Robbins, *The breakdown of continuum models for mechanical contacts.* Nature, 2005. **435**(7044): p. 929-932.
164. Tapasztó, L., et al., *Breakdown of continuum mechanics for nanometre-wavelength rippling of graphene.* Nature Physics, 2012. **8**(10): p. 739-742.
165. Shimada, T., et al., *Breakdown of continuum fracture mechanics at the nanoscale.* Scientific reports, 2015. **5**(1): p. 1-6.
166. Yang, W., et al., *Review on auxetic materials.* Journal of Materials Science, 2004. **39**(10): p. 3269-3279.
167. Timoshenko, S., *Theory of elasticity*. 1951: Oxford.
168. Donald Turcotte, G.S., *Geodynamics*. 1982: Cambride University Press.
169. Nejati, M., M.L.T. Dambly, and M.O. Saar, *A methodology to determine the elastic properties of anisotropic rocks from a single uniaxial compression test.* Journal of Rock Mechanics and Geotechnical Engineering, 2019. **11**(6): p. 1166-1183.
170. Kelly, P., *Solid mechanics part I: An introduction to solid mechanics.* A Creative Commons Attributions, Mountain View, CA, 2013. **94042**.
171. Mols, R.H.M., et al., *Microscopic Carriers of Plasticity in Glassy Polystyrene.* Macromolecular Theory and Simulations, 2021. **30**(5): p. 2100021.
172. Argon, A.S., *The Physics of Deformation and Fracture of Polymers.* MRS Bulletin, 2014. **39**(8): p. 747-747.

173. Falk, M.L., *The Flow of Glass.* Science, 2007. **318**(5858): p. 1880-1881.
174. Cubuk, E.D., et al., *Structure-property relationships from universal signatures of plasticity in disordered solids.* Science, 2017. **358**(6366): p. 1033-1037.
175. Langer, J.S., *Shear-transformation-zone theory of deformation in metallic glasses.* Scripta Materialia, 2006. **54**(3): p. 375-379.
176. Falk, M.L. and J.S. Langer, *Deformation and Failure of Amorphous, Solidlike Materials.* Annual Review of Condensed Matter Physics, 2011. **2**(1): p. 353-373.
177. Li, J.C.M., *Plastic Deformation of Noncrystalline Materials*, in *Encyclopedia of Materials: Science and Technology*, K.H.J. Buschow, et al., Editors. 2001, Elsevier: Oxford. p. 7071-7078.
178. Greer, A.L., Y.Q. Cheng, and E. Ma, *Shear bands in metallic glasses.* Materials Science and Engineering: R: Reports, 2013. **74**(4): p. 71-132.
179. Loo, L.S., R.E. Cohen, and K.K. Gleason, *Deuterium nuclear magnetic resonance of deuterium oxide in nylon 6 under active uniaxial deformation.* Polymer, 2000. **41**(21): p. 7699-7704.
180. Loo, L.S., R.E. Cohen, and K.K. Gleason, *Chain Mobility in the Amorphous Region of Nylon 6 Observed under Active Uniaxial Deformation.* Science, 2000. **288**(5463): p. 116-119.
181. R. O. Davis, A.P.S.S., *Plasticity and Geomechanics*. 2001: Cambridge University Press.
182. Shames, I.H., *Elastic and inelastic stress analysis*. 1997: CRC Press.
183. Kazimi, S.M.A., *Solid Mechanics*. 2001: Tata McGraw-Hill.
184. Hill, R., *The mathematical theory of plasticity*. Vol. 11. 1998: Oxford university press.
185. Kelly, P., *An Introduction to Solid Mechanics*. 2023, University of Auckland.
186. Taylor, G.I., *Plastic strain in metals.* our. Inst. Metals., 1938. **62**: p. 307-324.
187. Hill, R. and E. Orowan, *A theory of the yielding and plastic flow of anisotropic metals.* Proceedings of the Royal Society of London. Series A. Mathematical and Physical Sciences, 1948 **193**(1033): p. 281-297.
188. Hill, R., *Theoretical plasticity of textured aggregates.* Mathematical Proceedings of the Cambridge Philosophical Society, 1979. **85**(1): p. 179-191.
189. Hosford, W.F., *Comments on anisotropic yield criteria.* International Journal of Mechanical Sciences, 1985. **27**(7): p. 423-427.
190. Karafillis, A.P. and M.C. Boyce, *A general anisotropic yield criterion using bounds and a transformation weighting tensor.* Journal of the Mechanics and Physics of Solids, 1993. **41**(12): p. 1859-1886.
191. Kim, E. and C. Chen, *Calculation of bulk modulus for highly anisotropic materials.* Physics Letters A, 2004. **326**(5): p. 442-448.
192. Cheng, A.H.D., *Material coefficients of anisotropic poroelasticity.* International Journal of Rock Mechanics and Mining Sciences, 1997. **34**(2): p. 199-205.
193. Makse, H.A., et al., *Why Effective Medium Theory Fails in Granular Materials.* Physical Review Letters, 1999. **83**(24): p. 5070-5073.
194. Magnanimo, V., et al., *Characterizing the shear and bulk moduli of an idealized granular material.* Europhysics Letters, 2008. **81**(3): p. 34006.
195. Kerimov, A., et al., *The Influence of Convex Particles' Irregular Shape and Varying Size on Porosity, Permeability, and Elastic Bulk Modulus of Granular Porous Media: Insights From Numerical Simulations.* Journal of Geophysical Research: Solid Earth, 2018. **123**(12): p. 10,563-10,582.
196. Jones Parry, E. and D. Tabor, *Pressure dependence of the shear modulus of various polymers.* Journal of Materials science, 1974. **9**: p. 289-292.
197. Liao, C.L., et al., *Pressure-dependent elastic moduli of granular assemblies.* International Journal for Numerical and Analytical Methods in Geomechanics, 2000. **24**(3): p. 265-279.
198. Mehl, M.J., *Pressure dependence of the elastic moduli in aluminum-rich Al-Li compounds.* Physical Review B, 1993. **47**(5): p. 2493.

199. Assimaki, D. and E. Kausel, *An equivalent linear algorithm with frequency-and pressure-dependent moduli and damping for the seismic analysis of deep sites.* Soil Dynamics and Earthquake Engineering, 2002. **22**(9-12): p. 959-965.
200. Goddard, J.D. and J.E. Enderby, *Nonlinear elasticity and pressure-dependent wave speeds in granular media.* Proceedings of the Royal Society of London. Series A: Mathematical and Physical Sciences, 1997. **430**(1878): p. 105-131.
201. Kim, J.W., G.A. Medvedev, and J.M. Caruthers, *Observation of yield in triaxial deformation of glassy polymers.* Polymer, 2013. **54**(11): p. 2821-2833.
202. Ward, I.M., *Review: The yield behaviour of polymers.* Journal of Materials Science, 1971. **6**(11): p. 1397-1417.
203. Roscoe, K.H. and J. Burland, *On the generalized stress-strain behaviour of wet clay.* 1968.
204. Roscoe, K., A. Schofield, and A. Thurairajah, *Yielding of clays in states wetter than critical.* Geotechnique, 1963. **13**(3): p. 211-240.
205. Ravi-Chandar, K. and Z. Ma, *Inelastic deformation in polymers under multiaxial compression.* Mechanics of Time-Dependent Materials, 2000. **4**: p. 333-357.
206. Roland, C., et al., *Supercooled dynamics of glass-forming liquids and polymers under hydrostatic pressure.* Reports on Progress in Physics, 2005. **68**(6): p. 1405.
207. Fujimoto, D., et al. *8Li Spin Relaxation as a Probe of the Modification of Molecular Dynamics by Inelastic Deformation of Glassy Polystyrene*. in *Journal of Physics: Conference Series*. 2023. IOP Publishing.
208. Nakada, O., *Theory of viscoelasticity of amorphous polymers.* Journal of the Physical Society of Japan, 1955. **10**(9): p. 804-813.
209. Shaw, M.T. and W.J. MacKnight, *Introduction to polymer viscoelasticity*. 2018: John Wiley & Sons.
210. Alferov, Z.I., *The semiconductor revolution in the 20th century.* Russian Chemical Reviews, 2013. **82**(7): p. 587.
211. Haguenau, F., et al., *Key Events in the History of Electron Microscopy.* Microscopy and Microanalysis, 2003. **9**(2): p. 96-138.
212. Berkovich, E., *Three faceted diamond pyramid for micro-hardness testing.* Industrial Diamond Review, 1951. **11**(127): p. 129.
213. Sakharova, N.A., et al., *Comparison between Berkovich, Vickers and conical indentation tests: A three-dimensional numerical simulation study.* International Journal of Solids and Structures, 2009. **46**(5): p. 1095-1104.
214. Oliver, W.C. and J.B. Pethica, *Method for continuous determination of the elastic stiffness of contact between two bodies*. 1989, Google Patents.
215. Hay, J., P. Agee, and E. Herbert, *Continuous stiffness measurement during instrumented indentation testing.* Experimental Techniques, 2010. **34**(3): p. 86-94.
216. Hertz, H., *Ueber die Berührung fester elastischer Körper.* 1882.
217. Johnson, K.L., *Contact Mechanics*. 1985, Cambridge: Cambridge University Press.
218. Johnson, K.L., et al., *Surface energy and the contact of elastic solids.* Proceedings of the Royal Society of London. A. Mathematical and Physical Sciences, 1971. **324**(1558): p. 301-313.
219. Derjaguin, B.V., V.M. Muller, and Y.P. Toporov, *Effect of contact deformations on the adhesion of particles.* Journal of Colloid and Interface Science, 1975. **53**(2): p. 314-326.
220. Wald, M.J., J.M. Considine, and K.T. Turner, *Determining the Elastic Modulus of Compliant Thin Films Supported on Substrates from Flat Punch Indentation Measurements.* Experimental Mechanics, 2013. **53**(6): p. 931-941.
221. Vlassak, J.J. and W.D. Nix, *A new bulge test technique for the determination of Young's modulus and Poisson's ratio of thin films.* Journal of Materials Research, 1992. **7**(12): p. 3242-3249.
222. Nix, W.D., *Mechanical properties of thin films.* Metallurgical Transactions A, 1989. **20**(11): p. 2217.

223. Hay, J. and B. Crawford, *Measuring substrate-independent modulus of thin films.* Journal of Materials Research, 2011. **26**(6): p. 727-738.
224. Bec, S., A. Tonck, and J.L. Loubet, *A simple guide to determine elastic properties of films on substrate from nanoindentation experiments.* Philosophical Magazine, 2006. **86**(33-35): p. 5347-5358.
225. Yang, F., *Asymptotic solution to axisymmetric indentation of a compressible elastic thin film.* Thin Solid Films, 2006. **515**(4): p. 2274-2283.
226. Xu, H. and G.M. Pharr, *An improved relation for the effective elastic compliance of a film/substrate system during indentation by a flat cylindrical punch.* Scripta Materialia, 2006. **55**(4): p. 315-318.
227. Mujika, F., *On the difference between flexural moduli obtained by three-point and four-point bending tests.* Polymer Testing, 2006. **25**(2): p. 214-220.
228. Mbam, S.O., et al., *Thin-film coating; historical evolution, conventional deposition technologies, stress-state micro/nano-level measurement/models and prospects projection: a critical review.* Materials Research Express, 2019. **6**(12): p. 122001.
229. Bhushan, B., *Depth-sensing nanoindentation measurement techniques and applications.* Microsystem Technologies, 2017. **23**(5): p. 1595-1649.
230. Sinnott, A.D., et al., *Pressure Dependent Mechanical Properties of Thin Films under Uniaxial Strain via the Layer Compression Test*. 2023, Trinity College Dublin: TARA preprint.
231. McManamon, C., et al., *Effect of cross-linking and hydration on microscale flat punch indentation contact to collagen-hyaluronic acid films in the viscoelastic limit.* Acta Biomaterialia, 2020. **111**: p. 279-289.
232. Luo, M., et al., *Simultaneous Measurement of Single-Cell Mechanics and Cell-to-Materials Adhesion Using Fluidic Force Microscopy.* Langmuir, 2022. **38**(2): p. 620-628.
233. Li, J.C.M., *Impression creep and other localized tests.* Materials Science and Engineering: A, 2002. **322**(1): p. 23-42.
234. *Simulia software packages*. 2023 [cited 2023 20/07/2023]; Simulia website]. Available from: https://www.3ds.com/products/simulia.
235. Cross, G.L.W., B.S. O'Connell, and J.B. Pethica, *Influence of elastic strains on the mask ratio in glassy polymer nanoimprint.* Applied Physics Letters, 2005. **86**(8): p. 081902.
236. Wang, H.F., *Theory of Linear Poroelasticity with Applications to Geomechanics and Hydrogeology*. 2017, Princeton University Press. p. 116-149.
237. Sinnott, A.D., et al., *Pressure-dependent mechanical properties of thin films under uniaxial strain via the layer compression test.* Journal of Materials Research, 2023.
238. Buchko, C.J., et al., *Processing and microstructural characterization of porous biocompatible protein polymer thin films.* Polymer, 1999. **40**(26): p. 7397-7407.
239. Jones, R.L., et al., *Chain conformation in ultrathin polymer films.* Nature, 1999. **400**(6740): p. 146-149.
240. García, N.A. and J.-L. Barrat, *Entanglement Reduction Induced by Geometrical Confinement in Polymer Thin Films.* Macromolecules, 2018. **51**(23): p. 9850-9860.
241. Brazil, O., et al., *Densification of a polymer glass under high-pressure shear flow.* Physical Review B, 2022. **106**(6): p. L060103.
242. Hughes, D.S. and J.L. Kelly, *Second-Order Elastic Deformation of Solids.* Physical Review, 1953. **92**(5): p. 1145-1149.
243. Crook, A.J.L., et al., *Predictive modelling of structure evolution in sandbox experiments.* Journal of Structural Geology, 2006. **28**(5): p. 729-744.
244. Bigoni, D. and A. Piccolroaz, *Yield criteria for quasibrittle and frictional materials.* International Journal of Solids and Structures, 2004. **41**(11): p. 2855-2878.
245. Quinson, R., et al., *Yield criteria for amorphous glassy polymers.* Journal of Materials Science, 1997. **32**(5): p. 1371-1379.
246. Kim, J.W., G.A. Medvedev, and J.M. Caruthers, *Mobility evolution during tri-axial deformation of a glassy polymer.* Polymer, 2014. **55**(6): p. 1570-1573.

247. Stephens, D., H. Heard, and R. Schock, *High-pressure mechanical properties of polymethylmethacrylate*. 1972, California Univ., Livermore (USA). Lawrence Livermore Lab.

248. Han, E., et al., *Ultrasoft slip-mediated bending in few-layer graphene.* Nature Materials, 2020. **19**(3): p. 305-309.

249. Hall, L.D., *Nuclear Magnetic Resonance*, in *Advances in Carbohydrate Chemistry*, M.L. Wolfrom, Editor. 1964, Academic Press. p. 51-93.

250. Mlynárik, V., *Introduction to nuclear magnetic resonance.* Analytical Biochemistry, 2017. **529**: p. 4-9.

251. Abov, Y.G., A. Gulko, and F. Dzheparov, *Beta-NMR spectroscopy: Modern state and prospects.* Physics of Atomic Nuclei, 2006. **69**(10): p. 1701-1710.

252. McKenzie, I., et al., *Enhanced high-frequency molecular dynamics in the near-surface region of polystyrene thin films observed with β-NMR.* Soft Matter, 2015. **11**(9): p. 1755-1761.

253. McKenzie, I., et al., *Direct measurements of the temperature, depth and processing dependence of phenyl ring dynamics in polystyrene thin films by β-detected NMR.* Soft Matter, 2018. **14**(36): p. 7324-7334.

254. Schaefer, J., et al., *Molecular motion in glassy polystyrenes.* Macromolecules, 1984. **17**(6): p. 1107-1118.

255. Spiess, H.W., *Molecular dynamics of solid polymers as revealed by deuteron NMR.* Colloid and Polymer Science, 1983. **261**(3): p. 193-209.

256. Ziegler, J.F., M.D. Ziegler, and J.P. Biersack, *SRIM – The stopping and range of ions in matter (2010).* Nuclear Instruments and Methods in Physics Research Section B: Beam Interactions with Materials and Atoms, 2010. **268**(11): p. 1818-1823.

257. Lindsey, C.P. and G.D. Patterson, *Detailed comparison of the Williams–Watts and Cole–Davidson functions.* The Journal of Chemical Physics, 1980. **73**(7): p. 3348-3357.

258. Brazil, O., et al., *In situ measurement of bulk modulus and yield response of glassy thin films via confined layer compression.* Journal of Materials Research, 2020. **35**(6): p. 644-653.

259. Cross, G.L.W., et al., *Variable temperature thin film indentation with a flat punch.* Rev. Sci. Instrum., 2008. **79**: p. 013904-013904-13.

260. Eshelby, J.D. and R.E. Peierls, *The elastic field outside an ellipsoidal inclusion.* Proceedings of the Royal Society of London. Series A. Mathematical and Physical Sciences, 1997. **252**(1271): p. 561-569.

261. Uhlířová, T. and W. Pabst, *Poisson's ratio of porous and cellular materials with randomly distributed isometric pores or cells.* Journal of the American Ceramic Society, 2020. **103**(12): p. 6961-6977.

262. Lutz, M.P. and R.W. Zimmerman, *The effect of pore shape on the Poisson ratio of porous materials.* Mathematics and Mechanics of Solids, 2021. **26**(8): p. 1191-1203.

263. Sayers, C.M., *The effect of anisotropy on the Young's moduli and Poisson's ratios of shales.* Geophysical Prospecting, 2013. **61**(2 - Rock Physics for Reservoir Exploration, Characterisation and Monitoring): p. 416-426.

264. Witten, T.A., *Stress focusing in elastic sheets.* Reviews of Modern Physics, 2007. **79**(2): p. 643-675.

265. Barwich, S. and M.E. Möbius, *The elastic response of graphene oxide gels as a crumpling phenomenon.* Soft Matter, 2022. **18**(43): p. 8223-8228.

266. Xiong, S. and G. Cao, *Bending response of single layer MoS2.* Nanotechnology, 2016. **27**(10): p. 105701.

267. Huang, X., et al., *Binder-free highly conductive graphene laminate for low cost printed radio frequency applications.* Applied Physics Letters, 2015. **106**(20): p. 203105.

268. Chen, X., C. Yi, and C. Ke, *Bending stiffness and interlayer shear modulus of few-layer graphene.* Applied Physics Letters, 2015. **106**(10): p. 101907.

269. Jiang, J.W., *The buckling of single-layer MoS2 under uniaxial compression.* Nanotechnology, 2014. **25**(35): p. 355402.

270. Cross, G.L.W., et al., *Room Temperature Mechanical Thinning and Imprinting of Solid Films.* Nano Letters, 2007. **7**(2): p. 357-362.
271. Herbert, E.G., et al., *Measuring the constitutive behavior of viscoelastic solids in the time and frequency domain using flat punch nanoindentation.* Journal of Materials Research, 2009. **24**(3): p. 626-637.
272. Macaulay, M. and P. Rognon, *Viscosity of cohesive granular flows.* Soft matter, 2021. **17**(1): p. 165-173.
273. Yang, W.-L. and S.-S. Hsiau, *The effect of liquid viscosity on sheared granular flows.* Chemical Engineering Science, 2006. **61**(18): p. 6085-6095.
274. Rauter, M., T. Barker, and W. Fellin, *Granular viscosity from plastic yield surfaces: The role of the deformation type in granular flows.* Computers and Geotechnics, 2020. **122**: p. 103492.
275. Sweat, M.L., A.S. Parker, and S.P. Beaudoin, *Compressive behavior of high-viscosity granular systems: Effects of viscosity and strain rate.* Powder Technology, 2016. **302**: p. 480-487.
276. Plazek, D.J. and V.M. O'Rourke, *Viscoelastic behavior of low molecular weight polystyrene.* Journal of Polymer Science Part A-2: Polymer Physics, 1971. **9**(2): p. 209-243.
277. Edgeworth, R., B.J. Dalton, and T. Parnell, *The pitch drop experiment.* European Journal of Physics, 1984. **5**(4): p. 198.
278. Boland, C.S., et al., *Sensitive electromechanical sensors using viscoelastic graphene-polymer nanocomposites.* Science, 2016. **354**(6317): p. 1257-1260.
279. Torres, J., et al., *Adhesion Energies of 2D Graphene and MoS2 to Silicon and Metal Substrates.* physica status solidi (a), 2018. **215**(1): p. 1700512.
280. Chen, S., et al., *Surface-Dependent Adhesion Properties of Graphene on Diamonds for the Fabrication of Nanodevices: A Molecular Dynamics Investigation.* ACS Applied Nano Materials, 2023. **6**(4): p. 2942-2951.
281. Gabbett, C., *Electrical, Mechanical & Morphological Characterisation of Nanosheet Networks*, in *School of Physics*. 2020, Trinity College Dublin: Dublin.
282. Hetnarski, R.B., *Encyclopedia of Thermal Stresses*. 1st ed. ed. 2014, Dordrecht: Springer Netherlands : Imprint: Springer.
283. Fan, J. and G. Li, *High enthalpy storage thermoset network with giant stress and energy output in rubbery state.* Nature Communications, 2018. **9**(1): p. 642.
284. Wick, C.D., A.J. Peters, and G. Li, *Quantifying the contributions of energy storage in a thermoset shape memory polymer with high stress recovery: A molecular dynamics study.* Polymer, 2021. **213**: p. 123319.
285. Falk, M.L. and J.S. Langer, *Dynamics of viscoplastic deformation in amorphous solids.* Physical Review E, 1998. **57**(6): p. 7192-7205.
286. Mott, P.H., A.S. Argon, and U.W. Suter, *Atomistic modelling of plastic deformation of glassy polymers.* Philosophical Magazine A, 1993. **67**(4): p. 931-978.
287. Lee, H.-N., et al., *Dye reorientation as a probe of stress-induced mobility in polymer glasses.* The Journal of Chemical Physics, 2008. **128**(13): p. 134902.
288. Lacks, D.J. and M.J. Osborne, *Energy Landscape Picture of Overaging and Rejuvenation in a Sheared Glass.* Physical Review Letters, 2004. **93**(25): p. 255501.
289. Wallace, M.L. and B. Joós, *Shear-Induced Overaging in a Polymer Glass.* Physical Review Letters, 2006. **96**(2): p. 025501.
290. Liu, F., et al., *Synthesis of graphene materials by electrochemical exfoliation: Recent progress and future potential.* Carbon Energy, 2019. **1**(2): p. 173-199.
291. Lu, Y. and D.M. Shinozaki, *Microindentation induced debonding of polymer thin films from rigid substrates.* Journal of Materials Science, 2002. **37**(7): p. 1283-1293.